Technische Universität München
TUM School of Computation, Information and Technology

Paradigms for the Low-Frequency Stable Solution of Electromagnetic Scattering, Radiation, and Equivalent Source Reconstruction Problems

Bernd Hofmann

Vollständiger Abdruck der von der TUM School of Computation, Information and Technology der Technischen Universität München zur Erlangung eines

Doktors der Ingenieurwissenschaften (Dr.-Ing.)

genehmigten Dissertation.

Vorsitz:	Prof. Dr.-Ing. Norbert Hanik
Prüfende der Dissertation:	1. Prof. Dr.-Ing. Thomas Eibert
	2. Prof. Dr.-Ing. Simon B. Adrian
	3. Prof. Dr. Kristof Cools

Die Dissertation wurde am 15.04.2024 bei der Technischen Universität München eingereicht und durch die TUM School of Computation, Information and Technology am 18.09.2024 angenommen.

Kurzbeschreibung

Im Rahmen der vorliegenden Arbeit werden zwei Teilgebiete der numerischen elektromagnetischen Feldberechnung behandelt: Die Streuung und Abstrahlung von ideal leitenden Körpern sowie die Rekonstruktion äquivalenter Quellen anhand von Messungen des elektromagnetischen Feldes.

Bezüglich des ersten Teilgebietes, werden Paradigmen zur Stabilisierung der weit verbreiteten elektrischen Feldintegralgleichung bei niedrigen Frequenzen vorgestellt. Ausgehend von einer Galerkin-Diskretisierung mit Rao-Wilton-Glisson-Basisfunktionen und der etablierten Vorkonditionierung mittels Quasi-Helmholtz-Projektoren, wird ein Verfahren präsentiert, welches die katastrophalen Rundungsfehler beseitigt, welche entstehen, wenn ein Feld mit solenoidalen (divergenzfreien) Funktionen getestet wird. Weiterhin, wird ein adaptives Normierungsverfahren für die Quasi-Helmholtz-Projektoren vorgestellt, welches sich selbst an die vorhandene Anregung anpasst. Dadurch wir das Problem der katastrophalen Rundungsfehler in der Lösung der elektrischen Feldintegralgleichung gelöst, indem sichergestellt wird, dass sowohl die solenoidalen als auch die nicht-solenoidalen Komponenten des zu bestimmenden Oberflächenstroms mit ähnlicher relativer Genauigkeit bestimmt werden. In der Folge können beliebige Anregungen für Streu- und Abstrahlungsprobleme behandelt werden ohne die Notwendigkeit Vorwissen über die Anregung vorauszusetzen und ohne ad-hoc Anpassungen an spezifische Anregungen. Außerdem wird für die Diskretisierung der elektrischen Feldintegralgleichung basierend auf B-Spline Basisfunktionen eine Quasi-Helmholtz-Zerlegung hergeleitet. Diese kann explizit in Form von dünnbesetzten Transformationsmatrizen ausgedrückt werden und erlaubt somit die in diesem Zusammenhang von linearen Basisfunktionen bekannten vorteilhaften Eigenschaften auf B-Spline Basisfunktionen beliebiger Polynomordnung zu übertragen.

Bezüglich des zweiten Teilgebietes, der Rekonstruktion äquivalenter Quellen, wird ein Verfahren zur niederfrequenten Stabilisierung der Rekonstruktion äquivalenter elektrischer Ströme anhand von Messwerten des elektromagnetischen Feldes vorgestellt. Hierzu werden die aus Streuproblemen bekannten Quasi-Helmholtz-Projektoren adaptiert, sowie die adaptive Frequenznormierung und die Stabilisierung des Testens von Feldern mit solenoidalen Funktionen mit einbezogen. Als ein letztes Paradigma wird gezeigt, wie die als Compressed Sensing (CS) bezeichneten Signalverarbeitungsverfahren zuverlässig im Bereich der sphärischen Nahfeld-Fernfeld-Transformation angewendet werden können. Ziel dabei ist es grund-

sätzlich, die Anzahl der Messwerte zu verringern, die aufgenommen werden müssen, um das abgestrahlte Feld einer Antenne an beliebigen Punkten bestimmen zu können. Im Rahmen dessen wird ein Verfahren vorgestellt, um die minimal benötigte Anzahl an Messwerten zu bestimmen, sodass mittels CS die äquivalenten Quellen mit einer vordefinierten Genauigkeit rekonstruiert werden können. Hierbei werden auch Einflussfaktoren wie die Wahl der Messorte, das Messrauschen oder der Einfluss der Messantenne berücksichtigt.

Abstract

Two problem areas encountered in computational electromagnetics (CEM) are addressed in this dissertation: the radiation and the scattering from perfectly electrically conducting (PEC) bodies and the reconstruction of equivalent sources from measurements of electromagnetic fields with probe antennas.

Concerning the first area, paradigms are presented to low-frequency stabilize the well-established electric field integral equation (EFIE). Starting from a Galerkin discretization with Rao-Wilton-Glisson (RWG) basis functions and the known stabilization via quasi-Helmholtz projectors, an excitation-agnostic scheme is derived to overcome the catastrophic round-off errors encountered when testing a field with solenoidal functions. Moreover, an excitation-agnostic and self-adaptive frequency normalization is introduced to the quasi-Helmholtz projectors to overcome catastrophic round-off errors in the solution of the EFIE. The self-adaptive normalization ensures that both solenoidal and non-solenoidal components of the determined surface current density are recovered with a similar relative accuracy, which is required to determine the radiated and scattered fields accurately. As a consequence, arbitrary excitations can be handled without a-priori information about the excitations and without ad-hoc adaptions. For the B-spline-based discretization of the EFIE, a quasi-Helmholtz decomposition is derived. The latter can be expressed explicitly in terms of sparse mapping matrices which allows to transfer the advantageous properties known from the low-order mesh-based stabilization schemes to the high-order B-spline-based discretization of arbitrary polynomial degree.

Concerning the second area, the reconstruction of equivalent sources, a scheme is presented to low-frequency stabilize the reconstruction of equivalent electric currents described by RWG functions. To this end, the quasi-Helmholtz projectors are adapted, and the self-adaptive frequency normalization, as well as the stabilized evaluation of arbitrary excitations by solenoidal functions, are incorporated. Finally, it is shown how compressed sensing (CS) can, in principle, be applied reliably to reduce the number of measurement samples that are required for a spherical near-field far-field transformation (NFFFT) based on the spherical vector wave expansion of the radiated field of a device under test (DUT). This includes a strategy to determine the minimum number of samples required for CS to achieve a predefined far field (FF) accuracy, considering influence factors such as noise, the sampling locations, or the probe antenna.

Acknowledgment

"Living is worthwhile if one can contribute in
some small way to this endless chain of progress."
Paul Dirac

I feel quite lucky that I got the chance to try to understand and overcome some of the problems in numerical field theory by working at the Chair of High-Frequency Engineering at the Technical University of Munich. Essential parts of my corresponding thoughts during this time found their way into this dissertation. In particular, and foremost, I would like to thank Professor Thomas Eibert, who, in the first place, provided this opportunity to me. It is he who introduced me to the world of field theory, gave me freedom in my research, yet offered me advice and directions when needed. Not less, I would like to thank Professor Simon Adrian. He became my second advisor shortly after he became a professor at the Universität Rostock. His introduction to the low-frequency stabilization of integral equations formed the foundation for my understanding of the topic. In countless video calls, he patiently advised and discussed with me, which, for me at all times, was fruitful in many regards. Not least, he introduced me to many colleagues in our field of research, of which I would like to highlight Professor Francesco Andriulli. I had the pleasure to learn from him, work, and discuss with him on many occasions. Moreover, I am grateful to Professor Kristof Cools, whose public code base was often the starting point for my own implementations and who honored me by serving on my thesis committee, as well as to Professor Norbert Hanik for chairing my committee.

The biggest pleasure during my time at the Chair of High-Frequency Engineering were all the colleagues, who each in their individual way, contributed to a wonderful working environment. May it be my early colleagues Dr. Ole Neitz who patiently advised me in my master thesis, Raimund Mauermeier, who introduced me to several important code bases, Dr. Gerhard Hamberger, Dr. Mehmet Taygur, Dr. Christian Koenen, Christoph Eisner, Dr. Safiullah Khan, Arslan Azhar and Dr. Clemens Moroder, or later companions Dr. Fabian Faul, Daniel Ostrzyharczik, Dr. Matthias Ehrensberger, Christian Fruth, Mohammad Mirmohammadsadeghi, Quanfeng Wang, Abdo Salah, Sina Moradi and Marius Brinkmann. Dr. Björn Möhring, Jonas Tiede, Han Na, and Denis Unruh made the participation in different conferences a unique experience. Stefan Punzet, Christian Herpers, Matthias Saurer, Dr. Uwe

Siart, and Thomas Mittereder did so also on many occasions in some joint after-work contemplations. Moreover, I would like to express my gratitude to Li Zhang, who brought the charisma of Shanghai to Munich, as well as to Joshua Tetzner and Paula Respondek, who felt like colleagues even though located in quite some distance in Rostock.

A special thanks goes to my roommate for many years, Jonas Weindl, who made the stress of everyday work substantially more bearable through many joyful discussions and common activities. Similarly, thanks to Danijel Jukic who became my roommate afterwards and also made the days a lot more enjoyable, not least with many insightful (Julia) programming related discussions. Invaluable for me was the time with Dr. Josef Knapp when teaching the Hauptseminar and when, on many occasions, discussing research and many aspects of life, even more so during a long period of home-office. Also, a special thanks goes to Dr. Alexander Paulus and Dr. Jonas Kornprobst for many insightful discussions, joint stays at conferences, and cultural experiences.

Last but not least, I would like to thank my friends and, even more, my family for their everlasting support. Especially, my parents and grandparents, my aunt, my sister, her husband, and my niece for always providing the best environment possible.

München, Germany — Bernd Hofmann
October 21, 2024

Contents

Kurzbeschreibung iii

Abstract v

Acknowledgment vii

Part I Preliminaries 1

1 Introduction 3
- 1.1 Numerical Techniques in Electromagnetics . . . 3
  - 1.1.1 Electromagnetic Radiation and Scattering . . . 4
  - 1.1.2 Equivalent Source Reconstruction . . . 6
- 1.2 Scope and Outline of the Thesis . . . 9
- 1.3 Notation . . . 10

2 Relevant Electromagnetic Principles 11
- 2.1 Considered Physical Model . . . 11
- 2.2 Electromagnetic Radiation in Free Space . . . 12
  - 2.2.1 Radiation in Terms of Potentials . . . 12
  - 2.2.2 Radiation in Terms of Spherical Vector Waves . . . 15
- 2.3 Scattering and Radiation from PEC Bodies—The EFIE . . . 17
- 2.4 Equivalent Source Reconstruction . . . 18

3 Discretization, Solution Uniqueness, and Conditioning 21
- 3.1 Galerkin Discretization of the EFIE . . . 21
  - 3.1.1 Surface Representation . . . 22
  - 3.1.2 Basis Functions . . . 24
  - 3.1.3 Matrix Elements . . . 25
- 3.2 Quasi-Helmholtz Decompositions . . . 25
  - 3.2.1 Loop-Star Decomposition . . . 26
  - 3.2.2 Quasi-Helmholtz Projectors . . . 27
- 3.3 Equivalent Source Reconstruction . . . 28

Part II Paradigms for Boundary Integral Scattering and Radiation Formulations 31

4 An Excitation Agnostic Right-Hand Side Discretization Scheme 33
4.1 Stable Evaluation of the Right-Hand Side On Multiply-Connected Geometries . . . 35
4.1.1 Analysis of the right-hand side (RHS) Round-Off Errors—When to Expect and When Not to Expect Them . . . 36
4.1.2 Handling Arbitrary Excitations—Construction of Scalar Functions ψ_m for Global RWG Loops . . . 38
4.2 Stable Right-Hand Side Evaluation for Quasi-Helmholtz Projectors 41
4.2.1 Stable Evaluation of the Right-Hand Side . . . 42
4.2.2 Efficient Evaluation of the Projected RHS . . . 42
4.3 Numerical Results . . . 44
4.3.1 Scattering from a Sphere . . . 45
4.3.2 Scattering from Multiply-Connected Geometries . . . 50
4.4 Conclusion . . . 53

5 An Excitation-Aware and Self-Adaptive Frequency Normalization 55
5.1 Analysis of the Frequency Normalization and Self-Adaptive Scheme 57
5.1.1 Relevant Current Components . . . 57
5.1.2 Self-Adaptive Normalization for Loop-Star Basis . . . 59
5.1.3 Quasi-Helmholtz Projector Normalization Factors . . . 61
5.2 Eigenvalue Distribution and Implementation Details . . . 65
5.2.1 On the Simplification of the Conditions to be Checked . 67
5.2.2 Loop-Star Decomposition . . . 67
5.2.3 Quasi-Helmholtz Projectors . . . 68
5.3 Numerical Results . . . 69
5.3.1 Scattering from a Sphere . . . 71
5.3.2 Scattering from Multiply-Connected Geometries . . . 74
5.3.3 Inductive and Capacitive Gap Excitation . . . 76
5.4 Conclusion . . . 78

6 A Low-Frequency Stabilization for the B-Spline-Based Isogeometric Discretization 81
6.1 Isogeometric Discretization of the Electric Field Integral Equation 83
6.1.1 Definition of the B-splines . . . 83
6.1.2 Geometry Representation . . . 84
6.1.3 Discretization . . . 85
6.2 Loop-Star Decomposition for the Isogeometric Discretization . . 88
6.2.1 Solenoidal Basis—Loop Mapping Matrix . . . 88
6.2.2 Non-solenoidal Basis—Star Mapping Matrix . . . 93
6.2.3 Complete Decomposition—Properties of the Mappings . 96
6.3 Quasi-Helmholtz Projectors . . . 98

6.4 Numerical Results . . . 99
6.4.1 Scattering from a Sphere . . . 100
6.4.2 Scattering from Open Geometries . . . 101
6.4.3 Scattering from Multiply-Connected Geometries . . . 102
6.5 Conclusion . . . 106

Part III Paradigms for Equivalent Source Reconstructions 107

7 A Low-Frequency Stable Equivalent Surface Current Reconstruction Scheme 109
7.1 Field Transformation Formulation . . . 110
7.1.1 Equivalent Current Description of the Probe . . . 110
7.1.2 Dipole Probe Antennas . . . 112
7.2 Low-Frequency Stabilization . . . 113
7.2.1 Testing with RWG Functions . . . 113
7.2.2 Testing with Dipole Probe Antennas . . . 114
7.3 Results . . . 115
7.3.1 Reconstruction of Fields Scattered by a Sphere . . . 115
7.3.2 Reconstruction of a Ring Current . . . 117
7.4 Conclusion . . . 118

8 On the Minimum Number of Samples for Sparse Recovery 121
8.1 Spherical Near-Field Measurements . . . 123
8.2 Applicability of Compressed Sensing . . . 125
8.2.1 Sparsity and Compressibility . . . 125
8.2.2 Recovery Strategy . . . 125
8.2.3 The Required Number of Measurements . . . 126
8.3 The Minimum Number of Samples for CS in Spherical NFFFT . . . 128
8.3.1 Setting up the PTDs . . . 128
8.3.2 Comparison with Theoretical Bounds . . . 129
8.3.3 The Error Definition . . . 131
8.3.4 Influence of the Sampling Grids . . . 132
8.3.5 Influence of the Problem Size . . . 134
8.3.6 Influence of Sparsity Defects—Stability . . . 134
8.3.7 Influence of Noise—Robustness . . . 135
8.3.8 Influence of Probe Correction . . . 137
8.3.9 Practically Relevant Case . . . 138
8.4 NFFFT Results Using CS . . . 138
8.4.1 Simulation of a Horn Antenna . . . 138
8.4.2 Concerning the Absolute Minimum of Samples . . . 141
8.4.3 Simulation of an Antenna Array . . . 142
8.4.4 Measurement of a Double-Ridged Horn Antenna . . . 144
8.5 Conclusion . . . 146

Part IV Addendum **147**

9 Conclusion **149**

A Asymptotic Scalings **153**
A.1 Right-Hand Side Scalings 153
A.2 Scaling of TE and TM Modes 154

B Derivatives of NURBS Surfaces **157**

Nomenclature **159**
List of Symbols 159
Abbreviations 161

Bibliography **192**

Publications of the Author **193**

Supervised Student Projects **197**

Part I

Preliminaries

1

Introduction

"The purpose of computation is insight, not numbers."
[Hamming 1962]

There is a multitude of applications where the interaction of electromagnetic fields, charges, currents, and matter play a central role. Typical examples are the design of antennas, wired and wireless communication, imaging for medical diagnoses, radar systems for aviation and automotive systems, and many more. Modeling such systems via computer simulations, an approach called computational electromagnetics (CEM), oftentimes allows for optimizations, fast trial of new concepts, and postprocessing of measurement data, overall improving the development process. To this end, in CEM either Maxwell's equations governing classical electrodynamics or the equations of quantum electrodynamics (QED) [Feynman 1961; Roth et al. 2019; Roth 2020] have to be solved (depending on the average number of photons present in the considered problem [Jackson 1999, p. 1]).

This thesis is concerned with two problem areas encountered in classical electrodynamics: the radiation and the scattering from perfectly electrically conducting (PEC) bodies, as well as the reconstruction of equivalent sources from measurements of electromagnetic fields. Since analytical solutions to the equations describing these problems are not available with only a few exceptions such as the scattering from a sphere [Mie 1908], numerical techniques are at the heart of CEM and are also subject of this thesis.

1.1 Numerical Techniques in Electromagnetics

Numerical techniques are in general concerned with finding algorithms to obtain approximate yet controllably accurate solutions to continuous equations in a limited time [Trefethen 1992]. In CEM these algorithms can be classified in different ways. Following, for example, [Jin 2015, pp. 651ff] one can distinguish time-domain and frequency-domain methods, which can be related via the Fourier transform. In each of the two categories,

there are partial differential equation (PDE) methods (also called local methods) and integral equation methods (also called global methods). For high frequencies, there are also asymptotic frequency-domain techniques such as physical optics (PO) or the geometrical theory of diffraction (GTD) and in hybrid methods different combinations of algorithms are formed.

Typical examples of PDE methods in the time domain are the finite-difference time-domain (FDTD) [Yee 1966] method, the finite integration technique (FIT) [Weiland 1977; Weiland 2003], or the transmission-line matrix (TLM) method [Hoefer 1985], and, in the frequency domain, the finite element method (FEM) [Courant 1943; Silvester 1969; Nédélec 1980; Jin 2014]. While these approaches lead to sparse linear systems of equations (LSEs) and are suitable to handle inhomogeneous media, they suffer from numerical dispersion [Jin 2014] and require the discretization of the entire solution domain. The latter makes the PDE methods less attractive for radiation problems with unbounded domain (where, e.g., absorbing boundary conditions [Engquist et al. 1977; Bayliss et al. 1980] or a perfectly matched layer [Berenger 1994] are needed for a truncation of the domain). Since the problems considered in this thesis are radiation and scattering problems, the focus is on integral equation methods.

1.1.1 Electromagnetic Radiation and Scattering

Integral equation methods do not exhibit numerical dispersion and automatically satisfy the (Silver-Müller) radiation condition by their formulation via a Green's function [Jin 2015, p. 655]. Moreover, for homogeneous subdomains only the surfaces separating the domains need to be discretized leading to surface integral equations (also called boundary integral equations). A drawback of this approach is that the discretization of the equations commonly leads to an LSE with a dense matrix. However, several algorithms have been proposed to overcome this issue. The algorithms allow to time- and memory-efficiently compute the matrix-vector product such that iterative solvers for the LSE can be employed. Examples in the frequency domain are the mulitlevel fast multipole method (MLFMM) [Greengard et al. 1987; Song et al. 1997; Darve 2000; Chew et al. 2001; Eibert 2005], the adaptive cross approximation (ACA) [Zhao et al. 2005a; Bebendorf 2008; Zhao et al. 2005b], hierarchical matrices [Hackbusch et al. 1989], the multilevel matrix decomposition algorithm (MLMDA) [Michielssen et al. 1996], or fast Fourier transform (FFT) based algorithms [Phillips et al. 1997; Schobert et al. 2012]. Analogously, in the time-domain, fast algorithms such as the time-domain adaptive integral method [Yilmaz et al. 2004] or the plane-wave time-domain (PWTD) algorithm [Shanker et al. 2003] have been developed.

The Electric Field Integral Equation

Specifically, we consider in this work the electric field integral equation (EFIE) as frequency domain formulation for the scattering and radiation from PEC bodies. Proposed by [Maue 1949] it is by now widely adopted and known to yield accurate solutions when discretized,

for example, by employing a Galerkin scheme. The involved electric field integral operator (EFIO) together with the operator of the magnetic field integral equation (MFIE) form the building blocks for many scattering and radiation formulations such as the Poggio-Miller-Chang-Harrington-Wu-Tsai integral equation (PMCHWT) [Poggio et al. 1973; Chang et al. 1977; Wu et al. 1977] or the Müller integral equation (MUIE) [Müller 1969] for penetrable bodies. Hence, it is of interest to overcome the difficulties tied to the EFIE. Namely, aspects of numerical quadrature involving improper integrals have been addressed, for example, in [Wilton et al. 1984; Dunavant 1985; Eibert et al. 1995; Sauter et al. 1997; Yla-Oijala et al. 2003]. Strategies for improving the conditioning of the (discretized) EFIE have been proposed, for instance, in [Alléon et al. 1997; Carpentieri et al. 2004; Eibert 2003]. Specifically, the ill-conditioning due to the spatial and the frequency dependence of the EFIE spectrum need to be cured for many applications: the dense-discretization and the low-frequency breakdown. The latter is also of major interest in this work and corresponding strategies are presented for a Galerkin discretization[1].

The Low-Frequency Breakdown

In essence, the low-frequency breakdown corresponds to a (quadratic) deterioration of the conditioning of the (discretized) EFIE when decreasing the frequency [Andriulli et al. 2010; Adrian et al. 2021]. While for small frequencies quasi-static approximations could be employed, it is desirable to have a formulation that is valid for all frequencies. This avoids finding estimates for the frequency ranges in which a certain formulation is valid, which is especially difficult for multiscale structures exhibiting fine and coarse geometry subdomains.

Consequently, after first observations of the low-frequency breakdown in [Mautz et al. 1980; Wilton et al. 1981] a solution strategy in the form of a quasi-Helmholtz decomposition was proposed in [Wilton et al. 1981; Mautz et al. 1982; Mautz et al. 1984], that is, it was suggested that basis and testing functions (for a Galerkin discretization) should each consist of a solenoidal and a non-solenoidal set. For the Rao-Wilton-Glisson (RWG) basis [Rao et al. 1982] a corresponding loop-star/tree basis was given in [Wilton et al. 1981; Lim et al. 1993; Lim 1994] and further studied in [Burton et al. 1995; Wu et al. 1995; Vecchi 1999; Eibert 2004; Andriulli 2012]. In this process, different difficulties of the low-frequency breakdown were identified (see also [Adrian et al. 2021]):

(a) The increasing ill-conditioning of the EFIE for decreasing frequency.
(b) The increasing ill-conditioning of the EFIE for increasing discretization density.
(c) The computational costly need to search for global loops for multiply-connected geometries, that is, geometries with handles and holes.
(d) The occurrence of round-off errors when testing the field with solenoidal functions so severe that the solution is off by orders of magnitude.
(e) The occurrence of round-off errors in the solution of the EFIE and the computed (radiated and scattered) fields so severe that the solution is off by orders of magnitude.

[1] For other approaches such as the Nyström method [Nyström 1930] or the collocation method similar problems occur [Young et al. 2012; Shafieipour et al. 2014; Chao et al. 1995; Vico et al. 2015].

While (b) is actually the dense-discretization breakdown, it is intimately related to the low-frequency breakdown and a joint treatment is ultimately of interest. As detailed in [Andriulli 2012], loop-star decompositions actually worsen the dense-discretization ill-conditioning. As mitigations to this additional ill-conditioning preconditioners have been proposed [Lee et al. 2003; Zhao et al. 2000] with a full avoidance of an additional ill-conditioning by the quasi-Helmholtz projectors proposed in [Andriulli et al. 2013]. In the same work, a combination with a multiplicative Calderón projector [Andriulli et al. 2008a; Adrian et al. 2019] was proposed overcoming all difficulties listed above (for a plan-wave excitation), which is why it is also the starting point for the strategies proposed in this work. While the Calderón projector, in principal, simultaneously overcomes (a)-(c), it needs to be combined with the quasi-Helmholtz projectors to also overcome (d)-(e). As an alternative, hierarchical loop-star bases have been proposed as preconditioner [Andriulli et al. 2007; Andriulli et al. 2008b; Andriulli et al. 2010] where for (b) only a logarithmic dependency remains and (c) was overcome in [Adrian et al. 2014].

Approaches not using a quasi-Helmholtz decomposition but instead introduce charges as additional unknowns (to the currents) such as [Bendali 1984a; Bendali 1984b; Taskinen et al. 2006] or the augmented EFIE [Qian et al. 2008b] still suffer from (b) and (d)-(e). As a means to overcome the round-off errors, perturbation methods have been proposed [Qian et al. 2010] which, however, require again to determine frequency ranges of validity. Another approach [Liu et al. 2018b] includes a boundary integral equation for the normal component of the magnetic field for this purpose. The so called partial element equivalent circuit (PEEC) method [Gope et al. 2007] is also based on using current and charges as unknowns but uses a different discretization strategy. An explicit inverse of the EFIE is proposed in [Zhu et al. 2014] leaving (b) unaddressed. In [Li et al. 2016; Alsnayyan et al. 2023] a full Helmholtz decomposition of the basis in combination with a Calderón preconditioner was proposed for smooth surfaces based on a subdivision surface description of the geometry.

Moreover, formulations have been proposed that no longer solve the EFIE but integral equations for potentials instead of the fields. Namely, the Debye-potential based approach [Epstein et al. 2009; Epstein et al. 2012; Fu et al. 2017] for simply-connected geometries. The approaches in [Vico et al. 2016] and [Liu et al. 2018a] are similar to current and charge formulations of the EFIE and solve for scalar and vector surface densities. Notably, the approach in [Vico et al. 2016] is immune to all low-frequency issues listed above but is limited to smooth surfaces.

1.1.2 Equivalent Source Reconstruction

The second kind of problems considered in this thesis, the reconstruction of (time-harmonic) equivalent sources from measurements with a probe antenna, is closely related to the scattering and radiation problem. In fact, the presented methods for the low-frequency stabilization of the EFIE are constructed also having the source reconstruction problem in mind. The source reconstruction problem is, in general, concerned with finding an equivalent representation of a radiating device under test (DUT) from a finite number of measurements.

This representation should allow then to compute the radiated fields at arbitrary locations in space (outside of the DUT) and leads, thus, to something known as a field transformation [Eibert et al. 2015]. If the measurements are performed in relatively close proximity to the DUT, that is, in its near field (NF), the transformation is commonly called near-field near-field transformation (NFNFT) or near-field far-field transformation (NFFFT) in the case the far field (FF) is the quantity of interest. This is often the case for the characterization of antennas. A direct measurement of the FF might in this case be tied to the need of a large measurement facility in order to ensure that the distance to the antenna is large enough to support the underlying assumption of FF conditions. In contrast, sampling in the NF allows to conduct the measurements in a relatively small anechoic chamber. Such a chamber provides the additional advantage of a controlled environment, where absorbers can be used to reduce reflections, echos, and approximately provide free-space conditions. These aspects are also beneficial for the related problems of determining the radar cross section (RCS) [Melin 1987; Schnattinger et al. 2014; Neitz et al. 2019b; Neitz et al. 2019a] or performing microwave imaging based on NF observations [Ahmad et al. 2004; Saurer et al. 2022].

For the equivalent representation of the radiating DUT, different options have been proposed. One of the first were expansions in terms of planar, cylindrical, or spherical modes [Yaghjian 1986; Hansen 1988]. For corresponding canonical scanning surfaces (planes, cylinders, spheres) and an equidistant or equiangular sampling, they offer the possibility for an acceleration of the field transformation by the FFT [Yaghjian 1986]. However, some relaxations towards the possibility of a more irregular sampling were given, for example, by employing a non-uniform FFT [Mauermayer et al. 2018]. As other options, propagating plane waves [Schmidt et al. 2008; Eibert et al. 2015], distributed spherical harmonics [Eibert et al. 2015; Ostrzyharczik et al. 2023], and equivalent electric and magnetic currents can be employed [Sarkar et al. 1999; Alvarez et al. 2007a; Alvarez et al. 2007b; Vecchi et al. 2010; Eibert et al. 2016; Kornprobst et al. 2021]. These approaches offer the advantage that the sampling locations can be irregular while keeping a low computational complexity for the field transformation by using, for instance, MLFMM techniques [Eibert et al. 2009].

The Low-Frequency Stability

Especially, the equivalent current representation has the advantage that it potentially offers accurate diagnostics capabilities. That is, (visualizations of) the determined currents provide information about the locations with strong radiation. This is amongst others of interest in the area of electromagnetic compatibility (EMC) and dosimetry measurements in order to ensure that devices have the desired radiation characteristics and that they are in compliance with the relevant standards and limitations. If field limitations are exceeded, the origin of the corresponding radiation has to be identified to eliminate it. However, since the operators linking the currents and the fields being measured are the ones of the EFIE and the MFIE, similar conditioning issues can be expected as discussed in Section 1.1.1. Hence, we propose a strategy to adapt the low-frequency stabilization techniques of radiation and scattering problems to the source reconstruction problem.

Existing approaches in the context of EMC model the DUT by six orthogonal dipoles (three electric and three magnetic dipoles), which offers only limited source localization capabilities [Sreenivasiah et al. 1981]. In [Regue et al. 2001], a larger number of dipoles is employed based on a genetic algorithm, which implies a high computational complexity, similarly to [Vives-Gilabert et al. 2009] where an LSE with dense matrix limits the number of dipoles and samples. While the direct interpretation of the measured magnetic fields as done, for instance, in [Vives-Gilabert et al. 2007; Song et al. 2014; Ravelo et al. 2015; Rinas et al. 2016; Hendijani et al. 2018] provides some insights, it captures only part of the information: at low frequencies the magnetic and the electric field increasingly decouple. Hence, measuring only the magnetic field potentially contains not all field information. Moreover, the NFNFT approach provides the capability to rapidly predict the fields at many locations, for example, to verify the compliance with different standards (i.e., the distances from the DUT where the field values need to be measured depend on the standard) by only one kind of measurement.

Reducing the Number of Samples

The second aspect concerning equivalent source reconstruction, which is considered in this thesis, is the reduction of the number of samples to a minimum in order to reduce the measurement time. Determining an absolute minimum of samples that is required to determine a set of equivalent sources for a DUT (with a certain accuracy) is, in general, an intricate task, even if measurement uncertainties such as noise are excluded from the analysis. A common approach to estimate the number of required samples, is via the diameter of the minimum sphere enclosing the DUT and the number of spherical modes required to represent fields radiated from the corresponding volume [Hansen 1988, pp. 15ff]. Yet, depending on the actual DUT this can be too few samples (e.g., if effects of super-directivity are present) or too many samples (e.g., due to band limiting effects of the DUT). Hence, tighter bounds were investigated, for instance, in [Bucci et al. 1987; Bucci et al. 1989; Bucci et al. 1998] using the concept of spatial band limitation to define degrees of freedom of radiated (and scattered) fields. Still, it is unclear whether fewer samples suffice when leveraging different a-priori information about the DUT, which restrictions on the sampling locations have to be imposed, and what the influence of measurement uncertainties is, all depending on the chosen equivalent source representation.

With respect to the number of samples suggested by the minimum sphere diameter of the DUT, different approaches have been proposed to reduce the number of samples: In [Bucci et al. 1994] and [D'Agostino et al. 2017] measurements on a coarse grid were interpolated to a finer grid in order to determine additional (virtual) measurements. In [Chiu et al. 2015] the initial number of samples is increased iteratively until the determined FF pattern does not considerably change anymore. However, these approaches, as well as the least squares solution proposed in [Kordella et al. 2016], suffer from a loss in accuracy. The authors of [Mauermayer et al. 2015] achieve a reduction of the number of unknowns (and consequently the number of measurements) by considering parts of the DUT with ray optical concepts. This is, however, only suitable for particular DUTs such as reflector antennas.

Instead, in this thesis the capability of compressed sensing (CS) is investigated, a theory dealing with the reconstruction of a signal from incomplete information [Candes et al. 2006a; Donoho 2006a; Candes et al. 2006b], to reduce the number of samples considerably below the ones suggested by the minimum sphere diameter of the DUT. Key idea is to leverage on a sparsity of the equivalent source representation. More precisely, a strategy is proposed to determine the minimum number of samples such that a predefined far-field accuracy can be achieved. To this end, spherical modes are considered as equivalent sources since for several examples the corresponding expansion has been shown to fulfill the requirements of CS [Cornelius et al. 2016; Bangun et al. 2016].

1.2 Scope and Outline of the Thesis

To summarize, this dissertation presents paradigms for the low-frequency stabilization of the EFIE as well as the reconstruction of equivalent sources from field measurements. To this end, Part I presents background material, where Chapter 2 introduces relevant electromagnetic principles concerning electromagnetic scattering and radiation, and Chapter 3 briefly discusses the considered discretization strategies of the continuous problems.

In Part II, strategies concerning the low-frequency stabilization of the EFIE are presented: An analysis of the origin of the catastrophic round-off errors when testing a field with solenoidal functions is provided in Chapter 4 together with a scheme to overcome the errors for arbitrary excitations on multiply-connected geometries. This constitutes a generalization of a technique proposed in [Mautz et al. 1982; Mautz et al. 1984; Wu et al. 1995] for a loop-star decomposition. Moreover, a method to combine the stabilization with the quasi-Helmholtz projectors [Andriulli et al. 2013] is proposed, facilitating their use with arbitrary excitations. In Chapter 5, a self-adaptive frequency normalization is introduced to quasi-Helmholtz decompositions which works irrespective of the specific excitation and irrespective of the underlying topology of the structure. This overcomes catastrophic round-off errors in the solution by ensuring that both solenoidal and non-solenoidal components of the surface current density are obtained with a similar relative accuracy such that the radiated and scattered fields can be determined accurately also for low-frequencies. In Chapter 6, a loop-star basis as well as quasi-Helmholtz projectors are derived for a B-spline based discretization of the EFIE, which is valid for arbitrary polynomial orders of the basis and applicable to open and closed, as well as to simply and multiply-connected geometries.

In Part III, strategies are proposed concerning the reconstruction of equivalent sources: A scheme to low-frequency stabilize a formulation in terms of equivalent electric currents is given in Chapter 7. The scheme is based on quasi-Helmholtz projectors and incorporates the proposed self-adaptive frequency normalization as well as the stabilized evaluation of arbitrary excitations by solenoidal functions. A thorough picture on the capability of CS to reduce the number of measurement samples that are required for an NFFFT, based on the spherical vector wave expansion of the radiated field of an DUT is presented in Chapter 8. This includes a strategy to determine the minimum number of samples required to achieve a predefined FF accuracy.

Finally, in Part IV, Chapter 9 a conclusion is given including an outline of possible future research.

1.3 Notation

Throughout this thesis a certain typographical style is employed to highlight certain entities: Vectors and matrices are written in a bold font where for vectors lower case letters are used and for matrices upper case letters. For vectors representing a physical quantity such as the electric field $\boldsymbol{e}$ or the position vector $\boldsymbol{r}$ serifs are used, whereas general N-dimensional vectors and matrices are denoted with sans-serif letters, for example, $\mathsf{\boldsymbol{a}} \in \mathbb{C}^N$ and $\mathsf{\boldsymbol{A}} \in \mathbb{C}^{M\times N}$, respectively. Specifically, points in $\mathbb{R}^3$ are denoted by $\boldsymbol{r} = (x, y, z)$ in Cartesian or $\boldsymbol{r} = (r, \vartheta, \varphi)$ in spherical coordinates, where $r = \|\boldsymbol{r}\|_2$ denotes the Euclidean norm and $\boldsymbol{u}_r$, $\boldsymbol{u}_\vartheta$, and $\boldsymbol{u}_\varphi$ denote the unit vectors of the spherical coordinate system. As an exception, for vectorial local loop functions $\boldsymbol{\Lambda}$, global loop functions $\boldsymbol{H}$, and star functions $\boldsymbol{\Sigma}$ uppercase letters are used to better highlight their correspondence to the mapping matrices $\boldsymbol{\Lambda}$, $\boldsymbol{H}$, and $\boldsymbol{\Sigma}$.

Scalar operators such as $\mathcal{T}$ are denoted with a calligraphic font and vector operators such as $\boldsymbol{\mathcal{T}}$ are in addition bold. For differential operators, the nabla notation is employed, that is, ∇ denotes the gradient, $\nabla\cdot$ the divergence, and $\nabla\times$ the curl. Whenever scalar and vector quantities are restricted to a surface Γ, we denote the surface differential operators by ∇_Γ. For a rigorous definition of these operators and their properties, we refer to [Nédélec 2001] for smooth surfaces, [Colton et al. 2013, pp. 202ff] for Hölder surfaces, and [Buffa et al. 2002; Buffa et al. 2003b] for Lipschitz surfaces. For specific parametrizations of surface quantities, a definition of the corresponding surface differential operators will be given when needed.

2

Relevant Electromagnetic Principles

> "Two souls dwell in the bosom of scattering theory. One is mathematical and handles the unitary equivalence of operators with continuous spectra. The other is physics ..."
>
> [Lax 2002]

The problems considered in this thesis can be classified into the area of classical physics and more precisely classical electrodynamics. The corresponding equations to describe the latter, namely Maxwell's equations, are introduced in Section 2.1 fixing some conventions, assumptions, and notation employed throughout this thesis. Frequently employed operators and functions for the radiation from (surface) currents via auxiliary potentials and via spherical vector waves are introduced in Section 2.2 before defining the EFIE for the radiation and scattering from PEC bodies in Section 2.3 and relevant aspects of the equivalent source reconstruction from field measurements in Section 2.4.

2.1 Considered Physical Model

Within the area of classical electrodynamics, we take as starting point the time-harmonic and macroscopic Maxwell's equations in differential form. As a convention, we use SI units and assume but suppress a time dependency of $\mathrm{e}^{\mathrm{j}\omega t}$ where t is the time and ω is the angular frequency. Moreover, we assume a homogeneous and isotropic background medium characterized by the permittivity $\varepsilon = \varepsilon_r \varepsilon_0$ and the permeability $\mu = \mu_r \mu_0$ with constant $\varepsilon_r \in \mathbb{C}$ and constant $\mu_r \in \mathbb{C}$. Based on this setting, the electric field $\boldsymbol{e}(\boldsymbol{r})$, the normalized magnetic field $\boldsymbol{h}(\boldsymbol{r})$, the normalized volume current density $\boldsymbol{j}_{\mathrm{V}}(\boldsymbol{r})$, and the volume charge density

$\rho_\mathrm{V}(\boldsymbol{r})$ (all dependent on the position vector $\boldsymbol{r}$) are related by [Harrington 2001; Jin 2015]

$$-\nabla \times \boldsymbol{e} = \mathrm{j}k\boldsymbol{h}\,, \tag{2.1a}$$

$$\nabla \times \boldsymbol{h} = \mathrm{j}k\boldsymbol{e} + \boldsymbol{j}_\mathrm{V}\,, \tag{2.1b}$$

$$\nabla \cdot \boldsymbol{e} = \rho_\mathrm{V}/\varepsilon\,, \tag{2.1c}$$

and

$$\nabla \cdot \boldsymbol{h} = 0\,, \tag{2.1d}$$

with the wavenumber

$$k = \omega\sqrt{\mu\varepsilon}\,. \tag{2.2}$$

The employed normalization of the magnetic field and the current density is with respect to the wave impedance $\eta = \sqrt{\mu/\varepsilon}$ in the sense $\boldsymbol{h} = \eta\bar{\boldsymbol{h}}$ and $\boldsymbol{j}_\mathrm{V} = \eta\bar{\boldsymbol{j}}_\mathrm{V}$, where $\bar{\boldsymbol{h}}$ and $\bar{\boldsymbol{j}}_\mathrm{V}$ are the classical quantities. Due to the normalization the electric field, the magnetic field, and the current density have with $\mathrm{V\,m^{-1}}$ the same unit, which simplifies the formalism. Taking the divergence of (2.1b), leveraging $\nabla \cdot (\nabla \times \boldsymbol{a}) = 0$, and inserting (2.1c) results in the continuity equation [Harrington 2001]

$$\nabla \cdot \boldsymbol{j}_\mathrm{V} = -\mathrm{j}k\rho_\mathrm{V}/\varepsilon \tag{2.3}$$

relating the current density $\boldsymbol{j}_\mathrm{V}$ and the charge density ρ_V. As a consequence of (2.3), the charge density can be eliminated from (2.1) and all sources can be expressed in terms of current densities only [Hansen et al. 1999, p. 73].

2.2 Electromagnetic Radiation in Free Space

Before formulating the radiation and scattering in the presence of a PEC body, we briefly describe the radiation of fields in free space. This corresponds to solving Maxwell's equations (2.1) for the radiated fields $(\boldsymbol{e}, \boldsymbol{h})$ from a given set of sources $\boldsymbol{j}_\mathrm{V}$ (and ρ_V). To this end, we consider two strategies. The first one reformulates (2.1) in terms of auxiliary potentials, while the second one uses a reformulation in terms of the curl-curl equation and a separation ansatz. For the scattering formulations considered in this work we will need to express the radiation in terms of potentials for sources that are restricted to a surface Γ. Therefore, we only consider surface current densities denoted by $\boldsymbol{j}$ and surface charge densities denoted by ρ (both with compact support).

2.2.1 Radiation in Terms of Potentials

Using some fundamental relationships of vector calculus, (2.1) can be expressed as (see, e.g., [Jin 2015, pp. 58ff])

$$\boldsymbol{e} = -\mathrm{j}k\boldsymbol{a} - \nabla\Phi\,, \tag{2.4}$$

and

$$\boldsymbol{h} = \nabla \times \boldsymbol{a} \tag{2.5}$$

via the vector potential $\boldsymbol{a}(\boldsymbol{r})$ and the scalar potential $\Phi(\boldsymbol{r})$ which satisfy the inhomogeneous Helmholtz equations

$$\Delta\, \boldsymbol{a} + k^2 \boldsymbol{a} = -\boldsymbol{j} \tag{2.6}$$

and

$$\Delta\Phi + k^2\Phi = -\rho/\varepsilon\,. \tag{2.7}$$

In these expressions, Δ denotes the Laplace operator and $\boldsymbol{\Delta}$ the vector Laplace operator (applying Δ to each component of the corresponding vector field). The vector and the scalar potential are not independent, but linked via the (employed) Lorenz gauge

$$\nabla \cdot \boldsymbol{a} = -\mathrm{j}k\Phi\,. \tag{2.8}$$

Solution of the Helmholtz Equations

For a surface current density $\boldsymbol{j}$ with compact support placed in free space, a solution to the Helmholtz equation for $\boldsymbol{a}$ can be expressed in terms of the Green's function of free space[1] [Hanson et al. 2013, pp. 38ff]

$$g(\boldsymbol{r}, \boldsymbol{r}') = \frac{\mathrm{e}^{-\mathrm{j}k|\boldsymbol{r}-\boldsymbol{r}'|}}{4\pi|\boldsymbol{r}-\boldsymbol{r}'|} \tag{2.9}$$

as

$$\boldsymbol{a} = \boldsymbol{\mathcal{T}}_{\mathrm{A}}\boldsymbol{j} \tag{2.10}$$

where we have introduced the vector potential operator (also known as singular operator [Sauter et al. 2011; Cools et al. 2009; Andriulli et al. 2013])

$$\boldsymbol{\mathcal{T}}_{\mathrm{A}}\boldsymbol{j} = \iint_{\Gamma} g(\boldsymbol{r}, \boldsymbol{r}')\boldsymbol{j}(\boldsymbol{r}')\,\mathrm{d}\boldsymbol{r}'\,. \tag{2.11}$$

Note that (2.11) constitutes an improper integral due to the singular Green's function $g(\boldsymbol{r}, \boldsymbol{r}')$. However, the integral can be shown to be convergent[2] [Hanson et al. 2013, pp. 26ff]. Analogously, we can solve (2.7) and using $\rho/\varepsilon = jk^{-1}\nabla_{\Gamma} \cdot \boldsymbol{j}$ from (2.3), we find [Nédélec 2001, pp. 238f]

$$\nabla\Phi = \mathrm{j}k^{-1}\boldsymbol{\mathcal{T}}_{\Phi}\boldsymbol{j} \tag{2.12}$$

[1] The Green's function of free space is the particular solution to $(\Delta + k^2)g(\boldsymbol{r}, \boldsymbol{r}') = -\delta(\boldsymbol{r} - \boldsymbol{r}')$ together with the Sommerfeld radiation condition, with $\delta(\boldsymbol{r})$ denoting the Dirac delta distribution.

[2] For a definition of convergent improper integrals see, e.g., [Kellogg 1929, pp. 146f] and [Budak et al. 1973, pp. 412ff].

with the scalar potential operator (also known as hypersingular operator [Sauter et al. 2011; Cools et al. 2009; Andriulli et al. 2013])

$$\mathcal{T}_\Phi \boldsymbol{j} = \nabla \iint_\Gamma g(\boldsymbol{r}, \boldsymbol{r}')\, \nabla'_\Gamma \cdot \boldsymbol{j}(\boldsymbol{r}')\, \mathrm{d}\boldsymbol{r}' \,, \tag{2.13}$$

which contains again an improper but convergent integral [Hanson et al. 2013, pp. 26ff]. Since from the Lorenz gauge (2.8) it follows that $\nabla\Phi = \mathrm{j}k^{-1}\nabla\nabla\cdot\mathcal{T}_\mathrm{A}\boldsymbol{j}$, the scalar and the vector potential operator are linked via

$$\mathcal{T}_\Phi \boldsymbol{j} = \nabla\nabla\cdot\mathcal{T}_\mathrm{A}\boldsymbol{j} \,, \tag{2.14}$$

which might also be shown via Stokes identities [Nédélec 2001, p. 73].

Radiated Fields

Inserting the obtained solutions (2.10) and (2.12) into (2.4), the radiated electric field can be expressed as

$$\boldsymbol{e} = -\mathcal{T}\boldsymbol{j} \tag{2.15}$$

via the EFIO

$$\mathcal{T}\boldsymbol{j} = \mathrm{j}k\mathcal{T}_\mathrm{A}\boldsymbol{j} + \mathrm{j}k^{-1}\mathcal{T}_\Phi\boldsymbol{j} \,. \tag{2.16}$$

By inserting (2.10) into (2.5) and applying the identity $\nabla\times\mathbf{I}g = \nabla g\times\mathbf{I}$ with the identity dyadic $\mathbf{I}$ [Hanson et al. 2013, p. 608], the magnetic field is given by

$$\boldsymbol{h} = \iint_\Gamma \nabla g(\boldsymbol{r}, \boldsymbol{r}') \times \boldsymbol{j}(\boldsymbol{r}')\, \mathrm{d}\boldsymbol{r}' \,. \tag{2.17}$$

Note that the latter integral is improper and not convergent [Hanson et al. 2013, pp. 31ff] in the sense that it is proper for $\boldsymbol{r} \notin \Gamma$ but for $\boldsymbol{r} \in \Gamma$ a subtle limiting procedure is required [Collin 1990, p. 142][Bladel 1996, p. 71][Colton et al. 2013, p. 201].

Radiated Far Fields

If the FF shall be determined, that is, the fields are evaluated for $r \to \infty$, the vector potential operator simplifies to [Jin 2015, p. 74]

$$\mathcal{T}_{\mathrm{A,FF}}\boldsymbol{j} = \iint_\Gamma \boldsymbol{j}(\boldsymbol{r}')\, \mathrm{e}^{\mathrm{j}k\boldsymbol{u}_r\cdot\boldsymbol{r}'}\, \mathrm{d}\boldsymbol{r}' \tag{2.18}$$

where a normalization with respect to $\mathrm{e}^{-\mathrm{j}kr}/(4\pi r)$ has been performed and $\boldsymbol{u}_r$ denotes the unit vector in radial direction. With (2.18), the electric FF $\boldsymbol{e}^\mathrm{FF}$ can be brought into the

form [Jin 2015, p. 74]

$$\boldsymbol{e}^{\mathrm{FF}} = -\mathrm{j}k\boldsymbol{u}_r \times \boldsymbol{u}_r \times \boldsymbol{\mathcal{T}}_{\mathrm{A,FF}}\boldsymbol{j} \tag{2.19}$$

and analogously, the magnetic FF $\boldsymbol{h}^{\mathrm{FF}}$ can be expressed as

$$\boldsymbol{h}^{\mathrm{FF}} = \mathrm{j}k\boldsymbol{u}_r \times \boldsymbol{\mathcal{T}}_{\mathrm{A,FF}}\boldsymbol{j}\,. \tag{2.20}$$

2.2.2 Radiation in Terms of Spherical Vector Waves

As an alternative to the representations (2.15) and (2.17), Maxwell's equations (2.1) can be reformulated by taking the curl of (2.1a) and inserting (2.1b). Taking also the curl of (2.1b) and inserting (2.1a) results in the curl-curl (also called vector wave) equations [Hansen et al. 1999, p. 74]

$$\nabla \times \nabla \times \boldsymbol{e} - k^2\boldsymbol{e} = -\mathrm{j}k\boldsymbol{j}_{\mathrm{V}} \tag{2.21a}$$

and

$$\nabla \times \nabla \times \boldsymbol{h} - k^2\boldsymbol{h} = \nabla \times \boldsymbol{j}_{\mathrm{V}}\,. \tag{2.21b}$$

Together with the continuity equation (2.3) (establishing the relation to the charge density ρ_{V}) these two equations are fully equivalent to (2.1) since the latter can be derived from (2.21) as shown in [Hansen et al. 1999, p. 74].

Solution of the Homogeneous Curl-Curl Equation

In a source-free region both the electric and the magnetic field $\boldsymbol{e}$ and $\boldsymbol{h}$ satisfy the homogeneous curl-curl equation

$$\nabla \times \nabla \times \boldsymbol{c} - k^2\boldsymbol{c} = \boldsymbol{0}\,, \tag{2.22}$$

for which a solution can be derived in spherical coordinates $\boldsymbol{r} = (r, \vartheta, \varphi)$ [Hansen 1935; Stratton 1941, pp. 392ff]. Employing a power normalization, the solution can be expressed as a superposition of the (dimensionless) TE_{mn} spherical vector wave functions (also called modes) [Hansen 1988, p. 13]

$$\boldsymbol{q}^{(c)}_{1mn}(r, \vartheta, \varphi) = \frac{1}{\sqrt{2\pi}} \frac{1}{\sqrt{n(n+1)}} \left[z^{(c)}_n(kr) \frac{\mathrm{j}m\bar{\mathrm{P}}^{|m|}_n(\cos\vartheta)}{\sin\vartheta} \mathrm{e}^{\mathrm{j}m\varphi}\, \boldsymbol{u}_\vartheta \right.$$
$$\left. - z^{(c)}_n(kr) \frac{\mathrm{d}\bar{\mathrm{P}}^{|m|}_n(\cos\vartheta)}{\mathrm{d}\vartheta} \mathrm{e}^{\mathrm{j}m\varphi}\, \boldsymbol{u}_\varphi \right] \tag{2.23}$$

and the TM_{mn} spherical vector wave functions

$$\boldsymbol{q}^{(c)}_{2mn}(r,\vartheta,\varphi) = \frac{1}{\sqrt{2\pi}}\,\frac{1}{\sqrt{n(n+1)}}\left[\frac{n(n+1)}{kr}\,z^{(c)}_n\,\bar{\mathrm{P}}^{|m|}_n(\cos\vartheta)\,\mathrm{e}^{\mathrm{j}m\varphi}\boldsymbol{u}_r\right.$$
$$+\frac{1}{kr}\,\frac{\mathrm{d}\big(kr\,z^{(c)}_n(kr)\big)}{\mathrm{d}(kr)}\,\frac{\mathrm{d}\bar{\mathrm{P}}^{|m|}_n(\cos\vartheta)}{\mathrm{d}\vartheta}\,\mathrm{e}^{\mathrm{j}m\varphi}\,\boldsymbol{u}_\vartheta$$
$$\left.+\frac{1}{kr}\,\frac{\mathrm{d}\big(kr\,z^{(c)}_n(kr)\big)}{\mathrm{d}(kr)}\,\frac{\mathrm{j}m\bar{\mathrm{P}}^{|m|}_n(\cos\vartheta)}{\sin\vartheta}\,\mathrm{e}^{\mathrm{j}m\varphi}\,\boldsymbol{u}_\varphi\right], \quad (2.24)$$

which are mutually orthogonal [Hansen 1988, pp. 330f]. In these expressions, the singularities (angles where $\sin\vartheta = 0$) have a finite limit, $\boldsymbol{u}_r$, $\boldsymbol{u}_\vartheta$, and $\boldsymbol{u}_\varphi$ are the spherical unit vectors,

$$\bar{\mathrm{P}}^m_n(\cos\vartheta) = \sqrt{\frac{2n+1}{2}\frac{(n-m)!}{(n+m)!}}\,\mathrm{P}^m_n(\cos\vartheta) \quad (2.25)$$

denote the normalized associated Legendre polynomials P^m_n for $n > 0, m \geq 0$, and

$$z^{(c)}_n = \begin{cases} \mathrm{j}_n(kr) & \text{for } c = 1 \quad \text{(standing wave)} \\ \mathrm{n}_n(kr) & \text{for } c = 2 \quad \text{(standing wave)} \\ \mathrm{h}^1_n(kr) & \text{for } c = 3 \quad \text{(inward traveling wave)} \\ \mathrm{h}^2_n(kr) & \text{for } c = 4 \quad \text{(outward traveling wave)} \end{cases} \quad (2.26)$$

represents the spherical Bessel function j_n, the spherical Neumann function n_n, the spherical Hankel function of the first kind h^1_n, or the spherical Hankel function of the second kind h^2_n depending on the superscript c. The choice of the latter corresponds to standing waves for $c = 1, 2$, inward traveling waves for $c = 3$, and outward traveling waves for $c = 4$.

Radiated Fields

By superimposing the spherical vector wave functions, the radiated electric field in a source-free region (limited by concentric spherical surfaces centered at the origin of the coordinate system) can be expressed as [Hansen 1988, p. 14]

$$\boldsymbol{e} = \lim_{L\to\infty} \frac{k}{\sqrt{\eta}} \sum_{n=1}^{L} \sum_{m=-n}^{n} \sum_{a=1}^{2} x_{amn}\boldsymbol{q}^{(4)}_{a,m,n} \quad (2.27)$$

with the expansion coefficients $x_{amn} \in \mathbb{C}$ and the corresponding magnetic field as

$$\boldsymbol{h} = \lim_{L\to\infty} \frac{\mathrm{j}k}{\sqrt{\eta}} \sum_{n=1}^{L} \sum_{m=-n}^{n} \sum_{a=1}^{2} x_{amn}\boldsymbol{q}^{(4)}_{3-a,m,n} \quad (2.28)$$

with the same expansion coefficients. Note that only outward traveling waves are included by fixing $c = 4$. A general (not radiated) field can, for instance, be expressed by the superposition of $c = 3$ and $c = 4$ waves [Hansen 1988, p. 14].

As a solution to the inhomogeneous curl-curl equations (2.21), the expansion coefficients x_{amn} for a given current density in a volume V can be determined as [Hansen 1988, p. 333]

$$x_{amn} = (-1)^{m+1} \frac{k}{\sqrt{\eta}} \iiint_V \boldsymbol{q}^{(1)}_{a,-m,n} \cdot \boldsymbol{j}_\mathrm{V} \, \mathrm{d}\boldsymbol{r} \tag{2.29}$$

which can be derived from reciprocity relations and orthogonality properties of the $\boldsymbol{f}^{(c)}_{a,m,n}$. The volume current density might also be replaced by a surface current density $\boldsymbol{j}$.

Radiated Far Fields

The radiated FF can be represented by

$$\boldsymbol{e}^\mathrm{FF} = \lim_{L\to\infty} \frac{k}{\sqrt{\eta}} \sum_{n=1}^{L} \sum_{m=-n}^{n} \sum_{a=1}^{2} x_{amn} \boldsymbol{q}^\mathrm{FF}_{amn} \tag{2.30}$$

where the FF vector wave functions $\boldsymbol{q}^\mathrm{FF}_{amn}$ are found by using the large argument approximations of the $z^{(4)}_n$ in the $\boldsymbol{q}^{(4)}_{amn}$ functions as [Hansen 1988, p. 328]

$$\boldsymbol{q}^\mathrm{FF}_{1mn}(\vartheta,\varphi) = \frac{\sqrt{2}}{\sqrt{n(n+1)}} \mathrm{e}^{\mathrm{j}m\varphi} \mathrm{j}^{n+1} \left[\frac{\mathrm{j}m\bar{\mathrm{P}}^{|m|}_n(\cos\vartheta)}{\sin\vartheta} \boldsymbol{u}_\vartheta - \frac{\mathrm{d}\,\bar{\mathrm{P}}^{|m|}_n(\cos\vartheta)}{\mathrm{d}\vartheta} \boldsymbol{u}_\varphi \right] \tag{2.31}$$

and

$$\boldsymbol{q}^\mathrm{FF}_{2mn}(\vartheta,\varphi) = \frac{\sqrt{2}}{\sqrt{n(n+1)}} \mathrm{e}^{\mathrm{j}m\varphi} \mathrm{j}^{n} \left[\frac{\mathrm{d}\,\bar{\mathrm{P}}^{|m|}_n(\cos\vartheta)}{\mathrm{d}\vartheta} \boldsymbol{u}_\vartheta + \frac{\mathrm{j}m\bar{\mathrm{P}}^{|m|}_n(\cos\vartheta)}{\sin\vartheta} \boldsymbol{u}_\varphi \right]. \tag{2.32}$$

Note that (2.30) is normalized with respect to $\mathrm{e}^{-\mathrm{j}kr}/(4\pi r)$ just as it was done in (2.18).

2.3 Scattering and Radiation from PEC Bodies—The EFIE

For the radiation in the presence of a PEC body, the Huygens equivalence principle (also known as surface equivalence principle) [Harrington 2001; Jin 2015, pp. 106ff] depicted in Fig. 2.1 can be employed: Given an external excitation field $(\boldsymbol{e}^\mathrm{ex}, \boldsymbol{h}^\mathrm{ex})$ causing a scattered field $\boldsymbol{e}^\mathrm{sc}, \boldsymbol{h}^\mathrm{sc}$ due to the PEC body with surface Γ, the scenario can be equivalently represented by a free-space setting with a surface current density $\boldsymbol{j}$ restricted to the location of Γ such that the total electric field $\boldsymbol{e}$ can be expressed as

$$\boldsymbol{e} = \boldsymbol{e}^\mathrm{ex} - \mathcal{T}\boldsymbol{j} \tag{2.33}$$

Fig. 2.1: Huygens equivalence principle (for the exterior problem): (a) A field $(\boldsymbol{e}^{ex}, \boldsymbol{h}^{ex})$ excites a PEC body with surface Γ and causes a scattered (radiated) field $\boldsymbol{e}^{sc}, \boldsymbol{h}^{sc}$. (b) The equivalent free space problem with the surface current density $\boldsymbol{j}$ and a zero field inside Γ.

where $-\mathcal{T}\boldsymbol{j}$ corresponds to the scattered field $\boldsymbol{e}^{sc}$. Leveraging the boundary condition for PEC enforcing the part of the total electric field tangential to Γ to be zero [Harrington 2001, p. 34], that is, $\boldsymbol{e}_{tan} = 0$, the EFIE

$$(\mathcal{T}\boldsymbol{j})_{tan} = \boldsymbol{e}^{ex}_{tan}\,, \tag{2.34}$$

is obtained, which was proposed first by [Maue 1949]. After solving this equation for $\boldsymbol{j}$, the scattered fields can be computed via (2.15) and (2.17).

Note that the EFIE is often defined with a surface normal vector $\boldsymbol{n}$ to express the notion of a (rotated) tangential component, that is, $\boldsymbol{n} \times \mathcal{T}\boldsymbol{j} = \boldsymbol{n} \times \boldsymbol{e}^{ex}$. However, following for example [Mautz et al. 1978] and defining the EFIE as in (2.34) has the advantage that non-orientable surfaces (which do not possess a canonically definable normal vector field) can be considered as scattering objects in a natural manner [Johnson et al. 1990; Buffa et al. 2003a]. Since the normal vector is only an auxiliary tool (when discretizing the EFIE the normal vectors can be canceled out of the equation), however, the in Part II proposed strategies are independent of the definition of the EFIE with or without a normal vector.

Moreover, throughout this thesis the surface Γ is assumed to be a Lipschitz-manifold which can be open or closed as well as simply- or multiply-connected, where we assume that Γ is orientable in the case that Γ is closed[3]. For such surfaces the EFIE is well-posed, that is, a solution exists and is unique, with the exception of resonant frequencies [Buffa et al. 2003a; Buffa et al. 2003b]. For the latter, uniqueness can be re-established, for instance, by combining the EFIE with the MFIE to form the combined field integral equation (CFIE) [Mautz et al. 1978] or the combined source integral equation (CSIE) [Mautz et al. 1979].

2.4 Equivalent Source Reconstruction

To capture the radiation behavior of a DUT, again the Huygens principle can be employed: the radiated field external to the DUT can be equivalently represented by a surface current

[3] A Möbius strip is an example of an open, multiply-connected, and non-orientable Γ. As noted in [Johnson et al. 1990; Buffa et al. 2003a], the EFIE can be solved on such Γ.

density $\boldsymbol{j}$ (on a surface enclosing the DUT) radiating into free space. As noted in Section 1.1.2, instead of a surface current density $\boldsymbol{j}$, other forms of current densities can be employed such as a magnetic surface current density, Love currents, or forms of directive currents. However, in this work we focus on the case of $\boldsymbol{j}$ only, such that only the EFIO is involved for which we propose a low-frequency stabilization. In order to determine the unknown $\boldsymbol{j}$, one can solve (2.15) by collecting samples of the (electric) field. This sampling of the field is done by a probe antenna which actually measures not the field directly but the output signal of the probe antenna corresponds to a form of weighted average of the field. A corresponding model to account for this will be discussed in Chapter 7.

In comparison to the scattering formulation via the EFIE, it can observed that not a boundary condition on a material interface is enforced but instead, the radiated field is sampled in some distance to the DUT.

Instead of determining a surface current density $\boldsymbol{j}$, the representation of the radiated field via spherical vector wave functions in (2.27) can be employed and solved for the expansion coefficients x_{amn} by sampling the field. By (2.29) the direct relation to the Huygens principle in terms of surface currents is established showing that the spherical expansion coefficients can be understood as a form of equivalent source.

3

Discretization, Solution Uniqueness, and Conditioning

> "Numerical analysis is the study of algorithms for the problems of continuous mathematics."
>
> [Trefethen 1992]

As fundamental solution strategy for the EFIE and the equivalent source reconstruction problem, we employ established discretization approaches of the continuous equations. Corresponding details and frequently used notation are introduced in this chapter: Concerning the EFIE, a Galerkin scheme is employed in this work as detailed in Section 3.1. For the resulting LSE, the concept of quasi-Helmholtz decompositions is introduced in Section 3.2 to form low-frequency stabilizing preconditioners of the original LSE. As discussed in Section 1.1.1, these are the starting points for the paradigms proposed in the remainder of this thesis. Analogously, the discretization strategies concerning the equivalent source reconstruction are outlined in Section 3.3.

3.1 Galerkin Discretization of the EFIE

Common discretization strategies for the EFIE are the Nyström method [Nyström 1930; Hackbusch 1995; Atkinson 2009], the collocation method [Hackbusch 1995; Atkinson 2009], the method of source potentials [Hazard et al. 1996; Buffa et al. 2003b], or the here considered Galerkin scheme, which is also known as method of moments (MoM) [Harrington 1993; Buffa et al. 2003b]. An advantage of the latter is that a rigorous convergence theory is available, that is, via the so-called inf-sup-conditions [Babuška 1971; Xu et al. 2003], existence, uniqueness, and asymptotically optimal convergence of the discrete solution to the analytical (for non-resonant frequencies unique) solution have been proven [Buffa et al. 2003a; Buffa et al. 2003b; Sauter et al. 2011; Dölz et al. 2019].

In practice, for the Galerkin scheme[1], the unknown surface current density $\boldsymbol{j}$ of the EFIE $(\boldsymbol{\mathcal{T}}\boldsymbol{j})_{\tan} = \boldsymbol{e}^{\mathrm{ex}}_{\tan}$ given in (2.34) is approximated by N basis functions $\boldsymbol{f}_n(\boldsymbol{r})$ as

$$\boldsymbol{j} \approx \sum_{n=1}^{N} [\boldsymbol{j}]_n \boldsymbol{f}_n(\boldsymbol{r}) \,, \tag{3.1}$$

with $\boldsymbol{j} \in \mathbb{C}^N$ containing the expansion coefficients. The resulting equation is then tested (the scalar product is formed and integrated) with the same $\boldsymbol{f}_n$ resulting in the LSE

$$\boldsymbol{T}\boldsymbol{j} = \boldsymbol{e}^{\mathrm{ex}} \,, \tag{3.2}$$

with the system matrix

$$\boldsymbol{T} = \mathrm{j}k\boldsymbol{T}_{\mathrm{A}} + \mathrm{j}k^{-1}\boldsymbol{T}_{\Phi} \,, \tag{3.3}$$

where the matrix $\boldsymbol{T}_{\mathrm{A}} \in \mathbb{C}^{N\times N}$ consists of the entries

$$[\boldsymbol{T}_{\mathrm{A}}]_{mn} = \iint_{\Gamma} \boldsymbol{f}_m \cdot \boldsymbol{\mathcal{T}}_{\mathrm{A}} \boldsymbol{f}_n \, \mathrm{d}\boldsymbol{r} \,, \tag{3.4}$$

the matrix $\boldsymbol{T}_{\Phi} \in \mathbb{C}^{N\times N}$ consists of the entries (evaluated in a weak sense as further detailed in Section 3.1.3)

$$[\boldsymbol{T}_{\Phi}]_{mn} = \iint_{\Gamma} \boldsymbol{f}_m \cdot \boldsymbol{\mathcal{T}}_{\Phi} \boldsymbol{f}_n \, \mathrm{d}\boldsymbol{r} \,, \tag{3.5}$$

and the right-hand side (RHS) vector $\boldsymbol{e}^{\mathrm{ex}} \in \mathbb{C}^N$ consists of the entries

$$[\boldsymbol{e}^{\mathrm{ex}}]_m = \iint_{\Gamma} \boldsymbol{f}_m \cdot \boldsymbol{e}^{\mathrm{ex}} \, \mathrm{d}\boldsymbol{r} \,. \tag{3.6}$$

In consequence, a description of the surface Γ is required in order to integrate over it and appropriate basis functions need to be chosen.

3.1.1 Surface Representation

We consider in this work two ways of representing the surface Γ exemplified in Fig. 3.1. The first is a mesh of flat triangular patches which for most surfaces involves an approximation of the actual surface. The second is a union of curvilinear rectangular patches. In both cases, Γ is described by a union of A patches Γ_a whose pairwise intersections are either empty, a vertex, or an edge, that is, $\Gamma = \bigcup_{a=1}^{A} \Gamma_a$, where each Γ_a is described by a mapping $\boldsymbol{s}_a(u,v) : \hat{\Gamma}_a \mapsto \Gamma_a$ from the parametric space $\hat{\Gamma}_a = (u,v)$ to the physical space $\Gamma_a \subset \mathbb{R}^3$. Specifically, the triangular reference element is given by the unit triangle

$$\hat{\Gamma}_a = \{(u,v) \in \mathbb{R}^2 \,:\, 0 < u < 1; 0 < v < 1-u\} \tag{3.7}$$

[1] Also known as Bubnov-Galerkin scheme [Elishakoff et al. 2004; Elishakoff et al. 2021].

(a) (b)

Fig. 3.1: Representation of a sphere by (a) a mesh of triangular patches and (b) by curvilinear rectangular patches.

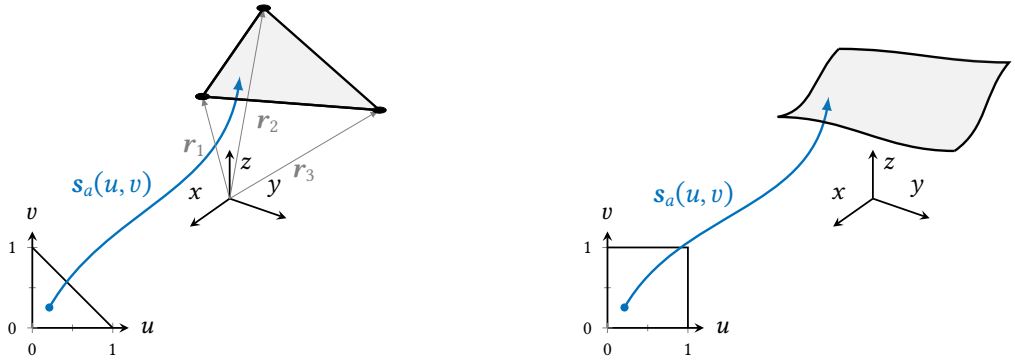

(a) (b)

Fig. 3.2: Mapping from reference elements to the physical space: (a) mapping from a unit triangle and (b) mapping from a unit square.

as depicted in Fig. 3.2 (a), and the rectangular reference element is given by the unit square

$$\hat{\Gamma}_a = (u, v) \in [0, 1]^2 \tag{3.8}$$

as depicted in Fig. 3.2 (b). With $\boldsymbol{r}_1^a$, $\boldsymbol{r}_2^a$, and $\boldsymbol{r}_3^a$ denoting the vertices of a triangle, the mapping to the physical space for the triangles can be defined by

$$\boldsymbol{s}_a(u, v) = \boldsymbol{r}_1^a + u(\boldsymbol{r}_2^a - \boldsymbol{r}_1^a) + v(\boldsymbol{r}_3^a - \boldsymbol{r}_1^a)\,. \tag{3.9}$$

The mapping to the physical space for a curvilinear rectangular element will be specified in Section 6.1 since several required definitions in terms of B-splines are only relevant to the corresponding Chapter 6. The Jacobi matrix $\boldsymbol{J}_a \in \mathbb{R}^{3\times 2}$ of the mapping (3.9) is

$$\boldsymbol{J}_a(u, v) = \begin{bmatrix} \partial_u \boldsymbol{s}_a & \partial_v \boldsymbol{s}_a \end{bmatrix} = \begin{bmatrix} (\boldsymbol{r}_2^a - \boldsymbol{r}_1^a) & (\boldsymbol{r}_3^a - \boldsymbol{r}_1^a) \end{bmatrix} \tag{3.10}$$

and its generalized determinant is

$$D_a(u, v) = \sqrt{\det\left(\boldsymbol{J}_a^{\mathrm{T}} \boldsymbol{J}_a\right)} = \|(\boldsymbol{r}_2^a - \boldsymbol{r}_1^a) \times (\boldsymbol{r}_3^a - \boldsymbol{r}_1^a)\|_2 = 2S_a\,, \tag{3.11}$$

where S_a denotes the area of the ath triangle.

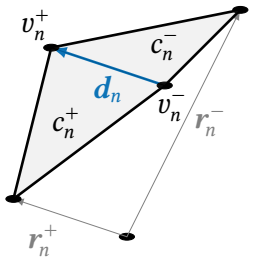

Fig. 3.3: Conventions for the definition of an RWG basis function in the physical domain: at the nth edge $\boldsymbol{d}_n$ with vertices $v_n^\pm$ the basis function exists on the cell domains $c_n^\pm$.

3.1.2 Basis Functions

From the EFIO $\mathcal{T}$, it follows that the basis functions should be divergence-conforming in the sense that the occurring operation $\nabla_\Gamma \cdot \boldsymbol{f}_n$ is well-defined[2]. In agreement with functional analytical considerations in the setting of Sobolev spaces[3] this also ensures that the testing is performed in the dual space of the range of $\mathcal{T}$ [Buffa et al. 2003b].

As detailed in [Peterson 2006] divergence-conforming basis functions can be defined in the parametric domain, here denoted as $\hat{\boldsymbol{f}}_n$, and mapped to the physical domain as [Peterson 2006, p. 85]

$$\boldsymbol{f}_n(\boldsymbol{r}) = \frac{\boldsymbol{J}(u,v)}{D(u,v)} \hat{\boldsymbol{f}}_n(u,v) \tag{3.12}$$

with $\boldsymbol{r} = \boldsymbol{s}_a(u,v)$. For the triangular patches, the basis function

$$\hat{\boldsymbol{f}}_n(u,v) = u\boldsymbol{u}_u + v\boldsymbol{u}_v \tag{3.13}$$

ensures normal continuity (and thus, divergence conformity) when combined across two triangles touching at an edge (specifically the edge connecting $\boldsymbol{r}_2^a$ and $\boldsymbol{r}_3^a$). By using (3.10) and (3.11), it can be verified that by doing so the well-established RWG functions are obtained, commonly defined directly in the physical domain as [Rao et al. 1982]

$$\boldsymbol{f}_n = \begin{cases} \dfrac{\boldsymbol{r} - \boldsymbol{r}_n^+}{2S_a^+} & \text{for} \quad \boldsymbol{r} \in c_n^+ \\ \dfrac{\boldsymbol{r}_n^- - \boldsymbol{r}}{2S_a^-} & \text{for} \quad \boldsymbol{r} \in c_n^- \end{cases} \tag{3.14}$$

[2]More precisely, that $\boldsymbol{j}$ and hence also the basis functions approximating $\boldsymbol{j}$ have to be divergence-conforming, is a necessary and sufficient condition following from the requirement that $\boldsymbol{e}$ and $\boldsymbol{h}$ are of finite energy in the sense that the (weak) curl of $\boldsymbol{e}$ and $\boldsymbol{h}$ should be finite. In terms of Sobolev spaces $\boldsymbol{e}, \boldsymbol{h} \in H(\nabla\times)$ if and only if $\boldsymbol{j} \in H^{-1/2}(\nabla_\Gamma\cdot, \Gamma)$ [Hsiao et al. 1997; Buffa et al. 2003b; Cessenat 1996, p. 49].

[3]For the chosen definition of the EFIO, we have the mapping $\mathcal{T} : H^{-1/2}(\nabla_\Gamma\cdot, \Gamma) \mapsto H^{-1/2}(\nabla_\Gamma\times, \Gamma)$ between Sobolev spaces $H^{-1/2}$ such that $\boldsymbol{f}_n \in H^{-1/2}(\nabla_\Gamma\cdot, \Gamma)$ ensures dual space testing. See, for example, [Sauter et al. 2011, pp. 57ff] for a corresponding introduction.

for the nth directed edge $\boldsymbol{d}_n$ of the triangular mesh and the conventions in Fig. 3.3. The domains of the cells are denoted as $c_n^{\pm}$, the vertices of the edge $\boldsymbol{d}_n$ as $v_n^{\pm}$, and the position vectors of the vertices opposite to $\boldsymbol{d}_n$ as $\boldsymbol{r}_n^{\pm}$. Note that in contrast to [Rao et al. 1982] no normalization with respect to the length of $\boldsymbol{d}_n$ is performed resulting in a more compact definition of the loop-star matrices [Andriulli et al. 2013]. The basis functions for the curvilinear rectangular elements will be specified in Chapter 6 in an analogous manner.

3.1.3 Matrix Elements

The parametric description of the surface Γ and the basis functions enables the evaluation of the matrix entries of $\boldsymbol{T}_{\mathrm{A}}$ as

$$[\boldsymbol{T}_{\mathrm{A}}]_{mn} = \iint_{\hat{\Gamma}} \boldsymbol{J}(u,v)\hat{\boldsymbol{f}}_m(u,v) \cdot \iint_{\hat{\Gamma}} g(\boldsymbol{s}(u,v),\boldsymbol{s}(u',v'))\, \boldsymbol{J}(u',v')\hat{\boldsymbol{f}}_n(u',v')\,\mathrm{d}u'\mathrm{d}v'\mathrm{d}u\mathrm{d}v \quad (3.15)$$

and the matrix $\boldsymbol{T}_{\Phi}$ as

$$[\boldsymbol{T}_{\Phi}]_{mn} = -\iint_{\hat{\Gamma}} \nabla_{\hat{\Gamma}} \cdot \hat{\boldsymbol{f}}_m(u,v) \iint_{\hat{\Gamma}} g(\boldsymbol{s}(u,v),\boldsymbol{s}(u',v'))\, \nabla_{\hat{\Gamma}} \cdot \hat{\boldsymbol{f}}_n(u',v')\,\mathrm{d}u'\mathrm{d}v'\mathrm{d}u\mathrm{d}v\,, \quad (3.16)$$

where we have used the Stokes identity [Nédélec 2001, p. 73]

$$\iint_{\Gamma} \boldsymbol{f} \cdot \nabla\phi\,\mathrm{d}\boldsymbol{r}' = -\iint_{\Gamma} \phi\,\nabla_{\Gamma} \cdot \boldsymbol{f}\,\mathrm{d}\boldsymbol{r}'\,. \quad (3.17)$$

as well as the relation $\nabla_{\Gamma} \cdot \boldsymbol{f}_n = D^{-1}\nabla_{\hat{\Gamma}} \cdot \hat{\boldsymbol{f}}_n$ [Peterson 2006, p. 88]. The RHS vector $\boldsymbol{e}^{\mathrm{ex}}$ can be evaluated as

$$[\boldsymbol{e}^{\mathrm{ex}}]_m = \iint_{\hat{\Gamma}} \boldsymbol{J}(u,v)\hat{\boldsymbol{f}}_m(u,v) \cdot \boldsymbol{e}^{\mathrm{ex}}(\boldsymbol{s}(u,v))\,\mathrm{d}u\mathrm{d}v \quad (3.18)$$

showing that the generalized Jacobi determinant cancels in all expressions and that all evaluations of the basis functions can be performed in the parametric domain.

3.2 Quasi-Helmholtz Decompositions

The discretized EFIE $\boldsymbol{T}\boldsymbol{j} = \boldsymbol{e}^{\mathrm{ex}}$ in (3.2) has been shown to exhibit an ill-conditioning [Andriulli et al. 2010]

$$\operatorname{cond} \boldsymbol{T} \propto \left(\frac{\lambda}{h}\right)^2 = \frac{1}{(kh)^2}\,, \quad (3.19)$$

where h is the average edge length of the triangulation. As discussed in Section 1.1.1, the ill-conditioning in k can be overcome by quasi-Helmholtz decompositions. Namely, we consider the loop-star decomposition mainly for purposes of analyzing different problems. The actual decomposition of interest are then obtained leveraging quasi-Helmholtz projectors.

(a) (b)

Fig. 3.4: Examples of loop-star basis functions: (a) RWG loop formed around a vertex by five RWG functions; (b) RWG star formed around a triangle by three RWG functions.

3.2.1 Loop-Star Decomposition

The basic idea of the loop-star decomposition is to express the surface current density $\boldsymbol{j}$ as a superposition of N_Λ local loops $\boldsymbol{\Lambda}_m$ and N_H global loops $\boldsymbol{H}_m$ (associated with the handles and holes of Γ) representing the solenoidal component of $\boldsymbol{j}$, as well as N_Σ stars $\boldsymbol{\Sigma}_m$ representing the non-solenoidal component of $\boldsymbol{j}$ [Wu et al. 1995; Burton et al. 1995; Vecchi 1999]. To do so, following [Andriulli 2012] the star to RWG expansion coefficient mapping matrix $\boldsymbol{\Sigma} \in \mathbb{Z}^{N\times N_\Lambda}$ defined via the cells $c_i^\pm$ of the mesh (see Fig. 3.3)

$$[\boldsymbol{\Sigma}]_{ij} = \begin{cases} 1 & \text{if} \quad c_j = c_i^+ \\ -1 & \text{if} \quad c_j = c_i^- \\ 0 & \text{else} \end{cases}, \tag{3.20}$$

the loop to RWG expansion coefficient mapping matrix $\boldsymbol{\Lambda} \in \mathbb{Z}^{N\times N_\Sigma}$ defined via the vertices $v_i^\pm$ of the mesh

$$[\boldsymbol{\Lambda}]_{ij} = \begin{cases} 1 & \text{if} \quad v_j = v_i^+ \\ -1 & \text{if} \quad v_j = v_i^- \\ 0 & \text{else} \end{cases}, \tag{3.21}$$

and the global loop to RWG expansion coefficient mapping matrix $\boldsymbol{H} \in \mathbb{R}^{N\times N_H}$ are introduced. An explicit definition of $\boldsymbol{H}$ will be given in Chapter 4. The transpose of these mapping matrices superimpose the original RWG functions to form the loops

$$\boldsymbol{\Lambda}_m = \sum_{n=1}^{N} \left[\boldsymbol{\Lambda}^{\mathrm{T}}\right]_{mn} \boldsymbol{f}_n \tag{3.22}$$

and the stars

$$\Sigma_m = \sum_{n=1}^{N} \left[\boldsymbol{\Sigma}^{\mathrm{T}}\right]_{mn} \boldsymbol{f}_n \tag{3.23}$$

as exemplified in Fig. 3.4. Applying the transformation matrix

$$\boldsymbol{Q} = [\boldsymbol{\Lambda}\ \boldsymbol{H}\ \boldsymbol{\Sigma}] \tag{3.24}$$

to (3.2) as

$$\boldsymbol{T}_{\Lambda H \Sigma} \boldsymbol{j}'' = \boldsymbol{Q}^{\mathrm{T}} \boldsymbol{T} \boldsymbol{Q} \boldsymbol{j}'' = \boldsymbol{Q}^{\mathrm{T}} \boldsymbol{e}^{\mathrm{ex}} , \tag{3.25}$$

with $\boldsymbol{j} = \boldsymbol{Q}\boldsymbol{j}''$, allows to remove the ill-conditioning of (3.2) with respect to k by introducing suitable diagonal block normalization matrices $\boldsymbol{D}_1$ and $\boldsymbol{D}_2$ yielding the stabilized system

$$\boldsymbol{D}_1 \boldsymbol{T}_{\Lambda H \Sigma} \boldsymbol{D}_2 \boldsymbol{j}' = \boldsymbol{D}_1 \boldsymbol{Q}^{\mathrm{T}} \boldsymbol{e}^{\mathrm{ex}} \tag{3.26}$$

with $\boldsymbol{j} = \boldsymbol{Q}\boldsymbol{D}_2\boldsymbol{j}'$. Since the choice of the matrices $\boldsymbol{D}_i$ is the central topic of Chapter 5 we define it here in a general form as

$$\boldsymbol{D}_i = \operatorname{diag}(\alpha_i, \gamma_i, \beta_i) = \begin{bmatrix} \alpha_i \mathbf{I}_{N_\Lambda \times N_\Lambda} & & \\ & \gamma_i \mathbf{I}_{N_H \times N_H} & \\ & & \beta_i \mathbf{I}_{N_\Sigma \times N_\Sigma} \end{bmatrix} \tag{3.27}$$

Consequently, the preconditioned system (3.2) is solved for $\boldsymbol{j}' = [\boldsymbol{j}_\Lambda^{\mathrm{T}} \ \boldsymbol{j}_H^{\mathrm{T}} \ \boldsymbol{j}_\Sigma^{\mathrm{T}}]^{\mathrm{T}}$ which is related to the actual current vector as

$$\boldsymbol{j} = \alpha_2 \boldsymbol{\Lambda} \boldsymbol{j}_\Lambda + \gamma_2 \boldsymbol{H} \boldsymbol{j}_H + \beta_2 \boldsymbol{\Sigma} \boldsymbol{j}_\Sigma . \tag{3.28}$$

Note that instead of stars also tree functions can be employed to complement the loops and form the loop-tree decomposition [Eibert 2004; Andriulli 2012]. However, they lack the orthogonality property [Andriulli et al. 2013]

$$\boldsymbol{\Lambda}^{\mathrm{T}} \boldsymbol{\Sigma} = \boldsymbol{\Sigma}^{\mathrm{T}} \boldsymbol{\Lambda} = \mathbf{0} \tag{3.29}$$

valid for the loop-star matrices. This property is a key to define the quasi-Helmholtz projectors in the following Section 3.2.2.

3.2.2 Quasi-Helmholtz Projectors

As an improvement over the loop-star decomposition, the quasi-Helmholtz projectors introduced in [Andriulli et al. 2013] can be employed: The orthogonal projectors $\boldsymbol{P}_\Sigma \in \mathbb{R}^{N \times N}$ defined by

$$\boldsymbol{P}_\Sigma = \boldsymbol{\Sigma} (\boldsymbol{\Sigma}^{\mathrm{T}} \boldsymbol{\Sigma})^{+} \boldsymbol{\Sigma}^{\mathrm{T}} , \tag{3.30}$$

where $(\cdot)^+$ denotes the Moore-Penrose pseudoinverse, $\boldsymbol{P}_\Lambda \in \mathbb{R}^{N \times N}$ defined by

$$\boldsymbol{P}_\Lambda = \boldsymbol{\Lambda} (\boldsymbol{\Lambda}^{\mathrm{T}} \boldsymbol{\Lambda})^{+} \boldsymbol{\Lambda}^{\mathrm{T}} , \tag{3.31}$$

and $\boldsymbol{P}_H \in \mathbb{R}^{N \times N}$ defined by

$$\boldsymbol{P}_H = \mathbf{I} - \boldsymbol{P}_\Lambda - \boldsymbol{P}_\Sigma \tag{3.32}$$

Table 3.1: Notation overview.

	loop-star	projectors
$\boldsymbol{j}'_{\text{sol}} \coloneqq$	$\boldsymbol{\Lambda} \boldsymbol{j}_{\boldsymbol{\Lambda}}$	$\boldsymbol{P}_{\boldsymbol{\Lambda}} \boldsymbol{j}'$
$\boldsymbol{j}'_{\text{hsol}} \coloneqq$	$\boldsymbol{H} \boldsymbol{j}_{\boldsymbol{H}}$	$\boldsymbol{P}_{\boldsymbol{H}} \boldsymbol{j}'$
$\boldsymbol{j}'_{\text{nsol}} \coloneqq$	$\boldsymbol{\Sigma} \boldsymbol{j}_{\boldsymbol{\Sigma}}$	$\boldsymbol{P}_{\boldsymbol{\Sigma}} \boldsymbol{j}'$

$\boldsymbol{j}_{\text{sol}} \coloneqq$	$\alpha_2 \boldsymbol{j}'_{\text{sol}}$
$\boldsymbol{j}_{\text{hsol}} \coloneqq$	$\gamma_2 \boldsymbol{j}'_{\text{hsol}}$
$\boldsymbol{j}_{\text{nsol}} \coloneqq$	$\beta_2 \boldsymbol{j}'_{\text{nsol}}$

	loop-star	projectors
$\boldsymbol{e}_{\text{sol}} \coloneqq$	$\boldsymbol{\Lambda}^{\mathrm{T}} \boldsymbol{e}^{\text{ex}}$	$\boldsymbol{P}_{\boldsymbol{\Lambda}} \boldsymbol{e}^{\text{ex}}$
$\boldsymbol{e}_{\text{hsol}} \coloneqq$	$\boldsymbol{H}^{\mathrm{T}} \boldsymbol{e}^{\text{ex}}$	$\boldsymbol{P}_{\boldsymbol{H}} \boldsymbol{e}^{\text{ex}}$
$\boldsymbol{e}_{\text{nsol}} \coloneqq$	$\boldsymbol{\Sigma}^{\mathrm{T}} \boldsymbol{e}^{\text{ex}}$	$\boldsymbol{P}_{\boldsymbol{\Sigma}} \boldsymbol{e}^{\text{ex}}$

$\boldsymbol{e}'_{\text{sol}} \coloneqq$	$\alpha_1 \boldsymbol{e}_{\text{sol}}$
$\boldsymbol{e}'_{\text{hsol}} \coloneqq$	$\gamma_1 \boldsymbol{e}_{\text{hsol}}$
$\boldsymbol{e}'_{\text{nsol}} \coloneqq$	$\beta_1 \boldsymbol{e}_{\text{nsol}}$

are introduced (note that the pseudoinverses can be computed efficiently via algebraic multigrid (AMG) preconditioning as detailed in [Andriulli et al. 2013, Section V]) as well as the decomposition operator

$$\boldsymbol{P}_i = \alpha_i \boldsymbol{P}_{\boldsymbol{\Lambda}} + \gamma_i \boldsymbol{P}_{\boldsymbol{H}} + \beta_i \boldsymbol{P}_{\boldsymbol{\Sigma}} \,. \tag{3.33}$$

Applying the latter to (3.2) as

$$\boldsymbol{P}_1 \boldsymbol{T} \boldsymbol{P}_2 \boldsymbol{j}' = \boldsymbol{P}_1 \boldsymbol{e}^{\text{ex}} \tag{3.34}$$

yields a well-conditioned LSE, which is better conditioned than the loop-star preconditioned system (3.26), with

$$\boldsymbol{j} = \boldsymbol{P}_2 \boldsymbol{j}' = \alpha_2 \boldsymbol{P}_{\boldsymbol{\Lambda}} \boldsymbol{j}' + \gamma_2 \boldsymbol{P}_{\boldsymbol{H}} \boldsymbol{j}' + \beta_2 \boldsymbol{P}_{\boldsymbol{\Sigma}} \boldsymbol{j}' \tag{3.35}$$

if α_i, β_i, and γ_i, $i = 1, 2$ are suitably chosen. Note, that in [Andriulli et al. 2013], a combined projector,

$$\boldsymbol{P}_{\boldsymbol{\Lambda H}} = \boldsymbol{P}_{\boldsymbol{\Lambda}} + \boldsymbol{P}_{\boldsymbol{H}} = \mathbf{I} - \boldsymbol{P}_{\boldsymbol{\Sigma}} \tag{3.36}$$

is used with $\alpha_1 = \alpha_2 = \gamma_1 = \gamma_2 = 1/\sqrt{k}$ and $\beta_1 = \beta_2 = \mathrm{j}\sqrt{k}$. In contrast, we chose with our definition of $\boldsymbol{P}_i$ to treat $\boldsymbol{P}_{\boldsymbol{\Lambda}}$ and $\boldsymbol{P}_{\boldsymbol{H}}$ separately as we need the general form in several places for our theoretical apparatus. All final formulations use again the combined projector $\boldsymbol{P}_{\boldsymbol{\Lambda H}}$.

For both decompositions, we define the quasi-Helmholtz components $\boldsymbol{j}'_{\text{sol}}$, $\boldsymbol{j}'_{\text{hsol}}$, and $\boldsymbol{j}'_{\text{nsol}}$, that is, the solenoidal component, the solenoidal component associated with the handles and holes of Γ, and the non-solenoidal component, respectively, as shown in Table 3.1. This leads to the preconditioner-agnostic definitions of $\boldsymbol{j}_{\text{sol}}$, $\boldsymbol{j}_{\text{hsol}}$, and $\boldsymbol{j}_{\text{nsol}}$. Moreover, we introduce $\boldsymbol{j}_{\text{sol,hsol}} = \boldsymbol{j}_{\text{sol}} + \boldsymbol{j}_{\text{hsol}}$. The RHS Helmholtz components $\boldsymbol{e}_{\text{sol}}$, $\boldsymbol{e}_{\text{hsol}}$, $\boldsymbol{e}_{\text{nsol}}$, as well as their primed variants are defined analogously.

3.3 Equivalent Source Reconstruction

Just as the EFIE, the continuous equations describing the equivalent source reconstruction problem are discretized to approximate the solution. Concerning the reconstruction of

equivalent surface currents a strategy similar to the one for the discretization of the EFIE is employed. Since it is part of the in this work proposed stabilization method, it is introduced in detail in Chapter 7.

The discretization of the spherical vector wave formulation for the equivalent source reconstruction follows without modification [Hansen 1988]. A brief summary is given at the beginning of Chapter 8.

Part II

Paradigms for Boundary Integral Scattering and Radiation Formulations

4

An Excitation Agnostic Right-Hand Side Discretization Scheme

> "The first important notions in topology were acquired in the course of the study of polyhedra."
>
> [Lebesgue 1924]

In order to accurately compute scattered and radiated fields in the presence of arbitrary excitations, a low-frequency stable discretization of the RHS of the quasi-Helmholtz preconditioned EFIE on multiply-connected geometries is introduced, which avoids an ad-hoc extraction of the static contribution of the RHS when tested with solenoidal functions. To obtain an excitation agnostic approach, the proposed approach generalizes a technique to multiply-connected geometries where the testing of the RHS with loop functions is replaced by a testing of the normal component of the magnetic field with a scalar function. To this end, we leverage orientable global loop functions that are formed by a chain of RWG functions around the holes and handles of the geometry, for which we introduce cap surfaces that allow to uniquely define a suitable scalar function. It is shown that this approach works with open and closed, orientable and non-orientable geometries. The numerical results demonstrate the effectiveness of the approach.

This chapter is based on [Hofmann et al. 2023a] including substantial verbatim portions, where preliminary results were presented in [Hofmann et al. 2022b; Hofmann et al. 2021b; Hofmann et al. 2021a; Hofmann et al. 2022d; Hofmann et al. 2022a].

While the preconditioned EFIE (3.26) or (3.34) is no longer ill-conditioned in k, for the accurate computation of surface current densities and fields, a well-conditioned system matrix alone is not sufficient. One issue that must be resolved is that testing the incident field directly with solenoidal and, on multiply-connected geometries, with solenoidal functions associated with the handles and holes of the structure can lead to catastrophic round-off errors. In consequence, the physically

correct scaling in frequency of the RHS cannot be maintained resulting in incorrect surface current densities [Bogaert et al. 2014].

One strategy to obtain an accurate discretization of the RHS leverages a Taylor series expansion of the excitation field to set the static contribution to zero when tested with solenoidal functions [Andriulli et al. 2013; Chhim et al. 2020; Adrian et al. 2021]. Notably, this approach is independent of the topology of the underlying geometry. Since it is not agnostic of the RHS, the extraction of the static part must be derived and implemented for each excitation. For an impinging wave that is modeled based on measurement data, however, this might be impractical.

In the case that information on the magnetic field is available, an alternative solution is to replace the testing of the electric field with a solenoidal function by testing the normal component of the magnetic field with a corresponding scalar function. One of the earliest accounts of this method is by Mautz and Harrington [Mautz et al. 1982; Mautz et al. 1984], where they used a decomposition similar to the loop-star decomposition, but adapted to a body of revolution formulation. Moreover, the method was used in the context of magnetostatics [Arvas et al. 1983; Arvas et al. 1986], and later applied to the RWG discretized, loop-star decomposed EFIE [Wu et al. 1995]. In these works, the treatment of multiply-connected geometries was only partial. For example, [Wu et al. 1995] notes that global loops must be incorporated into the quasi-Helmholtz basis, but the discretization of the RHS is only studied for local loops, for which a corresponding scalar function is straightforward to define. In [Mautz et al. 1984], open surfaces with holes are treated and it is suggested to introduce a cap surface in order to close the hole. However, while the analysis was general, the basis functions provided were limited to bodies of revolution. Closed bodies, such as a torus, or non-orientable surfaces were not treated. Hence it is unclear, how such an approach can be extended to global loops on surfaces of arbitrary topology.

In this chapter, we generalize the approach of Mautz and Harrington to the case of an RWG-based discretization, where the underlying geometry may be open or closed, simply- or multiply-connected, and orientable or non-orientable, thus, enabling the treatment of arbitrary excitations in an RHS agnostic approach. Specifically, the contribution is two-fold: i) We show how a scalar function can be efficiently derived for global RWG loops which are constructed as a chain of RWG functions forming an orientable strip. This allows to introduce a cap surface such that a scalar function can be defined. The obtained scalar function is then used to test the normal component of the magnetic field resulting in a stable testing procedure for arbitrary RHS excitations. ii) We demonstrate how this generalized excitation agnostic RHS scheme can be combined with the quasi-Helmholtz projectors $\boldsymbol{P}_i$ of [Andriulli et al. 2013], thus, facilitating their use with arbitrary excitations. Numerical results corroborate the presented theory and demonstrate the effectiveness of our approach, including cases of non-orientable and multiply-connected geometries such as the Möbius strip.

To this end, this chapter is organized as follows: Section 4.1 elaborates on the numerically accurate testing scheme for arbitrary incident waves, including an analysis for the root causes of the occurring round-off errors. The analysis is carried out in the first place based on a loop-star decomposition in order to highlight different low-frequency issues related to

the excitations. In a second step, we will then show how to adapt the solution strategies such that they become applicable to the quasi-Helmholtz projectors—the actual decomposition we are interested in. The corresponding adaption of the projector based approach is deduced in Section 4.2, and numerical studies on the influence of the RHS evaluation on the solution accuracy are presented in Section 4.3.

4.1 Stable Evaluation of the Right-Hand Side On Multiply-Connected Geometries

In the following, we are interested in stabilizing the evaluation of the RHS

$$\boldsymbol{Q}^{\mathrm{T}}\boldsymbol{e}^{\mathrm{ex}} = \begin{bmatrix} \boldsymbol{\Lambda}^{\mathrm{T}}\boldsymbol{e}^{\mathrm{ex}} \\ \boldsymbol{H}^{\mathrm{T}}\boldsymbol{e}^{\mathrm{ex}} \\ \boldsymbol{\Sigma}^{\mathrm{T}}\boldsymbol{e}^{\mathrm{ex}} \end{bmatrix} \tag{4.1}$$

in (3.26). We note that the m-th entry of $\boldsymbol{\Lambda}^{\mathrm{T}}\boldsymbol{e}^{\mathrm{ex}}$ corresponds to testing the incident field $\boldsymbol{e}^{\mathrm{ex}}$ with the m-th loop function $\boldsymbol{\Lambda}_m$, that is,

$$\left[\boldsymbol{\Lambda}^{\mathrm{T}}\boldsymbol{e}^{\mathrm{ex}}\right]_m = \sum_{n=1}^{N} \left[\boldsymbol{\Lambda}^{\mathrm{T}}\right]_{mn} \iint_{\Gamma} \boldsymbol{f}_n \cdot \boldsymbol{e}^{\mathrm{ex}} \,\mathrm{d}\boldsymbol{r} = \iint_{\Gamma} \boldsymbol{\Lambda}_m \cdot \boldsymbol{e}^{\mathrm{ex}} \,\mathrm{d}\boldsymbol{r}\,. \tag{4.2}$$

The same is true for the m-th entry of $\boldsymbol{H}^{\mathrm{T}}\boldsymbol{e}^{\mathrm{ex}}$, where the corresponding loop $\boldsymbol{H}_m$ is a global one. Evaluating (4.2) by numerical integration, either by adding up the contributions from each test function $\boldsymbol{f}_n$ or by directly testing with $\boldsymbol{\Lambda}_m$, can lead to catastrophic round-off errors, the precise behavior depending on the RHS as will be discussed in the following subsection. For a plane wave excitation $\boldsymbol{e}^{\mathrm{ex}} = \boldsymbol{e}_0 \mathrm{e}^{-\mathrm{j}\boldsymbol{k}\cdot\boldsymbol{r}}$, a known remedy is to leverage a Taylor series expansion of $\mathrm{e}^{-\mathrm{j}\boldsymbol{k}\cdot\boldsymbol{r}}$ around $\boldsymbol{k}\cdot\boldsymbol{r} = 0$ and subtracting the static contribution [Andriulli et al. 2013; Adrian et al. 2021], that is,

$$\left[\boldsymbol{\Lambda}^{\mathrm{T}}\boldsymbol{e}^{\mathrm{ex}}\right]_m = \sum_{n=1}^{N} \left[\boldsymbol{\Lambda}^{\mathrm{T}}\right]_{mn} \iint_{\Gamma} \boldsymbol{f}_n \cdot \boldsymbol{e}_0 \, \mathfrak{T}\left(\mathrm{e}^{-\mathrm{j}\boldsymbol{k}\cdot\boldsymbol{r}} - 1\right) \mathrm{d}\boldsymbol{r} \tag{4.3}$$

where

$$\mathfrak{T}\left(\mathrm{e}^{-\mathrm{j}\boldsymbol{k}\cdot\boldsymbol{r}} - 1\right) = \begin{cases} \displaystyle\sum_{q=1}^{Q} \frac{(-\mathrm{j}\boldsymbol{k}\cdot\boldsymbol{r})^q}{q!} & \text{for} \quad |\boldsymbol{k}\cdot\boldsymbol{r}| < 1 \\ \mathrm{e}^{-\mathrm{j}\boldsymbol{k}\cdot\boldsymbol{r}} - 1 & \text{else} \end{cases} \tag{4.4}$$

denotes the Taylor series expansion around $\boldsymbol{k}\cdot\boldsymbol{r} = 0$ with a sufficiently large Q. However, such an approach requires its adaption to each and every excitation, which is impractical. Remedies for general excitations are known for $\boldsymbol{\Lambda}_m$ that avoid ad-hoc extractions of the static part of the RHS. In the following, we generalize these to $\boldsymbol{H}_m$, after an analysis for which RHSs we expect round-off errors.

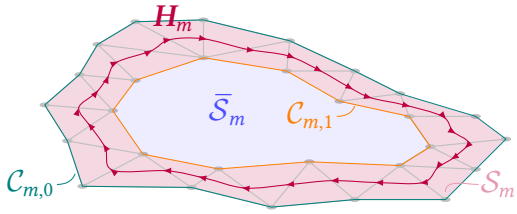

Fig. 4.1: Example of a global loop $\boldsymbol{H}_m$ as a chain of RWG functions with support $\mathcal{S}_m$ and boundary $\partial\mathcal{S}_m = \mathcal{C}_{m,0} \cup \mathcal{C}_{m,1}$. © 2023 IEEE.

4.1.1 Analysis of the RHS Round-Off Errors—When to Expect and When Not to Expect Them

As local loops $\boldsymbol{\Lambda}_m$ and global loops $\boldsymbol{H}_m$ will be treated in a similar way, we call their union $\boldsymbol{\ell}_m$. That is, $\boldsymbol{\ell}_m$ can represent $\boldsymbol{\Lambda}_m$ or $\boldsymbol{H}_m$. Since all $\boldsymbol{\ell}_m$ are solenoidal, i.e., $\nabla_\Gamma \cdot \boldsymbol{\ell}_m = 0$ with $\nabla_\Gamma \cdot$ denoting the surface divergence, they can be expressed by the surface gradient of a scalar function[1] ψ_m as [Bladel 1993; Bladel 2007, (A1.65)]

$$\boldsymbol{\ell}_m = \boldsymbol{n}_m \times \nabla_\Gamma \psi_m(\boldsymbol{r}) \,, \tag{4.5}$$

where $\boldsymbol{n}_m$ denotes the normal vector field associated with the loop $\boldsymbol{\ell}_m$. While for general $\boldsymbol{H}_m$ this can lead to multi-valued ψ_m [Verite 1987], we consider here only $\boldsymbol{H}_m$ which are constructed as a chain of RWG functions forming an orientable surface with surface normal $\boldsymbol{n}_m$ (as noted in Section 2.3 a surface normal for the whole surface Γ is neither needed for the EFIE nor introduced, as for non-orientable surfaces there is no canonical normal vector-field on Γ [Johnson et al. 1990; Buffa et al. 2003a]). An example of such a chain is shown in Fig. 4.1. The construction of global loops is a common problem in many branches of finite and boundary element method problems, see, for example [Alonso Rodríguez et al. 2017]. Specifically, algorithms [Dey et al. 2013; Hiptmair et al. 2002; Erickson et al. 2004; Erickson et al. 2005; Dey 1994; Yin et al. 2007] are suitable for finding global loops on a surface.[2]

Naturally, this poses the question if for any Γ for which the EFIE is admissible we can find such an orientable surface. As noted in Section 2.3, we limit ourselves to manifolds (e.g., this excludes geometries with T-junctions) in order to leverage results from topology, though we conjecture that the method would work even for more general geometries. More specifically, invoking the classification theorem for surfaces [Richeson 2012, p. 181], the topological constraints on Γ denoted in Section 2.3 imply that Γ is either homeomorphic to a sphere, to the connected sum of tori, or to a non-orientable Möbius strip, where each of these may have a finite number of holes cut out. It turns out that on such Γ, we can always find $\boldsymbol{H}_m$ with the desired properties: for Γ homeomorphic to a sphere or to the connected

[1] In this context, ψ_m is also called scalar potential [Bladel 2007; Bladel 1993; Verite 1987] or solenoidal potential [Vecchi 1999].

[2] The reader should be reminded that the found loops are not uniquely determined. Even when the sequence is optimized such that the shortest possible loops are determined, the found global loops are not unique. E.g., for a torus several poloidal loops of equal length can exist.

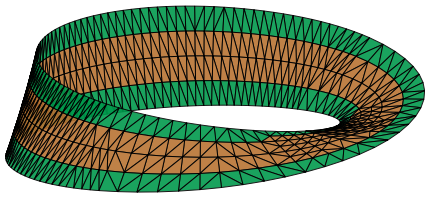

Fig. 4.2: Mesh of a non-orientable Möbius strip discretized with 852 triangles and 1180 RWGs. The green triangles form an orientable surface that could serve as support for a global loop. © 2023 IEEE

sum of tori, this follows from the fact that they are orientable surfaces; for Γ homeomorphic to a Möbius strip, we recall that when the strip is cut along its center line, the resulting strip is no longer a Möbius strip but a longer orientable strip with two half twists [Richeson 2012, pp. 162ff]. On this orientable strip, which is homeomorphic to a sphere with two holes, we can construct a global loop with the desired properties. For example, the green triangles shown in Fig. 4.2 form an orientable surface that could serve as support for a global loop (evidently, the Möbius strip must be meshed finely enough so that there is a center line). Hence, no additional restrictions on Γ are imposed.

Constructing the $\boldsymbol{H}_m$ in such a manner (as chain of RWG functions) ensures that the boundary $\partial\mathcal{S}_m$ of the support $\mathcal{S}_m$ of any $\boldsymbol{H}_m$ consists of two disjoint curves $\mathcal{C}_{m,0}$ and $\mathcal{C}_{m,1}$ (see Fig. 4.1). As will be shown in Section 4.1.2, it allows to choose the corresponding ψ_m to be zero on one of the boundary curves, and it ensures ψ_m to be single-valued by implicitly considering one of the curves as a cut, where ψ_m otherwise would be discontinuous.

Inserting (4.5) into (4.2) and using the identity of [Mautz et al. 1982, (C-1)], the representation

$$\iint_\Gamma \boldsymbol{\ell}_m \cdot \boldsymbol{e}^{\mathrm{ex}} \,\mathrm{d}\boldsymbol{r} = -\iint_\Gamma \psi_m \boldsymbol{n}_m \cdot (\nabla \times \boldsymbol{e}^{\mathrm{ex}}) \,\mathrm{d}\boldsymbol{r} + \int_{\partial\mathcal{S}_m} \psi_m (\boldsymbol{e}^{\mathrm{ex}} \cdot \boldsymbol{u}_m) \,\mathrm{d}\boldsymbol{r} \tag{4.6}$$

is obtained. Here the line integral is along the boundary $\partial\mathcal{S}_m$ of the support $\mathcal{S}_m$ of $\boldsymbol{\ell}_m$, and $\boldsymbol{u}_m$ is the unit vector tangent to $\partial\mathcal{S}_m$ forming a right-handed system with $\boldsymbol{n}_m$. For $\boldsymbol{\Lambda}_m$, the contribution of the line integral is zero as $\psi_m = 0$ on $\partial\mathcal{S}_m$. For $\boldsymbol{H}_m$, we have $\psi_m = 0$ only on one of the two disjoint curves forming $\partial\mathcal{S}_m$, for example, $\mathcal{C}_{m,0}$, whereas we have $\psi_m = 1$ on the other curve $\mathcal{C}_{m,1}$. Thus, the line integral does not vanish on $\mathcal{C}_{m,1}$. To remove this line integral, we introduce an arbitrary cap surface $\bar{\mathcal{S}}_m$ with $\partial\bar{\mathcal{S}}_m = \mathcal{C}_{m,1}$ (see Fig. 4.1), apply Stokes' theorem with respect to $\bar{\mathcal{S}}_m$, and leverage that ψ_m is constant on $\mathcal{C}_{m,1}$ resulting in

$$\iint_\Gamma \boldsymbol{\ell}_m \cdot \boldsymbol{e}^{\mathrm{ex}} \,\mathrm{d}\boldsymbol{r} = -\iint_\Gamma \psi_m \boldsymbol{n}_m \cdot \nabla \times \boldsymbol{e}^{\mathrm{ex}} \,\mathrm{d}\boldsymbol{r} + \iint_{\bar{\mathcal{S}}_m} \boldsymbol{n}_m \cdot \nabla \times \boldsymbol{e}^{\mathrm{ex}} \,\mathrm{d}\boldsymbol{r}\,. \tag{4.7}$$

This representation shows that testing the incident field $\boldsymbol{e}^{\mathrm{ex}}$ with a loop function (i.e., when evaluating (4.2)) corresponds to computing the curl of $\boldsymbol{e}^{\mathrm{ex}}$ perpendicular to $\boldsymbol{n}_m$ weighted with a scalar function (see also the remark for local loops in [Wu et al. 1995]). Such a computation is stable whenever $|\nabla \times \boldsymbol{e}^{\mathrm{ex}}|$ and $|\boldsymbol{e}^{\mathrm{ex}}|$ have a similar order of magnitude. Otherwise, the limitation of the numerical precision can lead to a loss of significant digits resulting in

an erroneous RHS. In general, $|\nabla \times \boldsymbol{e}^{\mathrm{ex}}|$ and $|\boldsymbol{e}^{\mathrm{ex}}|$ will asymptotically scale differently in k for $k \to 0$, and thus result in unstable discretizations of the RHS. However, it is interesting to note that if

$$\mathcal{O}(|\nabla \times \boldsymbol{e}^{\mathrm{ex}}|) = \mathcal{O}(|\boldsymbol{e}^{\mathrm{ex}}|) \tag{4.8}$$

is satisfied (i.e., $|\nabla \times \boldsymbol{e}^{\mathrm{ex}}|$ and $|\boldsymbol{e}^{\mathrm{ex}}|$ have the same asymptotic scaling in k) and if a sufficient machine precision is used, then the testing with loop functions is stable independent from k (and thus, also the evaluation in (4.2)). To obtain a numerical test that detects whether or not this condition is satisfied, we recast (4.8) by leveraging Faraday's law $\nabla \times \boldsymbol{e}^{\mathrm{ex}} = -\mathrm{j}k\boldsymbol{h}^{\mathrm{ex}}$ resulting in the equivalent condition

$$\mathcal{O}(|\boldsymbol{e}^{\mathrm{ex}}|) = \mathcal{O}(k\,|\boldsymbol{n}_m \cdot \boldsymbol{h}^{\mathrm{ex}}|)\,. \tag{4.9}$$

Again, it should be stressed that, in general, an excitation will not satisfy this condition and thus its discretization will become unstable for $k \to 0$. For example, neither a plane-wave excitation, where we have $\mathcal{O}(|\boldsymbol{e}^{\mathrm{ex}}|) = \mathcal{O}(|\boldsymbol{h}^{\mathrm{ex}}|) = \mathcal{O}(1)$, nor a Hertzian dipole excitation, where we have $\mathcal{O}(|\boldsymbol{e}^{\mathrm{ex}}|) = \mathcal{O}(1/k)$ and $\mathcal{O}(|\boldsymbol{h}^{\mathrm{ex}}|) = \mathcal{O}(1)$, satisfies (4.9). A notable exception is an electric ring current, where we have $\mathcal{O}(|\boldsymbol{e}^{\mathrm{ex}}|) = \mathcal{O}(k)$ and $\mathcal{O}(|\boldsymbol{h}^{\mathrm{ex}}|) = \mathcal{O}(1)$ resulting in no k-dependent round-off errors. This will be confirmed by the numerical results in Section 4.3.

4.1.2 Handling Arbitrary Excitations—Construction of Scalar Functions ψ_m for Global RWG Loops

Equation (4.7) can be leveraged to obtain a stable RHS evaluation scheme for $\boldsymbol{H}_m$: We forgo the implicit computation of $\nabla \times \boldsymbol{e}^{\mathrm{ex}}$ by using its analytical expression $\nabla \times \boldsymbol{e}^{\mathrm{ex}} = -\mathrm{j}k\boldsymbol{h}^{\mathrm{ex}}$ (as was originally suggested in [Mautz et al. 1984] in the context of simply-connected body of revolution problems) resulting in

$$\iint_{\Gamma} \boldsymbol{\ell}_m \cdot \boldsymbol{e}^{\mathrm{ex}}\,\mathrm{d}\boldsymbol{r} = \mathrm{j}k \iint_{\Gamma} \psi_m \boldsymbol{n}_m \cdot \boldsymbol{h}^{\mathrm{ex}}\,\mathrm{d}\boldsymbol{r} - \mathrm{j}k \iint_{\hat{S}_m} \boldsymbol{n}_m \cdot \boldsymbol{h}^{\mathrm{ex}}\,\mathrm{d}\boldsymbol{r}\,. \tag{4.10}$$

To derive an expression for ψ_m corresponding to $\boldsymbol{H}_m$, we first consider the well-known local loop case. Here, the scalar function ψ_m can be expressed in closed form on the d-th triangle as [Zhao et al. 2002; Zhao et al. 2000]

$$\psi_{md}(\boldsymbol{r}) = 1 + \frac{1}{2S_d}(\boldsymbol{r} - \boldsymbol{c}_m) \cdot ((\boldsymbol{r}_{2d} - \boldsymbol{r}_{1d}) \times \boldsymbol{n}_{md})\,, \tag{4.11}$$

which corresponds to a pyramid shape around the center node $\boldsymbol{c}_m$ as shown in Fig. 4.3. Since the integration is carried out in the parametric domain, it is useful to express ψ directly in the parametric domain as

$$\psi_{md}(u, v) = 1 - u - v\,. \tag{4.12}$$

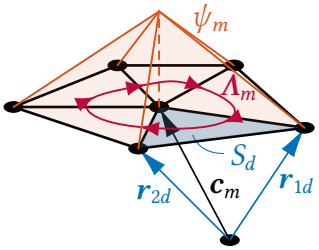

Fig. 4.3: Representation of a loop formed by D_m RWG functions around the center node $\boldsymbol{c}_m$ by the scalar function ψ_m. © 2023 IEEE

That this expression is equivalent to (4.11) can be verified by inserting

$$\boldsymbol{r}(u,v) = \boldsymbol{c}_m + u(\boldsymbol{r}_{2d} - \boldsymbol{c}_m) + v(\boldsymbol{r}_{1d} - \boldsymbol{c}_m) \tag{4.13}$$

and leveraging $\boldsymbol{a}\cdot(\boldsymbol{b}\times\boldsymbol{c}) = -\boldsymbol{b}\cdot(\boldsymbol{a}\times\boldsymbol{c})$. The vectors $\boldsymbol{r}_{1d}$ and $\boldsymbol{r}_{2d}$ are defined per triangle with area S_d. Inserting (4.11) or (4.12) into (4.10), the products $\boldsymbol{\Lambda}^{\mathrm{T}}\boldsymbol{e}^{\mathrm{ex}}$ can be evaluated as

$$\left[\boldsymbol{\Lambda}^{\mathrm{T}}\boldsymbol{e}^{\mathrm{ex}}\right]_m = \mathrm{j}k \sum_{d=1}^{D_m} \iint_{\Gamma} \psi_{md}\boldsymbol{n}_{md}\cdot\boldsymbol{h}^{\mathrm{ex}}\,\mathrm{d}\boldsymbol{r} \tag{4.14}$$

(since $\bar{S}_m$ vanishes) and in the parametric domain as

$$\left[\boldsymbol{\Lambda}^{\mathrm{T}}\boldsymbol{e}^{\mathrm{ex}}\right]_m = \mathrm{j}k \sum_{d=1}^{D_m} \iint_{\hat{\Gamma}} \psi_{md}(u,v)\left[(\boldsymbol{r}_{2d} - \boldsymbol{c}_m)\times(\boldsymbol{r}_{1d} - \boldsymbol{c}_m)\right]\cdot\boldsymbol{h}^{\mathrm{ex}}(\boldsymbol{r}(u,v))\,\mathrm{d}u\mathrm{d}v \tag{4.15}$$

with $D_m = \left\|[\boldsymbol{\Lambda}^{\mathrm{T}}]_m\right\|_1$ the number of RWGs spanning $\boldsymbol{\Lambda}_m$ and the normal vectors $\boldsymbol{n}_{md} = (\boldsymbol{r}_{2d} - \boldsymbol{c}_m)\times(\boldsymbol{r}_{1d} - \boldsymbol{c}_m)/(2S_d)$.

To derive ψ_m for a global RWG loop $\boldsymbol{H}_m$, we exemplify the discussion by considering the $\boldsymbol{H}_m$ with support $\mathcal{S}_m$ around the hole shown in Fig. 4.4 (a). First, we introduce a vertex at an arbitrary point (e.g., in the center of the hole) such that a triangulated cap surface is introduced (see Fig. 4.4 (b)) corresponding to $\bar{S}_m$ in Section 4.1.1.[3] The global loop can then be expressed by introducing local loops of equal strength around each vertex inside the global loop. Figure 4.4 (b) shows that the overall current density of the global loop is left unaltered, since all other contributions cancel each other. In consequence, ψ_m is the superposition of the scalar functions of the local loops such that ψ_m is constant on the parts of Γ lying inside $\mathcal{C}_{m,1}$ (the inner part of $\partial\mathcal{S}_m$) and on the cap surface, which is illustrated in Fig. 4.4 (c). Hence, the support of ψ_m partially lies outside of Γ. This corresponds well with the expression derived in (4.7), where by applying Stokes' theorem a cap surface was introduced.

Expressing ψ_m through (4.11), using $\psi_{md} = 1$ on the cap surface elements $\bar{S}_{md}$, the stable

[3] Alternatively, several vertices can be introduced or one of the vertices on one of the boundary curves can be selected and connected to all other vertices of the same boundary curve.

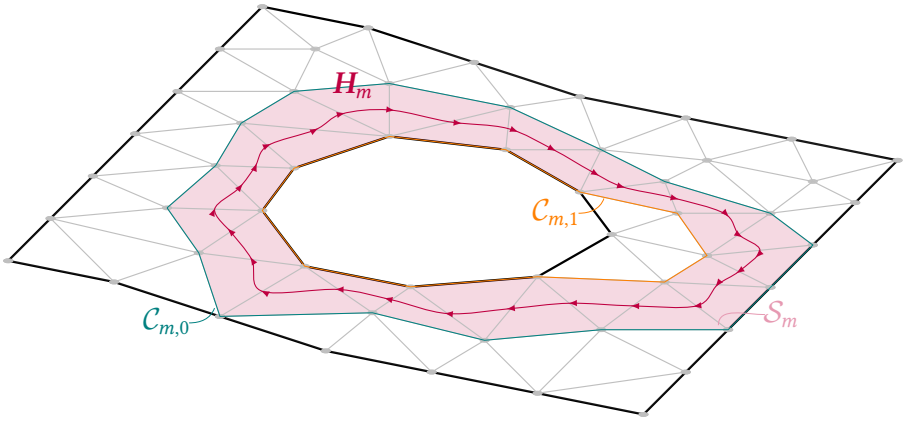

(a) A global RWG loop.

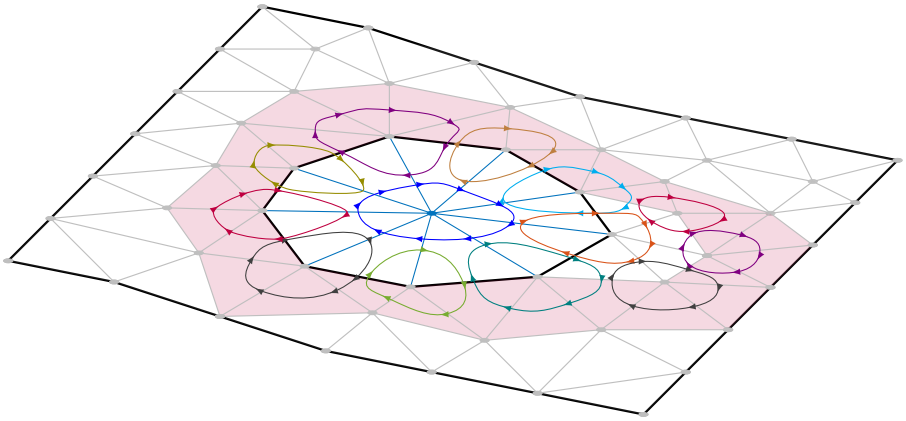

(b) Expressing the global loop by local loops.

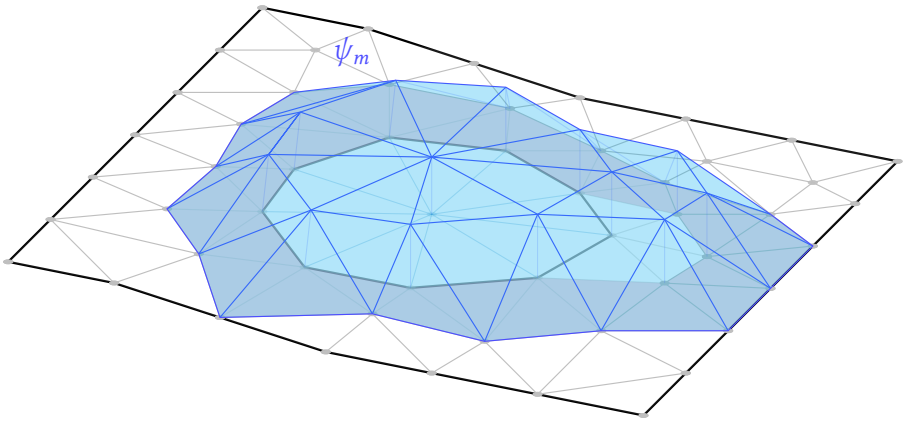

(c) Resulting scalar function.

Fig. 4.4: Construction of the the scalar function ψ_m by representing a global loop $\boldsymbol{H}_m$ as the superposition of local loops. © 2023 IEEE

evaluation scheme

$$\left[\boldsymbol{H}^{\mathrm{T}}\boldsymbol{e}^{\mathrm{ex}}\right]_m = \mathrm{j}k \sum_{d=1}^{D_m} \iint_{\mathcal{S}_{md}} \psi_{md}\, \boldsymbol{n}_{md} \cdot \boldsymbol{h}^{\mathrm{ex}}\, \mathrm{d}\boldsymbol{r} - \mathrm{j}k \sum_{d=1}^{D_m} \iint_{\bar{\mathcal{S}}_{md}} \boldsymbol{n}_{md} \cdot \boldsymbol{h}^{\mathrm{ex}}\, \mathrm{d}\boldsymbol{r} \tag{4.16}$$

for global loops is obtained with $D_m = \left\|[\boldsymbol{H}^{\mathrm{T}}]_m\right\|_1$ (the integrals in the parametric domain can be expressed analogously to (4.15)). As a consequence, the numerically stable testing requires the evaluation of the incident fields across the holes and handles of a multiply-connected surface Γ.

It should be stressed that the support of $\boldsymbol{H}_m$ does not necessarily have to touch $\partial\Gamma$, that is, it is not required to find the shortest global loop. Also, the cap surface does not necessarily have to be introduced over the inner boundary (in the example $\mathcal{C}_{m,1}$), but also the outer boundary ($\mathcal{C}_{m,0}$) can be chosen. As noted before, this approach can also be applied to multiply-connected surfaces which are closed, such as a torus, where both toroidal and poloidal loops can be treated in the same manner.

It is also interesting to note that the introduction of cap surfaces strikes some resemblance to the introduction of so-called cutting surfaces in the context of Eddy current problems using a magneto-quasistatic approximation (see, e.g., [Brown 1984; Ren 2002]). In the latter case, the cutting surfaces are needed to render the involved potentials single-valued as a fundamental requirement to obtain correct solutions [Brown 1984; Ren 2002; Kotiuga 1987; Kotiuga 1988; Kotiuga 1989; Hiptmair et al. 2005]. In contrast to the cap surfaces employed in this work, however, the introduced surfaces can have a finite thickness, they cut the domain instead of closing handles and holes, the potential itself is part of the unknowns, and the setting is commonly based on a tetrahedral discretization of the volume [Dlotko et al. 2013; Dlotko et al. 2014].

4.2 Stable Right-Hand Side Evaluation for Quasi-Helmholtz Projectors

As discussed in Section 3.2, instead of directly using decomposition (3.26), it is advantageous to utilize the quasi-Helmholtz projectors introduced in [Andriulli et al. 2013], in particular, when combined with the (refinement-free) Calderón multiplicative preconditioner [Adrian et al. 2019], even though the required search for global loops in our scheme loses one of the advantages of quasi-Helmholtz projectors, which do not require this search. One could think of avoiding the construction of global loops; however, introducing a cap surface that closes the handles and holes requires a cut in the surface. Finding such a cut corresponds to finding a global loop. Analogous issues for the stable evaluation of the RHS arise and we need to establish how (4.14) and (4.16) can be used in this context.

4.2.1 Stable Evaluation of the Right-Hand Side

A direct evaluation of the RHS $\boldsymbol{P}_1\boldsymbol{e}^{\mathrm{ex}}$ in (3.34) as

$$\boldsymbol{P}_1\boldsymbol{e}^{\mathrm{ex}} = \alpha_1(\mathbf{I} - \boldsymbol{P}_{\boldsymbol{\Sigma}})\boldsymbol{e}^{\mathrm{ex}} + \beta_1\boldsymbol{P}_{\boldsymbol{\Sigma}}\boldsymbol{e}^{\mathrm{ex}} \tag{4.17}$$

results in similar round-off errors as for the loop-star decomposition. To see why, we construct $\boldsymbol{P}_{\Lambda H}$ explicitly. This can be done by applying $[\boldsymbol{\Lambda}\ \boldsymbol{H}]^{\mathrm{T}}$ to (3.28) yielding

$$\begin{bmatrix}\boldsymbol{\Lambda}^{\mathrm{T}}\\ \boldsymbol{H}^{\mathrm{T}}\end{bmatrix}\boldsymbol{j} = \begin{bmatrix}\boldsymbol{\Lambda}^{\mathrm{T}}\boldsymbol{\Lambda} & \boldsymbol{\Lambda}^{\mathrm{T}}\boldsymbol{H}\\ \boldsymbol{H}^{\mathrm{T}}\boldsymbol{\Lambda} & \boldsymbol{H}^{\mathrm{T}}\boldsymbol{H}\end{bmatrix}\begin{bmatrix}\boldsymbol{j}_{\Lambda}\\ \boldsymbol{j}_{H}\end{bmatrix}, \tag{4.18}$$

where the orthogonality relations $\boldsymbol{\Lambda}^{\mathrm{T}}\boldsymbol{\Sigma} = \mathbf{0}$ and $\boldsymbol{H}^{\mathrm{T}}\boldsymbol{\Sigma} = \mathbf{0}$ were used. After solving for $\boldsymbol{j}_{\Lambda}$ and $\boldsymbol{j}_{H}$ and mapping back to $\boldsymbol{\Lambda}\boldsymbol{j}_{\Lambda}$ and $\boldsymbol{H}\boldsymbol{j}_{H}$, the projector

$$\boldsymbol{P}_{\Lambda H} = \begin{bmatrix}\boldsymbol{\Lambda} & \boldsymbol{H}\end{bmatrix}\begin{bmatrix}\boldsymbol{\Lambda}^{\mathrm{T}}\boldsymbol{\Lambda} & \boldsymbol{\Lambda}^{\mathrm{T}}\boldsymbol{H}\\ \boldsymbol{H}^{\mathrm{T}}\boldsymbol{\Lambda} & \boldsymbol{H}^{\mathrm{T}}\boldsymbol{H}\end{bmatrix}^{+}\begin{bmatrix}\boldsymbol{\Lambda}^{\mathrm{T}}\\ \boldsymbol{H}^{\mathrm{T}}\end{bmatrix} \tag{4.19}$$

is obtained. In consequence, evaluating $\boldsymbol{P}_{\Lambda H}\boldsymbol{e}^{\mathrm{ex}}$ involves the products $\boldsymbol{\Lambda}^{\mathrm{T}}\boldsymbol{e}^{\mathrm{ex}}$ and $\boldsymbol{H}^{\mathrm{T}}\boldsymbol{e}^{\mathrm{ex}}$ exhibiting the round-off errors discussed in the previous Section 4.1. At the same time, using (4.19) instead of $\boldsymbol{P}_{\Lambda H} = \mathbf{I} - \boldsymbol{P}_{\boldsymbol{\Sigma}}$ for the RHS product allows to employ the stable evaluation schemes given in (4.14) and (4.16) for the quasi-Helmholtz projectors rendering the product $\boldsymbol{P}_{\Lambda H}\boldsymbol{e}^{\mathrm{ex}}$ numerically stable.

However, evaluating the pseudoinverse in (4.19) involves matrices $\boldsymbol{\Lambda}^{\mathrm{T}}\boldsymbol{\Lambda}$ which exhibit a condition number which grows with the average edge length h of the triangulation as $1/h^2$ [Andriulli 2012]. Hence, an efficient inversion strategy is required.

4.2.2 Efficient Evaluation of the Projected RHS

As $\boldsymbol{\Lambda}^{\mathrm{T}}\boldsymbol{\Lambda}$ is a graph Laplacian, it can be inverted with a constant number of iterations independent of h by employing an AMG preconditioner [Livne et al. 2012; Andriulli 2012]. In order to maintain this property for (4.19), we propose to employ the Schur complement (see, e.g., [Boyd 2004, p. 650]). More precisely,

$$\boldsymbol{P}_{\Lambda H}\boldsymbol{e}^{\mathrm{ex}} = \begin{bmatrix}\boldsymbol{\Lambda} & \boldsymbol{H}\end{bmatrix}\begin{bmatrix}\boldsymbol{y}_{\Lambda}\\ \boldsymbol{y}_{H}\end{bmatrix} \tag{4.20}$$

is evaluated, where $\boldsymbol{y}_{\Lambda}$ and $\boldsymbol{y}_{H}$ are the solutions to

$$\begin{bmatrix}\boldsymbol{\Lambda}^{\mathrm{T}}\boldsymbol{e}_{\mathrm{ex}}\\ \boldsymbol{H}^{\mathrm{T}}\boldsymbol{e}_{\mathrm{ex}}\end{bmatrix} = \begin{bmatrix}\boldsymbol{\Lambda}^{\mathrm{T}}\boldsymbol{\Lambda} & \boldsymbol{\Lambda}^{\mathrm{T}}\boldsymbol{H}\\ \boldsymbol{H}^{\mathrm{T}}\boldsymbol{\Lambda} & \boldsymbol{H}^{\mathrm{T}}\boldsymbol{H}\end{bmatrix}\begin{bmatrix}\boldsymbol{y}_{\Lambda}\\ \boldsymbol{y}_{H}\end{bmatrix}. \tag{4.21}$$

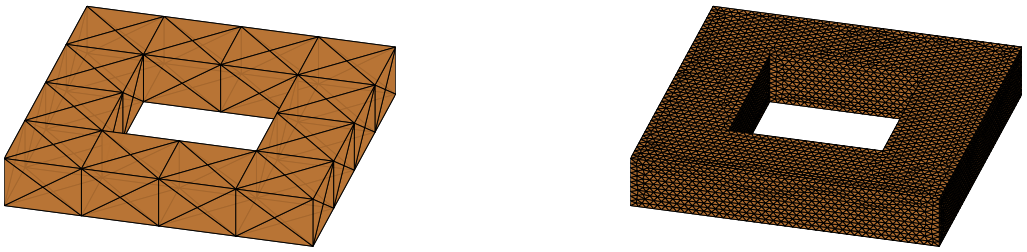

(a) (b)

Fig. 4.5: Rectangular torus of size 1 m × 1 m × 0.4 m and inner radius of 0.3 m with a $1/h = 5\,\mathrm{m}^{-1}$ and b $1/h = 40\,\mathrm{m}^{-1}$. © 2023 IEEE

These solutions are obtained by first solving the LSE

$$\boldsymbol{S}\,\boldsymbol{y}_H = \boldsymbol{H}^{\mathrm{T}}(\mathbf{I} - \boldsymbol{P}_\Lambda)\boldsymbol{e}^{\mathrm{ex}} \tag{4.22}$$

containing the Schur complement

$$\boldsymbol{S} = \boldsymbol{H}^{\mathrm{T}}\boldsymbol{H} - \boldsymbol{H}^{\mathrm{T}}\boldsymbol{\Lambda}(\boldsymbol{\Lambda}^{\mathrm{T}}\boldsymbol{\Lambda})^{+}\boldsymbol{\Lambda}^{\mathrm{T}}\boldsymbol{H} = \boldsymbol{H}^{\mathrm{T}}(\mathbf{I} - \boldsymbol{P}_\Lambda)\boldsymbol{H} \tag{4.23}$$

with $\boldsymbol{P}_\Lambda = \boldsymbol{\Lambda}(\boldsymbol{\Lambda}^{\mathrm{T}}\boldsymbol{\Lambda})^{+}\boldsymbol{\Lambda}^{\mathrm{T}}$ and subsequently solving

$$\boldsymbol{\Lambda}^{\mathrm{T}}\boldsymbol{\Lambda}\,\boldsymbol{y}_\Lambda = \boldsymbol{\Lambda}^{\mathrm{T}}(\boldsymbol{e}^{\mathrm{ex}} - \boldsymbol{H}\boldsymbol{y}_H)\,. \tag{4.24}$$

This allows to use an AMG preconditioner each time an inverse of $\boldsymbol{\Lambda}^{\mathrm{T}}\boldsymbol{\Lambda}$ is formed, and thus, fully removes the ill-conditioning with respect to h in (4.24). We do not expect an h-ill-conditioning of $\boldsymbol{S}$ in (4.22) due to the global nature of the $\boldsymbol{H}_m$.

As an example consider the rectangular torus shown in Fig. 4.5 for which $1/h$ is varied between 2 and 100. The corresponding number of iterations for conjugate gradient (CG) to compute the pseudoinverse when evaluating $\boldsymbol{P}_{\Lambda H}\boldsymbol{e}^{\mathrm{ex}}$ is depicted at the top of Fig. 4.6. Clearly, if no preconditioner is employed, the iteration count increases with $1/h$. This is improved by applying an AMG preconditioner directly to the whole matrix in (4.21). However, a detrimental dependency on h remains. Only when computing the pseudoinverse via the Schur complement, the number of iterations (summed up for both LSEs to be solved) is constant and overall the smallest for all considered cases.

As the pseudoinverse depends also on $\boldsymbol{H}$, it is of interest to investigate the influence of the number of global loops N_H. To this end, we vary the number of handles of the plate with finite thickness depicted in Fig. 4.7, where there are two global loops per handle. The corresponding number of iterations is shown at the bottom of Fig. 4.6. Again, the overall fewest iterations are required when the proposed Schur complement scheme is used. The remaining dependency on N_H for the LSE in (4.22) is acceptable in most realistic cases, since the involved matrix is only of size $N_H \times N_H$ and the LSE has to be solved only once in the overall solution process.

In addition, it should be noted that the proposed approach is fully compatible with a Calderón

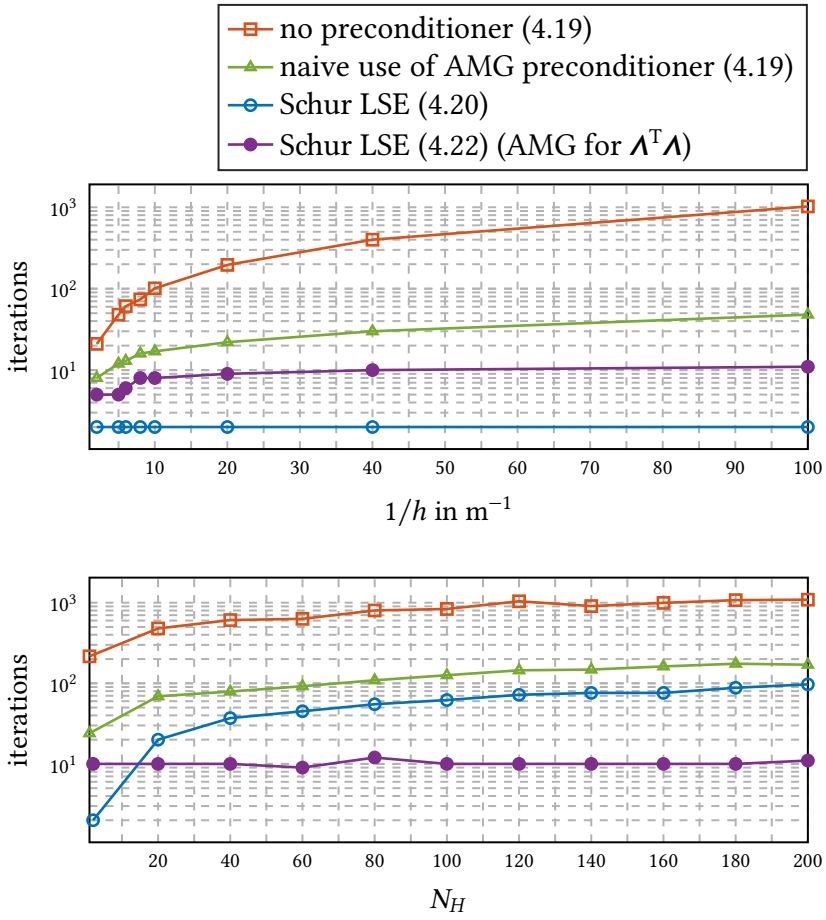

Fig. 4.6: Number of iterations for the iterative computation of the pseudoinverse in the projector $\boldsymbol{P}_{\Lambda H}$ via CG. © 2023 IEEE

preconditioner. The latter is commonly combined with the stabilized system (3.34) to prevent a dense-discretization breakdown, that is, an ill-conditioning of the system matrix with respect to h [Andriulli et al. 2013; Andriulli et al. 2008a]. As this does neither affect the problems with the RHS (the same kind of RHS stabilization is needed) nor the proposed solution strategy all benefits of the Calderón preconditioning are maintained.

4.3 Numerical Results

In order to show the impact of the stabilized RHS evaluation on the accuracy of the computed scattered and radiated fields, several scenarios are investigated. For all of them, a GMRES solver is employed without restarts and a relative residual of $\epsilon_{\text{res}} = 1 \times 10^{-6}$ as stopping criterion. Furthermore, the quasi-Helmholtz projectors $\boldsymbol{P}_i = \alpha_i \boldsymbol{P}_{\Lambda H} + \beta_i \boldsymbol{P}_{\Sigma}$ are employed as done in (3.34) in all scenarios. For the normalization coefficients α_i and β_i we employ the approach derived in the next Chapter 5, where also details are provided why specifically this choice of coefficients is crucial. The implementation of (3.2) is based on [Cools 2021].

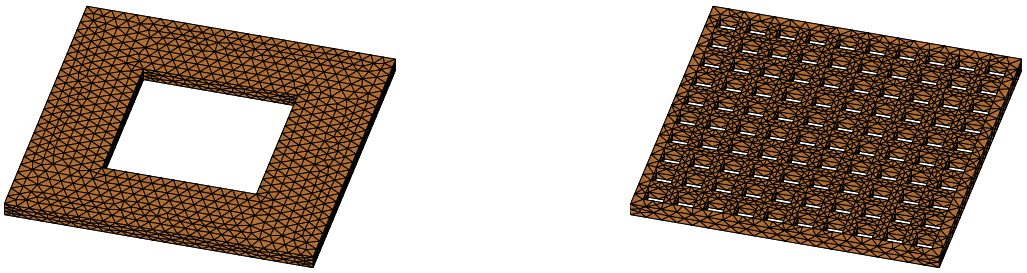

(a) (b)

Fig. 4.7: Finite-height plate of size 1 m × 1 m × 0.2 m with varying number of global loops N_H and a constant average edge length with $1/h = 25\,\mathrm{m}^{-1}$: from a $N_H = 2$ to b $N_H = 200$. © 2023 IEEE

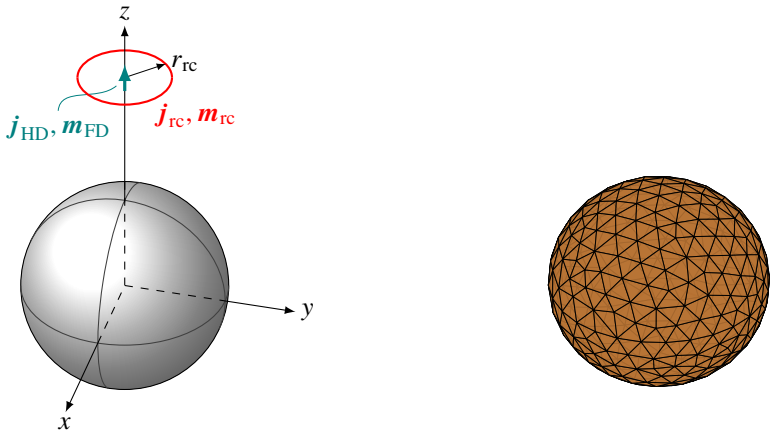

(a) (b)

Fig. 4.8: Scattering from a sphere of radius $r_s = 1$ m (a) excited by dipoles and ring currents at position $z = 2$ m and radius $r_{rc} = 0.5$ m; (b) discretized with 624 triangles and 936 RWGs. © 2023 IEEE

4.3.1 Scattering from a Sphere

We begin with a study of the scattering from a sphere since a semi-analytic reference is available. The sphere has radius $r_s = 1$ m and is excited by a plane wave, a Hertzian dipole $\boldsymbol{j}_{HD}$ [Jin 2015, pp. 69 f.], a magnetic dipole $\boldsymbol{m}_{FD}$ [Jin 2015, pp. 76 ff.], an electric ring current $\boldsymbol{j}_{rc}$ [Jin 2015, pp. 362 ff.], and a magnetic ring current $\boldsymbol{m}_{rc}$ (employing duality) as depicted in Fig. 4.8. For all of these excitations, the scattered fields can be determined semi-analytically in form of a series expansion (see [Jin 2015, pp. 368 ff.] and [Hofmann et al. 2023e; Hofmann 2022f] for implementation details), which serves as reference solution. The error with respect to this solution is determined for the FF, the electric, and the magnetic NF at a distance of $r = 5$ m. To this end, the fields are computed on a spherical 5° grid and the relative loga-

Table 4.1: Scaling of the RHS components for $k \to 0$. © 2023 IEEE

	plane wave	Hertzian dipole	el. ring current	mag. dipole	mag. ring current	TE_{mn}	TM_{mn}
$\|\boldsymbol{e}_{\mathrm{sol}}\|$	$\mathcal{O}(k)$	$\mathcal{O}(k)$	$\mathcal{O}(k)$	$\mathcal{O}(1)$	$\mathcal{O}(k^2)$	$\mathcal{O}(k^{-n})$	$\mathcal{O}(k^{-(n-1)})$
$\|\boldsymbol{e}_{\mathrm{hsol}}\|$	$\mathcal{O}(k)$	$\mathcal{O}(k)$	$\mathcal{O}(k)$	$\mathcal{O}(1)$	$\mathcal{O}(k^2)$	$\mathcal{O}(k^{-n})$	$\mathcal{O}(k^{-(n-1)})$
$\|\boldsymbol{e}_{\mathrm{nsol}}\|$	$\mathcal{O}(1)$	$\mathcal{O}(1/k)$	$\mathcal{O}(k)$	$\mathcal{O}(1)$	$\mathcal{O}(1)$	$\mathcal{O}(k^{-n})$	$\mathcal{O}(k^{-(n+1)})$

rithmic worst case error

$$\aleph = \max_{\vartheta,\varphi}\left\{20\log\frac{|a(\vartheta,\varphi)-\hat{a}(\vartheta,\varphi)|}{\max\limits_{\vartheta,\varphi}|a(\vartheta,\varphi)|}\right\} \tag{4.25}$$

with $a \in \{e, h, e^{\mathrm{FF}}\}$ is determined.

For the plane-wave excitation, the results over frequency are shown at the top of Fig. 4.10 (a) for the cases where $\boldsymbol{P}_{\Lambda}\boldsymbol{e}^{\mathrm{ex}}$ is evaluated in a naïve manner and where $\boldsymbol{P}_{\Lambda}\boldsymbol{e}^{\mathrm{ex}}$ is evaluated via the scalar functions ψ. Clearly, for the naïve RHS evaluation, all fields are erroneous when going below 1×10^{-4} Hz. Using the RHS evaluation via ψ solves this for all fields. The second plot of Fig. 4.10 (a) shows the norms of the solenoidal components of the RHS $\boldsymbol{e}_{\mathrm{sol,hsol}} = \boldsymbol{P}_{\Lambda H}\boldsymbol{e}^{\mathrm{ex}}$ and the non-solenoidal components of the RHS $\boldsymbol{e}_{\mathrm{nsol}} = \boldsymbol{P}_{\Sigma}\boldsymbol{e}^{\mathrm{ex}}$. From these it can be seen that the physically correct scalings (see Table 4.1 which generalizes the findings of [Bogaert et al. 2014]) are only obtained for the evaluation via ψ. Otherwise, a deviation is observed below 1×10^{-8} Hz, showing that the scalings reflect the breakdown in accuracy. The same is true for the norms of the solenoidal and non-solenoidal components of the solution current $\boldsymbol{j}$ as shown in the third plot of Fig. 4.10 (a).

For the Hertzian dipole, it can be seen from Fig. 4.10 (b) that the breakdown in accuracy occurs already in the kHz region. This can be explained by the fact that the solenoidal and the non-solenoidal component of the RHS differ in their scaling by k^2 (see Table 4.1), which is in contrast to the plane wave, where the difference is only k. Consequently, the naïve RHS evaluation breaks down earlier. Evaluating the RHS via ψ leads to correct FFs and NFs over the whole frequency range. Notably, other than the FF and the magnetic NF, the electric NF is determined correctly also with the naïve RHS evaluation. The reason is that the non-solenoidal current component, which represents the charge and thus determines the electric NF, dominates asymptotically and is thus recovered sufficiently accurately (see third plot of Fig. 4.10 (b)). At the same time, for this specific excitation the electric NF is dominated by the non-solenoidal current in the low-frequency regime as can be shown by an asymptotic analysis [Hofmann et al. 2023b, Table II]. One should not jump, however, to the conclusion that the electric NF is always recovered accurately. In fact, for the plane-wave excitation both current components are recovered erroneous below 1×10^{-8} Hz leading to all fields being erroneous as well.

A similar behavior is observed for the magnetic ring current as depicted in Fig. 4.11 (a). As it

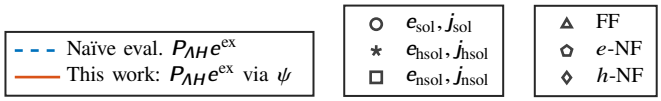

Fig. 4.9: Legend for the numerical results in this chapter including Fig. 4.10, Fig. 4.11, Fig. 4.13, Fig. 4.15, Fig. 4.17, and Fig. 4.18.

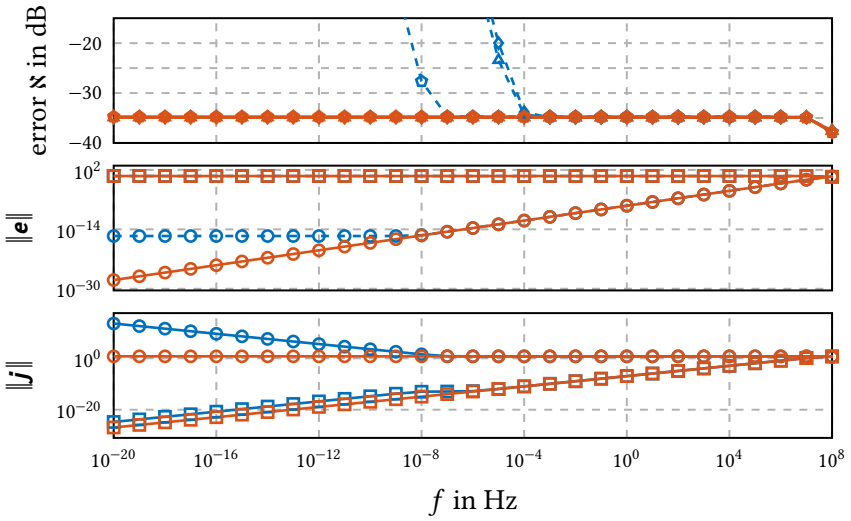

(a) plane wave

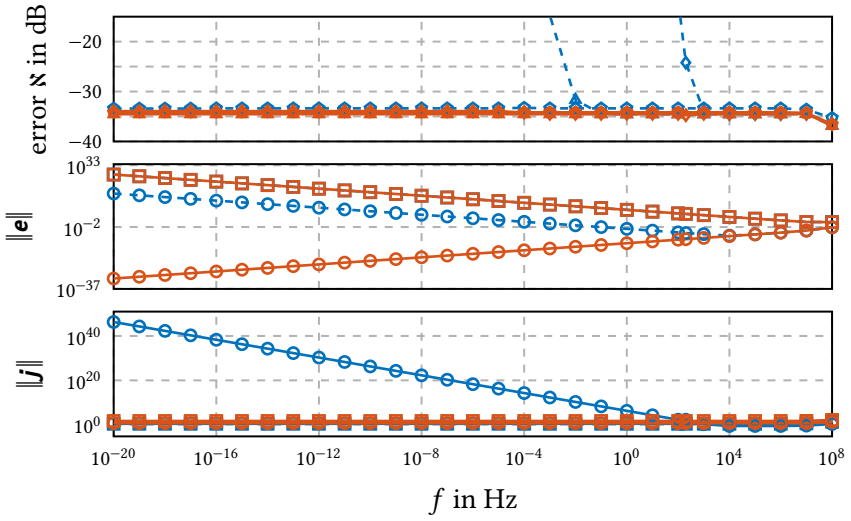

(b) Hertzian dipole

Fig. 4.10: Scattering from a sphere: worst case errors of the FF, the electric, and the magnetic NF, as well as the scaling of the RHS components for different excitations with and without stabilized RHS. © 2023 IEEE

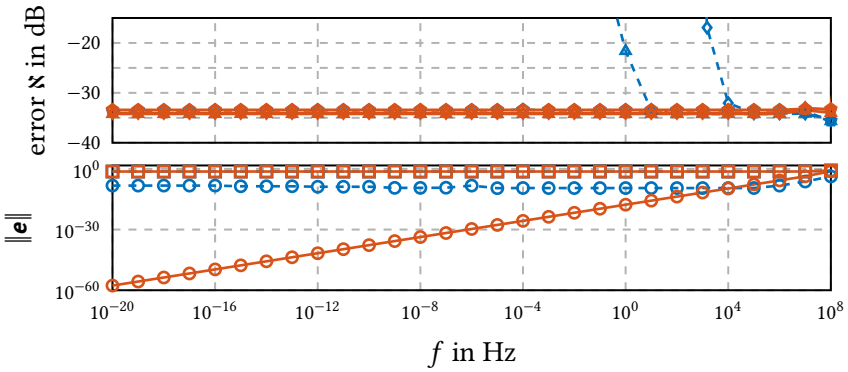

(a) magnetic ring current

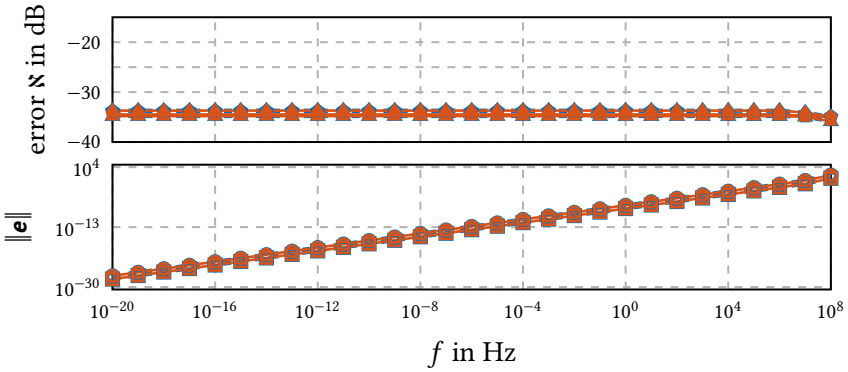

(b) electric ring current

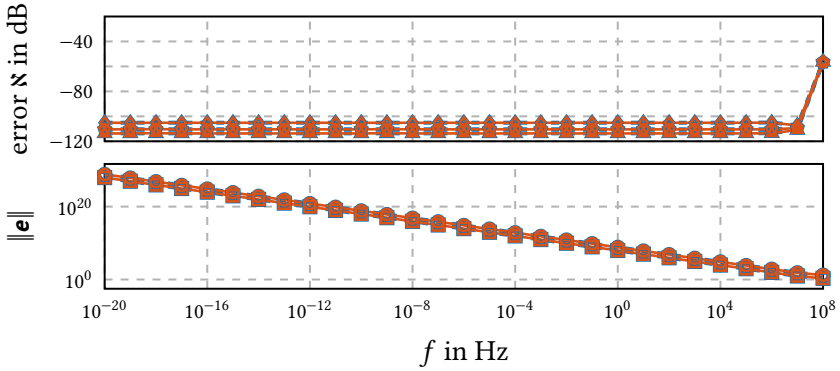

(c) spherical mode TE_{11}

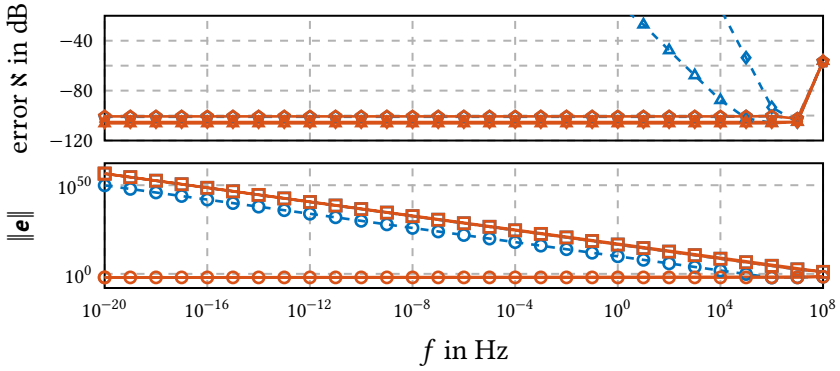

(d) spherical mode TM_{11}

Fig. 4.11: Scattering from a sphere: worst case errors of the FF, the electric, and the magnetic NF, as well as the scaling of the RHS components for different excitations with and without stabilized RHS. © 2023 IEEE

behaves like a Hertzian dipole in the low-frequency regime, it shows the same breakdown frequencies. Only the scalings of the RHS components are different, however, the ratio between solenoidal and non-solenoidal components stays the same.

The results for the electric ring current shown in Fig. 4.11 (b) are particularly insightful. In Section 4.1.1, we predicted that if $\mathcal{O}(|\boldsymbol{e}|) = \mathcal{O}(|\boldsymbol{n}_m \cdot \boldsymbol{h}|k)$, then the ψ-based evaluation of the RHS is unnecessary. We observe that, indeed, there is no further improvement in the error and the physically correct scalings for the RHS are recovered in both approaches. As an interesting observation, we note that this is directly reflected by the scalings of the RHS components: Considering (4.7) together with Faraday's law and using $\boldsymbol{e}_{\mathrm{sol,hsol}} = \boldsymbol{P}_{\Lambda H}\boldsymbol{e}^{\mathrm{ex}}$, we find $\mathcal{O}(|\boldsymbol{n}_m \cdot \boldsymbol{h}^{\mathrm{ex}}|k) = \mathcal{O}(\|\boldsymbol{e}_{\mathrm{sol,hsol}}\|)$. Analogously, with $\boldsymbol{e}_{\mathrm{nsol}} = \boldsymbol{P}_{\Sigma}\boldsymbol{e}^{\mathrm{ex}}$, we get $\mathcal{O}(|\boldsymbol{e}^{\mathrm{ex}}|) = \mathcal{O}(\|\boldsymbol{e}_{\mathrm{nsol}}\|)$. Hence, condition (4.9) can be expressed equivalently as

$$\mathcal{O}(\|\boldsymbol{e}_{\mathrm{nsol}}\|) = \mathcal{O}(\|\boldsymbol{e}_{\mathrm{sol,hsol}}\|)\,, \tag{4.26}$$

showing that no numerical round-off errors occur if the non-solenoidal component scales as the solenoidal components of the RHS. As the asymptotic behavior of the magnetic dipole differs from the electric ring current only by a constant factor, we omit it here.

As another class of excitations, we consider the spherical vector waves $\boldsymbol{q}^{(3)}_{1mn}$ in (2.23) referred to as TE_{mn} and $\boldsymbol{q}^{(3)}_{2mn}$ in (2.24) referred to as TM_{mn}, both traveling towards the origin. Again the scattered fields can be determined analytically by enforcing the boundary conditions providing a reference solution (see also [Hofmann et al. 2023e]). From the asymptotic behavior of the involved spherical Hankel functions as $k \to 0$ and leveraging that $\mathcal{O}(\|\boldsymbol{e}_{\mathrm{TE/TM,sol,hsol}}\|) = \mathcal{O}(|k\,\boldsymbol{h}_{\mathrm{TE/TM}}|)$, it can be concluded that the TE modes exhibit a scaling of

$$\|\boldsymbol{e}_{\mathrm{TE,nsol}}\| = \mathcal{O}(k^{-n}) \tag{4.27}$$

and

$$\|\boldsymbol{e}_{\mathrm{TE,sol,hsol}}\| = \mathcal{O}(k^{-n}) \tag{4.28}$$

such that no problems with the RHS are expected as proven by the results in Fig. 4.11 (c). However, the TM modes scale as

$$\|\boldsymbol{e}_{\mathrm{TM,nsol}}\| = \mathcal{O}(k^{-(n+1)}) \tag{4.29}$$

and

$$\|\boldsymbol{e}_{\mathrm{TM,sol,hsol}}\| = \mathcal{O}(k^{-(n-1)}) \tag{4.30}$$

as long as the scatterer is not a sphere placed in the origin. In the latter case, we have $\boldsymbol{e}_{\mathrm{TM,sol,hsol}} = \boldsymbol{0}$ as the surface curl of the TM modes vanishes on the surface of a sphere [Hsiao et al. 1997]. The results for a TM_{11} excitation in Fig. 4.11 (d) show that without the stabilization scheme the error level increases already below a frequency of 10 MHz. Notably, despite $\boldsymbol{e}_{\mathrm{TM,sol,hsol}}$ not fully vanishing with the stabilized RHS, it is kept small enough such that the fields are computed correctly. This property is maintained if $\boldsymbol{q}^{(1)}_{2mn}$ waves (with spherical Bessel instead of Hankel function in the radial dependency) are used as TM ex-

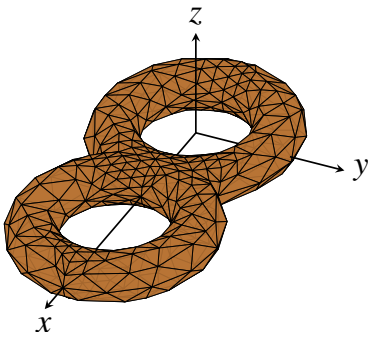

Fig. 4.12: Double torus with $N_H = 4$ global loops discretized by 848 triangles and 1272 RWGs. © 2023 IEEE

citation modes. The increase of the error at $f = 1 \times 10^8$ Hz, on the other hand, stems from the (geometrical) approximation error. Increasing the number of triangles from 624 to only 1526 restores an error level of about −80 dB.

4.3.2 Scattering from Multiply-Connected Geometries

As a first example of a multiply-connected geometry, we consider the double torus depicted in Fig. 4.12. The results for a plane-wave excitation are shown in Fig. 4.13 (a). The reference solution is determined by stabilizing the RHS with a Taylor series expansion following [Adrian et al. 2021]. The comparison with the stabilization via scalar functions ψ_m shows good agreement over the whole frequency range, clearly demonstrating the correctness of the proposed scalar function formulation for multiply-connected geometries. The same applies for a Hertzian dipole excitation as depicted in Fig. 4.13 (b). For the latter, the error is determined in form of a manufactured solution [Roache 2001; Steinberg et al. 1985]: The dipole is placed inside the scatterer, and we leverage that the total field $\boldsymbol{e}^{\mathrm{sc}} + \boldsymbol{e}^{\mathrm{ex}} = \mathbf{0}$ outside the scatterer. The latter condition is then checked on the spherical 5° grid. Note, that this is not the same approach as in [Freno et al. 2021], where the current density itself is compared to a manufactured solution. The obtained error ℵ shows that the stabilization of the RHS via scalar functions yields accurate solutions. The strong relevance of the stabilized RHS evaluation in this case can be explained by the close proximity of the excitation to the scatterer.

As a more challenging scatterer, the geometric model of a (PEC) Fokker Dr.I shown in Fig. 4.14 with $N_H = 390$ global loops excited by a Hertzian dipole is considered. In order to accelerate the computation, an ACA algorithm is used [Zhao et al. 2005a; Bebendorf 2008] with compression rate 1×10^{-4}. The error of the solution is determined in the same manner as for the double torus. The results in Fig. 4.15 prove again the necessity of the proposed scheme.

To demonstrate that also topologically challenging geometries can be successfully handled by the proposed approach, the trefoil knot depicted in Fig. 4.16 (a) is excited by a Hertzian dipole. The hole of the toroidal loop is closed by introducing a point in the center of the

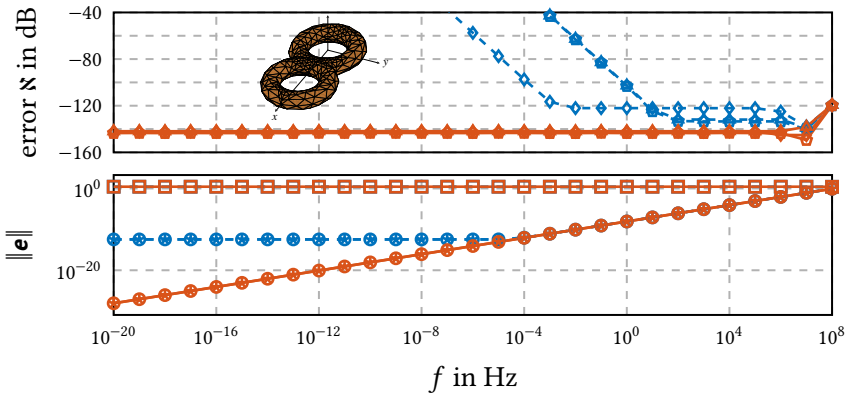

(a) plane wave

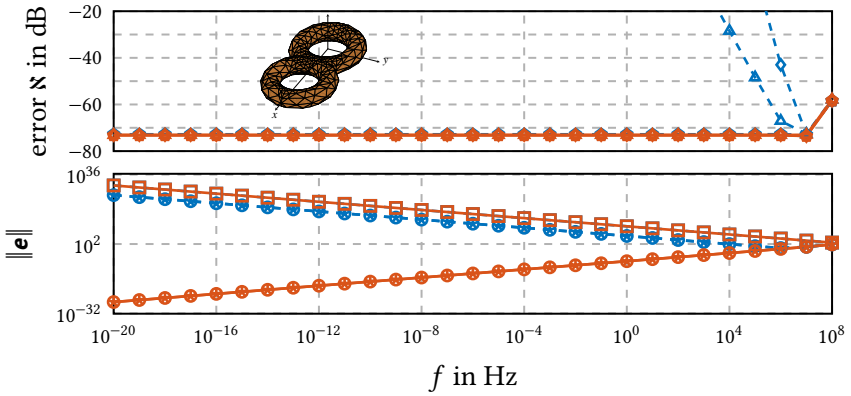

(b) Hertzian dipole

Fig. 4.13: Scattering from a double torus: worst case errors and scaling of the RHS components for different excitations with and without stabilized RHS. © 2023 IEEE

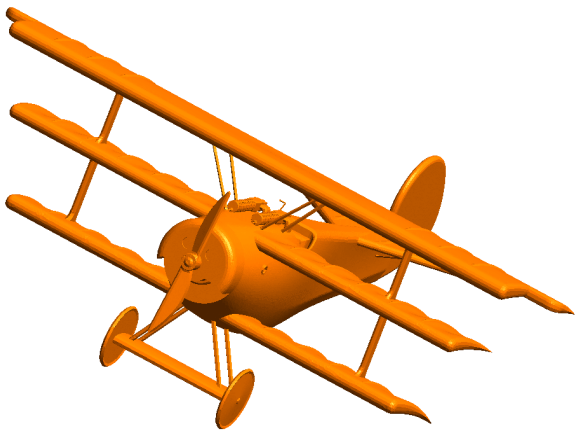

Fig. 4.14: Model of a Fokker Dr.I with an approximate wingspan of 7 m containing $N_H = 390$ global loops. The model is discretized with 196 280 triangles and 294 420 RWGs. © 2023 IEEE

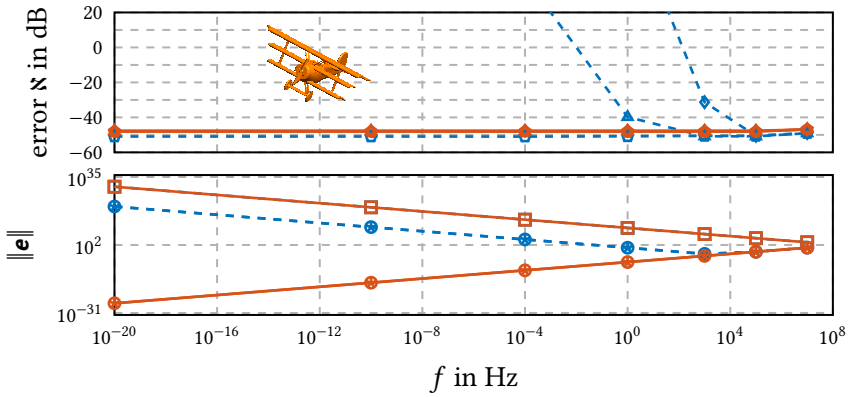

Fig. 4.15: Scattering from the Fokker Dr.I model excited by a Hertzian dipole: worst case errors and scaling of the RHS components. © 2023 IEEE

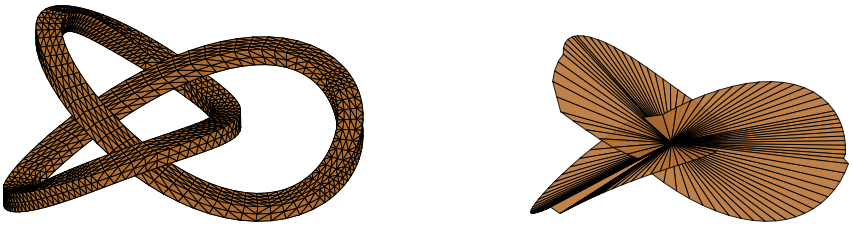

(a) (b)

Fig. 4.16: Scattering from a trefoil knot: (a) rectangular profile swept along $x(t) = \sin(t) + 2\sin(2t)$, $y(t) = \cos(t) - 2\cos(2t)$, $z(t) = -\sin(3t)$ with $t \in [0, 2\pi]$; discretized with 3580 triangles and 5370 RWGs. (b) Mesh to close the toroidal global loop of the trefoil knot. © 2023 IEEE

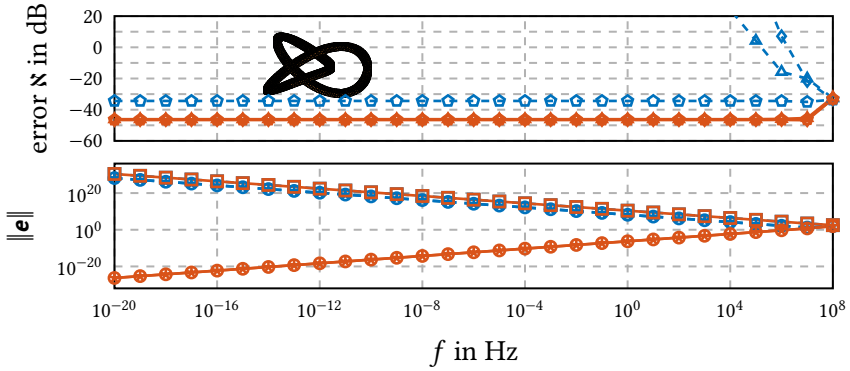

Fig. 4.17: Scattering from the trefoil knot excited by a Hertzian dipole which is placed inside the knot: worst case errors and scaling of the RHS components. © 2023 IEEE

knot. Consequently, the resulting surface is intersecting itself as shown in Fig. 4.16 (b). While in principle this can be avoided by introducing a more complex (Seifert) surface [Sullivan 1996], the results in Fig. 4.17 confirm that the correct fields are obtained. Figure 4.18 confirms that also the non-orientable Möbius strip depicted in Fig. 4.2 can be handled.

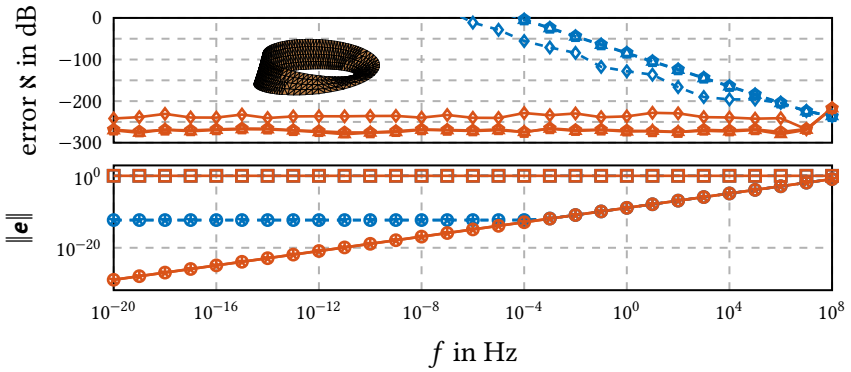

Fig. 4.18: Scattering from the Möbius strip: worst case errors and scaling of the RHS components for a plane wave excitation with and without stabilized RHS. © 2023 IEEE

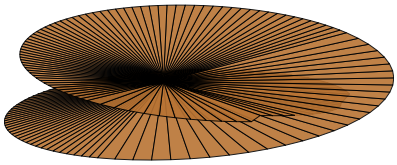

Fig. 4.19: Self-intersecting mesh to close the global loop of the Moebius strip shown in Fig. 4.2. © 2023 IEEE

Again, we use as reference solution a Taylor series expansion for the plane-wave excitation. Similar to the trefoil knot, the cap surface closing the hole is self-intersecting as shown in Fig. 4.19.

4.4 Conclusion

We showed how to evaluate the RHS of the quasi-Helmholtz decomposed EFIE in an excitation agnostic manner such that no catastrophic round-off errors occur in the presence of a multiply-connected geometry due to the testing of the incident field with global loops. The numerical results show that, depending on the scattering object and the specific excitation, without the adaptions inaccurate fields are obtained already for frequencies below the MHz region, but with the stabilized evaluation the scattered and radiated FFs can be determined correctly down to the static limit.

5

An Excitation-Aware and Self-Adaptive Frequency Normalization

> "Even if rounding errors vanished, numerical analysis would remain. Approximating mere numbers, the task of floating point arithmetic, is indeed a rather small topic and maybe even a tedious one. The deeper business of numerical analysis is approximating unknowns, not knowns."
>
> [Trefethen 1992]

A second key aspect for the accurate solution of the quasi-Helmholtz decomposed EFIEs in the presence of arbitrary excitations is addressed in this chapter: Depending on the specific excitation, the quasi-Helmholtz components of the induced current density do not have the same asymptotic scaling in frequency, and thus, the current components are solved for with, in general, different relative accuracies. In order to ensure the same asymptotic scaling, we propose a frequency normalization scheme of the quasi-Helmholtz decomposed EFIEs which adapts itself to the excitation and which is valid irrespective of the specific excitation and irrespective of the underlying topology of the structure. Specifically, neither an ad-hoc adaption nor a-priori information about the excitation is needed as the scaling factors are derived based on the norms of the RHS components and the frequency. Numerical results corroborate the presented theory and show the effectiveness of our approach.

This chapter is based on [Hofmann et al. 2023b] including substantial verbatim portions, where preliminary results were presented in [Hofmann et al. 2022a; Hofmann et al. 2022c; Hofmann et al. 2023d].

As demonstrated in the previous Chapter 4, ensuring that the system matrix of the discretized EFIE is well-conditioned is insufficient if one desires to accurately compute the fields, but testing the RHS with solenoidal functions (which is needed for the considered low-frequency stabilizations) can lead to catastrophic round-off errors. A means to overcome this issue has been proposed in Chapter 4 and in the

following, it is assumed that this or an equally effective stabilization is applied since all further derivations rely on an accurately discretized RHS reflecting the physically correct asymptotic scalings in frequency of the quasi-Helmholtz components.

A second key problem is addressed in this chapter: It has to be ensured that all quasi-Helmholtz components of the decomposed surface current density, that is, the solenoidal and the non-solenoidal component, are recovered with sufficient accuracy to obtain accurate scattered and radiated fields [Andriulli et al. 2013; Chhim et al. 2020]. More precisely, the unknown vector of the LSE to be solved has two contributions (i.e, the solenoidal and the non-solenoidal quasi-Helmholtz component), which can differ largely in their order of magnitude. This is due to the, in general, different asymptotic scaling of the quasi-Helmholtz components in the wavenumber k as $k \to 0$, where the specific behavior is dependent on the excitation source. Still both contributions need to be determined accurately.[1]

As the employed preconditioners entail a rescaling of the quasi-Helmholtz decomposed expansion and basis functions, they enforce a different scaling of the quasi-Helmholtz components of the preconditioned current (i.e., the unknown vector) compared to the physical (non-rescaled) one. The same is true for the RHS components. Different choices for the corresponding scaling coefficients have been employed in the past. Typical choices are, for example, given in [Mautz et al. 1984; Zhao et al. 2000; Andriulli et al. 2013; Echeverri Bautista et al. 2014; Adrian et al. 2017]. While they are suitable for a plane-wave excitation, it is in general not ensured that all components can be recovered correctly for arbitrary excitations, since the scaling coefficients in these existing schemes do not reflect the scaling of the quasi-Helmholtz components of the excitation. Yet, excitations such as voltage gaps sources are commonly used, and thus, the EFIE should be solved accurately for these as well. The same is true for spherical waves, which are able to represent the field radiated by antennas, or line currents representing radiation from wire structures.

A remedy is using ad-hoc techniques as done in [Andriulli et al. 2013]. However, this approach constitutes an approximation which limits the overall accuracy and the behavior of the quasi-Helmholtz components of the excitation needs to be known a-priori. Moreover, in [Andriulli et al. 2013] only three types of excitations were studied (plane wave, capacitive gap excitation, and inductive gap excitation). For other excitations such as spherical TM or TE waves, we find, however, that the approach is not applicable.

In this chapter, we propose a frequency normalization scheme which adapts itself to the excitation requiring neither a-priori information nor ad-hoc adaptions. To this end, the scaling coefficients incorporate the norms of the quasi-Helmholtz components of the discretized RHS in a black-box like manner. Hence, the approach is agnostic to the specific excitation (and the topology of the structure). More precisely, the scaling coefficients are determined such that all quasi-Helmholtz components of the preconditioned current and of the RHS have the same asymptotic scaling. Thereby, all components are recovered with a

[1] An investigation whether similar problems occur also for other proposed low-frequency stabilization schemes for scattering and radiation problems such as the augmented EFIE or potential-based approaches [Qian et al. 2008a; Qian et al. 2010; Epstein et al. 2009; Li et al. 2016; Vico et al. 2016] is beyond the scope of this work.

similar relative accuracy ensuring that all radiated and scattered fields can be computed accurately. Numerical results corroborate the effectiveness of our approach both for canonical and complex geometries.

This chapter is organized as follows: In Section 5.1, the implications of the frequency normalization in quasi-Helmholtz decompositions of the EFIE are analyzed; from the gained insights, the adaptive normalization scheme is derived for the loop-star decomposition as well as for the quasi-Helmholtz projectors. In Section 5.2, we show how to achieve positive eigenvalues of the preconditioned system matrix, again for both decompositions, and implementation specific aspects are addressed. Numerical studies are presented in Section 5.3.

Again, we consider as first approach the loop-star decomposition. It allows to carry out the analysis in a demonstrative way before adapting it to the actual decomposition of interest: quasi-Helmholtz projectors. Moreover, note that in order to also cure the dense-discretization breakdown of the EFIE (i.e., the ill-conditioning with respect to the average edge length of the triangulation of Γ), formulation (3.34) could be combined with a Calderón preconditioner similar to what has been done using the choice of scaling coefficients in [Andriulli et al. 2013; Andriulli et al. 2008a]. While such a combination should be compatible with the here proposed frequency normalization scheme, further investigations would be necessary which are beyond the scope of this work.

5.1 Analysis of the Frequency Normalization and Self-Adaptive Scheme

Before deriving our new formulation, we start by investigating the influence of the different quasi-Helmholtz components of $\boldsymbol{j} = \boldsymbol{j}_{\text{sol,hsol}} + \boldsymbol{j}_{\text{nsol}}$ on the scattered or radiated near and far fields, where we refer again to Table 3.1 for in the following frequently employed notation conventions.

5.1.1 Relevant Current Components

To assess the influence of a surface current density component on the FF, we insert the expansion $\boldsymbol{j} \approx \sum_n [\boldsymbol{j}_{\text{sol,hsol}} + \boldsymbol{j}_{\text{nsol}}]_n \, \boldsymbol{f}_n$ into (2.19) and stabilize the evaluation by explicitly setting the static contributions for the solenoidal current density to zero as [Adrian et al. 2021]

$$\boldsymbol{e}^{\text{FF}}(\boldsymbol{r}) = \sum_{n=1}^{N} \left[\boldsymbol{j}_{\text{sol,hsol}}\right]_n \boldsymbol{u}_r \times \boldsymbol{u}_r \times \iint_{\Gamma} \boldsymbol{f}_n(\boldsymbol{r}') \, \mathfrak{T}\left(\mathrm{e}^{-\mathrm{j}k\boldsymbol{u}_r\cdot\boldsymbol{r}'} - 1\right) \mathrm{d}\boldsymbol{r}' + \sum_{n=1}^{N} [\boldsymbol{j}_{\text{nsol}}]_n \, \boldsymbol{u}_r \times \boldsymbol{u}_r \times \iint_{\Gamma} \boldsymbol{f}_n(\boldsymbol{r}') \, \mathrm{e}^{-\mathrm{j}k\boldsymbol{u}_r\cdot\boldsymbol{r}'} \, \mathrm{d}\boldsymbol{r}' \,, \quad (5.1)$$

Table 5.1: Relevant current components required to recover NFs and FF for $k \to 0$. © 2023 IEEE

	plane wave	Hertzian dipole	el. ring current	mag. dipole	mag. ring current
e-NF	$\boldsymbol{j}_{\text{nsol}}$	$\boldsymbol{j}_{\text{nsol}}$	$\boldsymbol{j}_{\text{sol,hsol}}, \boldsymbol{j}_{\text{nsol}}$	$\boldsymbol{j}_{\text{sol,hsol}}, \boldsymbol{j}_{\text{nsol}}$	$\boldsymbol{j}_{\text{nsol}}$
h-NF	$\boldsymbol{j}_{\text{sol,hsol}}$	$\boldsymbol{j}_{\text{sol,hsol}}, \boldsymbol{j}_{\text{nsol}}$	$\boldsymbol{j}_{\text{sol,hsol}}$	$\boldsymbol{j}_{\text{sol,hsol}}$	$\boldsymbol{j}_{\text{sol,hsol}}, \boldsymbol{j}_{\text{nsol}}$
FF	$\boldsymbol{j}_{\text{sol,hsol}}, \boldsymbol{j}_{\text{nsol}}$	$\boldsymbol{j}_{\text{nsol}}$	$\boldsymbol{j}_{\text{sol,hsol}}$	$\boldsymbol{j}_{\text{sol,hsol}}$	$\boldsymbol{j}_{\text{nsol}}$

	ind. gap	cap. gap	TE_{mn}	TM_{mn}
e-NF	$\boldsymbol{j}_{\text{sol,hsol}}, \boldsymbol{j}_{\text{nsol}}$	$\boldsymbol{j}_{\text{nsol}}$	$\boldsymbol{j}_{\text{sol,hsol}}, \boldsymbol{j}_{\text{nsol}}$	$\boldsymbol{j}_{\text{nsol}}$
h-NF	$\boldsymbol{j}_{\text{sol,hsol}}$	$\boldsymbol{j}_{\text{sol,hsol}}, \boldsymbol{j}_{\text{nsol}}$	$\boldsymbol{j}_{\text{sol,hsol}}$	$\boldsymbol{j}_{\text{sol,hsol}}, \boldsymbol{j}_{\text{nsol}}$
FF	$\boldsymbol{j}_{\text{sol,hsol}}$	$\boldsymbol{j}_{\text{nsol}}$	$\boldsymbol{j}_{\text{sol,hsol}}$	$\boldsymbol{j}_{\text{nsol}}$

where $\mathfrak{T}(\cdot)$ denotes a Taylor series expansion around $k\boldsymbol{u}_r \cdot \boldsymbol{r}' = 0$ as detailed in (4.4), and where we divided by a normalization factor $-\mathrm{j}k$. Since $\mathfrak{T}(\mathrm{e}^{-\mathrm{j}k\boldsymbol{u}_r\cdot\boldsymbol{r}'} - 1) = \mathcal{O}(k)$, the combined current component $\boldsymbol{j}_{\text{sol,hsol}}$ is scaled with an additional factor k compared to $\boldsymbol{j}_{\text{nsol}}$. Adopting the notation

$$\mathcal{O}(k^a) < \mathcal{O}(k^b) \Leftrightarrow a < b\,, \tag{5.2}$$

we consider $\boldsymbol{j}_{\text{sol,hsol}}$ relevant for the FF computation if $\mathcal{O}(k\boldsymbol{j}_{\text{sol,hsol}}) \leq \mathcal{O}(\boldsymbol{j}_{\text{nsol}})$. Likewise, $\boldsymbol{j}_{\text{nsol}}$ is relevant for the FF computation if $\mathcal{O}(\boldsymbol{j}_{\text{nsol}}) \leq \mathcal{O}(k\boldsymbol{j}_{\text{sol,hsol}})$. Analogously, we can determine if a current component is relevant for the computation of the electric or the magnetic NF. In the case of the electric NF, we use its stabilized evaluation

$$\boldsymbol{e}^{\text{NF}}(\boldsymbol{r}) = -\mathrm{j}\sum_{n=1}^{N}[\boldsymbol{j}_{\text{nsol}}]_n\left[k\boldsymbol{\mathcal{T}}_{\text{A}}\boldsymbol{f}_n + k^{-1}\boldsymbol{\mathcal{T}}_{\Phi}\boldsymbol{f}_n\right] - \mathrm{j}\sum_{n=1}^{N}\left[\boldsymbol{j}_{\text{sol,hsol}}\right]_n k\boldsymbol{\mathcal{T}}_{\text{A}}\boldsymbol{f}_n\,, \tag{5.3}$$

which introduces a scaling of $\boldsymbol{j}_{\text{sol,hsol}}$ with k and of $\boldsymbol{j}_{\text{nsol}}$ with $1/k$. In the case of the magnetic NF evaluation in (2.17), both current components are weighted identically.

As an example, consider a plane-wave excitation, where we have $\|\boldsymbol{j}_{\text{sol,hsol}}\| = \mathcal{O}(1)$ and $\|\boldsymbol{j}_{\text{nsol}}\| = \mathcal{O}(k)$: here, only $\boldsymbol{j}_{\text{nsol}}$ is relevant for the electric NF, only $\boldsymbol{j}_{\text{sol,hsol}}$ is relevant for the magnetic NF, but both current components are relevant for the FF. Analogously, the relevant current components that are required to recover the NFs and the FF can be derived for the excitations shown in Table 5.1, where we used the physical current scalings given in [Bogaert et al. 2014; Andriulli et al. 2013]. In addition, we have included the cases of the spherical TE_{mn} and TM_{mn} modes (see Section 2.2.2) based on the physically correct scalings of the current components

$$\|\boldsymbol{j}_{\text{TE,sol,hsol}}\| = \mathcal{O}(k^{-(n+1)}) \tag{5.4}$$

and

$$\|\boldsymbol{j}_{\text{TE,nsol}}\| = \mathcal{O}(k^{-(n-1)}) \tag{5.5}$$

for TE modes as well as

$$\|\boldsymbol{j}_{\mathrm{TM,sol,hsol}}\| = \mathcal{O}(k^{-n}) \tag{5.6}$$

and

$$\|\boldsymbol{j}_{\mathrm{TM,nsol}}\| = \mathcal{O}(k^{-n}) \tag{5.7}$$

for TM modes. The asymptotic scalings can be derived from the RHS component scalings given in (4.27)-(4.30) and a Schur complement analysis of $\boldsymbol{j}'' = \boldsymbol{T}_{\boldsymbol{\Lambda H \Sigma}}^{-1}\boldsymbol{Q}^{\mathrm{T}}\boldsymbol{e}^{\mathrm{ex}}$ (see also the following sections).

Clearly, for all of the excitations in Table 5.1, both $\boldsymbol{j}_{\mathrm{nsol}}$ and $\boldsymbol{j}_{\mathrm{sol,hsol}}$ must be recovered accurately if one desires to compute both FF and NFs accurately. Even more, both current components have to be recovered with a similar relative accuracy as one component can solely determine the accuracy of a field even though its magnitude might be small compared to the other current component. To ensure accurate recovery, we study, in a first step, the frequency scalings of the loop-star decomposed system $\boldsymbol{D}_1\boldsymbol{T}_{\boldsymbol{\Lambda H \Sigma}}\boldsymbol{D}_2\boldsymbol{j}' = \boldsymbol{D}_1\boldsymbol{Q}^{\mathrm{T}}\boldsymbol{e}^{\mathrm{ex}}$ in (3.26).

5.1.2 Self-Adaptive Normalization for Loop-Star Basis

As will be shown in the following, while for a plane-wave excitation the normalization matrices in (3.26) can be chosen as $\boldsymbol{D}_1 = \boldsymbol{D}_2 = (1, 1, k)$ [Mautz et al. 1984], $\boldsymbol{D}_1 = \boldsymbol{D}_2 = \mathrm{diag}(1/\sqrt{k}, 1/\sqrt{k}, \sqrt{k})$ [Andriulli et al. 2013], or $\boldsymbol{D}_1 = \mathrm{diag}(1/k, 1/k, 1)$ and $\boldsymbol{D}_2 = \mathrm{diag}(1, 1, k)$ [Zhao et al. 2000], for arbitrary excitations this yields, in general, wrong solutions; instead, a more flexible approach is required. For the analysis, we use $\boldsymbol{D}_i = \mathrm{diag}(\alpha_i, \gamma_i, \beta_i)$ from (3.27), which allows for an asymmetric normalization. Performing a Schur-complement analysis for the inverse of $\boldsymbol{D}_1\boldsymbol{T}_{\boldsymbol{\Lambda H \Sigma}}\boldsymbol{D}_2$ for $k \to 0$, we obtain

$$\begin{bmatrix} \mathcal{O}\left(\|\boldsymbol{j}'_{\mathrm{sol}}\|\right) \\ \mathcal{O}\left(\|\boldsymbol{j}'_{\mathrm{hsol}}\|\right) \\ \mathcal{O}\left(\|\boldsymbol{j}'_{\mathrm{nsol}}\|\right) \end{bmatrix} = (\boldsymbol{D}_1\boldsymbol{T}_{\boldsymbol{\Lambda H \Sigma}}\boldsymbol{D}_2)^{-1} \begin{bmatrix} \mathcal{O}\left(\alpha_1 \|\boldsymbol{e}_{\mathrm{sol}}\|\right) \\ \mathcal{O}\left(\gamma_1 \|\boldsymbol{e}_{\mathrm{hsol}}\|\right) \\ \mathcal{O}\left(\beta_1 \|\boldsymbol{e}_{\mathrm{nsol}}\|\right) \end{bmatrix}, \tag{5.8}$$

where we note that $\mathcal{O}(\|\boldsymbol{j}'_{\mathrm{sol}}\|) = \mathcal{O}(\|\boldsymbol{j}_{\boldsymbol{\Lambda}}\|)$, $\mathcal{O}(\|\boldsymbol{j}'_{\mathrm{hsol}}\|) = \mathcal{O}(\|\boldsymbol{j}_{\boldsymbol{H}}\|)$, as well as $\mathcal{O}(\|\boldsymbol{j}'_{\mathrm{nsol}}\|) = \mathcal{O}(\|\boldsymbol{j}_{\boldsymbol{\Sigma}}\|)$ since the multiplication with the mapping matrices $\boldsymbol{\Lambda}$, $\boldsymbol{H}$, and $\boldsymbol{\Sigma}$ does not change the scaling in k. The blocks of the matrix $(\boldsymbol{D}_1\boldsymbol{T}_{\boldsymbol{\Lambda H \Sigma}}\boldsymbol{D}_2)^{-1}$ exhibit the scaling

$$\begin{bmatrix} \mathcal{O}(1/(\alpha_1\alpha_2 k)) & \mathcal{O}(1/(\gamma_1\alpha_2 k)) & \mathcal{O}(k/(\beta_1\alpha_2)) \\ \mathcal{O}(1/(\alpha_1\gamma_2 k)) & \mathcal{O}(1/(\gamma_1\gamma_2 k)) & \mathcal{O}(k/(\beta_1\gamma_2)) \\ \mathcal{O}(k/(\alpha_1\beta_2)) & \mathcal{O}(k/(\gamma_1\beta_2)) & \mathcal{O}(k/(\beta_1\,\beta_2)) \end{bmatrix}, \tag{5.9}$$

which is a direct generalization of the findings in [Bogaert et al. 2014]. In order to obtain a well-conditioned matrix for $k \to 0$, we enforce that the blocks on the main diagonal scale

as $\mathcal{O}(1)$; thus, the coefficients must obey

$$\alpha_1\alpha_2 = \mathcal{O}(1/k)\,, \quad \gamma_1\gamma_2 = \mathcal{O}(1/k)\,, \tag{5.10}$$

and

$$\beta_1\beta_2 = \mathcal{O}(k)\,. \tag{5.11}$$

Inserting (5.10) and (5.11) into (5.9) and forming the matrix-vector product in (5.8) results in

$$\begin{bmatrix} \mathcal{O}\left(\|\boldsymbol{j}'_{\mathrm{sol}}\|\right) \\ \mathcal{O}\left(\|\boldsymbol{j}'_{\mathrm{hsol}}\|\right) \\ \mathcal{O}\left(\|\boldsymbol{j}'_{\mathrm{nsol}}\|\right) \end{bmatrix} = \begin{bmatrix} \mathcal{O}\left(\alpha_1\|\boldsymbol{e}_{\mathrm{sol}}\| + \alpha_1\|\boldsymbol{e}_{\mathrm{hsol}}\| + \alpha_1 k^2\|\boldsymbol{e}_{\mathrm{nsol}}\|\right) \\ \mathcal{O}\left(\gamma_1\|\boldsymbol{e}_{\mathrm{sol}}\| + \gamma_1\|\boldsymbol{e}_{\mathrm{hsol}}\| + \gamma_1 k^2\|\boldsymbol{e}_{\mathrm{nsol}}\|\right) \\ \mathcal{O}\left(\beta_1\|\boldsymbol{e}_{\mathrm{nsol}}\| + \beta_1\|\boldsymbol{e}_{\mathrm{sol}}\| + \beta_1\|\boldsymbol{e}_{\mathrm{hsol}}\|\right) \end{bmatrix}, \tag{5.12}$$

which shows that, dependant on the scalings of the incident field, the Helmholtz components of $\boldsymbol{j}'$ will differ in their asymptotic behavior in k.

While the standard choices $\alpha_1 = \alpha_2 = \gamma_1 = \gamma_2 = 1/\sqrt{k}$ and $\beta_1 = \beta_2 = \sqrt{k}$ [Andriulli et al. 2013] or alternatively $\alpha_1 = \gamma_1 = 1/k$, $\beta_1 = \alpha_2 = \gamma_2 = 1$, and $\beta_2 = k$ [Zhao et al. 2000] satisfy (5.10) and (5.11), the resulting quasi-Helmholtz components of $\boldsymbol{j}'$ will, in general, not have the same asymptotic scaling. Consequently, a large relative error in one of the Helmholtz components remains undetected if, for example, the relative residual error of $\boldsymbol{D}_1\boldsymbol{Q}^{\mathrm{T}}\boldsymbol{e}^{\mathrm{ex}} - \boldsymbol{D}_1\boldsymbol{T}_{\Lambda H \Sigma}\boldsymbol{D}_2\boldsymbol{j}'$ is studied (as done by typical iterative solvers for the LSE). As noted, however, in Section 5.1.1, all current components must be recovered with a similar relative accuracy when solving (3.26) in order to accurately compute all fields. These considerations lead us to impose a second requirement on α_i, γ_i, and β_i: all current components should scale identically, where we, due to the constraints of finite-precision arithmetic, opt for an $\mathcal{O}(1)$-type of scaling.

With the aim of satisfying this additional requirement, we first note that the scalings derived in (5.12) show that the solenoidal components associated with the local and the ones associated with the global loops can be treated identically. Consequently, in all of the following, we set

$$\gamma_i = \alpha_i\,, \tag{5.13}$$

and define

$$\|\boldsymbol{e}_{\mathrm{sol,hsol}}\| = \sqrt{\|\boldsymbol{e}_{\mathrm{sol}}\|^2 + \|\boldsymbol{e}_{\mathrm{hsol}}\|^2}\,. \tag{5.14}$$

Moreover, we introduce the ratio of the norms of the solenoidal components over the non-solenoidal component

$$w = \|\boldsymbol{e}_{\mathrm{sol,hsol}}\|/\|\boldsymbol{e}_{\mathrm{nsol}}\|\,. \tag{5.15}$$

Excluding the trivial case $\|\boldsymbol{e}_{\mathrm{sol,hsol}}\| = \|\boldsymbol{e}_{\mathrm{nsol}}\| = 0$, the scalings in (5.12) then dictate

$$\alpha_1 = \begin{cases} 1/\|\boldsymbol{e}_{\mathrm{sol,hsol}}\| & \text{for } w \leq \mathcal{O}(k^2) \\ 1/(k^2\,\|\boldsymbol{e}_{\mathrm{nsol}}\|) & \text{for } w > \mathcal{O}(k^2) \end{cases} \tag{5.16}$$

and

$$\beta_1 = \begin{cases} 1/\|\boldsymbol{e}_{\mathrm{nsol}}\| & \text{for } w \geq \mathcal{O}(1) \\ 1/\|\boldsymbol{e}_{\mathrm{sol,hsol}}\| & \text{for } w < \mathcal{O}(1) \end{cases}. \tag{5.17}$$

Note that the case $w > \mathcal{O}(k^2)$ includes $\|\boldsymbol{e}_{\mathrm{sol,hsol}}\| = 0$ when interpreting it as the result of $w \to 0$ and the case $w < \mathcal{O}(1)$ includes the case $\|\boldsymbol{e}_{\mathrm{nsol}}\| = 0$ when interpreting it as the result of $w \to \infty$. Moreover, definition (5.14) covers also the cases where $\mathcal{O}(\|\boldsymbol{e}_{\mathrm{sol}}\|) \neq \mathcal{O}(\|\boldsymbol{e}_{\mathrm{hsol}}\|)$ including the cases where not both but either $\boldsymbol{e}_{\mathrm{sol}}$ or $\boldsymbol{e}_{\mathrm{hsol}}$ vanishes (e.g., as encountered for gap excitations).

Together with (5.10) and (5.11) for the remaining coefficients, we find

$$\alpha_2 = 1/(k\alpha_1) \quad \text{and} \quad \beta_2 = k/\beta_1\,, \tag{5.18}$$

arriving at a scheme that adapts itself to the incident field based on the norms of the RHS components. Hence, there is no need to have *a-priori* information about the nature of the incident field.

5.1.3 Quasi-Helmholtz Projector Normalization Factors

When employing the quasi-Helmholtz projector stabilized system (3.34) instead of the loop-star decomposition, the very same normalization factors (5.16)-(5.18) can be employed[2] with the corresponding definitions $\boldsymbol{e}_{\mathrm{sol,hsol}} = \boldsymbol{P}_{\Lambda H}\boldsymbol{e}^{\mathrm{ex}}$ and $\boldsymbol{e}_{\mathrm{nsol}} = \boldsymbol{P}_{\Sigma}\boldsymbol{e}^{\mathrm{ex}}$. This follows from an intrinsic relation which can be established to the loop-star decomposition, that is,

$$\boldsymbol{P}_1\boldsymbol{T}\boldsymbol{P}_2 = \boldsymbol{Q}\boldsymbol{N}\boldsymbol{D}_1\boldsymbol{T}_{\Lambda H\Sigma}\boldsymbol{D}_2\boldsymbol{N}\boldsymbol{Q}^{\mathrm{T}} \tag{5.19}$$

with

$$\boldsymbol{N} = \mathrm{diag}((\boldsymbol{\Lambda}^{\mathrm{T}}\boldsymbol{\Lambda})^{+}, (\boldsymbol{H}^{\mathrm{T}}\boldsymbol{H})^{+}, (\boldsymbol{\Sigma}^{\mathrm{T}}\boldsymbol{\Sigma})^{+})\,. \tag{5.20}$$

However, it should be verified that α_i and β_i in (3.33) properly take care of another aspect only relevant for the projectors: since solenoidal and non-solenoidal components are stored in the same vector, that is, $\boldsymbol{j}' = \boldsymbol{j}'_{\mathrm{sol,hsol}} + \boldsymbol{j}'_{\mathrm{nsol}}$ and $\boldsymbol{P}_1\boldsymbol{e}^{\mathrm{ex}} = \boldsymbol{e}'_{\mathrm{sol,hsol}} + \boldsymbol{e}'_{\mathrm{nsol}}$, significant digits can be lost if the asymptotic scaling in k of $\boldsymbol{j}'_{\mathrm{sol,hsol}}$ and $\boldsymbol{j}'_{\mathrm{nsol}}$ (or $\boldsymbol{e}'_{\mathrm{sol,hsol}}$ and $\boldsymbol{e}'_{\mathrm{nsol}}$) is different. This is precisely the reason why an imaginary constant was included in the definition of the projectors in [Andriulli et al. 2013], where $\boldsymbol{P}_1 = \boldsymbol{P}_2 = \boldsymbol{P}_{\Lambda H}/\sqrt{k} + \mathrm{j}\sqrt{k}\boldsymbol{P}_{\Sigma}$ was employed.

[2] Note that due to (5.13) there is no need to split $\boldsymbol{P}_{\Lambda H}$ into $\boldsymbol{P}_{\Lambda}$ and $\boldsymbol{P}_{H}$.

Due to the imaginary constant, for example, for the inductive gap excitation the dominant contribution of $\boldsymbol{j}'_{\text{sol,hsol}}$ was stored in the imaginary part and the dominant contribution of $\boldsymbol{j}'_{\text{nsol}}$ in the real part of $\boldsymbol{j}'$, where we consider a component as dominant if its asymptotic behavior $\mathcal{O}(k^a) < \mathcal{O}(k^b)$ with k^b as the scaling for the other component.[3] This approach relies on the circumstance that real and imaginary part of each quasi-Helmholtz component often exhibit a different asymptotic scaling, so that, in fact, only one of the parts is relevant for an accurate field computation in low-frequency scenarios. However, using the factors α_i and β_i as defined in (5.16)-(5.18) for $\boldsymbol{P}_i$, the inclusion of an imaginary constant is in the first place no longer necessary.

In order to illustrate this problem of the significant digits in more detail, we consider the physical frequency scalings of the RHS for seven different types of excitations. Those can be derived as shown in Appendix A.1, where the findings of [Bogaert et al. 2014] are generalized, resulting in the first three rows of Table 5.2. Note that in contrast to the analysis so far, we study now real and imaginary part separately to show that indeed no dominant contribution is lost. The scalings show that directly storing the components in one vector would lead to a loss of significant digits for a Hertzian dipole or a magnetic ring current excitation, since the solenoidal components scale differently than the non-solenoidal components. The next three rows show the scalings using the normalization from [Andriulli et al. 2013]. Here the real and the imaginary part of the non-solenoidal components are interchanged, which allows to store the components in one vector for all the considered excitations. However, for the excitation by spherical TE and TM modes, this approach fails as shown by Table 5.2. Both, real and imaginary part have the same asymptotic scaling such that none can be neglected. At the same time, the here proposed normalization shown in the last rows (of Table 5.2) works independently of the specific scalings of the RHS and without introducing an imaginary constant, since it does not rely on storing one dominant component in the real and the other in the imaginary part: each dominant component is normalized to scale as $\mathcal{O}(1)$, and thus, they can be added without the danger of losing significant digits.

To complete the picture, we study also the scalings of the solution current components in Table 5.3: the first three rows show the physical scalings as obtained by separately handling real and imaginary part in (5.8). Evidently, storing the physical current components in one vector fails for the electric ring current, the magnetic (Fitzgerald) dipole, and the inductive gap excitation. From $\boldsymbol{j} = \boldsymbol{j}_{\text{sol,hsol}} + \boldsymbol{j}_{\text{nsol}} = \boldsymbol{P}_2\boldsymbol{j}' = \alpha_2\boldsymbol{j}'_{\text{sol,hsol}} + \beta_2\boldsymbol{j}'_{\text{nsol}}$, it can be seen that the solution current of the preconditioned LSE scales as

$$\boldsymbol{j}'_{\text{sol,hsol}} = \boldsymbol{j}_{\text{sol,hsol}}/\alpha_2 \qquad \text{and} \qquad \boldsymbol{j}'_{\text{nsol}} = \boldsymbol{j}_{\text{nsol}}/\beta_2\,. \tag{5.21}$$

Using the normalization from [Andriulli et al. 2013], rows two to six in Table 5.3 show that, at least for the considered excitations, all current components can be stored in one vector. However, again for the TE_{mn} and TM_{mn} modes this fails as, for example, $\|\boldsymbol{j}_{\text{TE,sol,hsol}}\|_\star = \mathcal{O}(k^{-(n+1)}) + \text{j}\mathcal{O}(k^{-(n+1)})$ and $\|\boldsymbol{j}_{\text{TE,nsol}}\|_\star = \mathcal{O}(k^{-(n-1)}) + \text{j}\mathcal{O}(k^{-(n-1)})$. Even more, for all the ex-

[3] For the actual recovery of the relevant current components, the normalization of [Andriulli et al. 2013] of course requires an ad-hoc technique, which is avoided by the here proposed approach.

Table 5.2: Scaling of real and imaginary part of the RHS components for $k \to 0$ with $\|\boldsymbol{a}\|_\star = \|\mathrm{Re}\{\boldsymbol{a}\}\| + \mathrm{j}\|\mathrm{Im}\{\boldsymbol{a}\}\|$. © 2023 IEEE

	plane wave	Hertzian dipole	el. ring current	mag. dipole	mag. ring current
$\|\boldsymbol{e}_{\mathrm{sol}}\|_\star$	$\mathcal{O}(k^2) + \mathrm{j}\mathcal{O}(k)$	$\mathcal{O}(k^4) + \mathrm{j}\mathcal{O}(k)$	$\mathcal{O}(k^4) + \mathrm{j}\mathcal{O}(k)$	$\mathcal{O}(1) + \mathrm{j}\mathcal{O}(k^3)$	$\mathcal{O}(k^2) + \mathrm{j}\mathcal{O}(k^5)$
$\|\boldsymbol{e}_{\mathrm{hsol}}\|_\star$	$\mathcal{O}(k^2) + \mathrm{j}\mathcal{O}(k)$	$\mathcal{O}(k^4) + \mathrm{j}\mathcal{O}(k)$	$\mathcal{O}(k^4) + \mathrm{j}\mathcal{O}(k)$	$\mathcal{O}(1) + \mathrm{j}\mathcal{O}(k^3)$	$\mathcal{O}(k^2) + \mathrm{j}\mathcal{O}(k^5)$
$\|\boldsymbol{e}_{\mathrm{nsol}}\|_\star$	$\mathcal{O}(1) + \mathrm{j}\mathcal{O}(k)$	$\mathcal{O}(k^2) + \mathrm{j}\mathcal{O}(1/k)$	$\mathcal{O}(k^4) + \mathrm{j}\mathcal{O}(k)$	$\mathcal{O}(1) + \mathrm{j}\mathcal{O}(k^3)$	$\mathcal{O}(1) + \mathrm{j}\mathcal{O}(k^3)$
$1/\sqrt{k}\|\boldsymbol{e}_{\mathrm{sol}}\|_\star$	$\mathcal{O}(k^{3/2}) + \mathrm{j}\mathcal{O}(k^{1/2})$	$\mathcal{O}(k^{7/2}) + \mathrm{j}\mathcal{O}(k^{1/2})$	$\mathcal{O}(k^{7/2}) + \mathrm{j}\mathcal{O}(k^{1/2})$	$\mathcal{O}(k^{-1/2}) + \mathrm{j}\mathcal{O}(k^{5/2})$	$\mathcal{O}(k^{3/2}) + \mathrm{j}\mathcal{O}(k^{9/2})$
$1/\sqrt{k}\|\boldsymbol{e}_{\mathrm{hsol}}\|_\star$	$\mathcal{O}(k^{3/2}) + \mathrm{j}\mathcal{O}(k^{1/2})$	$\mathcal{O}(k^{7/2}) + \mathrm{j}\mathcal{O}(k^{1/2})$	$\mathcal{O}(k^{7/2}) + \mathrm{j}\mathcal{O}(k^{1/2})$	$\mathcal{O}(k^{-1/2}) + \mathrm{j}\mathcal{O}(k^{5/2})$	$\mathcal{O}(k^{3/2}) + \mathrm{j}\mathcal{O}(k^{9/2})$
$\mathrm{j}\sqrt{k}\|\boldsymbol{e}_{\mathrm{nsol}}\|_\star$	$\mathcal{O}(k^{3/2}) + \mathrm{j}\mathcal{O}(k^{1/2})$	$\mathcal{O}(k^{-1/2}) + \mathrm{j}\mathcal{O}(k^{5/2})$	$\mathcal{O}(k^{3/2}) + \mathrm{j}\mathcal{O}(k^{9/2})$	$\mathcal{O}(k^{7/2}) + \mathrm{j}\mathcal{O}(k^{1/2})$	$\mathcal{O}(k^{7/2}) + \mathrm{j}\mathcal{O}(k^{1/2})$
$\alpha_1\|\boldsymbol{e}_{\mathrm{sol}}\|_\star$	$\mathcal{O}(k) + \mathrm{j}\mathcal{O}(1)$	$\mathcal{O}(k^3) + \mathrm{j}\mathcal{O}(1)$	$\mathcal{O}(k^3) + \mathrm{j}\mathcal{O}(1)$	$\mathcal{O}(1) + \mathrm{j}\mathcal{O}(k^3)$	$\mathcal{O}(1) + \mathrm{j}\mathcal{O}(k^3)$
$\alpha_1\|\boldsymbol{e}_{\mathrm{hsol}}\|_\star$	$\mathcal{O}(k) + \mathrm{j}\mathcal{O}(1)$	$\mathcal{O}(k^3) + \mathrm{j}\mathcal{O}(1)$	$\mathcal{O}(k^3) + \mathrm{j}\mathcal{O}(1)$	$\mathcal{O}(1) + \mathrm{j}\mathcal{O}(k^3)$	$\mathcal{O}(1) + \mathrm{j}\mathcal{O}(k^3)$
$\beta_1\|\boldsymbol{e}_{\mathrm{nsol}}\|_\star$	$\mathcal{O}(1) + \mathrm{j}\mathcal{O}(k)$	$\mathcal{O}(k^3) + \mathrm{j}\mathcal{O}(1)$	$\mathcal{O}(k^3) + \mathrm{j}\mathcal{O}(1)$	$\mathcal{O}(1) + \mathrm{j}\mathcal{O}(k^3)$	$\mathcal{O}(1) + \mathrm{j}\mathcal{O}(k^3)$

	ind. gap	cap. gap	TE_{mn}	TM_{mn}
$\|\boldsymbol{e}_{\mathrm{sol}}\|_\star$	$0 + \mathrm{j}0$	$0 + \mathrm{j}0$	$\mathcal{O}(k^{-n}) + \mathrm{j}\mathcal{O}(k^{-n})$	$\mathcal{O}(k^{-(n-1)}) + \mathrm{j}\mathcal{O}(k^{-(n-1)})$
$\|\boldsymbol{e}_{\mathrm{hsol}}\|_\star$	$\mathcal{O}(1) + \mathrm{j}0$	$0 + \mathrm{j}0$	$\mathcal{O}(k^{-n}) + \mathrm{j}\mathcal{O}(k^{-n})$	$\mathcal{O}(k^{-(n-1)}) + \mathrm{j}\mathcal{O}(k^{-(n-1)})$
$\|\boldsymbol{e}_{\mathrm{nsol}}\|_\star$	$\mathcal{O}(1) + \mathrm{j}0$	$\mathcal{O}(1) + \mathrm{j}0$	$\mathcal{O}(k^{-n}) + \mathrm{j}\mathcal{O}(k^{-n})$	$\mathcal{O}(k^{-(n+1)}) + \mathrm{j}\mathcal{O}(k^{-(n+1)})$
$1/\sqrt{k}\|\boldsymbol{e}_{\mathrm{sol}}\|_\star$	$0 + \mathrm{j}0$	$0 + \mathrm{j}0$	$\mathcal{O}(k^{-n-1/2}) + \mathrm{j}\mathcal{O}(k^{-n-1/2})$	$\mathcal{O}(k^{-(n-1/2)}) + \mathrm{j}\mathcal{O}(k^{-(n-1/2)})$
$1/\sqrt{k}\|\boldsymbol{e}_{\mathrm{hsol}}\|_\star$	$\mathcal{O}(k^{-1/2}) + \mathrm{j}0$	$0 + \mathrm{j}0$	$\mathcal{O}(k^{-n-1/2}) + \mathrm{j}\mathcal{O}(k^{-n-1/2})$	$\mathcal{O}(k^{-(n-1/2)}) + \mathrm{j}\mathcal{O}(k^{-(n-1/2)})$
$\mathrm{j}\sqrt{k}\|\boldsymbol{e}_{\mathrm{nsol}}\|_\star$	$0 + \mathrm{j}\mathcal{O}(k^{1/2})$	$0 + \mathrm{j}\mathcal{O}(k^{1/2})$	$\mathcal{O}(k^{-n+1/2}) + \mathrm{j}\mathcal{O}(k^{-n+1/2})$	$\mathcal{O}(k^{-(n+1/2)}) + \mathrm{j}\mathcal{O}(k^{-(n+1/2)})$
$\alpha_1\|\boldsymbol{e}_{\mathrm{sol}}\|_\star$	$0 + \mathrm{j}0$	$0 + \mathrm{j}0$	$\mathcal{O}(1) + \mathrm{j}\mathcal{O}(1)$	$\mathcal{O}(1) + \mathrm{j}\mathcal{O}(1)$
$\alpha_1\|\boldsymbol{e}_{\mathrm{hsol}}\|_\star$	$\mathcal{O}(1) + \mathrm{j}0$	$0 + \mathrm{j}0$	$\mathcal{O}(1) + \mathrm{j}\mathcal{O}(1)$	$\mathcal{O}(1) + \mathrm{j}\mathcal{O}(1)$
$\beta_1\|\boldsymbol{e}_{\mathrm{nsol}}\|_\star$	$\mathcal{O}(1) + \mathrm{j}0$	$\mathcal{O}(1) + \mathrm{j}0$	$\mathcal{O}(1) + \mathrm{j}\mathcal{O}(1)$	$\mathcal{O}(1) + \mathrm{j}\mathcal{O}(1)$

Table 5.3: Scaling of real and imaginary part of the current components for $k \to 0$ with $\|\boldsymbol{a}\|_\star = \|\mathrm{Re}\{\boldsymbol{a}\}\| + \mathrm{j}\|\mathrm{Im}\{\boldsymbol{a}\}\|$. © 2023 IEEE

	plane wave	Hertzian dipole	el. ring current	mag. dipole
$\|\boldsymbol{j}_{\mathrm{sol}}\|_\star$	$\mathcal{O}(1) + \mathrm{j}\mathcal{O}(k)$	$\mathcal{O}(1) + \mathrm{j}\mathcal{O}(k^3)$	$\mathcal{O}(1) + \mathrm{j}\mathcal{O}(k^3)$	$\mathcal{O}(k^2) + \mathrm{j}\mathcal{O}(1/k)$
$\|\boldsymbol{j}_{\mathrm{hsol}}\|_\star$	$\mathcal{O}(1) + \mathrm{j}\mathcal{O}(k)$	$\mathcal{O}(1) + \mathrm{j}\mathcal{O}(k^3)$	$\mathcal{O}(1) + \mathrm{j}\mathcal{O}(k^3)$	$\mathcal{O}(k^2) + \mathrm{j}\mathcal{O}(1/k)$
$\|\boldsymbol{j}_{\mathrm{nsol}}\|_\star$	$\mathcal{O}(k^2) + \mathrm{j}\mathcal{O}(k)$	$\mathcal{O}(1) + \mathrm{j}\mathcal{O}(k^3)$	$\mathcal{O}(k^2) + \mathrm{j}\mathcal{O}(k^5)$	$\mathcal{O}(k^4) + \mathrm{j}\mathcal{O}(k)$
$\|\boldsymbol{j}_{\mathrm{sol}}\|_\star \sqrt{k}$	$\mathcal{O}(k^{1/2}) + \mathrm{j}\mathcal{O}(k^{3/2})$	$\mathcal{O}(k^{1/2}) + \mathrm{j}\mathcal{O}(k^{7/2})$	$\mathcal{O}(k^{1/2}) + \mathrm{j}\mathcal{O}(k^{7/2})$	$\mathcal{O}(k^{5/2}) + \mathrm{j}\mathcal{O}(k^{-1/2})$
$\|\boldsymbol{j}_{\mathrm{hsol}}\|_\star \sqrt{k}$	$\mathcal{O}(k^{1/2}) + \mathrm{j}\mathcal{O}(k^{3/2})$	$\mathcal{O}(k^{1/2}) + \mathrm{j}\mathcal{O}(k^{7/2})$	$\mathcal{O}(k^{1/2}) + \mathrm{j}\mathcal{O}(k^{7/2})$	$\mathcal{O}(k^{5/2}) + \mathrm{j}\mathcal{O}(k^{-1/2})$
$\|\boldsymbol{j}_{\mathrm{nsol}}\|_\star \mathrm{j}/\sqrt{k}$	$\mathcal{O}(k^{1/2}) + \mathrm{j}\mathcal{O}(k^{3/2})$	$\mathcal{O}(k^{5/2}) + \mathrm{j}\mathcal{O}(k^{-1/2})$	$\mathcal{O}(k^{9/2}) + \mathrm{j}\mathcal{O}(k^{3/2})$	$\mathcal{O}(k^{1/2}) + \mathrm{j}\mathcal{O}(k^{7/2})$
$\|\boldsymbol{j}_{\mathrm{sol}}\|_\star / \alpha_2$	$\mathcal{O}(1) + \mathrm{j}\mathcal{O}(k)$	$\mathcal{O}(1) + \mathrm{j}\mathcal{O}(k^3)$	$\mathcal{O}(1) + \mathrm{j}\mathcal{O}(k^3)$	$\mathcal{O}(k^3) + \mathrm{j}\mathcal{O}(1)$
$\|\boldsymbol{j}_{\mathrm{hsol}}\|_\star / \alpha_2$	$\mathcal{O}(1) + \mathrm{j}\mathcal{O}(k)$	$\mathcal{O}(1) + \mathrm{j}\mathcal{O}(k^3)$	$\mathcal{O}(1) + \mathrm{j}\mathcal{O}(k^3)$	$\mathcal{O}(k^3) + \mathrm{j}\mathcal{O}(1)$
$\|\boldsymbol{j}_{\mathrm{nsol}}\|_\star / \beta_2$	$\mathcal{O}(k) + \mathrm{j}\mathcal{O}(1)$	$\mathcal{O}(1) + \mathrm{j}\mathcal{O}(k^3)$	$\mathcal{O}(1) + \mathrm{j}\mathcal{O}(k^3)$	$\mathcal{O}(k^3) + \mathrm{j}\mathcal{O}(1)$

	mag. ring current	ind. gap	cap. gap
$\|\boldsymbol{j}_{\mathrm{sol}}\|_\star$	$\mathcal{O}(k^4) + \mathrm{j}\mathcal{O}(k)$	$\mathcal{O}(k^2) + \mathrm{j}\mathcal{O}(1/k)$	$\mathcal{O}(k^4) + \mathrm{j}\mathcal{O}(k)$
$\|\boldsymbol{j}_{\mathrm{hsol}}\|_\star$	$\mathcal{O}(k^4) + \mathrm{j}\mathcal{O}(k)$	$\mathcal{O}(k^2) + \mathrm{j}\mathcal{O}(1/k)$	$\mathcal{O}(k^4) + \mathrm{j}\mathcal{O}(k)$
$\|\boldsymbol{j}_{\mathrm{nsol}}\|_\star$	$\mathcal{O}(k^4) + \mathrm{j}\mathcal{O}(k)$	$\mathcal{O}(k^4) + \mathrm{j}\mathcal{O}(k)$	$\mathcal{O}(k^4) + \mathrm{j}\mathcal{O}(k)$
$\|\boldsymbol{j}_{\mathrm{sol}}\|_\star \sqrt{k}$	$\mathcal{O}(k^{9/2}) + \mathrm{j}\mathcal{O}(k^{3/2})$	$\mathcal{O}(k^{5/2}) + \mathrm{j}\mathcal{O}(k^{-1/2})$	$\mathcal{O}(k^{9/2}) + \mathrm{j}\mathcal{O}(k^{3/2})$
$\|\boldsymbol{j}_{\mathrm{hsol}}\|_\star \sqrt{k}$	$\mathcal{O}(k^{9/2}) + \mathrm{j}\mathcal{O}(k^{3/2})$	$\mathcal{O}(k^{5/2}) + \mathrm{j}\mathcal{O}(k^{-1/2})$	$\mathcal{O}(k^{9/2}) + \mathrm{j}\mathcal{O}(k^{3/2})$
$\|\boldsymbol{j}_{\mathrm{nsol}}\|_\star \mathrm{j}/\sqrt{k}$	$\mathcal{O}(k^{1/2}) + \mathrm{j}\mathcal{O}(k^{7/2})$	$\mathcal{O}(k^{1/2}) + \mathrm{j}\mathcal{O}(k^{7/2})$	$\mathcal{O}(k^{1/2}) + \mathrm{j}\mathcal{O}(k^{7/2})$
$\|\boldsymbol{j}_{\mathrm{sol}}\|_\star / \alpha_2$	$\mathcal{O}(k^3) + \mathrm{j}\mathcal{O}(1)$	$\mathcal{O}(k^3) + \mathrm{j}\mathcal{O}(1)$	$\mathcal{O}(k^3) + \mathrm{j}\mathcal{O}(1)$
$\|\boldsymbol{j}_{\mathrm{hsol}}\|_\star / \alpha_2$	$\mathcal{O}(k^3) + \mathrm{j}\mathcal{O}(1)$	$\mathcal{O}(k^3) + \mathrm{j}\mathcal{O}(1)$	$\mathcal{O}(k^3) + \mathrm{j}\mathcal{O}(1)$
$\|\boldsymbol{j}_{\mathrm{nsol}}\|_\star / \beta_2$	$\mathcal{O}(k^3) + \mathrm{j}\mathcal{O}(1)$	$\mathcal{O}(k^3) + \mathrm{j}\mathcal{O}(1)$	$\mathcal{O}(k^3) + \mathrm{j}\mathcal{O}(1)$

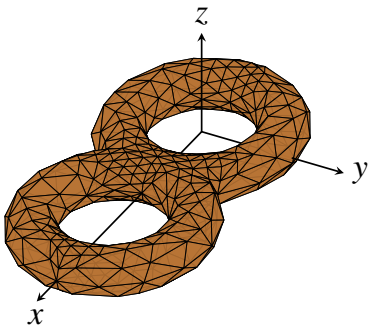

Fig. 5.1: Double torus with $N_H = 4$ global loops: each torus with outer radius 1 m and inner radius 0.5 m. Second torus at $x = 1.55$ m. Discretized by 848 triangles and 1272 RWGs. © 2023 IEEE

citations (except for the plane wave) the dominant components of the current still scale differently, hinting that they cannot be recovered with a similar relative accuracy in a straightforward manner but an ad-hoc technique is required. This can be avoided when the proposed normalization scheme is employed as shown in the last three rows.

As an example of which current components can be recovered, we consider the double torus in Fig. 5.1 excited by a magnetic diople. Real and imaginary part of the determined current components are depicted in Fig. 5.2 (a) for the standard normalization and in Fig. 5.2 (b) for the proposed normalization. In order to ensure a high accuracy, a direct solver is employed. While the standard normalization, at first glance, seems to approximate the theoretical scalings (indicated by dashed lines) better, only the adaptive normalization maintains the correct scalings of the dominant components for all frequencies. This is, however, the decisive property. The worse agreement of the non-dominant components is not relevant for the resulting fields as the non-dominant components are (in this case 13) orders of magnitude smaller than the dominant components. A similar behavior can be observed for an excitation by an electric ring current as shown in Fig. 5.2 (c) and (d), which confirms, again, the preceding analysis.

5.2 Eigenvalue Distribution and Implementation Details

The definition of the normalization constants α_i and β_i in (5.16)-(5.18) allows for two more improvements leading typically to faster convergence of iterative solvers. By reintroducing an imaginary constant j and a constant C (to be defined for the loop-star basis and the quasi-Helmholtz projectors, respectively, in the following subsections), we ultimately propose to choose the normalization factors

$$\alpha_1 = \begin{cases} \sqrt{-\mathrm{j}C}/\|\boldsymbol{e}_{\mathrm{sol,hsol}}\| & \text{for } \|\boldsymbol{e}_{\mathrm{sol,hsol}}\| \neq 0\,, \\ \sqrt{-\mathrm{j}C}/(k^2\,\|\boldsymbol{e}_{\mathrm{nsol}}\|) & \text{for } \|\boldsymbol{e}_{\mathrm{sol,hsol}}\| = 0\,, \end{cases} \tag{5.22}$$

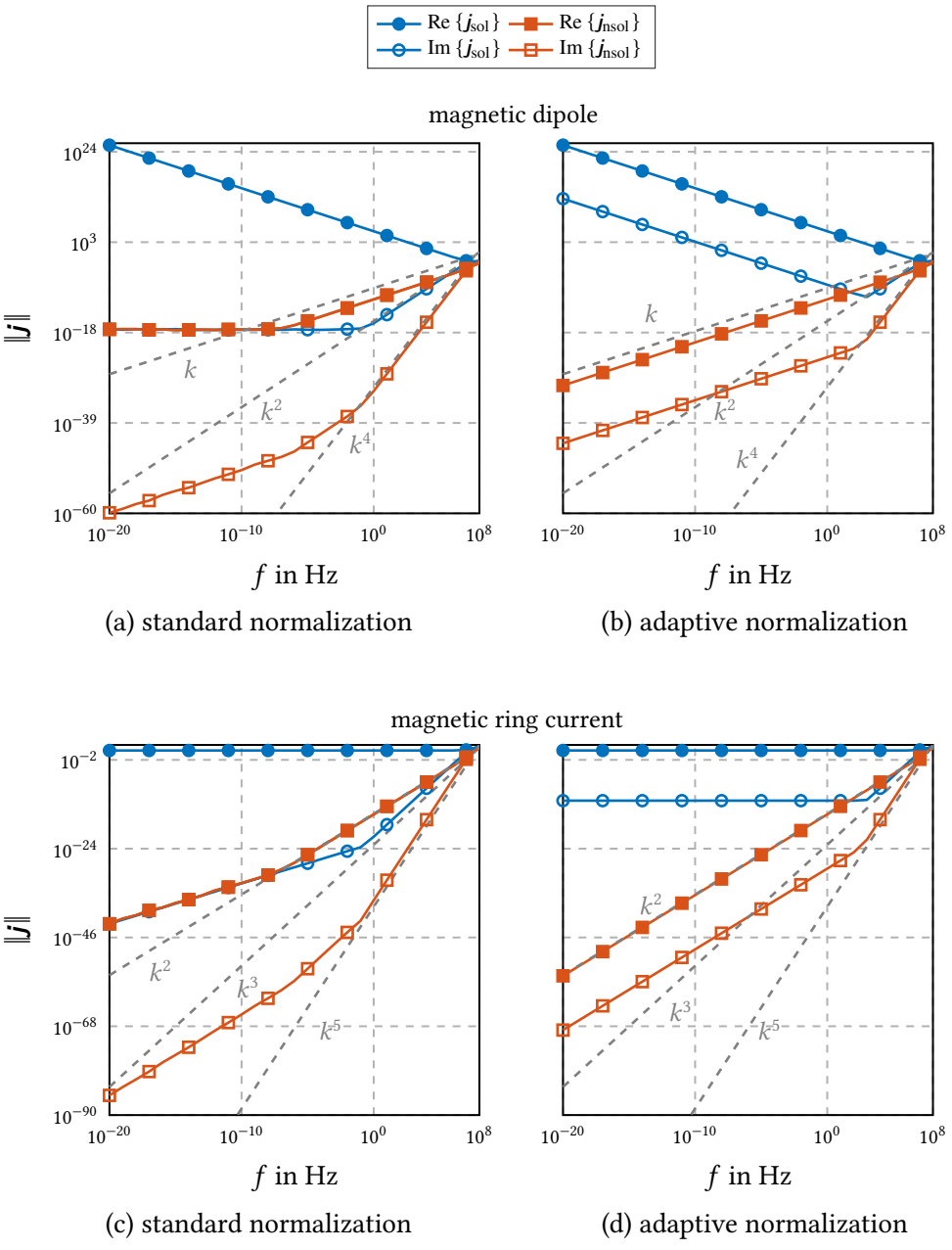

(a) standard normalization (b) adaptive normalization

(c) standard normalization (d) adaptive normalization

Fig. 5.2: Scaling of real and imaginary part of the recovered current components for a double torus excited by a magnetic dipole and ring current. © 2023 IEEE

and

$$\beta_1 = \begin{cases} 1/(\sqrt{-\mathrm{j}C}\|\boldsymbol{e}_{\mathrm{nsol}}\|) & \text{for } \|\boldsymbol{e}_{\mathrm{nsol}}\| \neq 0\,, \\ 1/(\sqrt{-\mathrm{j}C}\,\|\boldsymbol{e}_{\mathrm{sol,hsol}}\|) & \text{for } \|\boldsymbol{e}_{\mathrm{nsol}}\| = 0\,, \end{cases} \tag{5.23}$$

where the simplified conditions for the case distinctions (not involving w) are sufficient for practical purposes as will be detailed in the following section. Together with (5.10) and (5.11), we then find for the remaining coefficients

$$\alpha_2 = C/(\mathrm{j}k\alpha_1) \quad \text{and} \quad \beta_2 = \mathrm{j}k/(C\beta_1)\,, \tag{5.24}$$

where still (5.13) is employed for the γ_i in the context of the loop-star decomposition. The motivation for these modifications will again be discussed first for the loop-star decomposition and then for the quasi-Helmholtz projectors.

5.2.1 On the Simplification of the Conditions to be Checked

The suggested simplified conditions for the case distinctions in (5.22) and (5.23) are based on the observation, that, except for the capacitive gap excitation for all standard excitations listed in Table 5.2, the ratio in (5.15) satisfies

$$\mathcal{O}(1) \leq w \leq \mathcal{O}(k^2) \tag{5.25}$$

as can be seen from the first three rows. The capacitive gap excitation, on the other hand, is accounted for by the case $\|\boldsymbol{e}_{\mathrm{sol,hsol}}\| = 0$. Even when combining arbitrary TE_{mn} and TM_{mn} modes with arbitrary orders n, the relation (5.25) is satisfied with the sole exception when Γ is a sphere placed in the origin, all shown in Appendix A.2. In this particular case, $\|\boldsymbol{e}_{\mathrm{TM,sol}}\| = 0$. Consequently, if no other excitations than the ones listed are present, the case distinctions only require to check whether one of the norms is zero. For cases not covered by (5.25), the more general conditions on w given in (5.16) and (5.17) can be checked by evaluating the norms at least at two frequencies.

5.2.2 Loop-Star Decomposition

The idea of introducing the constant C in (5.22) and (5.23) is to improve the overall condition number of the system matrix. Choosing it similar to the one suggested in [Adrian et al. 2021] as

$$C = \sqrt{\frac{k\|\boldsymbol{\Sigma}^{\mathrm{T}}\boldsymbol{T}\boldsymbol{\Sigma}\|}{\|[\boldsymbol{\Lambda}\ \boldsymbol{H}]^{\mathrm{T}}\boldsymbol{T}_{\mathrm{A}}[\boldsymbol{\Lambda}\ \boldsymbol{H}]\|}} \tag{5.26}$$

enforces an equal contribution of the scalar and the vector potential. The matrix norms in this expression can be determined efficiently as $\|\boldsymbol{\Upsilon}\| = \sqrt{\lambda_{\max}(\boldsymbol{\Upsilon}^{\mathrm{H}}\boldsymbol{\Upsilon})}$ for a square matrix $\boldsymbol{\Upsilon}$

with $\lambda_{\max}(\boldsymbol{\Upsilon}^{\mathrm{H}}\boldsymbol{\Upsilon})$ denoting the largest eigenvalue of $\boldsymbol{\Upsilon}^{\mathrm{H}}\boldsymbol{\Upsilon}$. This eigenvalue can be estimated, for example, via a few Arnoldi iterations or the power iteration method (which are both compatible with matrix-free methods) [Trefethen et al. 1997; Stewart 2002].

The factor j, on the other hand, causes $\boldsymbol{D}_1\boldsymbol{T}_{\Lambda H\Sigma}\boldsymbol{D}_2$ to have only positive eigenvalues in the static limit: For $\mathcal{O}(1) \leq w \leq \mathcal{O}(k^2)$, the matrix $\boldsymbol{D}_1\boldsymbol{T}_{\Lambda H\Sigma}\boldsymbol{D}_2$ exhibits the block structure

$$\begin{bmatrix} \boldsymbol{A}_{N_{\Lambda H}\times N_{\Lambda H}} & \boldsymbol{B}_{N_{\Lambda H}\times N_\Sigma} \\ \boldsymbol{C}_{N_\Sigma\times N_{\Lambda H}} & \boldsymbol{D}_{N_\Sigma\times N_\Sigma} \end{bmatrix} = \begin{bmatrix} \mathcal{O}(1) & \mathcal{O}(k^2/w) \\ \mathcal{O}(w) & \mathcal{O}(1) \end{bmatrix}, \tag{5.27}$$

with $N_{\Lambda H} = N_\Lambda + N_H$ and where

$$w = \mathcal{O}(k^\nu)\,. \tag{5.28}$$

In order for $\boldsymbol{C}$ not to vanish in the static limit, $\nu \leq 0$ has to hold. For $\boldsymbol{B}$ not to vanish, on the other hand, $\nu \geq 2$ has to hold. Since both conditions cannot be satisfied at the same time, either $\boldsymbol{C}$ or $\boldsymbol{B}$ or both vanish for $k \to 0$ independent of the RHS. For the case $w > \mathcal{O}(k^2)$, we find $\boldsymbol{B} = \mathcal{O}(1)$ and $\boldsymbol{C} = \mathcal{O}(k^2)$, and for the case $w < \mathcal{O}(1)$, we find $\boldsymbol{B} = \mathcal{O}(k^2)$ and $\boldsymbol{C} = \mathcal{O}(1)$. Thus, for all possible excitation scalings, $\boldsymbol{D}_1\boldsymbol{T}_{\Lambda H\Sigma}\boldsymbol{D}_2$ is at least block triangular (if not block diagonal). In consequence, for the determinant $\det(\boldsymbol{D}_1\boldsymbol{T}_{\Lambda H\Sigma}\boldsymbol{D}_2) = \det(\boldsymbol{A})\det(\boldsymbol{D})$ holds, which shows that the eigenvalues are solely determined by $\boldsymbol{A}$ and $\boldsymbol{D}$. As $\boldsymbol{A}$ and $\boldsymbol{D}$ are known to have positive eigenvalues [Steinbach 2008], so does $\boldsymbol{D}_1\boldsymbol{T}_{\Lambda H\Sigma}\boldsymbol{D}_2$ (for $k \to 0$). This property is, in general, beneficial as it leads to faster convergence for typical Krylov subspace methods [Saad 2003, pp. 205ff].

5.2.3 Quasi-Helmholtz Projectors

Similarly, for the quasi-Helmholtz projectors, we introduce [Adrian et al. 2021]

$$C = \sqrt{\frac{\|\boldsymbol{T}_\Phi\|}{\|\boldsymbol{P}_{\Lambda H}\boldsymbol{T}_{\mathrm{A}}\boldsymbol{P}_{\Lambda H}\|}} \tag{5.29}$$

to improve the overall condition number. Since the imaginary constants were demonstrated to be irrelevant for the significant digits in Section 5.1.3 (due to the new normalization scheme), imaginary constants can again be placed to improve the eigenvalue distribution. That this leads to positive eigenvalues in the static limit also for the quasi-Helmholtz projected EFIE, can be shown by using the block triangular nature of $\boldsymbol{D}_1\boldsymbol{T}_{\Lambda H\Sigma}\boldsymbol{D}_2$ for $k \to 0$ as starting point. Defining the matrix

$$\boldsymbol{G} = [\boldsymbol{\Lambda}(\boldsymbol{\Lambda}^{\mathrm{T}}\boldsymbol{\Lambda})^{-1/2}\ \boldsymbol{H}^{\mathrm{T}}(\boldsymbol{H}^{\mathrm{T}}\boldsymbol{H})^{-1/2}\ \boldsymbol{\Sigma}(\boldsymbol{\Sigma}^{\mathrm{T}}\boldsymbol{\Sigma})^{-1/2}] \tag{5.30}$$

and the matrix $\boldsymbol{G}_i = \boldsymbol{G}\boldsymbol{D}_i$, the matrix $\boldsymbol{G}_1^{\mathrm{T}}\boldsymbol{T}\boldsymbol{G}_2$ is also block triangular with positive eigenvalues. Furthermore, we have

$$\boldsymbol{P}_1\boldsymbol{T}\boldsymbol{P}_2 = \boldsymbol{G}\boldsymbol{G}_1^{\mathrm{T}}\boldsymbol{T}\boldsymbol{G}_2\boldsymbol{G}^{\mathrm{T}}\,, \tag{5.31}$$

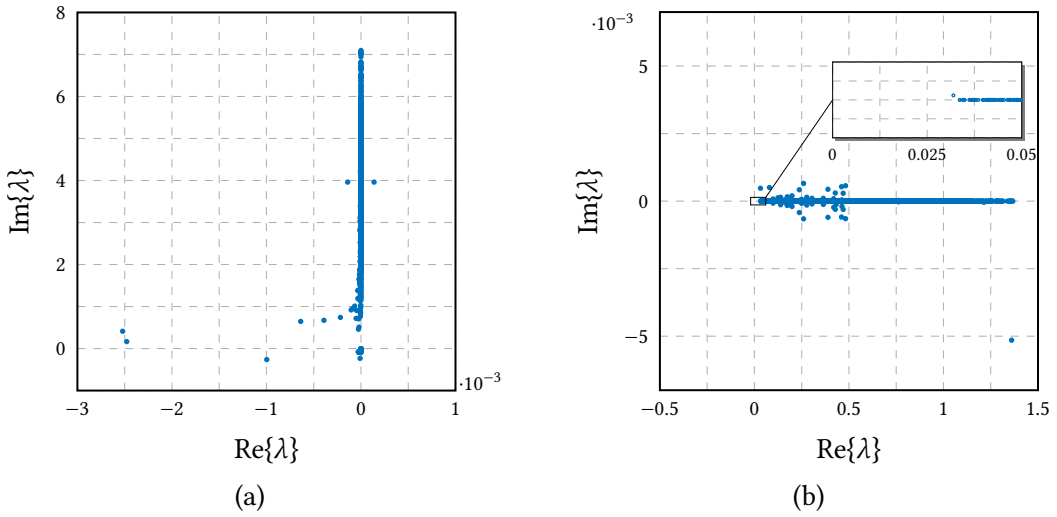

Fig. 5.3: Eigenvalues λ of the projected matrix of a double torus at 10 MHz (a) without and (b) with imaginary constants. © 2023 IEEE

which allows to deduce properties about the eigenvalues λ_i of $\boldsymbol{P}_1\boldsymbol{T}\boldsymbol{P}_2$. Due to the properties of similarity transforms, we have $\lambda_i(\boldsymbol{G}\boldsymbol{G}_1^{\mathrm{T}}\boldsymbol{T}\boldsymbol{G}_2\boldsymbol{G}^{\mathrm{T}}) = \lambda_i(\boldsymbol{G}^{\mathrm{T}}\boldsymbol{G}\boldsymbol{G}_1^{\mathrm{T}}\boldsymbol{T}\boldsymbol{G}_2\boldsymbol{G}^{\mathrm{T}}\boldsymbol{G}^{-\mathrm{T}})$ for $i = 1, \ldots, N$. Using $\boldsymbol{G}^{\mathrm{T}}\boldsymbol{G} = \mathbf{I}$ and $\boldsymbol{G}^{\mathrm{T}}\boldsymbol{G}^{-\mathrm{T}} = \mathbf{I}$, we find

$$\lambda_i(\boldsymbol{P}_1\boldsymbol{T}\boldsymbol{P}_2) = \lambda_i(\boldsymbol{G}_1^{\mathrm{T}}\boldsymbol{T}\boldsymbol{G}_2) \qquad \forall i = 1, \ldots, N, \tag{5.32}$$

from which the positive eigenvalues of $\boldsymbol{P}_1\boldsymbol{T}\boldsymbol{P}_2$ follow for $k \to 0$.

In order to illustrate the impact, the eigenvalues λ_i of the projected matrix $\boldsymbol{P}_1\boldsymbol{T}\boldsymbol{P}_2$ for the example of the double torus in Fig. 5.1 are shown in Fig. 5.3. Only if the imaginary constant is included, we have $\mathrm{Re}\{\lambda_i\} > 0$ and $\mathrm{Im}\{\lambda_i\}$ is close to being zero. If the frequency is decreased further down to the kHz region as depicted in Fig. 5.4, we see that the clustering on the real axis increases further. The influence on the number of iterations for the generalized minimum residual (GMRES) [Saad et al. 1986] solver, the induced dimension reduction (IDR) [Sonneveld et al. 2008] solver, and the stabilized bi-conjugate gradient (BiCGstab) [Sleijpen et al. 1993] solver are summarized in Table 5.4 for the case that the double torus is excited by a Hertzian dipole and a relative residual of $\epsilon_{\mathrm{res}} = 1 \times 10^{-6}$ as stopping criterion. Clearly, the iteration count (reflected by the number of matrix-vector products) is reduced if either the imaginary constant or the constant C is included. The best result is obtained if both constants are used simultaneously as is done in the proposed formulation.

5.3 Numerical Results

To demonstrate the impact of the frequency normalization on the accuracy of the computed scattered and radiated fields, several scenarios are investigated. To this end, we employ the quasi-Helmholtz projectors and compare the standard choice of scaling coefficients, $\alpha_1 = \alpha_2 = \sqrt{C/k}$ and $\beta_1 = \beta_2 = \mathrm{j}\sqrt{k/C}$, where we have included the constant C for a fairer

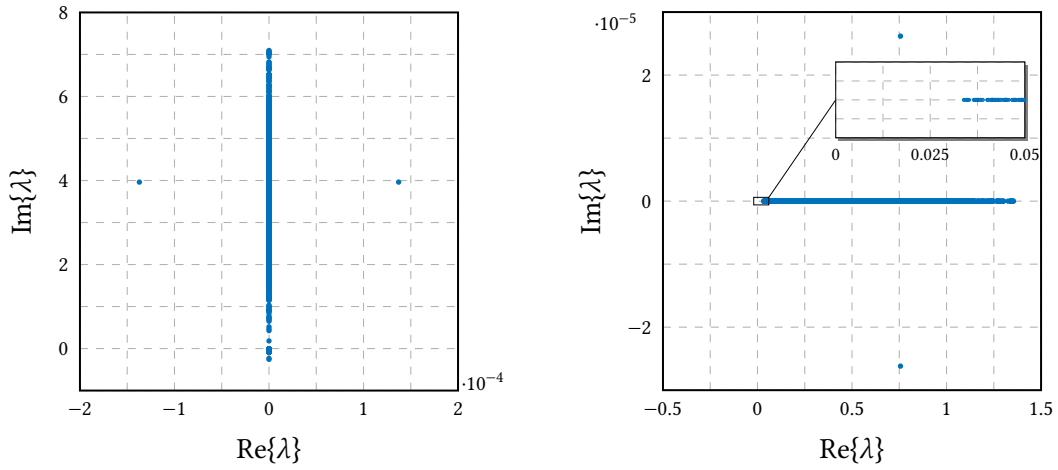

Fig. 5.4: Eigenvalues λ of the projected matrix of a double torus at 1 kHz (a) without and (b) with imaginary constants. © 2023 IEEE

Table 5.4: Number of matrix-vector products for a double torus excited by a Hertzian dipole with and without the inclusion of $\sqrt{\mathrm{j}C}$ in (5.16) and (5.17). © 2023 IEEE

solver	f	loop-star				projector			
		none	$\sqrt{\mathrm{j}}$	$\sqrt{C}$	$\sqrt{\mathrm{j}C}$	none	$\sqrt{\mathrm{j}}$	$\sqrt{C}$	$\sqrt{\mathrm{j}C}$
GMRES	10 MHz	945	761	1140	421	206	171	169	43
	1 kHz	945	761	1140	420	206	170	168	43
	1 Hz	945	761	1140	420	206	170	168	43
IDR(8)	10 MHz	7843	1186	2984	498	263	207	213	49
	1 kHz	8895	1119	2829	499	299	198	213	48
	1 Hz	9220	1142	3294	481	301	203	228	50
BiCGstab(2)	10 MHz	-	1272	-	792	488	312	384	52
	1 kHz	-	1272	-	784	476	264	372	48
	1 Hz	-	1272	-	808	508	296	384	52

comparison with the adaptive ones in (5.22) and (5.23). Again, if not stated otherwise, a GMRES solver is used without restarts and a relative residual of $\epsilon_{\mathrm{res}} = 1 \times 10^{-6}$ as stopping criterion. For the RHS stabilization the approach of Chapter 4 is employed and in order to accelerate the computation, an ACA algorithm is used [Zhao et al. 2005a; Bebendorf 2008] with compression rate 1×10^{-4}. The relative worst-case errors

$$\aleph = \max_{\vartheta,\varphi} \left\{ 20 \log \frac{|a(\vartheta,\varphi) - \hat{a}(\vartheta,\varphi)|}{\max_{\vartheta,\varphi} |a(\vartheta,\varphi)|} \right\}, \tag{5.33}$$

with $a \in \{e, h, e^{\mathrm{FF}}\}$ are computed based on a spherical 5° grid and NF distances of $r = 8$ m.

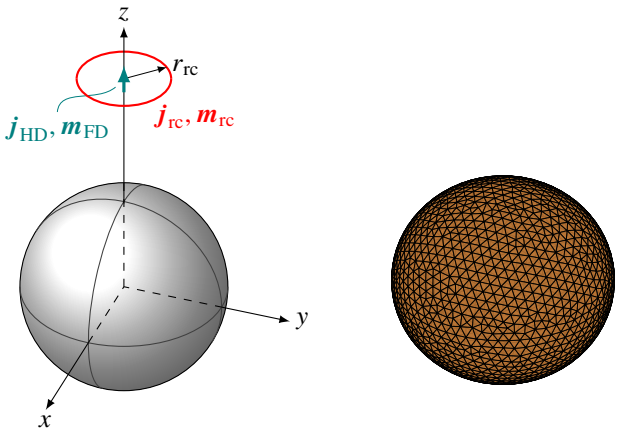

Fig. 5.5: Scattering from a sphere with radius $r_s = 1\,\mathrm{m}$ (a) excitation with dipoles and ring currents at position $z = 2\,\mathrm{m}$ and radius $r_{rc} = 0.5\,\mathrm{m}$; (b) discretized with 3214 triangles and 4821 RWGs. © 2023 IEEE

5.3.1 Scattering from a Sphere

We start with scattering from the sphere shown in Fig. 5.5, where series expansions are used as reference (see [Jin 2015, pp. 368 ff.] and [Hofmann et al. 2023e; Hofmann 2022f] for implementation details). The results for different excitations are depicted in Fig. 5.6. For a plane-wave excitation, the standard normalization is sufficient to determine all fields for the whole frequency range correctly. Figure 5.6 (b) shows that the adaptive normalization maintains this property. This is as expected: for the plane wave both schemes recover all current components with a similar relative accuracy.

Considering next the excitation by a Hertzian dipole, Fig. 5.6 (c) evidences that the adaptive frequency normalization removes an otherwise occurring breakdown in accuracy of the magnetic NF below 1 MHz. That specifically the magnetic NF is affected corresponds well with the preceding analysis (see especially Section 5.1.1): as an incorrect solenoidal current component is recovered, only the magnetic NF is affected in accordance with Table 5.1. Also depicted is the accuracy of an ad-hoc adaption technique using the projectors $\boldsymbol{P} = \boldsymbol{P}_1 = \boldsymbol{P}_2$ from [Andriulli et al. 2013] with $\alpha_1 = \alpha_2 = \sqrt{C/k}$ and $\beta_1 = \beta_2 = \mathrm{j}\sqrt{k/C}$. The ad-hoc technique requires that two LSEs are solved. More precisely, as $\|\mathrm{Re}\{\boldsymbol{PTP}\}\| \ll \|\mathrm{Im}\{\boldsymbol{PTP}\}\|$ for low frequencies, the two real valued systems

$$-\mathrm{Im}\{\boldsymbol{PTP}\}\mathrm{Im}\{\boldsymbol{j}'\} = \mathrm{Re}\{\boldsymbol{Pe}^{\mathrm{ex}}\} \tag{5.34}$$

and

$$\mathrm{Im}\{\boldsymbol{PTP}\}\mathrm{Re}\{\boldsymbol{j}'\} = \mathrm{Im}\{\boldsymbol{Pe}^{\mathrm{ex}}\} \tag{5.35}$$

are solved. Depending on the specific dominant components of the excitation (see Table 5.3) only $\mathrm{Re}\{\boldsymbol{j}'\}$ or $\mathrm{Im}\{\boldsymbol{j}'\}$ is used to determine $\boldsymbol{j}_{\mathrm{sol,hsol}}$ and in an analogue fashion to determine $\boldsymbol{j}_{\mathrm{nsol}}$. While this approach also removes the breakdown below 1 MHz it introduces a breakdown when going above that frequency. A similar behavior is observed for the electric ring

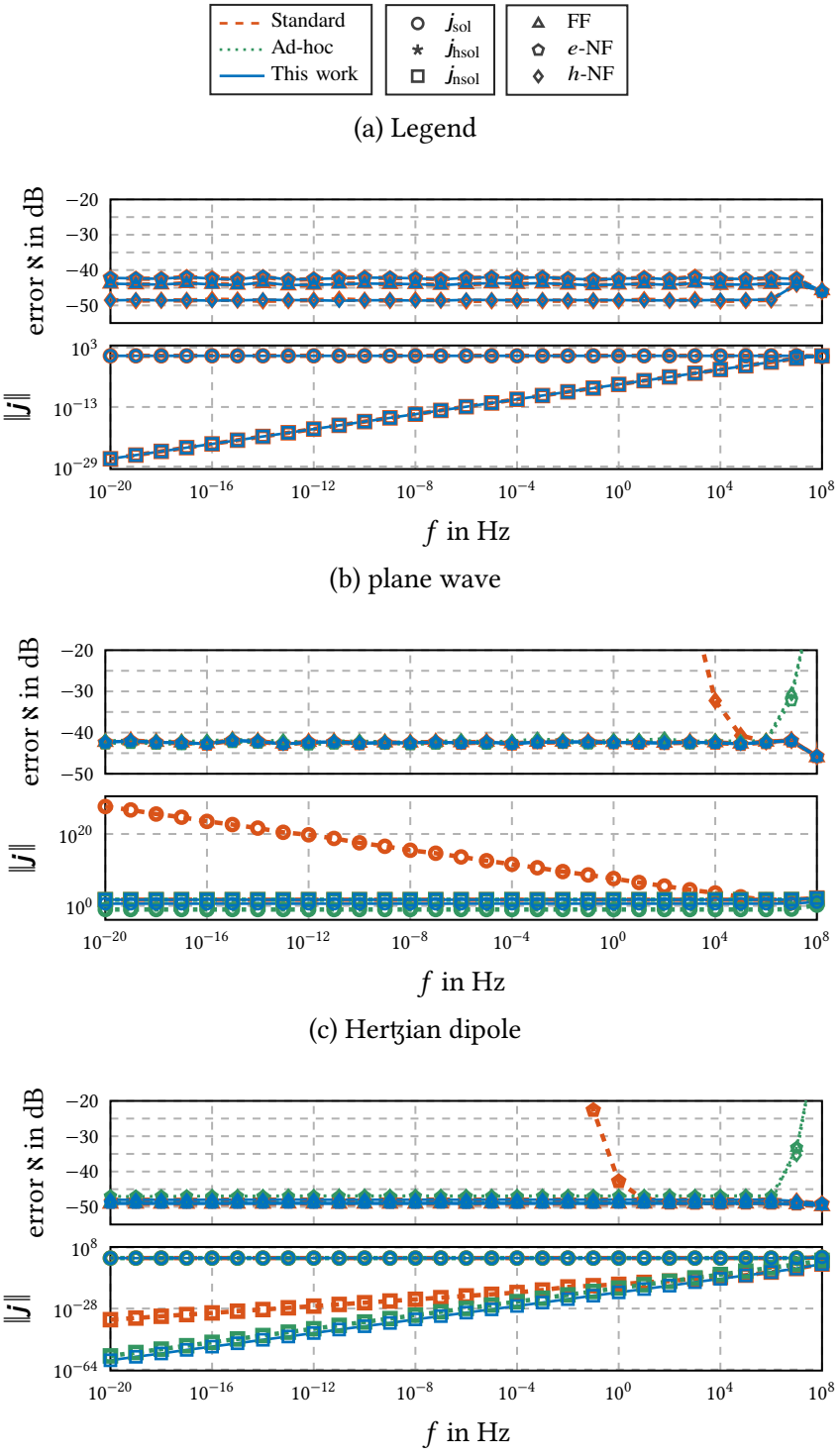

(a) Legend

(b) plane wave

(c) Hertzian dipole

(d) electric ring current

Fig. 5.6: Scattering from a sphere: worst case errors of the FF, the electric, and the magnetic NF, as well as the scaling of the current components. © 2023 IEEE

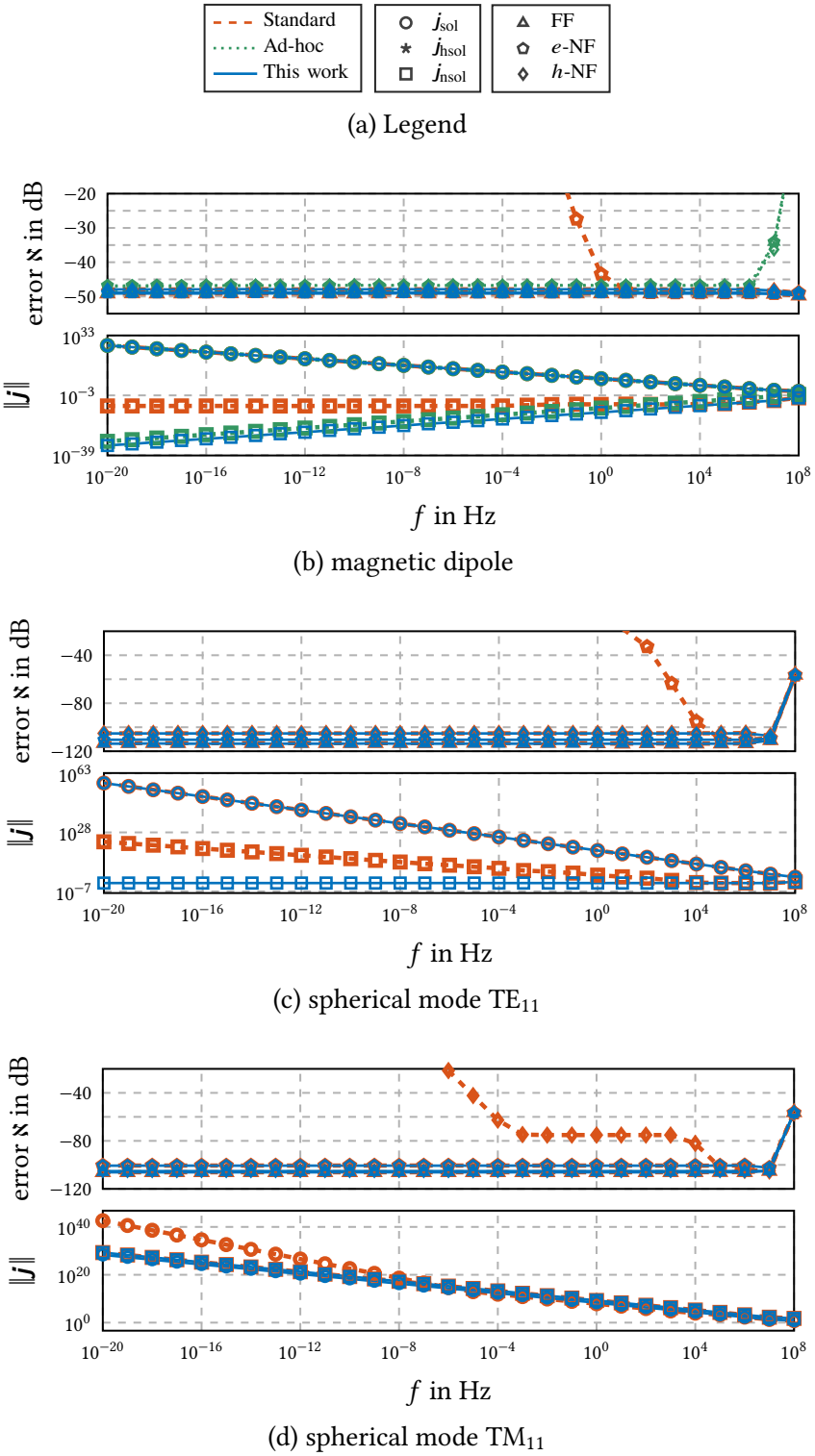

(a) Legend

(b) magnetic dipole

(c) spherical mode TE_{11}

(d) spherical mode TM_{11}

Fig. 5.7: Scattering from a sphere: worst case errors of the FF, the electric, and the magnetic NF, as well as the scaling of the current components. © 2023 IEEE

current as depicted in Fig. 5.6 (d) and the magnetic dipole in Fig. 5.7 (b). The errors in the current components correspond to the fields as predicted in Table 5.1, and only the adaptive normalization (in addition to a stabilized RHS) fully removes the issues for all fields and for arbitrarily low frequencies.

The same is true for the spherical mode excitations TE_{11} and TM_{11} as shown in Fig. 5.7 (c) and (d), respectively. Note that the ad-hoc approach is not possible in this case but only the adaptive normalization can overcome the problem.

As the analysis so far showed that the problem lies in an insufficient accuracy of the solution components, another investigation is conducted for the sphere excited by a magnetic dipole: we vary the relative residual ϵ_{res} of the GMRES solver. In this numerical experiment, the ACA is not used and we employ $C = 1$ (to emphasize the effect of the residual). The results for the standard normalization in Fig. 5.8 (a) reveal that indeed by lowering the residual, the breakdown can be shifted to lower frequencies. However, even when employing a direct solver (LU-decomposition), the breakdown cannot be fully avoided. For large problems, iterative solvers become the only option; a typical choice for ϵ_{res} is around 1×10^{-3} to 1×10^{-4}. This underlines the importance for using an adaptive normalization as shown in Fig. 5.8 (b), where we see that the error in the solution is dominated by the geometric approximation and discretization and not by the stopping criterion. Furthermore, the number of iterations remains constant when decreasing the frequency, whereas the iteration count for the standard normalization decreases with decreasing frequency: with the standard normalization only the solenoidal component is recovered, however, not the non-solenoidal component. Hence, the iterative solver only determines a part of the unknowns sufficiently accurately, but stops too early for the remaining unknowns resulting in the erroneous electric NF. Also note that separate residuals for solenoidal and non-solenoidal components are not possible (as the non-solenoidal component of the RHS depends on all current components) and if so, would lead to longer convergence times. Similarly, real and imaginary part of the RHS depend each on the real and the imaginary part of the current, thus, preventing a separate residual for real and imaginary part of the current without an approximation.

5.3.2 Scattering from Multiply-Connected Geometries

To validate our formulation also for multiply-connected geometries, we consider the double torus in Fig. 5.1 for a plane-wave and a Hertzian dipole excitation. The results in Fig. 5.9 demonstrate the effectiveness of our approach.

The results for the (PEC) model of a Fokker Dr.I shown in Fig. 5.10 excited by a Hertzian dipole in Fig. 5.11 highlight again that the breakdown in accuracy can occur at relatively high frequencies but is fully overcome by the proposed scheme.

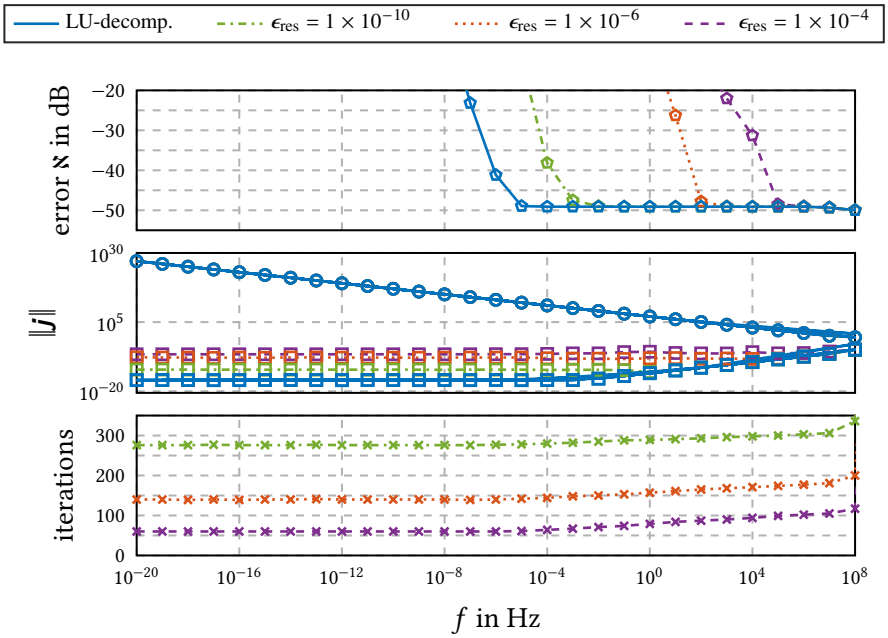

(a) standard normalization

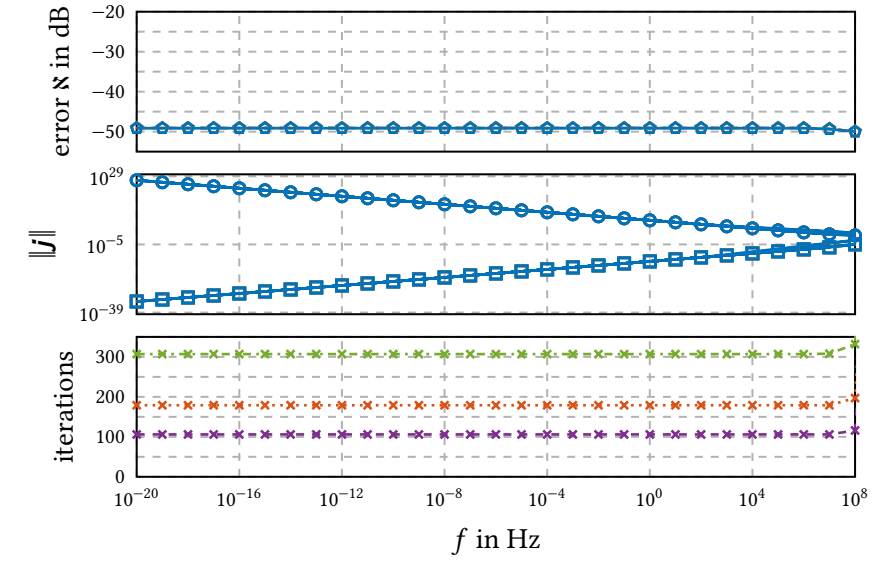

(b) this work: adaptive normalization

Fig. 5.8: Scattering from a sphere excited by a magnetic dipole using the standard and the adaptive frequency normalization employing different solvers: an LU-decomposition and GMRES with different relative residuals ϵ_{res}. Only the electric NF error is shown, no ACA is employed and $C = 1$. © 2023 IEEE

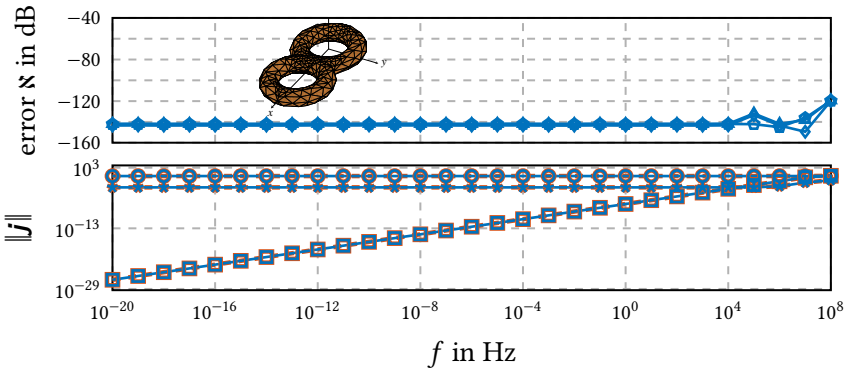

(a) plane wave

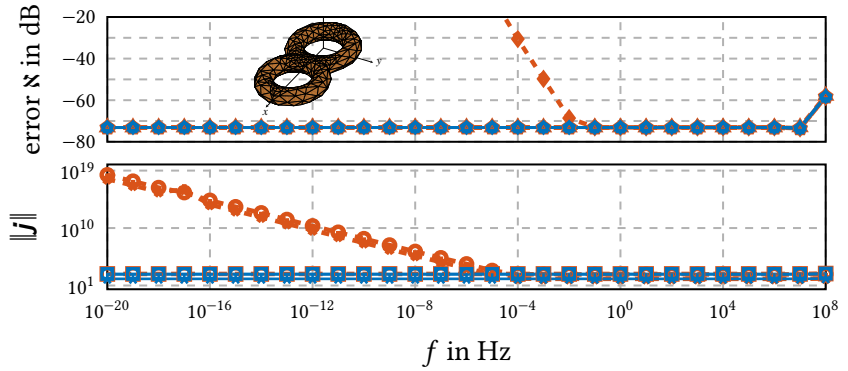

(b) Hertzian dipole

Fig. 5.9: Scattering from a double torus: worst case errors of the FF, the electric, and the magnetic NF, as well as the scaling of the current components for different excitations. The HD is placed at $x = 0.8\,\mathrm{m}$ and no ACA is used. © 2023 IEEE

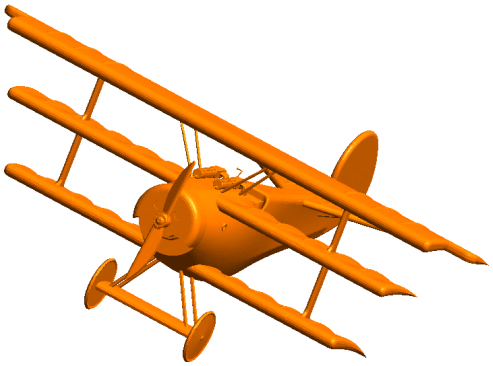

Fig. 5.10: Model of a Fokker Dr.I with an approximate wingspan of 7 m. The model is discretized with 196 280 triangles and 294 420 RWGs. © 2023 IEEE

5.3.3 Inductive and Capacitive Gap Excitation

As a last example, we consider the voltage gap excitation of the capacitive and the inductive structure depicted in Fig. 5.12. The capacitive structure consists of two plates of size 1 m ×

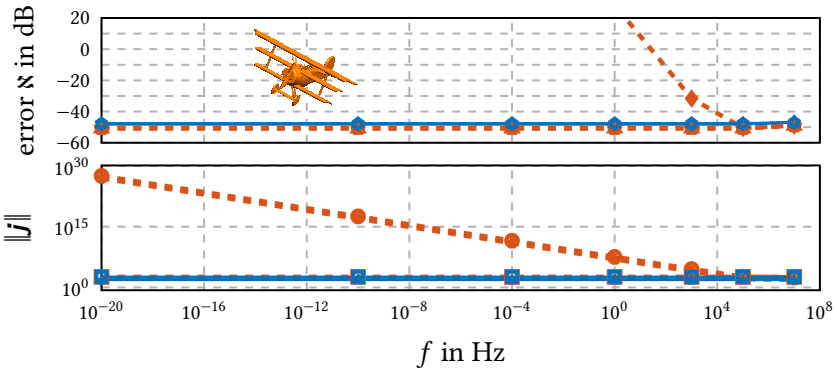

Fig. 5.11: Scattering from the model of a Fokker Dr.I excited by a Hertzian dipole. © 2023 IEEE

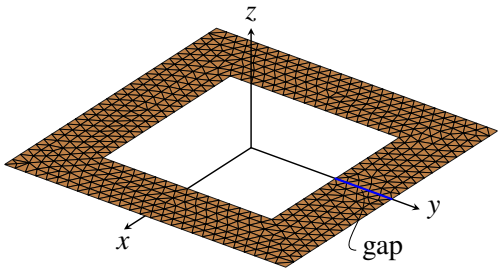

(a) inductive

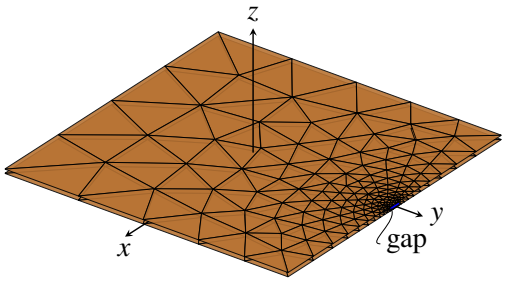

(b) capacitive

Fig. 5.12: Inductive and capacitive structure excited by voltage gaps (location highlighted in blue) (a) along positive y-axis and (b) in xy-plane. © 2023 IEEE

1 m separated by 0.01 m, where the non-uniformity of the mesh originates from the small size of the strip connecting the two plates. The inductive structure is a 1 m × 1 m ring with 0.25 m width. A comparison to the radiated fields when using the standard normalization is shown in Fig. 5.13. Clearly, for both structures only the adaptive scheme yields the physically correct scalings of the current components as given in Table 5.3. For the inductive structure, the non-solenoidal current is incorrect resulting in a difference in the electric NF. Dually, for the capacitive structure, the solenoidal current is incorrect resulting in a difference in the magnetic NF, all in accordance with Table 5.1. The determined inductivity of 964.3 nH agrees well with the 962.5 nH from a quasistatic simulation in Computer Simulation Technology Microwave Studio (CST MWS) [CST Computer Simulation Technology

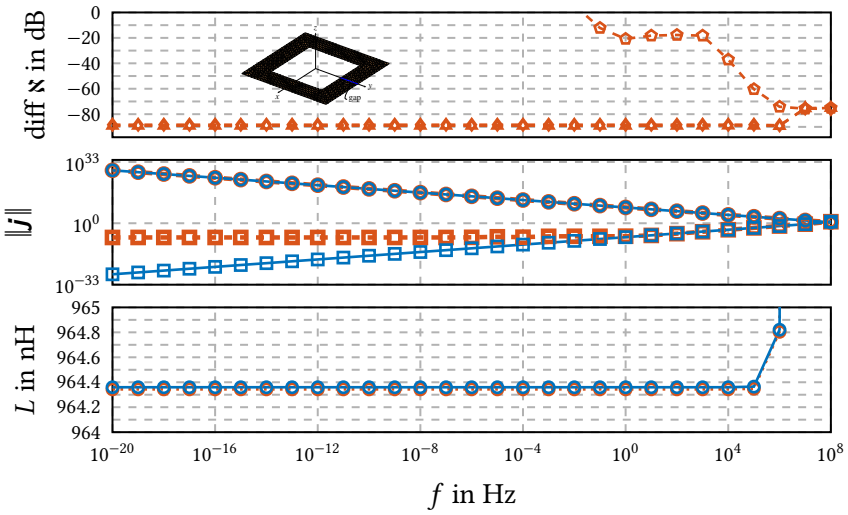

(a) inductive

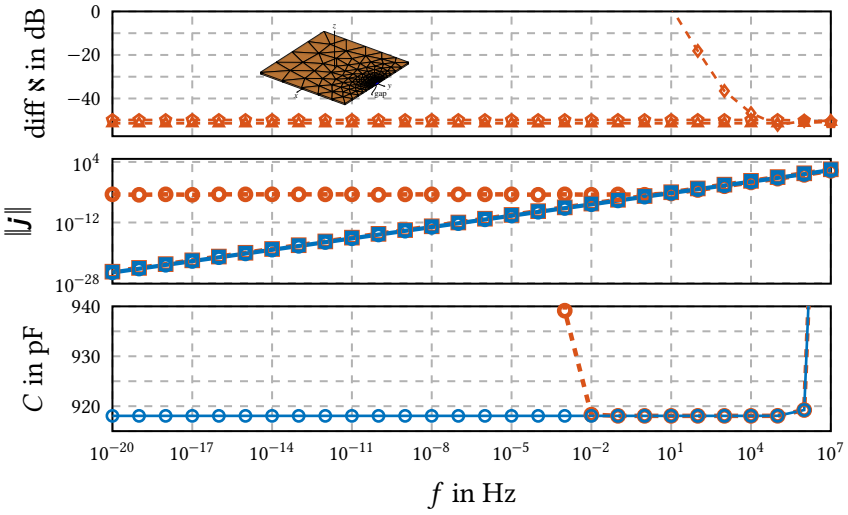

(b) capacitive

Fig. 5.13: Radiation from an inductive and a capacitive structure excited by a voltage gap excitation: comparison between the standard and the adaptive normalization scheme. © 2023 IEEE

2022]. Analogously, the determined capacitance of 918.05 pF agrees well with the 917.65 pF from an electrostatic simulation in CST MWS.

5.4 Conclusion

We have shown that scaling coefficients in the quasi-Helmholtz preconditioners, which lead to a well-conditioned impedance matrix, do not necessarily lead to current solutions that allow an accurate determination of all fields. In fact, despite a well-conditioned matrix, the current components are in general solved for with different relative accuracies, which is for

general excitations not sufficient. The numerical results demonstrated that the proposed adaptive frequency normalization method effectively resolves this effect for all excitations considered and, thus, allows for the accurate computation of near and far fields. In fact, depending on the structure and the specific excitation, standard approaches lead to inaccurately computed fields already in the MHz region, whereas with the proposed method, the scattered and radiated fields can be determined correctly with an overall reduced number of iterations down to the static limit. Given our theoretical considerations and the wide range of studied excitations, we conclude that our method can stabilize the EFIE in the presence of arbitrary excitations.

6

A Low-Frequency Stabilization for the B-Spline-Based Isogeometric Discretization

> "Some years ago a few researchers joked about NURBS, saying that the acronym really stands for nobody understands rational B-splines..."
>
> [Piegl 1995]

In order to low-frequency stabilize the EFIE when discretized with divergence conforming B-spline based basis and testing functions in an isogeometric approach, a corresponding quasi-Helmholtz preconditioner is proposed. To this end, we derive i) a loop-star decomposition for the B-spline basis in the form of sparse mapping matrices applicable to arbitrary polynomial orders of the basis as well as to open and closed geometries described by single- or multipatch parametric surfaces (as an example non-uniform rational B-splines (NURBS) surfaces are considered). Based on the loop-star analysis, it is shown ii) that quasi-Helmholtz projectors can be defined efficiently. This renders the proposed low-frequency stabilization directly applicable to multiply-connected geometries without the need to search for global loops and results in better-conditioned system matrices compared to directly using the loop-star basis. Numerical results demonstrate the effectiveness of the proposed approach.

This chapter is based on [Hofmann et al. 2024c] including substantial verbatim portions, where the first two authors share the first authorship: The first author had major contributions to the conceptual design, formal analysis, wrote the original draft of the article, created the figures and tables, and contributed several of the results. The second author had major contributions to the conceptual design, formal analysis, and the results. Preliminary results were presented in [Mirmohammadsadeghi et al. 2024; Hofmann et al. 2024d].

To solve the EFIE for the induced surface current density, the in the previous chapters employed discretization strategy to approximate the surface of the structure by a mesh and then expand the current into basis functions defined on that mesh, is a common approach. The divergence-conforming RWG functions (3.14) and higher-

order versions thereof (e.g., [Peterson et al. 1995; Graglia et al. 1997; Peterson 2006]) are widely employed.

Yet, the underlying mesh representation typically introduces a geometrical discretization error. In order to overcome this drawback, isogeometric methods have been proposed first in the context of structural mechanics [Hughes et al. 2005] and later also in other areas such as flow simulations [Bazilevs et al. 2007] or shell analysis [Kiendl et al. 2010]. The fundamental idea is to use an exact geometry description via parametric representations, for example, by NURBS or subdivision surfaces, and to use the same or a similar representation to approximate the unknowns of the equation to be solved.

In the context of electromagnetics, this has been analyzed first for FEMs in [Buffa et al. 2010; Veiga et al. 2014; Buffa et al. 2014a]. Specifically for the EFIE, approaches using B-spline representations have been proposed in [Buffa et al. 2014b; Simpson et al. 2018] with optimal convergence rate guarantees proven in [Dölz et al. 2019; Buffa et al. 2020] and numerical comparisons with higher-order RWG discretizations confirming the convergence behavior of the approach in [Dölz et al. 2020]. Investigations on a formulation similar to the PEEC method have been presented in [Nolte et al. 2023a; Nolte et al. 2023b]. An approach for the EFIE based on subdivision surfaces and basis functions derived from them has been given in [Li et al. 2016; Alsnayyan et al. 2023].

The latter approach directly addresses the low-frequency breakdown, where, in contrast to the quasi-Helmholtz decompositions employed in this work, in [Alsnayyan et al. 2023] not a quasi but a full Helmholtz decomposition is established which is facilitated by the assumption of a $\mathcal{C}^1$-continuity of the employed surface description. Also for higher order bases, approaches have been presented [Wildman et al. 2004; Jose Ma 2012]. For the B-spline based isogeometric modeling of the EFIE, however, no low-frequency stabilization is available.

In this chapter, such a low-frequency stable discretization of an EFIE is presented that is discretized with B-splines of arbitrary polynomial orders via the framework of quasi-Helmholtz projectors. To obtain the quasi-Helmholtz projectors for a B-spline basis, we first derive loop and star transformation matrices as the fundamental building blocks for the projectors. In particular, we ensure that the transformation matrices can be interpreted as incidence matrices of an equivalent graph which, in turn, ensures that the projectors can be efficiently computed. In doing so, and in contrast to existing quasi-Helmholtz decompositions for higher-order bases, we maintain all the advantages known from RWG discretizations for arbitrary polynomial orders. The presented approach is applicable to open and closed, simply- and multiply-connected geometries, where as a description for the geometries we consider single- and multi-patch NURBS surfaces but other parametric descriptions fit into the employed framework as well. Numerical results for both canonical and realistic geometries corroborate the effectiveness of this strategy.

To this end, this chapter is organized as follows: Section 6.1 introduces the background material about the isogeometric discretization of the EFIE fixing the notation. In Section 6.2,

the corresponding loop-star mapping matrices are derived for single- and multi-patch descriptions of the basis. The relation to quasi-Helmholtz projectors is established in Section 6.3 and numerical results are presented in Section 6.4 before a conclusion is given.

6.1 Isogeometric Discretization of the Electric Field Integral Equation

As the discretization strategy and the considered geometry description are based on B-splines we start by briefly repeating their definition.

6.1.1 Definition of the B-splines

The B-splines are functions of the real variable[1] $u \in [0,1]$. The partitioning of this unit interval is fundamental for the definition of the B-splines and is called knot vector.

The Knot Vector

The M entries $u_i \in [0,1]$ (the knots) of the knot vector

$$U = \{u_1, \dots, u_M\} \tag{6.1}$$

are sorted in ascending order, i.e., $u_i \leq u_{i+1}$ with $u_1 = 0$ and $u_M = 1$. Moreover, the first and last entry are each repeated $p+1$ times (they have a multiplicity of $r = p+1$) which defines a so called p-open knot vector [Piegl 1995, p. 66].

Recursive Definition

The ith B-spline basis functions $B_i^p(u)$ of degree $p \geq 0$ is defined on the knot vector U recursively, starting with the piecewise constant ($p = 0$) [Cox 1972; de Boor 1972; Piegl 1995, p. 50]

$$B_i^0(u) = \begin{cases} 1 & u_i \leq u < u_{i+1} \\ 0 & \text{otherwise} \end{cases} \tag{6.2}$$

and for $p > 0$ we have

$$B_i^p(u) = \frac{u - u_i}{u_{i+p} - u_i} B_i^{p-1}(u) + \frac{u_{i+p+1} - u}{u_{i+p+1} - u_{i+1}} B_{i+1}^{p-1}(u)\,. \tag{6.3}$$

[1] The restriction of u to the unit interval is not necessary, but makes the notation more concise.

Whenever one of the contained quotients exhibits a division by zero, the quotient is by convention defined to be zero itself. For a given knot vector with M entries, the number of B-splines of degree p is given by [Piegl 1995, p. 66]

$$N = M - p - 1\,. \tag{6.4}$$

Each basis function has only local support, that is, it is only different from zero in the interval $[u_i, u_{i+p}]$ and due to the assumption of an open knot vector $B_1^p(0) = B_N^p(1) = 1$.

As a normalized version of the B-splines the Curry-Schoenberg splines are defined as [Boor 2001, p. 88]

$$b_i^p(u) = \frac{p+1}{u_{i+p+1} - u_i} B_i^p(u)\,, \tag{6.5}$$

where again, by convention, for the case that the denominator in (6.5) becomes zero, we define $b_i^p(u) \coloneqq 0$.

Derivatives

The first derivative of $B_i^p(u)$ can be expressed concisely in terms of the Curry-Schoenberg splines as [Piegl 1995, p. 59]

$$\partial_u B_i^p(u) = b_i^{p-1}(u) - b_{i+1}^{p-1}(u)\,. \tag{6.6}$$

In order for this expression to be meaningful, the multiplicity r of the knots in (6.1) has to be smaller than p since at a knot, the spline B_i^p is $p - r$ times continuously differentiable [Piegl 1995, p. 57].

6.1.2 Geometry Representation

As discussed in Section 3.1.1 the surface Γ of the PEC structure shall be represented by a union of A non-overlapping surfaces Γ_a. The mapping from the parametric space $\hat{\Gamma}_a = (u, v) \in [0, 1]^2$ to the physical space $\Gamma_a \subset \mathbb{R}^3$ can now be described in terms of B-splines as [Hughes et al. 2005], [Piegl 1995, Chapter 4.4]

$$\boldsymbol{s}_a(u, v) = \frac{\sum_{i=1}^{N_u^a} \sum_{j=1}^{N_v^a} B_i^{a,q_u}(u)\, B_j^{a,q_v}(v)\, w_{ij}^a\, \boldsymbol{p}_{ij}^a}{\sum_{i=1}^{N_u^a} \sum_{j=1}^{N_v^a} B_i^{a,q_u}(u)\, B_j^{a,q_v}(v)\, w_{ij}^a} \tag{6.7}$$

with N_u^a and N_v^a B-spline basis functions B_i^{a,q_u} and B_j^{a,q_v} of polynomial degree $q_u, q_v \in \{0, 1, 2, \dots\}$, weights $w_{ij}^a \in \mathbb{R}_+$, and control points $\boldsymbol{p}_{ij}^a \in \mathbb{R}^3$ all on suitable knot vectors $U_\Gamma^a = \{u_1, u_2, \dots, u_{M_\Gamma}\}$

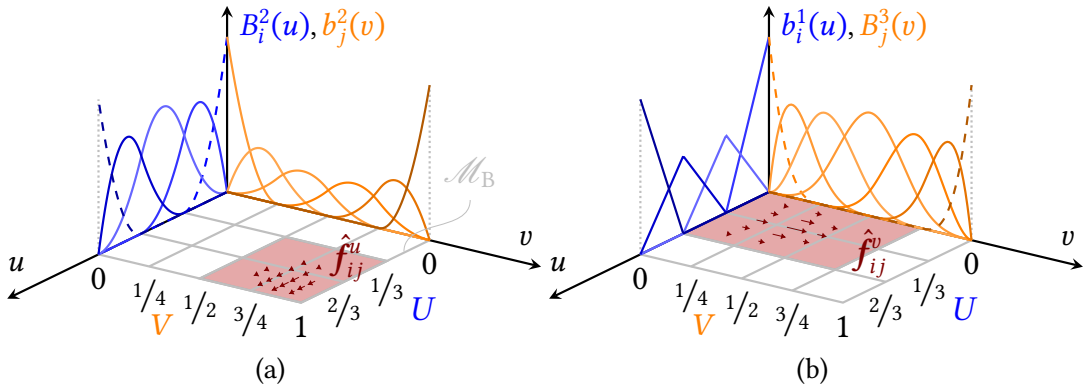

Fig. 6.1: Definition of the basis functions on a single patch a in the $\hat{\boldsymbol{e}}_u$ direction and b in the $\hat{\boldsymbol{e}}_v$ direction on the knot vectors $U = \{0,0,0,1/3,2/3,1,1,1\}$ and $V = \{0,0,0,0,1/4,1/2,3/4,1,1,1,1\}$ with $p_u = 2$ and $p_v = 3$ resulting in $N_u = 5$, $N_v = 7$ and a total of $N = 38$ basis functions. © 2024 IEEE

and $V_\Gamma^a = \{v_1, v_2, \dots, v_{M_\Gamma}\}$ with $u_i, v_i \in [0,1]$. Since (6.7) is a rational function of u and v defined via the tensor product of B-splines, it is called NURBS surface. The computation of the Jacobi matrix $\boldsymbol{J}_a(u,v)$ of (6.7) and the generalized determinant $D_a(u,v)$ is summarized in Appendix B.

While, in principle, other (nonsingular and invertible) mappings $\boldsymbol{s}_a(u,v) : [0,1]^2 \mapsto \Gamma_a$ can also be employed [Dölz et al. 2019], the rational nature of (6.7) makes it more flexible than descriptions based on (e.g., Lagrangian or Hermitian) polynomials (see, e.g., [Peterson 2006, pp. 9ff]). For example, the surface of spheres, ellipsoids, hyperboloids, paraboloids, circular cylinders, and circular cones can only be described exactly, by employing rational functions such as done by a NURBS description [Piegl 1995, pp. 333ff].

6.1.3 Discretization

As B-spline based (divergence conforming) basis functions we consider the ones introduced in [Veiga et al. 2014, Section 5] and similar to [Simpson et al. 2018], that is, analogous to (3.12)

$$\boldsymbol{f}_n(\boldsymbol{r}) = \boldsymbol{f}_{ij}^d(\boldsymbol{r}) = \frac{\boldsymbol{J}(u,v)}{D(u,v)} \hat{\boldsymbol{f}}_{ij}^d(u,v) \tag{6.8}$$

with the basis function[2] $\hat{\boldsymbol{f}}_{ij}^d(u,v) \in \mathbb{R}^2$ defined in the parametric domain $(u,v) \in [0,1]^2$ pointing in the unit direction $\hat{\boldsymbol{e}}_d$, with the freely selectable index mappings $i = i(n)$, $j = j(n)$, and $d = d(n) \in \{u,v\}$. The definition of the $\hat{\boldsymbol{f}}_{ij}^d(u,v)$ with an exemplified illustration in Fig. 6.1 is as follows:

[2] The reader shall be reminded, that the parametric counterpart to a vector $\boldsymbol{g}$ or a scalar g in the physical domain is be denoted with a hat as $\hat{\boldsymbol{g}}$ or $\hat{g}$.

Single-Patch Domain

For the case that Γ is described by a single patch (i.e., $a \in \{1\}$ in (6.7)), we introduce N_u B-splines $B_i^{p_u}(u)$ of polynomial degree $p_u \in \{0, 1, 2, \dots\}$ along the parameter u based on a p_u-open knot vector U of length M_u and maximum multiplicity $p_u - 1$ for the internal knots (which also for a NURBS description of Γ is independent of U_Γ). Analogously, the B-splines $B_j^{p_v}(v)$ of polynomial degree $p_v \in \{0, 1, 2, \dots\}$ are introduced on the p_v-open knot vector $V = \{v_1, v_2, \dots, v_{M_v}\}, v_i \in [0, 1]$ with maximum multiplicity $p_v - 1$. The unique entries of U and V form then the Bézier mesh $\mathscr{M}_\mathrm{B}$ as shown in Fig. 6.1. The supports of the B-splines start and end always at an edge of $\mathscr{M}_\mathrm{B}$. In addition, the Curry-Schoenberg splines $b_i^{p_u}(u)$ and analogously $b_j^{p_v}(v)$ are defined on the same knot vectors U and V, respectively. The incorporation of the Curry-Schoenberg splines into the definition of the basis functions will lead to a particularly simple form of the loop and star mapping matrices as further detailed in Section 6.2 (similar to the special edge length normalization of RWG functions [Rao et al. 1982] as employed in [Andriulli et al. 2013]).

The actual basis functions $\hat{\boldsymbol{f}}_{ij}^{d}(u, v)$ with $d \in \{u, v\}$ are then defined via

$$\hat{\boldsymbol{f}}_{ij}^{u}(u, v) = B_i^{p_u}(u) b_j^{p_v - 1}(v) \hat{\boldsymbol{e}}_u \qquad \begin{matrix} i = 2, 3, \dots, N_u - 1 \\ j = 2, 3, \dots, N_v \end{matrix} \tag{6.9}$$

along the u-direction as well as

$$\hat{\boldsymbol{f}}_{ij}^{v}(u, v) = b_i^{p_u - 1}(u) B_j^{p_v}(v) \hat{\boldsymbol{e}}_v \qquad \begin{matrix} i = 2, 3, \dots, N_u \\ j = 2, 3, \dots, N_v - 1 \end{matrix} \tag{6.10}$$

along the v-direction with $p_u \geq 1$ and $p_v \geq 1$. Note that via the indexing limits, we have removed basis functions which would correspond to current flowing off the boundaries of Γ as well as basis functions that are zero due to the definition of B-splines of polynomial degree $p - 1$ on an open knot vector for degree p. In consequence, there are a total of

$$N = (N_u - 2)(N_v - 1) + (N_u - 1)(N_v - 2) \tag{6.11}$$

basis functions. The entries of the discretized EFIE matrix $\boldsymbol{T}$ in (3.2) can again be obtained as described in Section 3.1.3.

Multi-Patch Domain

For the case that Γ is described by a union of A patches, we still introduce basis functions as defined in (6.9) and (6.10) on each patch. In addition, across each interface between two patches, basis functions normal to the interface are introduced such that normal continuity is ensured based on the requirement that the knot vectors of both patches along the interface are identical [Simpson et al. 2018]: the non-zero basis functions that we have removed in (6.9) and (6.10) by our choice of indexing limits are now used by combining on each interface the "twin" pairs of normal basis functions (while the tangential ones are not

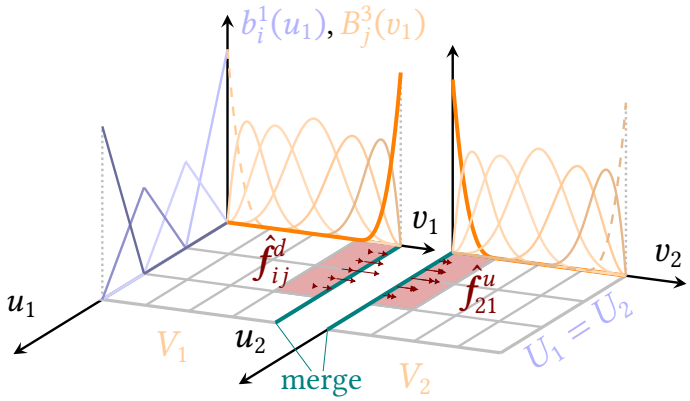

Fig. 6.2: Example of the merging process for functions at the interface of two patches: all (for the single patch excluded) functions normal to the interface are merged, and the tangential functions are left unaltered. © 2024 IEEE

merged) as depicted in Fig. 6.2. In terms of implementation, it has to be ensured that the contributions to the basis function across the interface have the same orientation which can be achieved, for example, via connectivity arrays [Simpson et al. 2018]. The overall number of basis functions can then be expressed as

$$N = \sum_{a=1}^{A} N^a + \sum_{l=1}^{L} N_{\mathrm{ni}}^l \tag{6.12}$$

where N^a denotes the number of basis functions on the ath patch as determined in (6.11), N_{ni}^l denotes the number of basis functions $\hat{f}_{\mathrm{ni},i}^l$ across the lth interface, and L denotes the total number of interfaces.

Greville Mesh

A geometric interpretation of the basis functions, which we will make frequent use of in the following, can be given in terms of the so-called Greville mesh $\mathscr{M}_{\mathrm{G}}$ depicted in Fig. 6.3. The Greville mesh is defined by the Greville sites [Boor 2001, p. 96]

$$\gamma_i^u = \frac{u_{i+1} + \cdots + u_{i+p_u}}{p_u} \qquad i = 1, \ldots, N_u \tag{6.13}$$

along the parametric direction u and analogously γ_j^v along the parametric direction v. As detailed in [Buffa et al. 2014a; Evans et al. 2020], each interior edge of $\mathscr{M}_{\mathrm{G}}$ is associated with exactly one basis function $\hat{f}_m$ (since the Greville sites uniquely correspond to one $B_i^{p_u}$ or $B_j^{p_v}$ and since the Curry-Schoenberg splines $b_i^{p_u}$ and $b_j^{p_v}$ have their polynomial degree reduced by precisely one).

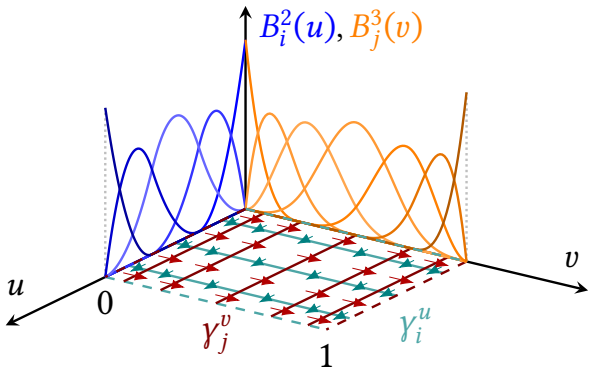

Fig. 6.3: Associating the basis functions to the Greville mesh $\mathscr{M}_\mathrm{G}$ with the Greville sites γ_i^d illustrating the connectivity. © 2024 IEEE

6.2 Loop-Star Decomposition for the Isogeometric Discretization

In order to address the low-frequency breakdown of (3.2), we first derive a corresponding loop-star decomposition (3.26). In consequence, the goal of the following two subsections is to derive the mapping matrices $\boldsymbol{\Lambda}$ and $\boldsymbol{\Sigma}$ for the B-spline discretization in analogy to RWG discretizations. Some properties of the found decomposition and the matrix $\boldsymbol{H}$ will be addressed afterwards. A fundamental relationship we are leveraging to do so is the fact that [Peterson 2006, p. 88]

$$\nabla_\Gamma \cdot \boldsymbol{g} = D^{-1} \nabla_{\hat{\Gamma}} \cdot \hat{\boldsymbol{g}} \,. \tag{6.14}$$

Hence, functions that are (not) divergence free in the parametric domain are also (not) divergence free in the physical domain. Consequently, it suffices to find the loop and star functions in the parametric domain, and the so found corresponding mapping matrices will be the same in the physical domain.

6.2.1 Solenoidal Basis—Loop Mapping Matrix

Recalling that the mapping matrix $\boldsymbol{\Lambda}$ describes how the original basis functions $\hat{\boldsymbol{f}}_n = \hat{\boldsymbol{f}}_{ij}^d$ are superimposed to form loop functions $\hat{\boldsymbol{\Lambda}}_{ij}$ with $\nabla_{\hat{\Gamma}} \cdot \hat{\boldsymbol{\Lambda}}_{ij} = 0$, we have

$$\hat{\boldsymbol{\Lambda}}_r = \hat{\boldsymbol{\Lambda}}_{i_\Lambda(r), j_\Lambda(r)} = \sum_{n=1}^{N} \left[\boldsymbol{\Lambda}^\mathrm{T}\right]_{rn} \hat{\boldsymbol{f}}_n \,, \tag{6.15}$$

with the freely selectable index mappings $i_\Lambda(r)$ and $j_\Lambda(r)$. To find the corresponding $\boldsymbol{\Lambda}$ we start with a single patch.

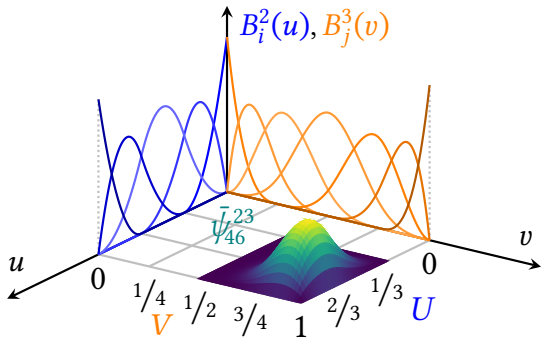

Fig. 6.4: Example of a scalar function $\bar{\psi}_{ij}^{p_u p_v}$ on the Bézier mesh $\mathscr{M}_{\mathrm{B}}$ of a single patch. © 2024 IEEE

Single-Patch Domain

Since by definition $\nabla_{\hat{\Gamma}} \cdot \hat{\boldsymbol{\Lambda}}_r = 0$, every (local) loop can be expressed by the surface gradient of a scalar function ψ_r as [Bladel 1993; Bladel 2007, (A1.65)]

$$\hat{\boldsymbol{\Lambda}}_r = \hat{\boldsymbol{n}} \times \nabla_{\hat{\Gamma}} \psi_r = \begin{bmatrix} -\partial_v \psi_r(u,v) \\ \partial_u \psi_r(u,v) \end{bmatrix} \tag{6.16}$$

with the patch unit normal vector $\hat{\boldsymbol{n}}$. At the same time, the relation to the $\hat{\boldsymbol{f}}_n$ implies that ψ_r has to be a superposition of B-splines on the same knot vectors U and V, that is,

$$\psi_r = \sum_{g=2}^{N_u-1} \sum_{h=2}^{N_v-1} \alpha_{gh}^{ij} B_g^{p_1}(u) B_h^{p_2}(v) := \sum_{g=2}^{N_u-1} \sum_{h=2}^{N_v-1} \alpha_{gh}^{ij} \bar{\psi}_{gh}^{p_1 p_2} \tag{6.17}$$

with an illustration of $\bar{\psi}_{46}^{23}$ shown in Fig. 6.4. Performing the derivatives in (6.16) using (6.6), comparing with (6.9), and identifying $p_1 = p_u$ and $p_2 = p_v$ we see that

$$-\partial_v \psi_r = \sum_{g=2}^{N_u-1} \sum_{h=2}^{N_v-1} \alpha_{gh}^{ij} \left(\hat{\boldsymbol{f}}_{g,h+1}^{u} - \hat{\boldsymbol{f}}_{gh}^{u} \right) \cdot \hat{\boldsymbol{e}}_u \tag{6.18}$$

as well as

$$\partial_u \psi_r = \sum_{g=2}^{N_u-1} \sum_{h=2}^{N_v-1} \alpha_{gh}^{ij} \left(\hat{\boldsymbol{f}}_{gh}^{v} - \hat{\boldsymbol{f}}_{g+1,h}^{v} \right) \cdot \hat{\boldsymbol{e}}_v \,. \tag{6.19}$$

In consequence, the loops with the smallest support are associated with the $\bar{\psi}_{gh}^{p_u p_v}$, which are continuous (i.e., are zero on the boundary of the patch), and the corresponding loops can be expressed as

$$\hat{\boldsymbol{\Lambda}}_{ij} = \hat{\boldsymbol{f}}_{i,j+1}^{u} - \hat{\boldsymbol{f}}_{ij}^{u} + \hat{\boldsymbol{f}}_{ij}^{v} - \hat{\boldsymbol{f}}_{i+1,j}^{v} \qquad \begin{matrix} i = 2, 3, \ldots, N_u - 1 \\ j = 2, 3, \ldots, N_v - 1 \end{matrix} \tag{6.20}$$

where by the indexing limits it is ensured that all four basis functions are different from zero, a necessary requirement to form a valid loop. Choosing loops with larger support is possible, but the $\boldsymbol{\Lambda}$ that we are constructing would become less sparse. Specifically, (6.18) and (6.19) can be understood as a motivation for defining the basis functions in the parametric domain via the Curry-Schoenberg splines as done in (6.9) and (6.10) resulting in the particularly simple representation in (6.20) with the $\alpha_{gh}^{ij} \in \{-1, 0, 1\}$. Otherwise, the α_{gh}^{ij} would have to carry the factors in (6.5). From the indexing limits of $\hat{\boldsymbol{\Lambda}}_{ij}$, it can be seen that there are

$$N_\Lambda = (N_u - 2)(N_v - 2) \tag{6.21}$$

loops. That the so obtained loops in combination with the (yet to be determined) star functions form a valid basis transformation will be shown in Section 6.2.3.

For the sake of simplicity, we assume without loss of generality that the current vector $\boldsymbol{j}$ is sorted such that it first contains the coefficients of the $\hat{\boldsymbol{f}}_{ij}^u$ and then of $\hat{\boldsymbol{f}}_{ij}^v$. Then, considering (6.20), the mapping matrix $\boldsymbol{\Lambda}$ in (3.28) can be expressed as

$$\boldsymbol{\Lambda}^\mathrm{T} = \begin{bmatrix} \boldsymbol{\Lambda}_u^\mathrm{T} & \boldsymbol{\Lambda}_v^\mathrm{T} \end{bmatrix} \in \mathbb{Z}^{N_\Lambda \times N} \tag{6.22}$$

with the matrix $\boldsymbol{\Lambda}_u^\mathrm{T} \in \mathbb{Z}^{N_\Lambda \times (N_u-2)(N_v-1)}$ relating the functions $\hat{\boldsymbol{f}}_{ij}^u$ to the loops as

$$\left[\boldsymbol{\Lambda}_u^\mathrm{T}\right]_{rs} = \begin{cases} 1 & \text{if} \quad i(s) = i_\Lambda(r) \quad \text{and} \quad j(s) = j_\Lambda(r) + 1 \\ -1 & \text{if} \quad i(s) = i_\Lambda(r) \quad \text{and} \quad j(s) = j_\Lambda(r) \\ 0 & \text{else} \end{cases} \tag{6.23}$$

where the index mappings $i(s)$ and $j(s)$ relate the indices i and j of $\hat{\boldsymbol{f}}_{ij}^u$ to the sth basis function and the mappings $i_\Lambda(r)$ and $j_\Lambda(r)$ relate the indices i and j of $\hat{\boldsymbol{\Lambda}}_r = \hat{\boldsymbol{\Lambda}}_{ij}$ to the rth loop depending on the chosen orderings in the coefficient vectors $\boldsymbol{j}$ and $\boldsymbol{j}_\Lambda$, respectively. Analogously, the matrix $\boldsymbol{\Lambda}_v^\mathrm{T} \in \mathbb{Z}^{N_\Lambda \times (N_u-1)(N_v-2)}$ relates the functions $\hat{\boldsymbol{f}}_{ij}^v$ to the loops as

$$\left[\boldsymbol{\Lambda}_v^\mathrm{T}\right]_{rt} = \begin{cases} 1 & \text{if} \quad i(t) = i_\Lambda(r) \quad \text{and} \quad j(t) = j_\Lambda(r) \\ -1 & \text{if} \quad i(t) = i_\Lambda(r) + 1 \quad \text{and} \quad j(t) = j_\Lambda(r) \\ 0 & \text{else} \end{cases} \tag{6.24}$$

for the chosen index mappings.

Sorting, for example, the current coefficients as $\boldsymbol{j} = [\boldsymbol{j}_u \; \boldsymbol{j}_v]^\mathrm{T}$ with

$$\boldsymbol{j}_u = \begin{bmatrix} j_{22}^u & j_{23}^u & \cdots & j_{2N_v}^u & j_{32}^u & \cdots & j_{N_u-1,N_v}^u \end{bmatrix} \tag{6.25}$$

and

$$\boldsymbol{j}_v = \begin{bmatrix} j_{22}^v & j_{23}^v & \cdots & j_{2,N_v-1}^v & j_{32}^v & \cdots & j_{N_u,N_v-1}^v \end{bmatrix} \tag{6.26}$$

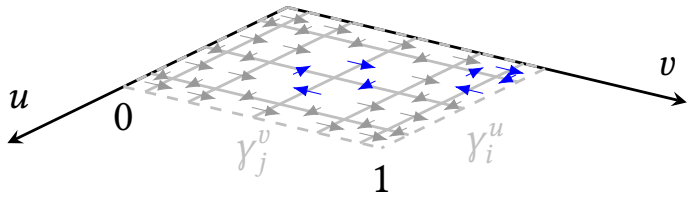

Fig. 6.5: Examples of loops associated with the vertices of the Greville mesh on a single patch. © 2024 IEEE

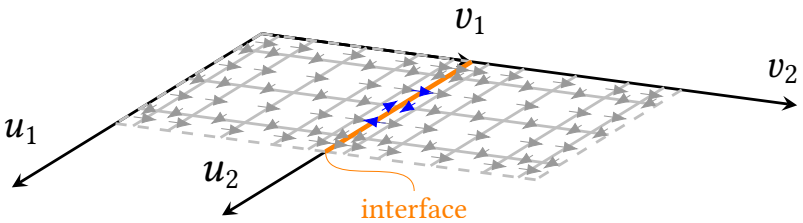

Fig. 6.6: Example of a loop formed at an interface using the additional normal basis functions across the interface between two patches. © 2024 IEEE

the matrices can be expressed as

$$\boldsymbol{\Lambda}_u^{\mathrm{T}} = \begin{bmatrix} \boldsymbol{B} & & \\ & \ddots & \\ & & \boldsymbol{B} \end{bmatrix} \tag{6.27}$$

with the auxiliary matrix

$$\boldsymbol{B} = \begin{bmatrix} -1 & 1 & & \\ & \ddots & \ddots & \\ & & -1 & 1 \end{bmatrix} \in \mathbb{Z}^{(N_v-2)\times(N_v-1)} \tag{6.28}$$

being repeated $N_u - 2$ times on the diagonal and

$$\left[\boldsymbol{\Lambda}_v^{\mathrm{T}}\right]_{rt} = \delta_{rt} - \delta_{r,t-(N_v-2)} \tag{6.29}$$

with δ_{rt} denoting the Kronecker delta.

A particularly intuitive interpretation of the composition of the loop functions $\hat{\boldsymbol{\Lambda}}_{ij}$ with respect to the $\hat{\boldsymbol{f}}_m$ can be given by considering the Greville mesh $\mathscr{M}_{\mathrm{G}}$ as depicted in Fig. 6.5. The loops in (6.20) formed by four basis functions can be identified to circulate around each inner vertex of $\mathscr{M}_{\mathrm{G}}$ involving two consecutive basis functions in u-direction and two consecutive basis functions in v-direction.

Multi-Patch Domain

The interpretation via the Greville mesh directly implies the extension of the loop functions to the multi-patch case: As illustrated in Fig. 6.6 at the interfaces between two patches, we

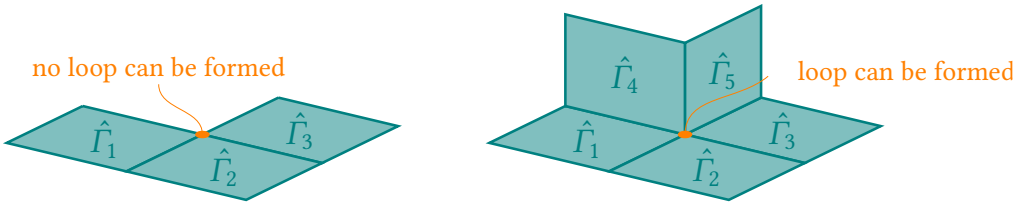

Fig. 6.7: Examples of patch configurations where a loop can be formed around a corner vertex and not. © 2024 IEEE

can form $(N_{\mathrm{ni}}^l - 1)$ additional loops due to the N_{ni}^l additional basis functions $\hat{\boldsymbol{f}}_{\mathrm{ni},i}^l$ across the lth interface. Furthermore, at each of the four corner vertices of a patch an additional loop can be formed, however, only if all the patches sharing the corresponding vertex are attached to each other as illustrated in Fig. 6.7. Hence, there are a total of

$$N_\Lambda = \sum_{a=1}^{A} N_\Lambda^a + \sum_{l=1}^{L} \left(N_{\mathrm{ni}}^l - 1 \right) + N_{\mathrm{c}} \tag{6.30}$$

loops, where N_{c} denotes the number of corner vertices of the patches around which a loop can be formed. The so-obtained loops give rise to a valid basis transformation, as will be shown in Section 6.2.3.

In order to determine the loop mapping matrix for the multi-patch case, we assume that the multi-patch current vector is sorted as

$$\boldsymbol{j} = \begin{bmatrix} \boldsymbol{j}_u^1 & \boldsymbol{j}_v^1 & \boldsymbol{j}_u^2 & \boldsymbol{j}_v^2 & \cdots & \boldsymbol{j}_v^A & \boldsymbol{j}_{\mathrm{ni}} \end{bmatrix}^{\mathrm{T}} \tag{6.31}$$

with the current coefficient vectors of the ath patch $\boldsymbol{j}_u^a$ and $\boldsymbol{j}_v^a$ as defined in (6.25) and (6.26), respectively, and $\boldsymbol{j}_{\mathrm{ni}}$ contains the current coefficients of all $N_{\mathrm{ni}} = \sum_{l=1}^{L} N_{\mathrm{ni}}^l$ normal basis functions on the first up to the Lth interface. In consequence, the multi-patch loop matrix can be expressed as

$$\boldsymbol{\Lambda} = \begin{bmatrix} \boldsymbol{\Lambda}^1 & & & \boldsymbol{\Lambda}_{\mathrm{ti}}^1 & \\ & \ddots & & \vdots & \\ & & \boldsymbol{\Lambda}^A & \boldsymbol{\Lambda}_{\mathrm{ti}}^A & \\ & & & \boldsymbol{\Lambda}_{\mathrm{ni}} & \boldsymbol{\Lambda}_{\mathrm{c}} \end{bmatrix} \in \mathbb{Z}^{N \times N_\Lambda} \tag{6.32}$$

where in accordance with (6.30) the first $\sum_{a=1}^{A} N_\Lambda^a$ columns correspond to the loop basis functions residing completely on single patches expressed by the loop mapping matrix of the ath patch $\boldsymbol{\Lambda}^a$ defined in (6.22). The next $\sum_{l=1}^{L} (N_{\mathrm{ni}}^l - 1)$ columns correspond to the additional loop basis functions across interfaces represented by the submatrices $\boldsymbol{\Lambda}_{\mathrm{ti}}^a \in \mathbb{Z}^{N^a \times \sum_l (N_{\mathrm{ni}}^l - 1)}$ superimposing the basis functions tangential to the interfaces and the submatrix $\boldsymbol{\Lambda}_{\mathrm{ni}} \in \mathbb{Z}^{N_{\mathrm{ni}} \times \sum_l (N_{\mathrm{ni}}^l - 1)}$ superimposing the normal basis functions. The last N_{c} columns of $\boldsymbol{\Lambda}$ correspond to the loop basis functions around the corner vertices represented by the submatrix $\boldsymbol{\Lambda}_{\mathrm{c}} \in \mathbb{Z}^{N_{\mathrm{ni}} \times N_{\mathrm{c}}}$ superimposing only normal basis functions.

6.2.2 Non-solenoidal Basis—Star Mapping Matrix

In analogy to the loop functions, the mapping matrix $\boldsymbol{\Sigma}$ describes how the basis functions $\hat{\boldsymbol{f}}_n = \hat{\boldsymbol{f}}_{ij}^d$ are superimposed to form star functions $\hat{\Sigma}_{ij}$, that is,

$$\hat{\Sigma}_r = \hat{\Sigma}_{i_\Sigma(r),j_\Sigma(r)} = \sum_{n=1}^{N} \left[\boldsymbol{\Sigma}^{\mathrm{T}}\right]_{rn} \hat{\boldsymbol{f}}_n \tag{6.33}$$

with the freely selectable index mappings $i_\Sigma(r)$ and $j_\Sigma(r)$. The star functions $\hat{\Sigma}_r$ have to complement the loop functions such that in total the same space is spanned as by the original basis $\hat{\boldsymbol{f}}_n$. In addition, a defining property of star functions is (in contrast to, e.g, co-tree functions [Eibert 2004; Andriulli 2012]) that the corresponding mapping matrix is a discretized version of the divergence operator on the coefficient space such that $\boldsymbol{\Sigma}^{\mathrm{T}}\boldsymbol{\Lambda} = \boldsymbol{0}$ [Vecchi 1999]. To obtain such a basis, we start again with the single-patch case.

Single-Patch Domain

As the matrix $\boldsymbol{\Sigma}$ is related to the charge, we generalize the analysis of [Vecchi 1999] and expand the divergence of the current in the parametric domain $\hat{\sigma}$ (which is proportional to the charge) as

$$\hat{\sigma}(u,v) = \nabla_{\hat{\Gamma}} \cdot \hat{\boldsymbol{j}} = \sum_{q=1}^{Q} [\boldsymbol{\sigma}]_q \, \varphi_q(u,v) \tag{6.34}$$

with the scalar functions

$$\varphi_q = \varphi_{i(q),j(q)} = b_i^{p_u-1}(u) b_j^{p_v-1}(v) \qquad \begin{matrix} i = 2,\dots,N_u \\ j = 2,\dots,N_v \end{matrix} . \tag{6.35}$$

The latter are chosen to expand the charge since the divergence of the basis functions $\hat{\boldsymbol{f}}_n$ can be expressed with the same φ_q and leveraging (6.6) we have

$$\nabla_{\hat{\Gamma}} \cdot \hat{\boldsymbol{j}} = \sum_n [\boldsymbol{j}_u]_n \left(\varphi_{ij} - \varphi_{i+1,j}\right) + \sum_n [\boldsymbol{j}_v]_n \left(\varphi_{ij} - \varphi_{i,j+1}\right) . \tag{6.36}$$

Equating (6.36) and (6.34), it can be seen that both representations constitute a different linear combination of the same basis functions φ_q. By comparison, we find that the expansion vector of the current $\boldsymbol{j} = [\boldsymbol{j}_u \; \boldsymbol{j}_v]^{\mathrm{T}}$ is related to the expansion vector of the charge $\boldsymbol{\sigma}$ by

$$\boldsymbol{\sigma} = \boldsymbol{\Sigma}^{\mathrm{T}} \boldsymbol{j} \tag{6.37}$$

where the matrix $\boldsymbol{\Sigma}^{\mathrm{T}} \in \mathbb{Z}^{N_\Sigma \times N}$ consists of the entries

$$\left[\boldsymbol{\Sigma}^{\mathrm{T}}\right]_{mn} = \chi_m(\nabla_{\hat{\Gamma}} \cdot \hat{\boldsymbol{f}}_n) \tag{6.38}$$

with χ_m denoting the indicator function (w.r.t. the set $\{\varphi_m\}$)

$$\chi_m(\varphi) = \begin{cases} \pm 1 & \text{if} \quad \varphi = \pm\varphi_m \\ 0 & \text{else} \end{cases} \tag{6.39}$$

with $\chi_m(\varphi + \psi) = \chi_m(\varphi) + \chi_m(\psi)$ as well as (dictated by the indexing limits in (6.35))

$$N_\Sigma = (N_u - 1)(N_v - 1)\,. \tag{6.40}$$

That $\boldsymbol{\Sigma}$ as defined in (6.38) is suitable to complement $\boldsymbol{\Lambda}$ follows from it having rank $N_\Sigma - 1$ and the orthogonality $\boldsymbol{\Sigma}^{\mathrm{T}}\boldsymbol{\Lambda} = \mathbf{0}$. Before giving a proof for these two properties in Section 6.2.3, we first note that the N_Σ star functions implied by (6.38) can be explicitly expressed as

$$\hat{\Sigma}_{ij} = \hat{\boldsymbol{f}}^u_{ij} - \hat{\boldsymbol{f}}^u_{i-1,j} + \hat{\boldsymbol{f}}^v_{ij} - \hat{\boldsymbol{f}}^v_{i,j-1} \qquad \begin{matrix} i = 2, 3, \dots, N_u \\ j = 2, 3, \dots, N_v \end{matrix} \tag{6.41}$$

where all $\hat{\boldsymbol{f}}^d_{ij}$ not in the sets defined by the indices in (6.9) and (6.10) vanish. An intuitive interpretation of the stars $\hat{\Sigma}_{ij}$ can again be given considering the Greville mesh $\mathscr{M}_\mathrm{G}$: Each star function can be uniquely associated with one face of $\mathscr{M}_\mathrm{G}$. More precisely, the up to four basis functions (at the boundaries of the patch, one or two of the basis functions can vanish) attached to each face form a star, that is, they are directed to point away from the face.

Based on this interpretation the Euler characteristic χ for open simply-connected surfaces (in analogy to the RWG discretization on triangles) implies that (excluding the boundary of the patch) the number of inner vertices $\mathscr{V}_\mathrm{G}$, inner edges $\mathscr{E}_\mathrm{G}$, and faces $\mathscr{F}_\mathrm{G}$ is related by $\chi = 1 = \mathscr{V}_\mathrm{G} - \mathscr{E}_\mathrm{G} + \mathscr{F}_\mathrm{G}$ [Richeson 2012, p. 182]. Hence, the number of basis functions N associated with the number of inner edges $\mathscr{E}_\mathrm{G}$ is the number of loops N_Λ associated with $\mathscr{V}_\mathrm{G}$ plus the number of stars associated with $\mathscr{F}_\mathrm{G}$ minus one, that is, there is one star basis function too many. This is, however, in accordance with the requirement of charge neutrality: since the star functions represent the charge (the divergence of the current) and the total charge has to be zero, the degrees of freedom are reduced by one [Vecchi 1999].

A more explicit form of the mapping matrix $\boldsymbol{\Sigma}$ (compared to (6.38)) follows from (6.41) as

$$\boldsymbol{\Sigma}^{\mathrm{T}} = \begin{bmatrix} \boldsymbol{\Sigma}_u^{\mathrm{T}} & \boldsymbol{\Sigma}_v^{\mathrm{T}} \end{bmatrix} \in \mathbb{Z}^{N_\Sigma \times N} \tag{6.42}$$

with the matrix $\boldsymbol{\Sigma}_u^{\mathrm{T}} \in \mathbb{Z}^{N_\Sigma \times (N_u-2)(N_v-1)}$ relating the functions $\hat{\boldsymbol{f}}^u_{ij}$ to the stars as

$$\left[\boldsymbol{\Sigma}_u^{\mathrm{T}}\right]_{rs} = \begin{cases} 1 & \text{if} \quad i(s) = i_\Sigma(r) \qquad \text{and} \quad j(s) = j_\Sigma(r)\,, \\ -1 & \text{if} \quad i(s) = i_\Sigma(r) - 1 \quad \text{and} \quad j(s) = j_\Sigma(r)\,, \\ 0 & \text{else,} \end{cases} \tag{6.43}$$

with the index mappings $i(s)$, $j(s)$, $i_\Sigma(r)$, and $j_\Sigma(r)$ depending on the chosen ordering in

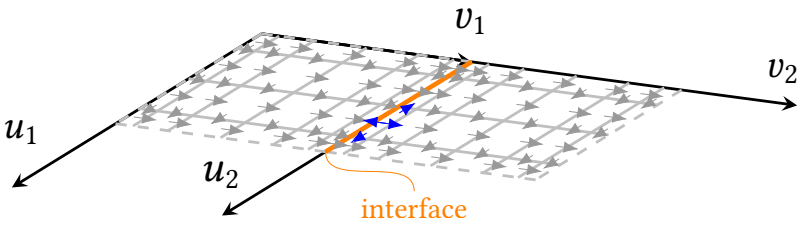

Fig. 6.8: Example of a star being completed by basis functions across the interface between two patches. © 2024 IEEE

the coefficient vectors $\boldsymbol{j}$ and $\boldsymbol{j}_\Sigma$. Analogously, the matrix $\boldsymbol{\Sigma}_v^{\mathrm{T}} \in \mathbb{Z}^{N_\Sigma \times (N_u-1)(N_v-2)}$ relating the functions $\hat{\boldsymbol{f}}_{ij}^v$ to the stars is

$$\left[\boldsymbol{\Sigma}_v^{\mathrm{T}}\right]_{rt} = \begin{cases} 1 & \text{if} \quad i(t) = i_\Sigma(r) \quad \text{and} \quad j(t) = j_\Sigma(r) \\ -1 & \text{if} \quad i(t) = i_\Sigma(r) \quad \text{and} \quad j(t) = j_\Sigma(r) - 1 \\ 0 & \text{else} \end{cases} \tag{6.44}$$

for the chosen index mappings. Sorting, for example, the current coefficients as in (6.25) and (6.26), the matrices in (6.42) can be expressed as

$$\left[\boldsymbol{\Sigma}_u^{\mathrm{T}}\right]_{rs} = \delta_{rs} - \delta_{r-(N_v-1),s} \tag{6.45}$$

and

$$\boldsymbol{\Sigma}_v^{\mathrm{T}} = \begin{bmatrix} -\boldsymbol{B}^{\mathrm{T}} & & \\ & \ddots & \\ & & -\boldsymbol{B}^{\mathrm{T}} \end{bmatrix} \tag{6.46}$$

where $\boldsymbol{B}^{\mathrm{T}}$ as defined in (6.28) is repeated $N_u - 1$ times on the diagonal.

Multi-Patch Domain

Again the interpretation via the Greville mesh directly implies how to handle multi-patch scenarios. As shown in Fig. 6.8, star basis functions in the multi-patch scenario are obtained by supplementing the stars on the individual patches across the interfaces with the corresponding (merged) normal basis functions (i.e., the otherwise vanishing terms in (6.41) are replaced with the interface basis functions). Consequently, we get a total of

$$N_\Sigma = \sum_{a=1}^{A} N_\Sigma^a \tag{6.47}$$

stars with N_Σ^a denoting the number of stars on the ath patch as determined in (6.40). Following the sorting of the basis functions as (6.31), we can represent the multi-patch star

matrix as

$$\boldsymbol{\Sigma} = \begin{bmatrix} \boldsymbol{\Sigma}^1 & & \\ & \ddots & \\ & & \boldsymbol{\Sigma}^A \\ \boldsymbol{\Sigma}^1_{\mathrm{ni}} & \dots & \boldsymbol{\Sigma}^A_{\mathrm{ni}} \end{bmatrix} \in \mathbb{Z}^{N \times N_\Sigma} \tag{6.48}$$

where the matrices $\boldsymbol{\Sigma}^a_{\mathrm{ni}} \in \mathbb{Z}^{N_{\mathrm{ni}} \times N^a_\Sigma}$ can be expressed as

$$\left[\boldsymbol{\Sigma}^a_{\mathrm{ni}}\right]_{sr} = \begin{cases} 1 & \text{if } \hat{\boldsymbol{f}}^l_{\mathrm{ni},s} \text{ complements } \hat{\Sigma}^a_r \\ -1 & \text{if } -\hat{\boldsymbol{f}}^l_{\mathrm{ni},s} \text{ complements } \hat{\Sigma}^a_r \\ 0 & \text{else} \end{cases}. \tag{6.49}$$

6.2.3 Complete Decomposition—Properties of the Mappings

To verify that the obtained loop-star decomposition constitutes a valid basis transformation, we discuss some of its properties.

Single-Patch Domain

For a single patch, the transformation matrix $\boldsymbol{Q} \in \mathbb{Z}^{N \times N}$ reduces to $\boldsymbol{Q} = [\boldsymbol{\Lambda}\ \boldsymbol{\Sigma}]$ in (3.24) as there are no global loops. In this context, one arbitrary column of $\boldsymbol{\Sigma}$ has to be removed in accordance with the Euler characteristic and charge conservation as discussed in Section III-B. It can also be seen by summing up the number of loop functions in (6.21) with the number of star functions in (6.40) and comparing this with the total number of original basis functions in (6.11) resulting in

$$N_\Lambda + N_\Sigma = N + 1\,. \tag{6.50}$$

Correspondingly, $\boldsymbol{\Lambda} = [\boldsymbol{\Lambda}_u^{\mathrm{T}}\ \boldsymbol{\Lambda}_v^{\mathrm{T}}]^{\mathrm{T}}$ has full rank, that is $\mathrm{rank}(\boldsymbol{\Lambda}) = N_\Lambda$ as can be seen from $\boldsymbol{\Lambda}_v^{\mathrm{T}}$ in (6.29) which is already in row echelon form with all entries on the main diagonal being minus one. Similarly, from the row echelon form of $\boldsymbol{\Sigma}$ (or from its underlying graph theoretical properties), it can be seen that $\mathrm{rank}(\boldsymbol{\Sigma}) = N_\Sigma - 1$ with the one-dimensional nullspace spanned by the all ones vector of length N_Σ, that is, $\boldsymbol{\Sigma}\mathbf{1} = \mathbf{0}$. Finally, it can be verified that the matrices $\boldsymbol{\Lambda}$ and $\boldsymbol{\Sigma}$ are indeed mutually orthogonal, that is,

$$\boldsymbol{\Lambda}^{\mathrm{T}}\boldsymbol{\Sigma} = \boldsymbol{\Sigma}^{\mathrm{T}}\boldsymbol{\Lambda} = \mathbf{0}\,. \tag{6.51}$$

More precisely, any superposition of Q loop functions is solenoidal and can be written as

$$\hat{\boldsymbol{j}}_{\mathrm{sol}} = \sum_{q=1}^{Q} [\boldsymbol{j}_\Lambda]_q\, \hat{\Lambda}_q = \sum_{n=1}^{N} [\boldsymbol{\Lambda}\boldsymbol{j}_\Lambda]_n \hat{\boldsymbol{f}}_n\,. \tag{6.52}$$

Taking the divergence of $\hat{\boldsymbol{j}}_{\text{sol}}$ (which is zero) can be expressed via $\boldsymbol{\Sigma}$ as

$$\nabla_{\hat{\Gamma}} \cdot \hat{\boldsymbol{j}}_{\text{sol}} = \sum_{q=1}^{N_{\boldsymbol{\Sigma}}} \left[\boldsymbol{\Sigma}^{\mathrm{T}} \boldsymbol{j}_{\text{sol}}\right]_q \varphi_q = \sum_{q=1}^{N_{\boldsymbol{\Sigma}}} \left[\boldsymbol{\Sigma}^{\mathrm{T}} \boldsymbol{\Lambda} \boldsymbol{j}_{\Lambda}\right]_q \varphi_q = 0\,. \tag{6.53}$$

This is only true for general $\boldsymbol{j}_{\Lambda}$ if and only if $\boldsymbol{\Sigma}^{\mathrm{T}}\boldsymbol{\Lambda} = \boldsymbol{0}$ showing property (6.51). Together with the ranks of $\boldsymbol{\Lambda}$ and $\boldsymbol{\Sigma}$, this ultimately implies that $\boldsymbol{Q}$ is full rank verifying that a valid basis transformation has been derived. Note that property (6.51) (by the choice of representing the non-solenoidal part by the star functions) is also a key for the definition of the quasi-Helmholtz projectors as detailed in Section 6.3.

Note also that some of the considerations so far are related to the interpretation in the framework of a spline de Rahm complex discussed in [Veiga et al. 2014; Dölz et al. 2019; Buffa et al. 2020] relating the spaces spanned by the functions ψ_{ij}, $\hat{\boldsymbol{f}}^d_{ij}$, and φ_{ij} for closed simply-connected geometries.

Multi-Patch Domain

In the case of multiple patches (i.e., $\Gamma = \cup_{a=1}^{A} \Gamma_a$), additional aspects have to be considered since, in contrast to the single patch case, the resulting surface Γ can be closed or be multiply connected. For a multiply-connected surface with G_{H} handles and G_{O} holes, the global loop mapping matrix $\boldsymbol{H} \in \mathbb{R}^{N\times(2G_{\mathrm{H}}+G_{\mathrm{O}})}$ can in principle be constructed such that chains of basis functions $\hat{\boldsymbol{f}}^d_{ij}$ and $\hat{\boldsymbol{f}}^l_{\mathrm{ni},i}$ are formed around the handles and holes of the surface $\hat{\Gamma}$. Alternatively, $\boldsymbol{H}$ can be determined as a solution to

$$[\boldsymbol{\Lambda}\ \boldsymbol{\Sigma}]^{\mathrm{T}} \boldsymbol{H} = \boldsymbol{0}\,. \tag{6.54}$$

This can be done, for example, by randomized projections as detailed in [Andriulli et al. 2011]. However, it can be avoided altogether when resorting to the quasi-Helmholtz projectors discussed in the following Section 6.3.

For each body, the matrix $\boldsymbol{\Sigma}$ has a one-dimensional nullspace, independent of the topology of the underlying geometry. Instead $\boldsymbol{\Lambda}$ is full rank for open geometries and has a rank one deficiency for closed geometries. That the right amount of basis functions is obtained (i.e., that the transformation matrix $\boldsymbol{Q}$ is full rank) also in the multi-patch case can be verified by graph theory considering the mesh $\mathscr{M}_{\Gamma}$ spanned by the patches: Using (6.30) and (6.47), the sum of the number of loop basis functions N_{Λ} and the number of star basis functions N_{Σ} adds up to

$$N_{\Sigma} + N_{\Lambda} = \sum_{a=1}^{A} N_{\Sigma}^{a} + \sum_{a=1}^{A} N_{\Lambda}^{a} + \sum_{l=1}^{L} \left(N_{\mathrm{ni}}^{l} - 1\right) + N_{\mathrm{c}}\,. \tag{6.55}$$

Due to (6.50) on each patch, this is equivalent to

$$N_\Sigma + N_\Lambda = \sum_{a=1}^{A} N^a + A + \sum_{l=1}^{L} N_{\mathrm{ni}}^l - L + N_{\mathrm{c}}\,, \tag{6.56}$$

and by (6.12), we obtain

$$N_\Sigma + N_\Lambda = N + \mathscr{F}_\Gamma - \mathscr{E}_\Gamma^{\mathrm{in}} + \mathscr{V}_\Gamma^{\mathrm{in}}\,, \tag{6.57}$$

where $\mathscr{F}_\Gamma = A$ is the number of faces (patches) forming Γ, $\mathscr{E}_\Gamma^{\mathrm{in}} = L$ is the number of interior edges, and $\mathscr{V}_\Gamma^{\mathrm{in}} = N_{\mathrm{c}}$ the number of interior vertices. Leveraging that in the rectangular network of patches forming Γ, the number of boundary edges $\mathscr{E}_\Gamma^{\mathrm{ex}}$ is always equal to the number of boundary vertices $\mathscr{V}_\Gamma^{\mathrm{ex}}$, we can add $\mathscr{V}_\Gamma^{\mathrm{ex}} - \mathscr{E}_\Gamma^{\mathrm{ex}} = 0$ to (6.57) and obtain

$$N_\Sigma + N_\Lambda = N + \chi \tag{6.58}$$

where χ is the Euler characteristic of the rectangular network of patches. This verifies that all cases are covered correctly: for example, for open simply-connected surfaces, $\chi = 1$, since one star should be removed; for closed simply-connected surfaces, $\chi = 2$, as in addition to one star also a loop function should be removed; and for closed multiply-connected surfaces with G_{H} handles (also called genus) $\chi = 2 - 2G_{\mathrm{H}}$ as $2G_{\mathrm{H}}$ global loops have to be added.

6.3 Quasi-Helmholtz Projectors

Instead of directly using the loop-star decomposition, it is advantageous to employ the quasi-Helmholtz projectors $\boldsymbol{P}_{\boldsymbol{\Sigma}} = \boldsymbol{\Sigma}(\boldsymbol{\Sigma}^{\mathrm{T}}\boldsymbol{\Sigma})^{+}\boldsymbol{\Sigma}^{\mathrm{T}}$ and $\boldsymbol{P}_{\boldsymbol{\Lambda H}} = \mathbf{I} - \boldsymbol{P}_{\boldsymbol{\Sigma}}$ as discussed in Section 3.2.2. This is in the first place possible, since by the way of constructing $\boldsymbol{\Lambda}$ and $\boldsymbol{\Sigma}$ we have ensured that property (6.51) holds.

Moreover, in order for the low-frequency stabilization via the projectors to be efficient, the pseudoinverse in $\boldsymbol{P}_{\boldsymbol{\Sigma}} = \boldsymbol{\Sigma}(\boldsymbol{\Sigma}^{\mathrm{T}}\boldsymbol{\Sigma})^{+}\boldsymbol{\Sigma}^{\mathrm{T}}$ should be computable in an efficient manner. By the way of constructing $\boldsymbol{\Sigma}$, however, this has been ensured as well: the product

$$\boldsymbol{\Sigma}^{\mathrm{T}}\boldsymbol{\Sigma} \tag{6.59}$$

is a graph Laplacian since $\boldsymbol{\Sigma}^{\mathrm{T}}$ is an incidence matrix associated with the graph dual to the Greville mesh. Consequently, the product of $(\boldsymbol{\Sigma}^{\mathrm{T}}\boldsymbol{\Sigma})^{+}$ with a vector can be computed iteratively with a constant number of iterations independent of N_Σ by employing an AMG preconditioner [Livne et al. 2012; Ruge et al. 1987]. The treatment of the one dimensional nullspace of $\boldsymbol{\Sigma}^{\mathrm{T}}\boldsymbol{\Sigma}$ depends on the specific AMG approach (see also [Andriulli 2012, Section IV], [Andriulli et al. 2013, Section V]). We note that also $\boldsymbol{\Lambda}^{\mathrm{T}}\boldsymbol{\Lambda}$ is a graph Laplacian so that, if needed, $\boldsymbol{P}_{\boldsymbol{\Lambda}} = \boldsymbol{\Lambda}(\boldsymbol{\Lambda}^{\mathrm{T}}\boldsymbol{\Lambda})^{+}\boldsymbol{\Lambda}^{\mathrm{T}}$ could be efficiently used.

To illustrate this we consider a single patch where we vary the number of basis functions and correspondingly the number of stars N_Σ from 1×10^2 to 1×10^6. The number of iterations

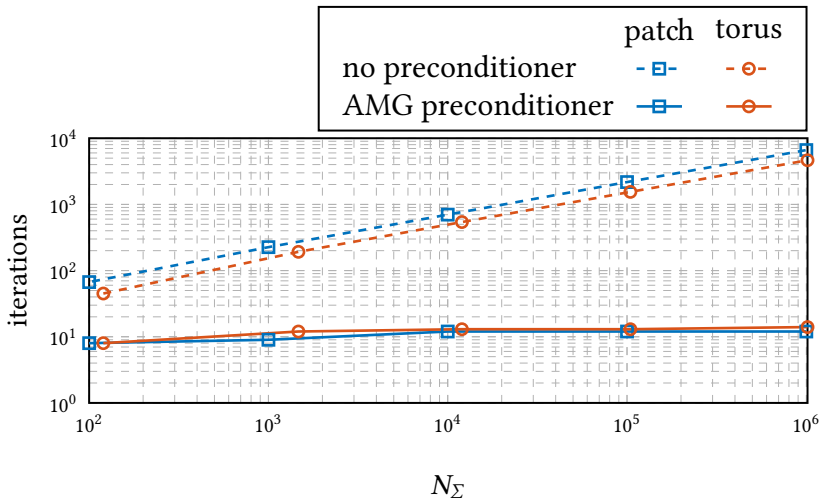

Fig. 6.9: Number of iterations for the iterative computation of the pseudoinverse in the projector $\boldsymbol{P}_{\boldsymbol{\Sigma}}$ via CG for a single patch and the 30-patch torus. © 2024 IEEE

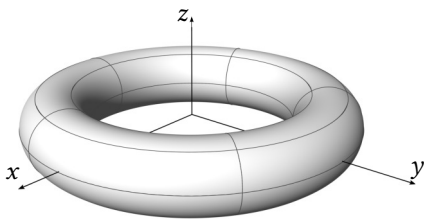

Fig. 6.10: Torus with major radius $R = 2\,\mathrm{m}$ and minor radius $r = 0.5\,\mathrm{m}$ described by $A = 30$ NURBS patches. © 2024 IEEE

for CG to compute the pseudoinverse with a relative accuracy of 1×10^{-12} when evaluating $\boldsymbol{P}_{\boldsymbol{\Sigma}}\boldsymbol{e}^{\mathrm{ex}}$ is depicted in Fig. 6.9. Clearly, when employing an AMG (in particular a Ruge-Stüben) preconditioner [Ruge et al. 1987], the number of iterations remains asymptotically bounded. The same is true for the torus described by $A = 30$ NURBS patches shown in Fig. 6.10.

6.4 Numerical Results

In order to verify that the derived preconditioners can indeed low frequency stabilize the isogeometrically discretized EFIE, several scenarios are studied. In all of these, a GMRES solver is employed without restarts and a relative residual of $\epsilon = 1 \times 10^{-4}$ as stopping criterion. The implementation itself is based on [Vázquez 2016; Hofmann 2023f] and the singularities in the integrals in (3.15) and (3.16) are treated by employing the regularizing coordinate transforms of [Sauter et al. 1997; Sauter et al. 2011, pp. 289ff]. To overcome the catastrophic round-of errors when evaluating the RHS $\boldsymbol{P}_{\Lambda H}\boldsymbol{e}^{\mathrm{ex}}$, we employ the Taylor series expansion approach given in (4.4). The approach of Chapter 4 should be applicable as well (in principle, the scalar functions ψ_r for the loops were already part of the derivation in (6.17)) but further investigations are necessary.

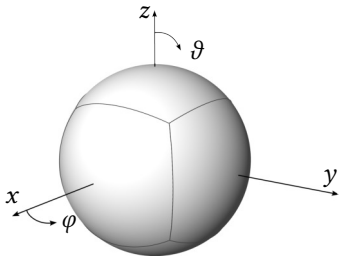

p_{uv}	M^a_{uv}	N^a_{uv}	N^a	N_{ni}	N	N_Λ	N_Σ
1	11	9	112	96	768	386	384
2	12	9	112	96	768	386	384
3	13	9	112	96	768	386	384

Fig. 6.11: Sphere of radius $r_\mathrm{s} = 1\,\mathrm{m}$ described exactly by $A = 6$ NURBS patches of degrees $q_u = q_v = 4$, involving $L = 12$ interfaces between patches and $N_\mathrm{c} = 8$ corner vertices. The table summarizes the employed discretization of the surface current density per patch. © 2024 IEEE

6.4.1 Scattering from a Sphere

As a first scenario, we consider the scattering from a sphere since a reference in terms of a series expansion is available (see, e.g., [Jin 2015, pp. 368ff] and [Hofmann et al. 2023e; Hofmann 2022f]). The sphere has a radius of $r_\mathrm{s} = 1\,\mathrm{m}$ described exactly (i.e., there is no approximation of the geometry) by $A = 6$ NURBS patches as depicted in Fig. 6.11 and is excited by a plane wave. The error with respect to the reference is determined for the FF, the electric, and the magnetic NF at a distance of $r = 5\,\mathrm{m}$. To do so, the fields are computed on a spherical grid with ϑ and φ in steps of 5°, and the relative logarithmic worst-case error

$$\aleph^a = \max_{\vartheta,\varphi}\left\{ 20\log\frac{|a(\vartheta,\varphi) - \hat{a}(\vartheta,\varphi)|}{\max\limits_{\vartheta,\varphi}|a(\vartheta,\varphi)|} \right\} \tag{6.60}$$

is computed with $a \in \{e, h, \mathrm{FF}\}$. Starting with the loop-star stabilized EFIE in (3.26), we consider three different discretizations summarized in the table in Fig. 6.11 where we set on each patch the polynomial degrees

$$p_u = p_v = p_{uv} \tag{6.61}$$

with uniform open knot vectors $U_a = V_a$ (i.e., equidistant spacing between the knots) of lengths $M \in \{11, 13, 15\}$ resulting in $\{64, 49, 36\}$ elements per patch and $N = 786$ total number of basis functions for each case which can be decomposed into $N_\Lambda = 386$ loop and $N_\Sigma = 384$ star basis functions. The results over frequency for the worst-case errors in the fields are shown in Fig. 6.12. Clearly, the proposed loop-star decomposition cures the low-frequency breakdown of the EFIE for all three polynomial degrees, where for higher degrees a higher accuracy is obtained with the same number of basis functions. While the stabilization via projectors following (3.34) yields virtually the same accuracy, a lower condition number is achieved resulting in fewer iterations for GMRES to converge as shown in Fig. 6.13.

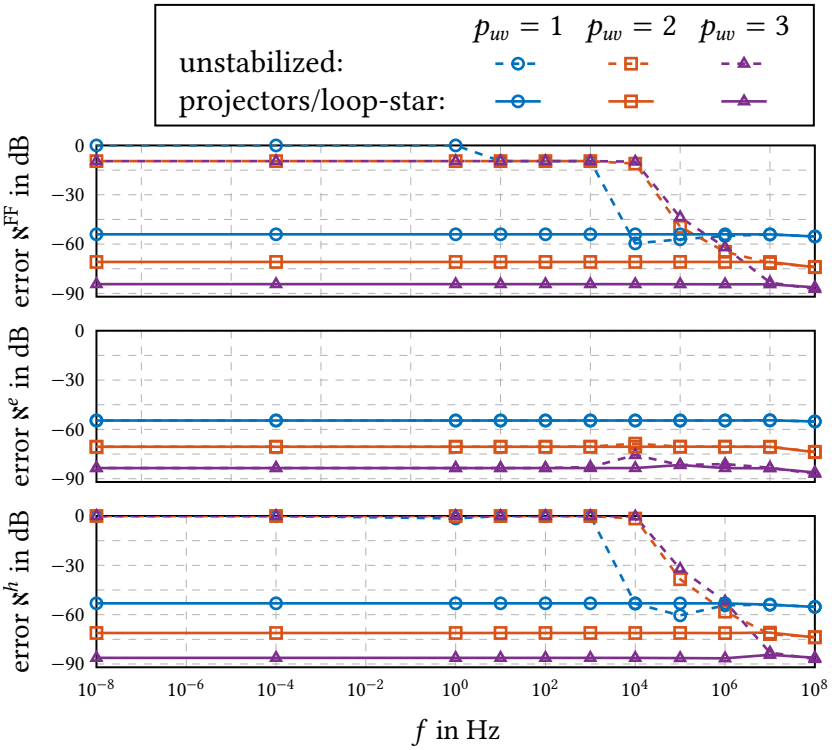

Fig. 6.12: Worst case errors for the FF, the electric, and the magnetic NF for the scattering from the sphere with and without stabilization for different polynomial degrees p_{uv} and same number of the basis functions. © 2024 IEEE

6.4.2 Scattering from Open Geometries

To show that also open geometries can be handled as well as different knot vectors and polynomial degrees on a patch, we consider the curved band shown in Fig. 6.14, which is described by a single patch. The discretization of the induced surface current density on this scatterer is chosen in a way to account for the shape of the geometry. Specifically, with $M_u = 27$, a fine discretization is chosen along the direction that exhibits a greater elongation, while along the other direction a coarser discretization is chosen with $M_v = 9$ with $p_{uv} = 2$. The results for a $\vartheta = 90^\circ$ cut of the electric NF at the frequencies $f = 1{\times}10^{8}$ Hz and $f = 1{\times}10^{-8}$ Hz are depicted in Fig. 6.15, where the quasi-Helmholtz projectors are employed to overcome the low-frequency breakdown. For comparison, a reference solution is obtained by triangulating the geometry with an average edge length of $h = 0.014$ m and correspondingly discretizing the EFIE with 11 975 RWG functions, stabilized by the quasi-Helmholtz projector approach of [Andriulli et al. 2013]. The low deviation from this reference solution confirms the correctness of the proposed stabilization also for different knot vectors. To show that also different polynomial degrees can be employed with our stabilization scheme (even though this no longer constitutes a mixed discretization scheme [Peterson 2006, pp. 33ff], [Nédélec 1980]), we set $p_u = 5$ and $p_v = 2$ while leaving the number of basis functions unaltered. The comparison with the RWG solution in Fig. 6.15 shows a low deviation also in this case.

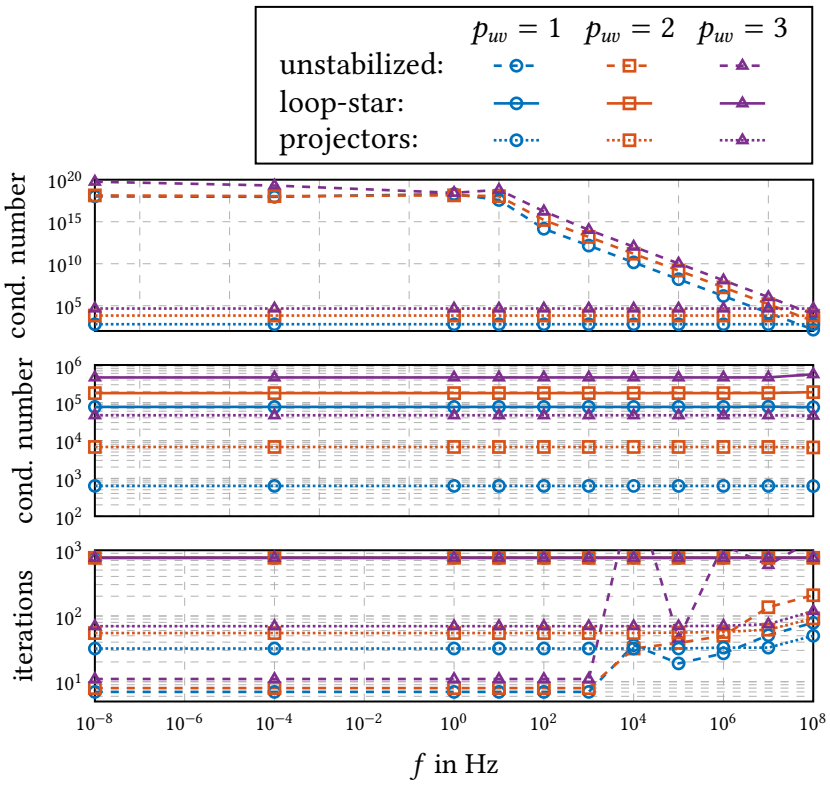

Fig. 6.13: Condition numbers and number of iterations for GMRES to converge for the sphere with different stabilizations, different polynomial degrees, and a fixed number of basis functions. © 2024 IEEE

6.4.3 Scattering from Multiply-Connected Geometries

As an example of a multiply-connected (and open) geometry, we consider next the flat folded ring shown in Fig. 6.16, which is described by 12 NURBS patches. The magnetic NF of this ring is obtained based on a third-order discretization. at the frequencies 1×10^8 Hz and $1{\times}10^{-50}$ Hz. The result for a $\varphi = 90^\circ$ cut is shown in Fig. 6.17. Again, the quasi-Helmholtz projectors are employed for the stabilization avoiding an explicit construction of the global loop. The comparison with a stabilized RWG discretization using 5994 basis functions and an average edge length of the triangulation of $h = 0.02$ m shows a good agreement below -40 dB at both frequencies.

For the 50-patch rectangular double-torus shown in Fig. 6.18, we compute the FF at the frequency of 1×10^{-50} Hz using three different discretizations summarized in the table in Fig. 6.18. The results for a $\varphi = 0^\circ$ cut are shown in Fig. 6.19, where the reference solution employs 16 494 RWG functions. Clearly, for increasing polynomial degrees, we can again observe an improved agreement with the reference. As a second means of verification, we check how well the condition $\boldsymbol{e}^{\mathrm{ex}} + \boldsymbol{e}^{\mathrm{sc}} = \boldsymbol{0}$ is fulfilled inside the torus. We do so on a circular path surrounding one of the holes inside the geometry as indicated in Fig. 6.20, which also verifies an improvement of the accuracy with increasing polynomial degrees.

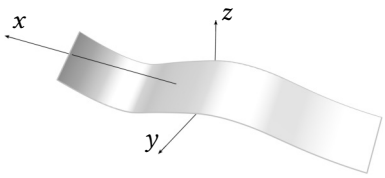

p_u	p_v	M_u	M_v	N_{ni}	N	N_Λ	N_Σ
2	2	24	9	0	175	76	100
5	2	27	9	0	175	76	100

Fig. 6.14: Curved band of width $l_v = 0.45\,\mathrm{m}$ and curved length $l_u = 3.12\,\mathrm{m}$ described by 1 patch of degrees $q_u = q_v = 2$. The table summarizes the employed discretization of the surface current density. © 2024 IEEE

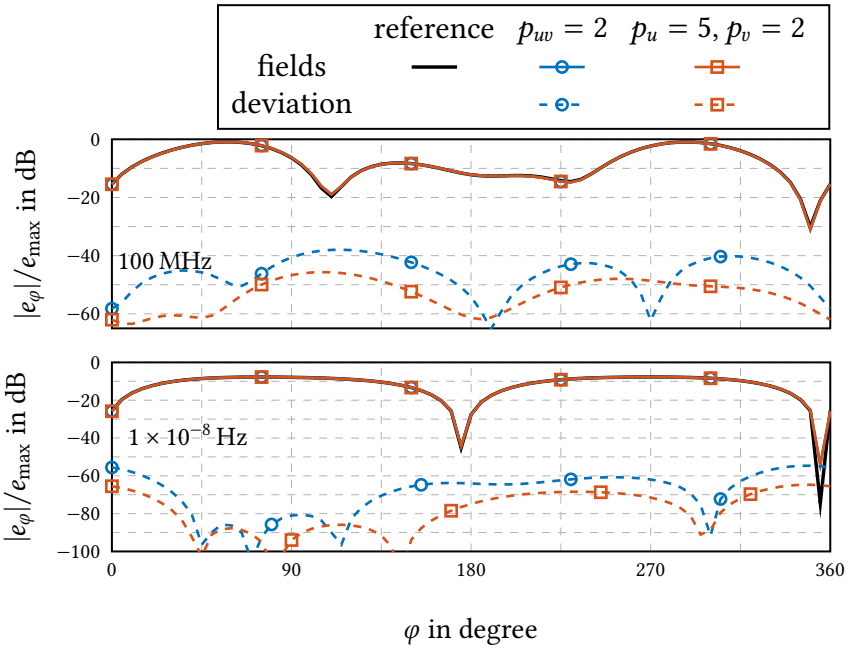

Fig. 6.15: Normalized NF cuts at $\vartheta = 90^\circ$ with 1.15° angular sampling for the scattering from the curved band at the frequencies of 1×10^8 Hz and 1×10^{-8} Hz. © 2024 IEEE

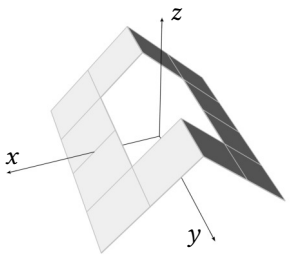

p_{uv}	M^a_{uv}	N^a	N_{ni}	N	N_Λ	N_Σ
3	11	60	$6 \times 12 = 72$	792	361	432

Fig. 6.16: Flat folded ring of size $0.88\,\mathrm{m} \times 1.13\,\mathrm{m}$ consisting of $A = 12$ patches each of degree $q_u = q_v = 1$. There are $L = 12$ interfaces and $N_c = 0$ corner vertices in the geometry. © 2024 IEEE

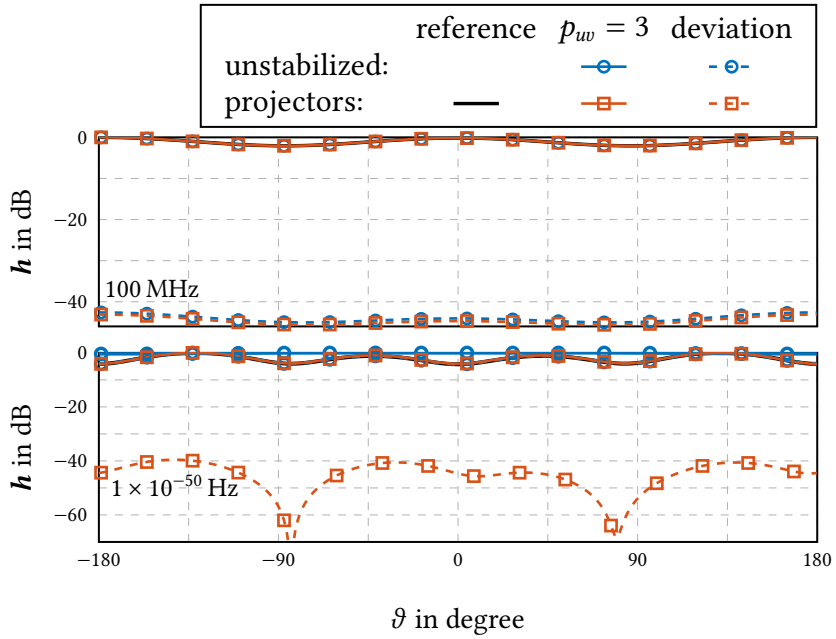

Fig. 6.17: Normalized magnetic NF cut at $\varphi = 90^\circ, \boldsymbol{r} = 5\,\mathrm{m}$ scattered from the folded flat ring at the frequencies of 1×10^8 Hz and 1×10^{-50} Hz. © 2024 IEEE

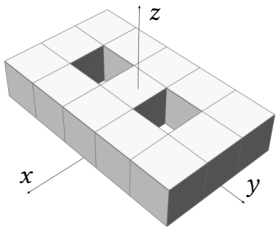

p_{uv}	M^a_{uv}	N^a	N_{ni}	N	N_Λ	N_Σ
1	7	24	$4 \times 100 = 400$	1600	798	800
2	9	40	$5 \times 100 = 500$	2500	1248	1250
3	11	60	$6 \times 100 = 600$	3600	1798	1800

Fig. 6.18: Rectangular double-torus with 50 NURBS patches of degrees $q_u = q_v = 1$ located at $(3.5, 1.5, 0.5)$. The geometry extends from $x = 1\,\mathrm{m}$ to $x = 6\,\mathrm{m}$,$y = 0\,\mathrm{m}$ to $y = 3\,\mathrm{m}$ and $z = 0\,\mathrm{m}$ to $z = 1\,\mathrm{m}$ in a Cartesian coordinate system. It involves $L = 100$ interfaces and $N_\mathrm{c} = 48$ corner vertices. © 2024 IEEE

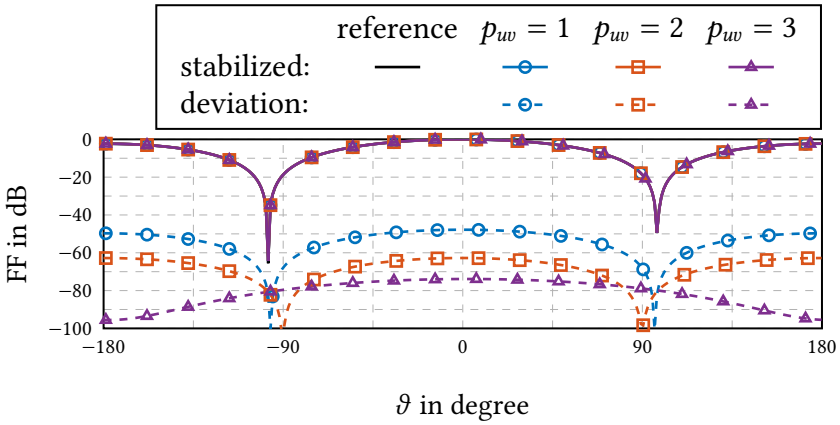

Fig. 6.19: Normalized FF cut at $\varphi = 0^\circ$ for the scattering from the rectangular-double torus at 1×10^{-50} Hz. © 2024 IEEE

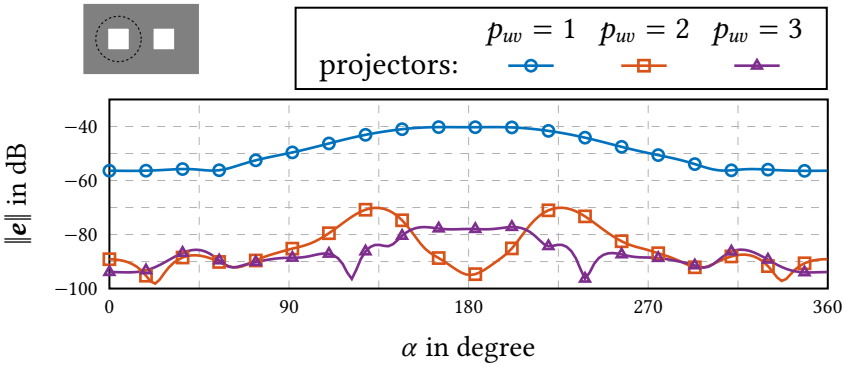

Fig. 6.20: Total electric field sampled over a circle of radius 1 m centered at (2.5, 1.5, 0.5) with 1.15° angular sampling, inside the rectangular-double torus at 1×10^{-50} Hz. © 2024 IEEE

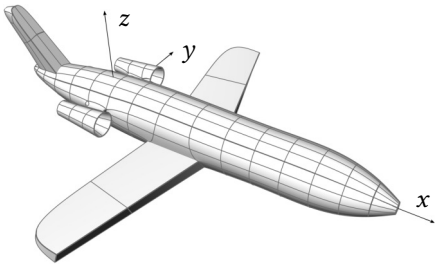

p_{uv}	M^a_{uv}	N^a	N_{ni}	N	N_Λ	N_Σ
1	5	4	$3 \times 828 = 2484$	3312	1654	1656
2	7	12	$4 \times 828 = 3312$	7452	3724	3726

Fig. 6.21: Model of an airplane with a total length of about 7 m described by $A = 414$ NURBS patches each of degree $q_u = q_v = 3$, involving $L = 828$ interfaces between patches and $N_c = 412$ corner vertices. The geometry contains two handles (on the engines), that is, four global loops. © 2024 IEEE

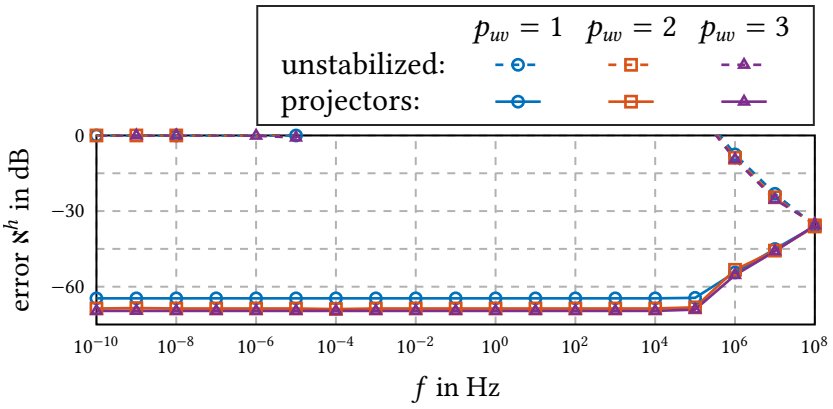

Fig. 6.22: Relative worst-case errors of the scattered magnetic NF for the airplane discretized with 7452 unknowns. © 2024 IEEE

As a last and more realistic scatterer, we consider the NURBS model of a tail-mounted engine airplane depicted in Fig. 6.21 employing $A = 414$ patches. The deviation from the condition $\boldsymbol{h}^{\mathrm{ex}} + \boldsymbol{h}^{\mathrm{sc}} = \boldsymbol{0}$ inside the plane is shown in Fig. 6.22 attesting a good accuracy.

6.5 Conclusion

An efficient method to low-frequency stabilize the EFIE when discretized in an isogeometric approach via B-splines of arbitrary polynomial degrees has been given. Especially, the employed definition of the basis functions by using the Curry-Schoenberg splines allows to express the involved quasi-Helmholtz decomposition concisely via sparse mapping matrices with advantageous properties. The provided interpretation on the Greville mesh explains the underlying structure of the basis transformation on single- and multi-patch domains and allows for a reasoning based on topological arguments as familiar from mesh based discretizations.

Part III

Paradigms for Equivalent Source Reconstructions

7

A Low-Frequency Stable Equivalent Surface Current Reconstruction Scheme

"Simulation is better than reality!"
[Hamming 1994]

A low-frequency stabilizing scheme for the reconstruction of equivalent surface currents based on the EFIO and the boundary element method (BEM) is investigated. In order to overcome the observed low-frequency breakdown, a stabilization scheme is studied based on a quasi-Helmholtz decomposition including an analysis of the required field sampling via probe antennas. The scheme incorporates the self-adaptive normalization and the stabilized RHS evaluation which are found of critical importance to determine all fields accurately as shown by the simulation of different inverse surface source reconstructions.

This chapter is based on [Hofmann et al. 2022e; Hofmann et al. 2023c] including verbatim portions.

Reconstructing equivalent electric surface currents from measurements of the fields radiated by a DUT, that is, performing a field transformation, involves the underlying EFIO. As discussed in Section 1.1.1, the latter is known to suffer from low-frequency issues in the context of scattering from PEC bodies [Wilton et al. 1981; Mautz et al. 1984]. The corresponding EFIE has a condition number that grows as $\mathcal{O}(1/k^2)$, with the wavenumber k [Andriulli et al. 2013]. In addition, significant round-off errors occur and prevent accurate solutions as discussed in Chapter 4 and Chapter 5. As a consequence, similar problems can be encountered for the equivalent source reconstruction as shown in [Mitharwal et al. 2015], where a Calderón identity based preconditioner was proposed.

In order to stabilize the inverse surface source field transformation based on the EFIO over a wide frequency range, we study a scheme that adapts the quasi-Helmholtz decomposi-

tions introduced in Section 3.2. This allows to remove the ill-conditioning in k when the frequency is decreased. To ensure that all components of the equivalent currents are recovered, we employ the adaptive normalization scheme of Chapter 5. Moreover, the evaluation of the sampled field is stabilized by the approach of Chapter 4. Via the simulation of different reconstruction scenarios, we investigate the accuracy of the transformed fields and verify our approach.

To this end, this chapter is organized as follows: In Section 7.1 the field transformation formulation is introduced including an analysis of the role of the field sampling via a probe antenna. The low-frequency stabilizing scheme is described in Section 7.2 and numerical results are discussed in Section 7.3 before a conclusion is given.

7.1 Field Transformation Formulation

To transform the time-harmonic fields measured by a probe antenna, we assume equivalent electric currents $\boldsymbol{j}$ on a Huygens' surface Γ_H around the DUT to be characterized. The electric field $\boldsymbol{e}$ radiated by the currents can be computed through the EFIO $\boldsymbol{\mathcal{T}}$ as

$$\boldsymbol{e} = -\boldsymbol{\mathcal{T}}\,\boldsymbol{j} = -\mathrm{j}k\boldsymbol{\mathcal{T}}_\mathrm{A}\boldsymbol{j} - \mathrm{j}k^{-1}\boldsymbol{\mathcal{T}}_\Phi\boldsymbol{j} \tag{7.1}$$

as discussed in Section 2.2.1. In contrast, to the scattering and radiation scenarios considered in Part II, not a boundary condition at a material interface is enforced to discretize the equation, but the radiated field is sampled at m locations by a probe antenna. More precisely, a general way to express the signal $[\boldsymbol{b}]_m$ received by the mth probe antenna is [Eibert et al. 2015]

$$[\boldsymbol{b}]_m = \iint_{\Gamma_\mathrm{P}} \boldsymbol{w}_m \cdot \boldsymbol{e}\,\mathrm{d}\boldsymbol{r}'\,, \tag{7.2}$$

where $\boldsymbol{w}_m$ is the weighting function of the probe defined on the surface Γ_P. This weighting function can be any equivalent current density in free space which radiates the same field as the probe antenna [Eibert et al. 2015]. Comparing (7.2) with the discretization of the EFIE in (3.6), it can be seen that the weighting functions $\boldsymbol{w}_m$ and, hence, the probe antennas, take the role of the testing functions. There are different ways to evaluate (7.2). For example, in [Eibert et al. 2015] it is reformulated to directly use the FF pattern of the probe antenna, that is, the Fourier transform of w_m. Since we are interested in a potential quasi-Helmholtz decomposition of the testing functions as done for the EFIE, we consider instead an expansion of the w_m into RWG functions [Rao et al. 1982].

7.1.1 Equivalent Current Description of the Probe

Similar to the EFIE, we triangulate the surface Γ_H and model the equivalent surface current density $\boldsymbol{j}$ representing the DUT with RWG functions $\boldsymbol{f}_n$ as $\boldsymbol{j} = \sum_{n=1}^{N} [\boldsymbol{j}]_n \boldsymbol{f}_n$. The surface Γ_P, on the other hand, can be described by a union of disjoint surfaces Γ_m, each representing

a probe antenna at a certain location $\boldsymbol{r}_m$. In practice, the surfaces Γ_m are often shifted and rotated versions of one surface. Each of the surfaces Γ_m is triangulated and the weighting functions $\boldsymbol{w}_m$ described by

$$\boldsymbol{w}_m = \sum_{p=1}^{P_m} [\boldsymbol{w}_m]_p \boldsymbol{f}_p^m \tag{7.3}$$

employing P_m RWG functions. The expansion coefficients $[\boldsymbol{w}_m]_p$ need to be determined separately of the equivalent current reconstruction problem to be solved (e.g., by a simulation) and are assumed to be known in the following. Inserting (7.3) into (7.2) and using (7.1), the mth received signal (i.e., the output signal of a probe antenna at position $\boldsymbol{r}_m$) can be expressed as

$$[\boldsymbol{b}]_m = \boldsymbol{w}_m^{\mathrm{T}} \boldsymbol{e}_m = \boldsymbol{w}_m^{\mathrm{T}} \boldsymbol{T}_m \boldsymbol{j} \,, \tag{7.4}$$

where the vector $\boldsymbol{e}_m$ consists of the entries

$$[\boldsymbol{e}_m]_p = \iint_{\Gamma_m} \boldsymbol{f}_p^m \cdot \boldsymbol{e} \, \mathrm{d}\boldsymbol{r} \tag{7.5}$$

and the matrix $\boldsymbol{T}_m$ consists of the entries

$$[\boldsymbol{T}_m]_{pn} = - \iint_{\Gamma_m} \boldsymbol{f}_p^m \cdot \mathcal{T} \boldsymbol{f}_n \, \mathrm{d}\boldsymbol{r} \,. \tag{7.6}$$

In other words, the receive signal of a probe at one position, is the linear combination of several rows of a discretization as known from the EFIE, however, with non-intersecting surfaces for basis and test functions. Collecting all M receive signals (from all probe positions) into the vector $\boldsymbol{b}$, the LSE

$$\boldsymbol{b} = \begin{bmatrix} b_1 \\ b_2 \\ \vdots \\ b_M \end{bmatrix} = \underbrace{\begin{bmatrix} \boldsymbol{w}_1^{\mathrm{T}} & & & \\ & \boldsymbol{w}_2^{\mathrm{T}} & & \\ & & \ddots & \\ & & & \boldsymbol{w}_M^{\mathrm{T}} \end{bmatrix}}_{\boldsymbol{W}} \underbrace{\begin{bmatrix} \boldsymbol{T}_1 \\ \boldsymbol{T}_2 \\ \vdots \\ \boldsymbol{T}_M \end{bmatrix}}_{\boldsymbol{T}} \boldsymbol{j} \tag{7.7}$$

is obtained, where we have collected all weighting coefficients into the matrix $\boldsymbol{W}$ and all the matrices $\boldsymbol{T}_m$ into the matrix $\boldsymbol{T}$ such that the LSE can be expressed more compactly as

$$\boldsymbol{b} = \boldsymbol{W} \boldsymbol{e} = \boldsymbol{W} \boldsymbol{T} \boldsymbol{j} \,. \tag{7.8}$$

This relationship shows that due to the probes, the RWG functions describing the testing process, are not accessible to be quasi-Helmholtz decomposed: the matrix is, in general, of size $M \times P$ with $P > M$ and, thus, not invertible. Hence, the testing process via probes constitutes a crucial difficulty. At the same time, the matrix $\boldsymbol{W}$ can be understood as a left preconditioner and choosing the $\boldsymbol{w}_m$ to directly superimpose the RWG functions to form

solenoidal and non-solenoidal functions, might be a possible solution. One set of probes which do precisely this are dipole probes, as detailed in the following Section 7.1.2.

7.1.2 Dipole Probe Antennas

The equivalent current describing a Hertzian dipole (HD) at position $\boldsymbol{r}_m$ and orientation $\boldsymbol{u}_m^{\mathrm{HD}}$ can be expressed explicitly as

$$\boldsymbol{w}_m^{\mathrm{HD}} = \boldsymbol{u}_m^{\mathrm{HD}} \delta(\boldsymbol{r} - \boldsymbol{r}_m) \tag{7.9}$$

with the Dirac delta distribution δ. Inserting $\boldsymbol{w}_m^{\mathrm{HD}}$ into (7.2) one obtains for the received signal

$$[\boldsymbol{b}^{\mathrm{HD}}]_m = \boldsymbol{u}_m^{\mathrm{HD}} \cdot \boldsymbol{e}(\boldsymbol{r}_m)\,. \tag{7.10}$$

Consequently, using HDs at the locations $\boldsymbol{r}_m$ as probe antennas the LSE

$$\boldsymbol{b}^{\mathrm{HD}} = \boldsymbol{T}^{\mathrm{HD}} \boldsymbol{j} \tag{7.11}$$

can be set up, with the matrix $\boldsymbol{T}^{\mathrm{HD}} = \mathrm{j}k\boldsymbol{T}_{\mathrm{A}}^{\mathrm{HD}} + \mathrm{j}k^{-1}\boldsymbol{T}_{\Phi}^{\mathrm{HD}}$ consisting of the entries

$$[\boldsymbol{T}_{\mathrm{A}}^{\mathrm{HD}}]_{mn} = \boldsymbol{u}_m^{\mathrm{HD}} \cdot \mathcal{T}_{\mathrm{A}} \boldsymbol{f}_n \Big|_{\boldsymbol{r}_m} \tag{7.12}$$

for the vector potential contributions and

$$[\boldsymbol{T}_{\Phi}^{\mathrm{HD}}]_{mn} = \boldsymbol{u}_m^{\mathrm{HD}} \cdot \mathcal{T}_{\Phi} \boldsymbol{f}_n \Big|_{\boldsymbol{r}_m} \tag{7.13}$$

for the scalar potential contributions. As a dual to the HD there is the magnetic dipole, also known as Fitzgerald dipole (FD), which can be expressed explicitly at location $\boldsymbol{r}_m$ as

$$\boldsymbol{v}_m^{\mathrm{FD}} = \boldsymbol{u}_m^{\mathrm{FD}} \delta(\boldsymbol{r} - \boldsymbol{r}_m) \tag{7.14}$$

with the orientation $\boldsymbol{u}_m^{\mathrm{FD}}$. In order to use it as probe antenna, by employing reciprocity relations, a dual to the relation in (7.2) can be derived: the receive current of a general probe antenna satisfies

$$i_m = \iint_{\Gamma_m} \boldsymbol{v}_m \cdot \boldsymbol{h}\, \mathrm{d}\boldsymbol{r}\,, \tag{7.15}$$

where $\boldsymbol{v}_m$ is an equivalent magnetic current density radiating the same field as the probe antenna. Since a FD with dipole moment $\mathrm{j}k$ can be equivalently described by an electric ring current, we have

$$[\boldsymbol{b}^{\mathrm{FD}}]_m = \mathrm{j}k\boldsymbol{u}^{\mathrm{FD}} \cdot \boldsymbol{h}(\boldsymbol{r}_m)\,, \tag{7.16}$$

that is, the FD measures the magnetic field along the dipole or perpendicular to the equivalent ring current describing the dipole. In consequence, the signal received by a FD, corresponds to a testing of the electric field with a solenoidal electric current (of infinitesimal diameter) and agrees with the relation $\iint_\Gamma \boldsymbol{\ell}_m \cdot \boldsymbol{e}^{\mathrm{ex}}\,\mathrm{d}\boldsymbol{r} = \mathrm{j}k\iint_\Gamma \psi_m \boldsymbol{n}_m \cdot \boldsymbol{h}^{\mathrm{ex}}\,\mathrm{d}\boldsymbol{r}$ for testing the electric field with a loop current $\boldsymbol{\ell}_m$ as derived in (4.10). Taking several samples with FDs the LSE

$$\boldsymbol{b}^{\mathrm{FD}} = \mathrm{j}k\boldsymbol{K}^{\mathrm{FD}}\boldsymbol{j} \tag{7.17}$$

can be formed, where the relation between the current $\boldsymbol{j}$ and the magnetic field $\boldsymbol{h}$ is given by (2.17) such that matrix $\boldsymbol{K}$ consists of the entries

$$[\boldsymbol{K}^{\mathrm{FD}}]_{mn} = \boldsymbol{u}_m^{\mathrm{HD}} \cdot \iint_\Gamma \nabla g(\boldsymbol{r},\boldsymbol{r}') \times \boldsymbol{f}_n(\boldsymbol{r}')\,\mathrm{d}\boldsymbol{r}'\Big|_{\boldsymbol{r}_m}. \tag{7.18}$$

As a result with (7.11) and (7.17) two LSEs for the equivalent source reconstruction problem have been obtained, which by the nature of the probe antennas already include a testing with non-solenoidal and solenoidal functions.

7.2 Low-Frequency Stabilization

To low-frequency stabilize the system (7.8) we consider two cases: dipoles and single RWG functions as test antennas. Although less realistic, the latter has the advantage that it deviates from the EFIE stabilization solely in that the surfaces for test and basis functions are separated. Consequently, we can study the effect this has separately from splitting up the test surface into a union of disjoint surfaces and receiving a single output signal per probe.

7.2.1 Testing with RWG Functions

Assuming that the test surface Γ_{P} is a single surface enclosing the Huygens' surface Γ_{H} and each probe consists of a single RWG defined on the triangulated Γ_{H}, the system (7.8) simplifies to

$$\boldsymbol{b} = \boldsymbol{T}\boldsymbol{j} = (\mathrm{j}k\boldsymbol{T}_{\mathrm{A}} + \mathrm{j}k^{-1}\boldsymbol{T}_{\Phi})\boldsymbol{j} \tag{7.19}$$

with $[\boldsymbol{T}_{\mathrm{A}}]_{mn} = \iint_{\Gamma_{\mathrm{P}}} \boldsymbol{f}_m \cdot \boldsymbol{\mathcal{T}}_{\mathrm{A}}\boldsymbol{f}_n\,\mathrm{d}\boldsymbol{r}$ and $[\boldsymbol{T}_{\Phi}]_{mn} = \iint_{\Gamma_{\mathrm{P}}} \boldsymbol{f}_m \cdot \boldsymbol{\mathcal{T}}_{\Phi}\boldsymbol{f}_n\,\mathrm{d}\boldsymbol{r}$. To stabilize (7.19), the surface current density and the weighting functions are decomposed into solenoidal and a non-solenoidal components by the decomposition operators

$$\boldsymbol{P}^s = \alpha^s\boldsymbol{P}^s_{\boldsymbol{\lambda H}} + \beta^s\boldsymbol{P}^s_{\boldsymbol{\Sigma}} \tag{7.20}$$

with $s \in \{\mathrm{H},\mathrm{P}\}$ and the orthogonal projectors $\boldsymbol{P}^s_{\boldsymbol{\Sigma}} = \boldsymbol{\Sigma}_s(\boldsymbol{\Sigma}_s^{\mathrm{T}}\boldsymbol{\Sigma}_s)^{+}\boldsymbol{\Sigma}_s^{\mathrm{T}}$ and $\boldsymbol{P}^s_{\boldsymbol{\lambda H}} = \mathbf{I} - \boldsymbol{P}^s_{\boldsymbol{\Sigma}}$. Note, that in contrast to (3.34) the projectors for basis and test functions are different ones. Matrices $\boldsymbol{\Sigma}_s$

as defined in (3.20) denote the star to RWG expansion coefficient mappings of the surfaces Γ_s and $(\cdot)^+$ denotes the Moore-Penrose pseudoinverse. The coefficients α_s and β_s are defined in analogy to Chapter 5 as

$$\alpha_\mathrm{P} = \sqrt{j}/\|\boldsymbol{b}_\mathrm{sol}\| \quad \text{and} \quad \beta_\mathrm{P} = 1/(\sqrt{j}\,\|\boldsymbol{b}_\mathrm{nsol}\|) \tag{7.21}$$

where $\boldsymbol{b}_\mathrm{sol} = \boldsymbol{P}^\mathrm{P}_{\boldsymbol{\Lambda H}}\boldsymbol{b}$ and $\boldsymbol{b}_\mathrm{nsol} = \boldsymbol{P}^\mathrm{P}_{\boldsymbol{\Sigma}}\boldsymbol{b}$. The remaining coefficients are determined as

$$\alpha_\mathrm{H} = 1/(\mathrm{j}k\,\alpha_\mathrm{P}) \quad \text{and} \quad \beta_\mathrm{H} = \mathrm{j}k/\beta_\mathrm{P}\,, \tag{7.22}$$

which overall ensures analogous to Chapter 5 that all components of $\boldsymbol{j}$ are recovered with a sufficient relative accuracy. Applying the so defined projectors (7.20) to the system in (7.19), we obtain the stabilized system

$$\boldsymbol{P}^\mathrm{P}\boldsymbol{b} = \boldsymbol{P}^\mathrm{P}\boldsymbol{T}\boldsymbol{P}^\mathrm{H}\boldsymbol{j}' = \left(\mathrm{j}k\boldsymbol{P}^\mathrm{P}\boldsymbol{T}_\mathrm{A}\boldsymbol{P}^\mathrm{H} + \frac{\mathrm{j}\beta_\mathrm{P}\beta_\mathrm{H}}{k}\boldsymbol{T}_\Phi\right)\boldsymbol{j}' \tag{7.23}$$

with $\boldsymbol{j} = \boldsymbol{P}_\mathrm{H}\boldsymbol{j}'$. As detailed in Chapter 4, special care has to be taken for the evaluation of $\boldsymbol{P}^\mathrm{P}_{\boldsymbol{\Lambda H}}\boldsymbol{b}$. Computing it as $\boldsymbol{P}^\mathrm{P}_{\boldsymbol{\Lambda H}}\boldsymbol{b} = \boldsymbol{b} - \boldsymbol{P}^\mathrm{P}_{\boldsymbol{\Sigma}}\boldsymbol{b}$ leads to significant round-off errors. Instead we evaluate the product as $\boldsymbol{P}^\mathrm{P}_{\boldsymbol{\Lambda H}}\boldsymbol{b} = \boldsymbol{\Lambda}_\mathrm{P}(\boldsymbol{\Lambda}^\mathrm{T}_\mathrm{P}\boldsymbol{\Lambda}_\mathrm{P})^+\boldsymbol{\Lambda}^\mathrm{T}_\mathrm{P}\boldsymbol{b}$. Especially, the relations (4.14) and (4.16) are used: for instance, for a simply connected Γ_P,

$$[\boldsymbol{\Lambda}^\mathrm{T}_\mathrm{P}\boldsymbol{b}]_m = -\mathrm{j}k\iint_{\Gamma_\mathrm{P}} \psi_m \boldsymbol{n}_m \cdot \boldsymbol{h}\,\mathrm{d}\boldsymbol{r} \tag{7.24}$$

is employed, which leverages the scalar potential ψ_m defined in (4.11) and the radiated magnetic field $\boldsymbol{h}$ of the device to be characterized. By $\boldsymbol{n}_m$ the normal vector of the surface Γ_P is denoted. As the stabilized system matrix $\boldsymbol{T}_\mathrm{stab} = \boldsymbol{P}^\mathrm{P}\boldsymbol{T}\boldsymbol{P}^\mathrm{H} \in \mathbb{C}^{M\times N}$ in (7.23) is rectangular (i.e., there is a different number of samples than there are unknowns), we solve the normal system

$$\boldsymbol{T}^\mathrm{H}_\mathrm{stab}\boldsymbol{P}^\mathrm{P}\boldsymbol{b} = \boldsymbol{T}^\mathrm{H}_\mathrm{stab}\boldsymbol{T}_\mathrm{stab}\boldsymbol{j}' \tag{7.25}$$

iteratively, where $(\cdot)^\mathrm{H}$ denotes the Hermitian (transpose complex conjugate) of the matrix.

7.2.2 Testing with Dipole Probe Antennas

As second scenario, we consider the case of HDs and FDs as probe antennas. To obtain a low-frequency stabilized LSE, we introduce a loop-star decomposition of the basis functions and leverage that testing with a FD corresponds to testing the electric field with a solenoidal electric current. More precisely, the stabilized system

$$\boldsymbol{D}_\mathrm{P}\boldsymbol{T}^\mathrm{DP}_{\boldsymbol{\Lambda H\Sigma}}\boldsymbol{D}_\mathrm{H}\boldsymbol{j}' = \boldsymbol{D}_\mathrm{P}\boldsymbol{b}^\mathrm{DP} \tag{7.26}$$

is formed, consisting of the RHS vector

$$\boldsymbol{b}^{\mathrm{DP}} = \begin{bmatrix} \boldsymbol{b}^{\mathrm{FD}} \\ \boldsymbol{b}^{\mathrm{HD}} \end{bmatrix} \tag{7.27}$$

(containing the vectors from (7.10) and (7.16)) as well as the matrix

$$\boldsymbol{T}_{\boldsymbol{\Lambda H \Sigma}}^{\mathrm{DP}} = \begin{bmatrix} \mathrm{j}k\boldsymbol{K}^{\mathrm{FD}}\boldsymbol{\Lambda} & \mathrm{j}k\boldsymbol{K}^{\mathrm{FD}}\boldsymbol{H} & \mathrm{j}k\boldsymbol{K}^{\mathrm{FD}}\boldsymbol{\Sigma} \\ \mathrm{j}k\boldsymbol{T}_{\mathrm{A}}^{\mathrm{HD}}\boldsymbol{\Lambda} & \mathrm{j}k\boldsymbol{T}_{\mathrm{A}}^{\mathrm{HD}}\boldsymbol{H} & \boldsymbol{T}^{\mathrm{HD}}\boldsymbol{\Sigma} \end{bmatrix}. \tag{7.28}$$

Notably, the blocks in (7.28) scale in k the same as the blocks of $\boldsymbol{T}_{\boldsymbol{\Lambda H \Sigma}}$ given in (3.25). Consequently, the coefficients of the diagonal matrices $\boldsymbol{D}_s$ can be chosen analogously to Chapter 5 as

$$\alpha_{\mathrm{P}} = \sqrt{j}/\|\boldsymbol{b}^{\mathrm{FD}}\| \quad \text{and} \quad \beta_{\mathrm{P}} = 1/(\sqrt{j}\,\|\boldsymbol{b}^{\mathrm{HD}}\|) \tag{7.29}$$

together with (7.22) for the remaining α_{H} and β_{H}. Moreover, the stabilized RHS evaluation is already evaluated via (7.16) which directly samples the magnetic field. As in (7.25) a normal system of (7.26) is formed, since the number of samples and the number of unknowns are, in general, not the same.

7.3 Results

For both stabilized equivalent surface current reconstruction problems introduced in Section 7.3, simulation examples are considered to study the effects of the low-frequency issues of the EFIO. To this end, we start with the case of single RWG functions as probe antennas on a single surface.

7.3.1 Reconstruction of Fields Scattered by a Sphere

As a first inverse reconstruction scenario, we sample the field that is scattered by a sphere of radius 1 m when excited by an electric ring current of radius 0.5 m placed 2 m above the sphere. For the Huygens' surface and the sampling surface we choose spheres with radii $r_{\mathrm{H}} = 1.1\,\mathrm{m}$ and $r_{\mathrm{P}} = 1.2\,\mathrm{m}$, which are discretized with 945 and 1209 RWG functions, respectively. This setup has the advantage that it is not overly simple, yet an absolute reference is available in terms of a series expansion [Hofmann et al. 2023e; Jin 2015, pp. 368 ff.].

The reconstruction is then performed in a frequency range from $1 \times 10^{-10}\,\mathrm{Hz}$ to $1 \times 10^{8}\,\mathrm{Hz}$ and the NFs are evaluated at a distance of 3 m from the origin on a spherical grid with 5° resolution in ϑ and φ. On this grid we determine the worst case reconstruction error

$$\aleph = \max_{\vartheta,\varphi} \left\{ 20 \log \frac{|a(\vartheta,\varphi) - \hat{a}(\vartheta,\varphi)|}{\max\limits_{\vartheta,\varphi} |a(\vartheta,\varphi)|} \right\}, \tag{7.30}$$

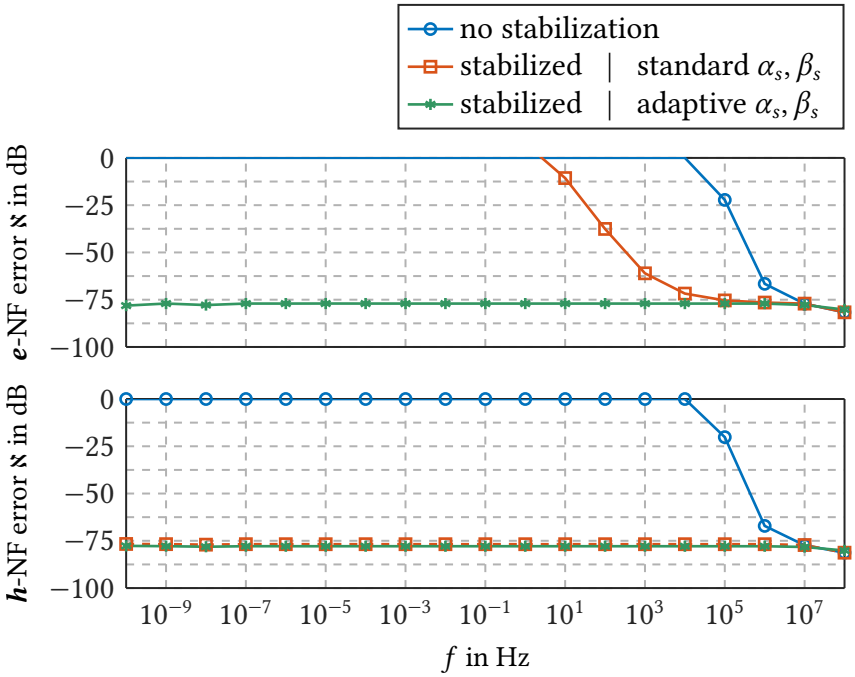

Fig. 7.1: Worst case errors of the reconstructed fields for the scattered fields from a sphere when excited by an electric ring current. The equivalent sources are placed on a spherical Huygens' surface of radius $r_\mathrm{H} = 1.1\,\mathrm{m}$. The spherical sampling surface 1209 RWG functions has a radius of $r_\mathrm{P} = 1.2\,\mathrm{m}$. © 2023 IEEE

where $a \in \{e, h\}$, that is, for the electric and magnetic NF. The result is depicted in Fig. 7.1, where we compare the unstabilized evaluation of $\boldsymbol{b} = \boldsymbol{T}\boldsymbol{j}$ with the stabilized one according to (7.23). For the latter, we furthermore distinguish between the symmetric normalization $\alpha_\mathrm{P} = \alpha_\mathrm{H} = 1/\sqrt{k}$ and $\beta_\mathrm{P} = \beta_\mathrm{H} = \sqrt{k}$, which is a popular choice for stabilizing quasi-Helmholtz decompositions in the context of the EFIE, and the adaptive normalization in (7.21) and (7.22). Clearly, without stabilization a breakdown occurs when going below 1 MHz, that is, the error for both, the electric and the magnetic NF increases abruptly. Using the stabilization via projectors the breakdown is prevented for the $\boldsymbol{h}$-field. However, the $\boldsymbol{e}$-field shows that only the adaptive normalization can ensure accurate fields. Employing the standard normalization shifts the breakdown only down to the kHz region.

Instead of testing with RWG functions we now place 2000 HDs and 1000 FDs on the surface of a sphere of radius $r_\mathrm{P} = 1.2\,\mathrm{m}$ as probes: 1000 points are placed on a spiral approximating a uniform distribution of points over the sphere following [Saff et al. 1997]. At each point two HDs are placed along $\boldsymbol{u}_\vartheta$ and $\boldsymbol{u}_\varphi$ and one FD is placed along $\boldsymbol{u}_r$ (i.e., normal to the surface). The worst case errors for the reconstructed fields are shown in Fig. 7.2. Also for this setup only the stabilized system (7.26) ensures accurate results when combined with the adaptive normalization. Notably, the overall error level is about 15 dB worse compared to testing the field with RWG functions. Moreover, at a frequency of about $f = 1 \times 10^8\,\mathrm{Hz}$ the error level increases notably. Both effects can potentially be attributed to the reduced sampling of the field: when testing the field with RWG functions, the field is evaluated at

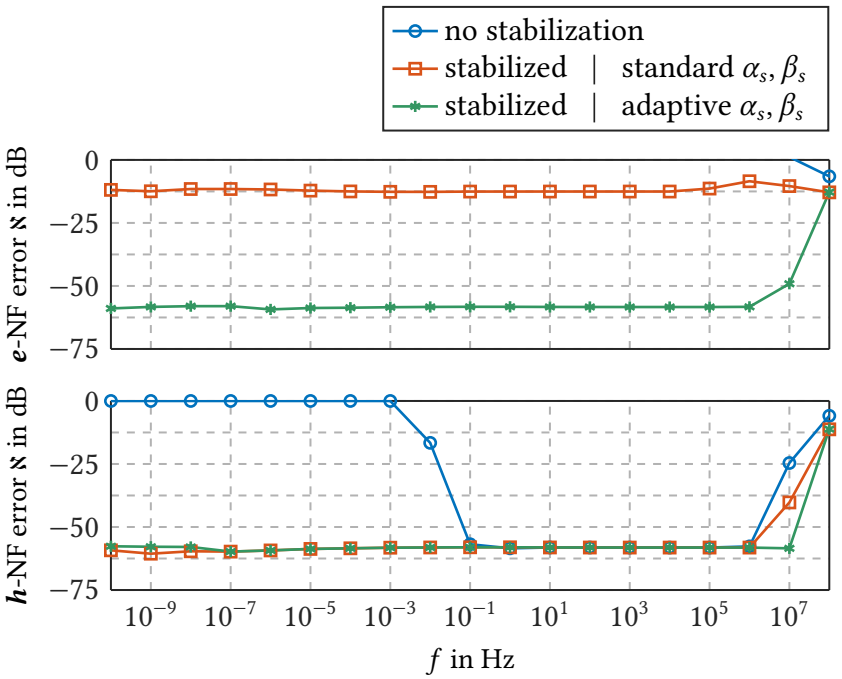

Fig. 7.2: Worst case errors of the reconstructed fields for the scattered fields from a sphere when excited by an electric ring current. The equivalent sources are placed on a spherical Huygens' surface of radius $r_{\mathrm{H}} = 1.1\,\mathrm{m}$. The 2000 HD and 1000 FD probes are placed on a spiral grid with radius $r_{\mathrm{P}} = 1.2\,\mathrm{m}$.

all quadrature points, which are about five time as many as for the dipoles.

To highlight the importance of the RHS evaluation in (7.24), we consider as a second reconstruction example the field that is scattered by the 1 m sphere when excited by a Hertzian dipole placed along the z-axis at $z = 2\,\mathrm{m}$. The worst case errors in the reconstructed fields for testing with RWG functions are depicted in Fig. 7.3. For the electric field, it can be seen that without the RHS stabilization both normalization strategies lead to a breakdown in accuracy, but with the RHS stabilization the breakdown is avoided. As the normalization coefficients of the adaptive normalization depend on the norms of the RHS, it is even more important to accurately determine the RHS components. The error in the $\boldsymbol{h}$-field reveals that problems occur already in the kHz region without the evaluation via scalar potentials. Again, only the adaptive normalization can ensure a low error level over the whole frequency range. A similar behavior can be observed in case the dipole probes are employed as shown in Fig. 7.4. Note that since the dipoles implicitly already evaluate the RHS in a stable manner, only standard and adaptive normalization are distinguished.

7.3.2 Reconstruction of a Ring Current

As a last and somewhat more realistic example, we excite the structure in Fig. 7.5 (a) by a voltage-gap source at $f = 1\,\mathrm{kHz}$. The fields are sampled on a box around the structure at

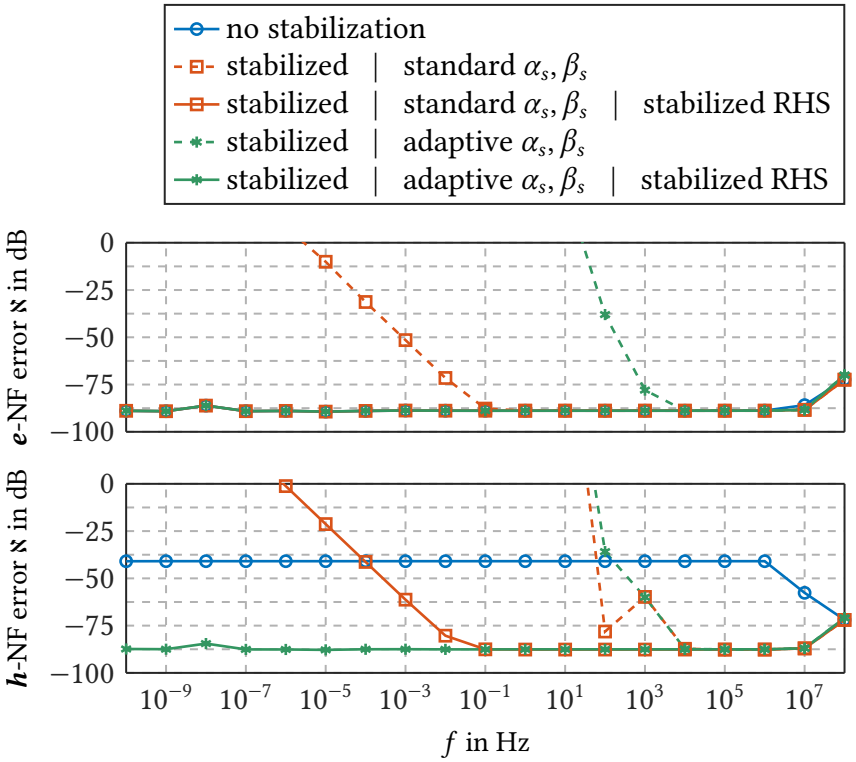

Fig. 7.3: Worst case errors of the reconstructed electric and magnetic NF for the scattered field from a sphere when excited by a HD. The equivalent sources are placed on a spherical Huygens' surface of radius $r_{\mathrm{H}} = 1.1\,\mathrm{m}$. The spherical sampling surface 1209 RWG functions has a radius of $r_{\mathrm{P}} = 1.2\,\mathrm{m}$. © 2023 IEEE

a distance of 4 cm, where the box is represented by 969 RWGs or by 3050 dipoles. For the stabilized reconstruction, the plate shown in Fig. 7.5 (b) discretized by 9506 RWGs is chosen as Huygens' surface. Clearly, the original currents can be identified well for both, the RWG and the dipole testing scheme. Notably, the dipole testing yields a more focused image, but contains more artifacts than when testing with RWG functions.

7.4 Conclusion

The investigations have shown that the low-frequency stabilization via quasi-Helmholtz projectors lead to accurate results. However, the adaptive normalization as well as a stable evaluation of the RHS (via a scalar potential) are substantial. As the latter requires the measurement of the magnetic field, it agrees with the circumstance that at low frequencies electric and magnetic field decouple. Consequently, it is advisable to measure both.

The process of sampling the field with probe antennas has been shown to constitute a crucial difficulty since it renders the necessary testing of the fields inaccessible to a quasi-Helmholtz decomposition. As a possible solution, a combination of special probe antennas has been investigated: one type of probe antenna corresponds to solenoidal testing functions and another type corresponds to non-solenoidal testing functions. The studied FD and HD

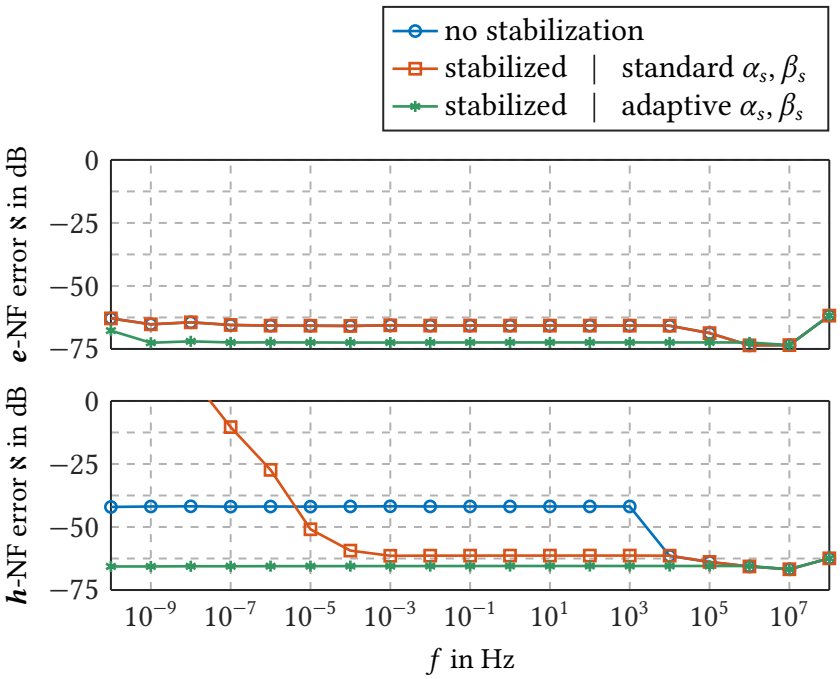

Fig. 7.4: Worst case errors of the reconstructed fields for the scattered fields from a sphere when excited by a HD. The equivalent sources are placed on a spherical Huygens' surface of radius $r_{\mathrm{H}} = 1.1\,\mathrm{m}$. The 2000 HD and 1000 FD probes are placed on a spiral grid with radius $r_{\mathrm{P}} = 1.2\,\mathrm{m}$.

indicate that this strategy is at least worth of further investigation with more realistic antennas.

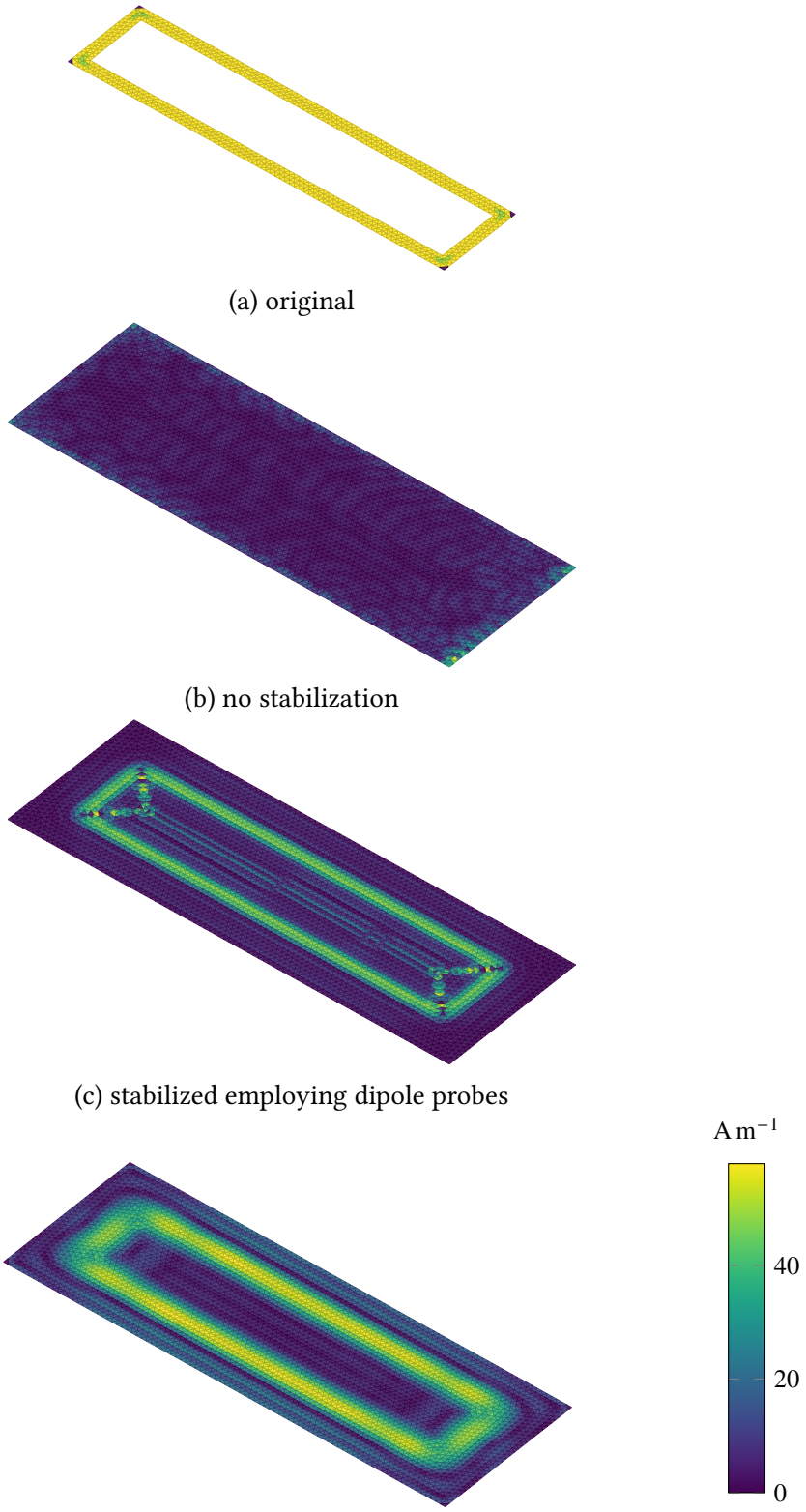

(a) original

(b) no stabilization

(c) stabilized employing dipole probes

(d) stabilized employing RWG probes

Fig. 7.5: Stabilized reconstruction of the magnitude of the surface current density of structure (a) when excited by a voltage gap source on the Huygen's surface (b) at a frequency of 1 kHz. © 2023 IEEE

8

On the Minimum Number of Samples for Sparse Recovery

"Measure what should be measured."
[Strohmer 2012]

A thorough picture is presented on the capability of compressed sensing to reduce the number of measurement samples that are required for a near-field to far-field transformation NFFFT, based on the spherical vector wave expansion of the radiated field of an antenna under test. To this end, the minimum number of samples for a sparse recovery is determined such that a predefined far-field accuracy can be achieved. As no suitable sampling theorem exists, this is done by performing extensive numerical simulations, considering possible deviations from exact sparsity, the influence of measurement noise, the sampling scheme, and the probe correction. Particularly, the influences are determined not only qualitatively but quantitatively. The resulting modified phase transition diagrams (PTDs) show that a reconstruction by the quadratically constraint basis pursuit strategy is sufficiently stable and robust for practical purposes. Simulation and measurement results of NFFFTs show that the predictions for the required number of samples hold true. Consequently, the presented approach using modified PTDs allows to reduce the number of measurement samples with predictable accuracy, when the sparsity level is known.

This chapter is based on [Hofmann et al. 2019d] including substantial verbatim portions, where preliminary results were presented in [Hofmann et al. 2018b; Hofmann et al. 2019c; Hofmann et al. 2019a; Hofmann et al. 2019b; Hofmann et al. 2020].

A major drawback of field transformations, is the long measurement time resulting from the large number of sampling points. A theory allowing to reduce the number of measurements for all antennas while keeping the accuracy is CS. It has its origin in the area of information theory, dealing with the reconstruction of a signal from incomplete frequency information [Candes et al. 2006a; Donoho 2006a; Candes

et al. 2006b]. It can be interpreted as a new sampling theorem, defining the framework to uniquely solve an underdetermined LSE by incorporating prior knowledge on the structure of the vector of unknowns and the system matrix. More specifically, the expansion coefficients are required to be sparse, that is, only a fraction of the coefficients is allowed to be considerably different from zero. In addition, the matrix of the LSE has to exhibit certain characteristics in order to guarantee that a unique solution exists. In the area of antenna and radar theory reviews of possible ways to apply CS are given in [Massa et al. 2015; Ender 2013; Migliore 2014]. However, concerning antenna measurements the focus was on array diagnosis from FF observations. In [Migliore 2015] different random sampling strategies for the more general problem of sampling the electromagnetic field radiated by sparse sources were compared.

A successful application to noisy FF antenna measurements has been reported in [Fuchs et al. 2017], where the FF was expanded as a linear combination of spherical harmonics. Indeed, in the context of cosmic microwave background radiation (CMB) a sparse spherical harmonics recovery with simulation data was already conducted in [Abrial et al. 2008]. However, in both cases neither the minimal required number of measurements nor the influence of noise or the sparsity (defects) have been investigated. Theoretical bounds concerning the minimum amount of measurements for the spherical harmonics recovery were initially determined in [Rauhut et al. 2011] and further improved by introducing different probability measures for the sampling locations in [Burq et al. 2012; Alem et al. 2014] and [Alem et al. 2013], where the latter was an empirical approach. Still, all these bounds turn out to be overly pessimistic, that is, it can be shown empirically that significantly less measurements suffice.

A first survey of possible challenges arising when applying CS to antenna NF measurements was given in [Cornelius et al. 2016], where the considered expansion basis was formed by the spherical vector waves. Yet, conclusions on the potential of CS in antenna NF measurements could only be conjectured. In [Löschenbrand et al. 2016] a modification of the basis was proposed by shifting the origin of the expansion to the phase center in order to increase the sparsity level. A theoretical investigation of the spherical vector wave expansion was performed in [Bangun et al. 2016] with a similar approach as the one used for the spherical harmonics. More precisely, sparse recovery in a Wigner-D expansion was treated. Again, however, the determined bounds on the number of measurements are overly pessimistic with virtually no hope for improvement (as will be further explained in Section 8.2).

As there are no approaches so far to establish a precise CS undersampling theorem as in [Donoho et al. 2010b] for the matrices occurring in the context of a spherical NFFFT, the idea developed in this chapter is to employ empirical investigations to determine the minimum number of samples for a sparse recovery. More specifically, inspired by the investigations in [Donoho et al. 2009], several phase transition diagrams (PTDs) are determined by simulations, however, in a modified form. They provide the number of measurements depending on the sparsity level and the desired accuracy of the reconstructed FF. In contrast to [Donoho et al. 2009] we investigate also the influences of measurement noise, deviations from exact sparsity, the sampling scheme, and the probe correction. The PTDs can furthermore be interpreted as a characterization of the system matrix of the NFFFT, showing that

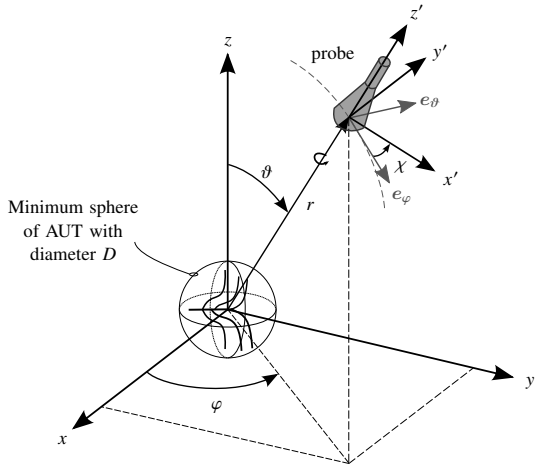

Fig. 8.1: Considered measurement setup: the probe coordinate system (x', y', z') always points to the origin of the AUT coordinate system (x, y, z). © 2019 IEEE

CS can be applied with predictable accuracy. As recovery strategy, basis pursuit (BP) and its quadratically constrained version are considered. Hence, a thorough picture is given on the capabilities of CS in the area of spherical NFFFTs. Some preliminary results using this approach have already been presented in [Hofmann et al. 2019a].

This chapter is organized as follows: Section 8.1 introduces the required principles of spherical antenna NF measurements. The applicability of CS to these is assessed in Section 8.2 by reviewing the relevant theoretical and practical aspects of CS. In Section 8.3 the minimum number of measurements is determined that is required for a successful NFFFT with CS. The influence of all relevant factors on this minimum, such as the sampling strategy and the probe correction, are considered qualitatively and quantitatively. Simulation and measurement results of NFFFTs by using CS are presented in Section 8.4, showing that the predictions for the amount of samples for a certain accuracy hold true.

8.1 Spherical Near-Field Measurements

The considered measurement setup for the spherical near-field to far-field transformation NFFFT is shown in Fig. 8.1. The antenna under test (AUT) is placed in the origin of the unprimed (AUT) coordinate system while the probe antenna and its primed coordinate system are assumed to always point to this origin. The position of the probe with respect to the AUT coordinates is defined by the spherical coordinates $(r^\mathrm{p}, \vartheta^\mathrm{p}, \varphi^\mathrm{p})$ summarized in the position vector $\boldsymbol{r}^\mathrm{p}$ and the rotation around the z'-axis by the angle χ^p with respect to the unit vector $\boldsymbol{e}_\varphi$.

Assuming the AUT radiates a signal into free space, the fields exterior to the minimum sphere of the AUT can be expressed as a linear combination of the (power normalized)

spherical vector wave functions $\boldsymbol{q}^{(4)}_{amn}$ as defined in Section 2.2.2, that is,

$$\boldsymbol{e}_{\mathrm{AUT}} = \frac{k}{\sqrt{\eta}} \sum_{n=1}^{L} \sum_{m=-n}^{n} \sum_{s=1}^{2} x_{amn} \boldsymbol{q}^{(4)}_{a,m,n} \tag{8.1}$$

with the expansion coefficients $x_{amn} \in \mathbb{C}\sqrt{\mathrm{W}}$ and the summation limit $L \to \infty$ (commonly referred to as the number of modes). Setting L in (8.1) to a finite value, leads to an acceptable error in the field representation if for an AUT of minimum sphere diameter D, it is chosen as [Hansen 1988, pp. 15ff]

$$L \geq \frac{kD}{2} + \epsilon\,, \tag{8.2}$$

where ϵ (often chosen in the order of 10) is introduced empirically to increase the accuracy (see [Hansen 1988, pp. 20ff] for the impact). The signal y received by the probe antenna can be related to the expansion coefficients by (the transmission formula)

$$y(\boldsymbol{r}^{\mathrm{p}}, \chi^{\mathrm{p}}) = \sum_{n=1}^{L} \sum_{m=-n}^{n} \sum_{s=1}^{2} x_{amn} A_{amn}(\boldsymbol{r}^{\mathrm{p}}, \chi^{\mathrm{p}})\,, \tag{8.3}$$

where the influence of the probe and its position is captured in the coefficients

$$A_{amn}(\boldsymbol{r}^{\mathrm{p}}, \chi^{\mathrm{p}}) = \frac{1}{2} \sum_{\mu=-n}^{n} \sum_{\sigma=1}^{2} \sum_{\substack{\nu=|\mu| \\ \nu\neq 0}}^{\infty} \mathrm{D}_{\mu nm}(\vartheta^{\mathrm{p}}, \varphi^{\mathrm{p}}, \chi^{\mathrm{p}}) \mathrm{C}_{\sigma\mu\nu sn}(k r^{\mathrm{p}})\, R^{\mathrm{p}}_{\sigma\mu\nu}\,. \tag{8.4}$$

Here, $\mathrm{D}_{\mu nm} = \mathrm{e}^{-\mathrm{j}m\varphi^{\mathrm{p}}} \mathrm{d}_{\mu nm}(\vartheta^{\mathrm{p}}) \mathrm{e}^{-\mathrm{j}\mu\chi^{\mathrm{p}}}$ are the Wigner-D functions with $\mathrm{d}_{\mu nm}$ as defined in [Hansen 1988, pp. 343ff] and $\mathrm{C}_{\sigma\mu\nu sn}$ constituting translation functions as defined in [Hansen 1988, pp. 355ff]. The coefficients $R^{\mathrm{p}}_{\sigma\mu\nu}$ capture the receiving characteristic of the probe antenna based on the multimode scattering matrix description derived in [Hansen 1988, pp. 27ff]. Moreover, for (8.3) to be valid multiple reflections between probe and AUT should be negligible.

The summations in (8.3) can be expressed in vector notation with an arbitrary ordering of the coefficients. Collecting M measurements and stacking the received signals y into the measurement vector $\boldsymbol{y} \in \mathbb{C}^M$, sorting the corresponding A_{amn} into the sensing matrix $\boldsymbol{A} \in \mathbb{C}^{M\times N}$ and calling the vector with the expansion coefficients $\boldsymbol{x} \in \mathbb{C}^N$, the LSE

$$\boldsymbol{y} = \boldsymbol{A}\boldsymbol{x} \tag{8.5}$$

can be formulated. The number of coefficients can be determined as $N = 2L(L+2)$. Solving (8.5) for $\boldsymbol{x}$ allows one to compute the field of the AUT by evaluating (8.1) or alternatively the FF by using the limit given in (2.30). A full rank LSE leading to a unique solution of (8.5) can be obtained by taking $M = N$ measurement samples. However, often more samples are taken in order to average out noise. Furthermore, and in contrast to the here proposed approach, often two orthogonal polarizations are measured at each point.

8.2 Applicability of Compressed Sensing

As mentioned in the introduction CS allows one to uniquely solve the LSE in (8.5) for $M \leq N$, that is, although the LSE is underdetermined. Requirement for this unique solution is that $\boldsymbol{x}$ is sparse or compressible.

8.2.1 Sparsity and Compressibility

The vector $\boldsymbol{x}$ is referred to as s-sparse, if at most s of its entries are different from zero. More formally,

$$\|\boldsymbol{x}\|_0 := \mathrm{card}(\mathrm{supp}(\boldsymbol{x})) \leq s \tag{8.6}$$

has to hold, with $\mathrm{supp}(\boldsymbol{x}) = \{i \in \{1, 2, \dots, N\} \mid x_i \neq 0\}$ denoting the support of $\boldsymbol{x}$ and $\mathrm{card}(\mathcal{S})$ denoting the cardinality of a set $\mathcal{S}$.

Since real world signals, represented by the vector $\boldsymbol{x}$, are rarely exactly s-sparse, a relaxation to compressible signals can be considered. A common approach is to approximate $\boldsymbol{x}$ by an s-sparse vector $\hat{\boldsymbol{x}}$ such that the introduced ℓ_p error σ_s is minimized, that is, $\sigma_s(\boldsymbol{x})_p = \min_{\hat{\boldsymbol{x}} \in \mathcal{S}_s} \|\boldsymbol{x} - \hat{\boldsymbol{x}}\|_p$, where $\mathcal{S}_s = \{\boldsymbol{x} \in \mathbb{C}^N \mid \|\boldsymbol{x}\|_0 \leq s\}$ defines the set of all s-sparse vectors (see, e.g., [Foucart et al. 2013, p. 42]). Without further specification the signal is then called compressible, if σ_s decays quickly with increasing s. However, in this thesis a more practical measure for the level of sparsity defects is introduced. With

$$\tau = \frac{\max |x_{\mathrm{defect}}|}{\max\limits_{amn} |x_{amn}|} \tag{8.7}$$

the ratio of the maximum magnitude of a coefficient x_{defect} considered as defective (i.e., close to but not exactly zero) to the maximum of all coefficients x_{amn} is measured. This definition will be used in Section IV to investigate the influence of deviations from exact sparsity.

8.2.2 Recovery Strategy

For the actual recovery of an s-sparse vector $\boldsymbol{x}$ different approaches (see, e.g., [Duarte et al. 2011] for an overview) have been proven to give the exact solution to the underdetermined LSE (under additional conditions outlined in the following subsection). The strategy considered in this thesis is to solve the optimization problem

$$\hat{\boldsymbol{x}} = \arg\min_{\boldsymbol{z} \in \mathbb{C}^N} \|\boldsymbol{z}\|_1 \quad \text{s.t.} \quad \boldsymbol{y} = \boldsymbol{A}\boldsymbol{z}\,, \tag{8.8}$$

which is called basis pursuit (BP). For the case that the measurements are contaminated with noise, such that (8.5) becomes $\boldsymbol{y} = \boldsymbol{A}\boldsymbol{x} + \boldsymbol{n}$, it might be advantageous to generalize the

minimization in (8.8) to

$$\hat{\boldsymbol{x}} = \arg\min_{\boldsymbol{z}\in\mathbb{C}^N} \|\boldsymbol{z}\|_1 \quad \text{s.t.} \quad \|\boldsymbol{A}\boldsymbol{z} - \boldsymbol{y}\|_2 \leq \eta\,, \tag{8.9}$$

what is referred to as quadratically constrained basis pursuit and abbreviated in this thesis as BP_η. The choice of the parameter η depends on the noise level (e.g., for bounded noise $\|\boldsymbol{n}\|_2 \leq \eta$) and will be addressed in more detail in Section IV. Note that the strategies (8.8) and (8.9) were also the ones considered in [Abrial et al. 2008; Rauhut et al. 2011; Burq et al. 2012; Alem et al. 2014; Alem et al. 2013; Cornelius et al. 2016; Löschenbrand et al. 2016; Fuchs et al. 2017]. While other approaches like greedy or thresholding based methods [Duarte et al. 2011] can be less computationally demanding (see [Foucart et al. 2013, p. 73] for a discussion), BP and BP_η usually require less measurements for a successful recovery [Eldar et al. 2012, pp. 358f].

8.2.3 The Required Number of Measurements

The most intricate aspect of CS is to determine recovery guarantees stating an exact number of measurements required for successful recovery. Ideally, for the underdetermined LSE in (8.5) and a specific recovery algorithm, a sampling theorem would give the exact minimum M as a function of s, N and $\boldsymbol{A}$ for a known sparsity s, that is, $M > f(s, N, \boldsymbol{A})$. Preferably, also noise and sparsity defects are considered. With the intention to do so, different approaches either classify the matrix $\boldsymbol{A}$ or capture its relevant properties in a characteristic value.

Null Space Property, Coherence and RIP

The first recovery guarantee for an arbitrary sensing matrix was given by characterizing its null space. This characterization is, however, non-deterministic polynomial-time hard (NP-hard) to compute and therefore not relevant for practical purposes [Eldar et al. 2012, p. 24]. In contrast, the coherence of a matrix (see [Donoho et al. 2001; Tropp 2004]) is feasible to compute but leads (necessarily) to guarantees in the form of $M \geq C\,s^2$ with a universal constant C [Foucart et al. 2013, p. 125]. Due to the contained quadratic dependency this approach is only suited for very sparse vectors $\boldsymbol{x}$, which can not be expected for general antennas.

The probably most dominant tool used to determine recovery guarantees in CS is the restricted isometry property (RIP) originally introduced in [Candes et al. 2005]. Despite the attention the RIP experienced, it has two major drawbacks making it uninteresting for antenna NF measurements (and other practical purposes). Like the null space property it is NP-hard to compute [Tillmann et al. 2014]. As a workaround only random matrices (e.g., Bernoulli, Gaussian and sub-Gaussian distributed) have been considered [Strohmer 2012]. For these it can be shown that the RIP holds with high probability. The second drawback is that even if the RIP constant can be determined, the lower bounds on the minimal number of required measurements are overly pessimistic. According to [Donoho et al. 2010b] the

most precise bound in terms of the RIP has been given by [Blanchard et al. 2011]. Still, it can be shown by numerical experiments that far fewer measurements suffice for a reliable recovery [Donoho et al. 2009]. This can partially be explained by the fact that the RIP is only a sufficient condition for the basis pursuit (BP) to be successful [Eldar et al. 2012, p. 310].

Bounded Orthonormal Systems

The only recovery guarantee given so far for antenna NF measurements is based on associating the sensing matrix to a bounded orthonormal system (BOS) [Bangun et al. 2016]. This means that the entries of the sensing matrix are linked to a set of orthonormal functions $\{\phi_1, \dots, \phi_N\}$ which are uniformly bounded with some constant B as $\|\phi\|_\infty \leq B$ in the form of $(\boldsymbol{A})_{lq} = \phi_q(\boldsymbol{t}_l)$, where $\boldsymbol{t}_l$ are the sampling points distributed according to a probability measure (see [Fornasier 2010, pp. 19ff]). Since for the Wigner-D functions $\mathrm{D}_{\mu nm}$ in (8.4) such a uniform bound can be found, this approach seems to be appropriate. However, the derived recovery guarantees are linked to the RIP and consequently overly pessimistic with virtually no hope for significant improvement [Donoho et al. 2010b].

Precise Undersampling Theorems

Due to the empirical observation of a phenomenon called phase transition in [Donoho 2006b; Donoho et al. 2005] new approaches have arisen. According to this phenomenon, if for a certain number of measurements the sparsity is below a certain threshold, the BP strategy will recover $\boldsymbol{x}$ with overwhelming probability, above the threshold the recovery fails with high probability. Theoretically, the phase transition was explained in [Donoho 2006b; Donoho et al. 2005; Donoho et al. 2008], summarized in [Donoho et al. 2010b].

Key feature of the projected polytope approach is that it gives a necessary and sufficient condition for successful recovery and consequently establishes a precise undersampling theorem. While the analysis is asymptotic in the first place (i.e., $N \to \infty$), it is shown in [Donoho et al. 2010a] that for finite N the number of samples has to be increased with decreasing N. Drawbacks are that the approach is limited to the real valued case and more importantly to Gaussian random matrices. The same limitations hold for the nullspace Grassmann angle approach proposed in [Xu et al. 2011], which, however, indicates that (as put in [Donoho et al. 2010b]) no "qualitative gap" occurs between the exact sparse case and compressible signals. With increasing deviations from exact sparsity the number of measurements have to be increased continuously for a recovery.

Observed Universality

Since in the considered field transformation the sensing matrix is complex valued and has no random Gaussian distribution, none of the available precise undersampling theorems is

fitting. (Note that there are also other but less sharp approaches aiming at a precise undersampling theorem, such as [Zhang 2013; Stojnic et al. 2008a; Stojnic et al. 2008b; Stojnic 2010].) Even though, they provide some insights, the perhaps most promising results are the ones obtained by extensive numerical simulations in [Donoho et al. 2009]. The idea was to determine the phase transition of different kinds of (random) matrices by simulating several combinations of sparsity s and number of samples M. The simulations reveal that all considered matrices exhibit the same phase transition. Furthermore, the results show that the asymptotic theory works accurately already at moderate N. This leads the authors of [Donoho et al. 2009] to the hypothesis that there has to be a larger class of matrices, which all obey the Gaussian phase transition. Although, up to now this class has not been identified, the results suggest that sparse recovery with a moderate amount of samples M is possible for a large variety of sensing matrices.

Uniform and Nonuniform Recovery

An important distinction made by the above approaches is between strong (uniform) and weak (nonuniform) recovery guarantees [Foucart et al. 2013, pp. 48ff]. In terms of antenna measurements the strong one can be interpreted as choosing the sampling points once at random (determining the sensing matrix) and using them for all AUTs. The weak guarantee corresponds to choosing the sampling points at random for each AUT anew. In the latter case considerably less measurements should be required to guarantee a successful recovery. A possible interpretation of this circumstance is that the probability that one distribution of sampling points is suitable for all AUTs is much smaller than the probability that a set of (random) points fits for only one AUT. However, as it turns out in the next section, even for a deterministic set of sampling points recovery guarantees very close to the weak ones can be achieved.

8.3 The Minimum Number of Samples for CS in Spherical NFFFT

Despite the lack of compressed sensing (CS) theories fully fitting to antenna measurements, their insights reveal that useful recovery guarantees can also be achieved for the matrices employed in antenna NF measurements. Therefore, it is proposed to determine the minimum number of samples by simulations yielding phase transition diagrams (PTDs). Beyond that, and for the first time, the impact of all potential influence factors is quantified with the PTDs.

8.3.1 Setting up the PTDs

The general concept of PTDs is to perform several reconstructions for all possible combinations of sparsity s and the number of measurements M for a certain sensing matrix $\boldsymbol{A}$ and to

record the percentage of success. To this end, the vector $\boldsymbol{x}$ of size N is generated by setting s random entries (chosen uniformly at random) of $\boldsymbol{x}$ to random complex numbers drawn from the standard normal distribution, all other entries are zero. After the selection of the sampling locations $\boldsymbol{r}^{\mathrm{p}}$ and the probe orientation angles χ^{p} the sensing matrix is constructed following (8.4) with an implementation following the approach described in [Mauermayer et al. 2018]. The number of modes is fixed to $L = 8$ resulting in $N = 160$ coefficients. While this would be a very small number of modes for actual antennas, it can be assumed that the results also hold for any larger L. This assumption is based on the results of [Donoho et al. 2010a] (for increasing N the results hold even better) and verified in the following Subsection E. For the values of $M = 16, 48, 80, 112, 144$ and 160 the sparsity s is varied and for each combination (M, s), $R = 150$ problem instances are considered. Usually, the sparsity is varied from 1 to M. However, in order to reduce the computation time, s is only increased until the percentage of success drops below 1 %. The remaining values for s are not simulated, since it can be expected that all reconstructions in this parameter regime are not successful. Furthermore, at each M the last s is recorded for which the recovery success is 100 %. This is then the first s to be simulated for the next M. Hence, only the area around the phase transition is simulated. For each problem instance, the BP or its quadratically constrained version BP_η is solved. To this end, the CVX MATLAB package is used [Grant et al. 2014; Grant et al. 2008] together with the solver from Mosek [MOSEK 2015]. (Note that a fast solution of the BP or the BP_η problem can be achieved by using, for example, the solution approach described in [Berg et al. 2009]. This approach does not require the sensing matrix explicitly, but only products of the form $\boldsymbol{A}\boldsymbol{x}$ (see also [Mauermayer et al. 2018]).) A success for the reconstructed solution is recorded if the maximum occurring reconstruction error $\aleph$ is below a certain threshold.

To verify that a phase transition occurs at all, the sampling points are initially distributed uniformly at random over the surface of a sphere with radius $r^{\mathrm{p}} = 5\,\mathrm{m}$ (i.e., $\varphi = 2\pi u$ and $\vartheta = \arccos(2v - 1)$ with u and v chosen randomly from $]0, 1[$) and the polarization angles χ^{p} are selected uniformly at random from the interval $[0, \pi/2]$. (The sampling locations are generated for each reconstruction anew, i.e., a weak transition bound is simulated). As probe antenna a HD is used. The determined PTD is depicted in Fig. 8.2. The number of measurements M and the sparsity s are related to the number N of entries in $\boldsymbol{x}$ by $\delta = M/N$ as well as $\zeta = s/N$. The domain $(\delta, \zeta) \in [0, 1]^2$ is called phase space. For a successful recovery by the BP strategy $\|\boldsymbol{x} - \hat{\boldsymbol{x}}\|_\infty \leq 10^{-6}$ is demanded. The colors indicate the percentage of success, from yellow 0 % to blue 100 %. The parameters in the white areas were not simulated. With the occurring steep change from 100 % to 0 % a phase transition can be identified.

8.3.2 Comparison with Theoretical Bounds

For a better comparison also with other bounds, the largest s are extracted for which 10 % and 100 % recovery success is achieved. The corresponding curves together with the theoretical bounds from the bounded orthonormal systems (BOS) and the projected polytope approach are depicted in Fig. 8.3. For interim values a cubic interpolation is performed (the

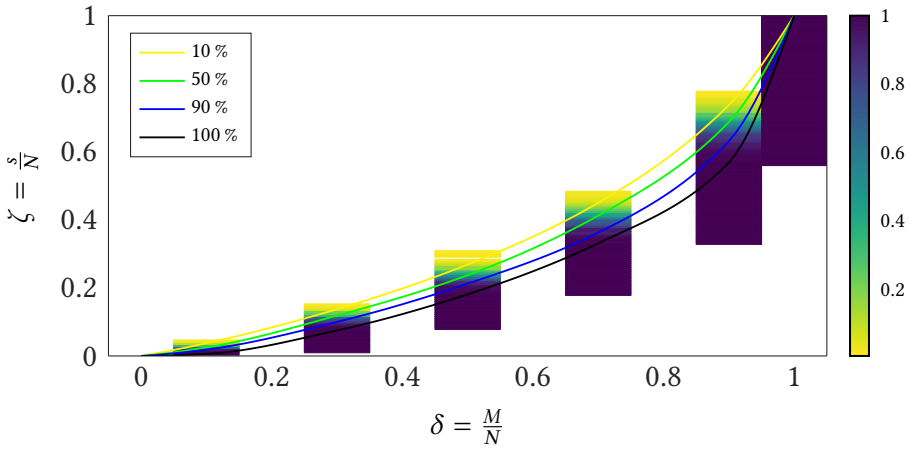

Fig. 8.2: PTD: The sampling points are distributed uniformly at random over the surface of a sphere with radius $r^{\mathrm{p}} = 5\,\mathrm{m}$. The polarization angles are selected uniformly at random from the interval $[0, \pi/2]$. For a successful recovery by the BP $\|\boldsymbol{x} - \hat{\boldsymbol{x}}\|_\infty \leq 10^{-6}$ is demanded. The depicted lines are in ascendig order from top to bottom form 10 % to 100 %. © 2019 IEEE

markers highlight the actually simulated points). It can be seen that not only a phase transition is occurring, but it is also close to the theoretical bound $\zeta(\delta, \text{weak})$ known from the projected polytope approach. This is quite notable, as the sensing matrix is not a random Gaussian matrix (but has considerable structure), $N = 160$ is of moderate size and the setting (sensing matrix, expansion coefficients and measurements) is complex valued. (Note that the numerical computation of $\zeta(\delta, \text{weak})$ and $\zeta(\delta, \text{strong})$ is described in [Donoho et al. 2010a] and tabulated values are provided in Matlab format in [Tanner 2012].) Furthermore, the empirical bounds excel the prediction of the theoretical curve $\zeta(\delta, \text{weak})$ for $M = N$. Consequently, a reconstruction in antenna NF measurements can be even successful for all levels of sparsity (i.e., also for $s = N$). The curve for the BOS method was determined according to the result of [Bangun et al. 2016], requiring

$$M \geq C\, N^{1/6}\, s\, \log^3(s)\, \log(N)\,, \tag{8.10}$$

where the universal constant C was chosen such that the bound is in all points not larger than the empirical 100 % curve (since no explicit values are available for C). Also note that while the bound given in [Bangun et al. 2016] was classified as strong, the same bound is achieved for weak recovery. This is due to the same functional dependency on s in the theorems for strong (see [Fornasier 2010, pp. 26ff]) and weak (see [Foucart et al. 2013, p. 393]) recovery, whereas all other dependencies are compensated by the universal constant. Compared to the (weak) empirical 100 % bound the BOS bound is far from being optimal.

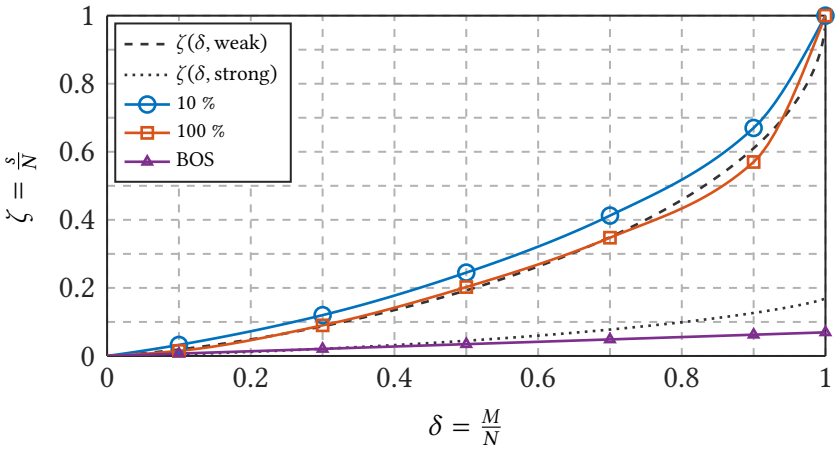

Fig. 8.3: Extracted success curves of 10 % and 100 % from the PTD in Fig. 8.2. The BOS bound corresponds to (8.10) with the constant C chosen such that the bound is in all points not larger than the empirical 100 % curve. © 2019 IEEE

8.3.3 The Error Definition

Before investigating different influences on the reconstruction performance the question arises how to properly define the reconstruction error for antenna NF measurements. Certainly, the so far used requirement $\|\boldsymbol{x}-\hat{\boldsymbol{x}}\|_\infty \leq 10^{-6}$ for a successful recovery is too restrictive when noise is included. The theorems for robust recovery suggest to consider errors of the form $\|\boldsymbol{x}-\hat{\boldsymbol{x}}\|_p \leq C\,\eta$ for bounded noise $\|\boldsymbol{e}\|_2 \leq \eta$. For the spherical harmonics recovery in [Fuchs et al. 2017] the mean squared error $\mathrm{MSE}(\hat{\boldsymbol{x}}) = \mathcal{E}[(\boldsymbol{x}-\hat{\boldsymbol{x}})^2]$ was put forward with $\mathcal{E}$ denoting the expected value. However, it is difficult to impose requirements on the error of the reconstructed coefficient vector (e.g., require that $\|\mathrm{MSE}(\hat{\boldsymbol{x}})\|_\infty$ is smaller than some bound). In antenna measurements the quantity of interest is usually the FF pattern, for which requirements on the accuracy are defined. A common (logarithmic) definition of a relative error $\aleph$ is

$$\aleph = \max_{\vartheta,\varphi}\left\{20\log\frac{\left|e^{\mathrm{FF}}(\vartheta,\varphi)-\hat{e}^{\mathrm{FF}}(\vartheta,\varphi)\right|}{\max\limits_{\vartheta,\varphi}|e^{\mathrm{FF}}(\vartheta,\varphi)|}\right\}, \tag{8.11}$$

which is then required to stay below a certain level (e.g., $\aleph \leq -60\,\mathrm{dB}$). Here, e^{FF} and $\hat{e}^{\mathrm{FF}}$ denote the magnitude of the reference and the reconstructed FF, respectively. In order to transfer such a definition to the coefficient vectors $\boldsymbol{x}$ and $\hat{\boldsymbol{x}}$ a kind of propagation of error would be necessary based on the relationship in (8.1) together with (2.30). However, since no recovery guarantees of the form $\|\boldsymbol{x}-\hat{\boldsymbol{x}}\|_p \leq C\,\eta$ are at hand, it seems more natural to just evaluate the error in the FF pattern. To this end, $e^{\mathrm{FF}}(\vartheta,\varphi)$ and $\hat{e}^{\mathrm{FF}}(\vartheta,\varphi)$ are determined from $\boldsymbol{x}$ and $\hat{\boldsymbol{x}}$ on a grid with a resolution of approximately 5.6° in ϑ and φ (32 values in ϑ and 64 values in φ) and the worst case error (8.11) is determined.

Having defined the error $\aleph$ it is useful to introduce a modified PTD as the one shown in Fig. 8.4. Instead of the success rate (for a certain required error), the average of the R

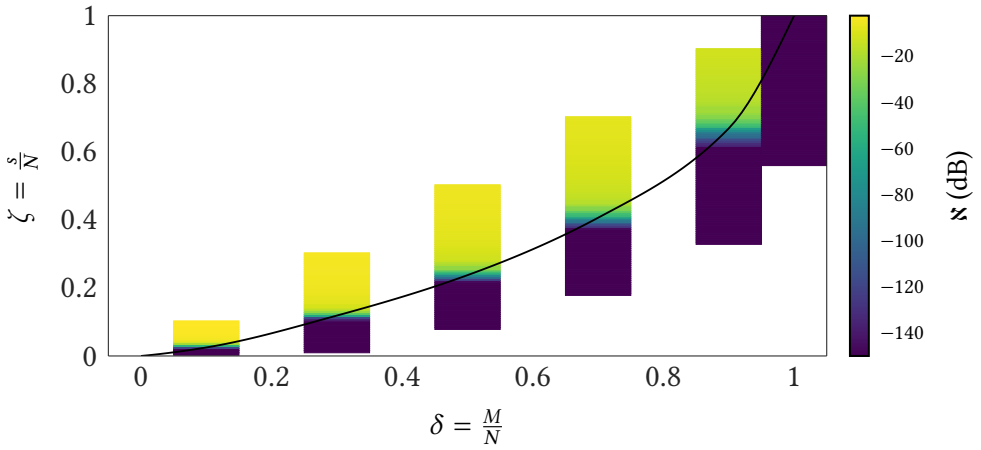

Fig. 8.4: PTD not showing the success rate, but the average reconstruction error א (in dB) for different combinations of (k, M). In order to increase the resolution for lower accuracies, all error levels smaller than −150 dB were set to −150 dB. The depicted transition bound corresponds to the largest s for which $א \leq -60$ dB is achieved. © 2019 IEEE

reconstruction errors א for the combinations (s, M) is depicted. In this way the required number of measurements can be determined for a certain sparsity and a desired error from the diagram. In the following mostly extracted transition bounds from such PTDs are used for comparisons. The choice of $א \leq -60$ dB for the noiseless case is somewhat arbitrary, but is in a practical range and well suited for the comparisons. As can be seen from Fig. 8.4 far smaller errors can be achieved.

8.3.4 Influence of the Sampling Grids

As a next step the influence of different sampling grids is investigated. The corresponding transition bounds are depicted in Fig. 8.5 (still for a Hertzian dipole (HD) as probe antenna). Again for interim values between the markers cubic interpolation is used. Firstly, grids are compared where the polarization angles were selected uniformly at random from the interval $[0, \pi/2]$ (pol. 1). As can be expected (from the classical PTD in Fig. 8.3), distributing the M sampling points uniformly at random over the surface of a sphere yields a useful transition bound. In contrast, when using an equiangular grid the bound shifts downwards considerably. It might be conjectured that, when using so few samples, it is detrimental to have areas where the sampling locations are concentrated more densely. This is also confirmed by the "igloo" distribution introduced in [Fuchs et al. 2017] with a spacing of $\Delta\varphi = \Delta\vartheta / \sin\vartheta$ and $\Delta\vartheta = \text{const}$. The scheme reduces the density at the poles but does not achieve a uniform distribution. Consequently, the bound is closer to the one with random sampling but still slightly worse. Almost identical to the random sampling is the bound of a spiral grid which is designed to approximate a uniform distribution of the sample points over the sphere. In particular, the used spiral grid is the one presented in [Saff et al. 1997].

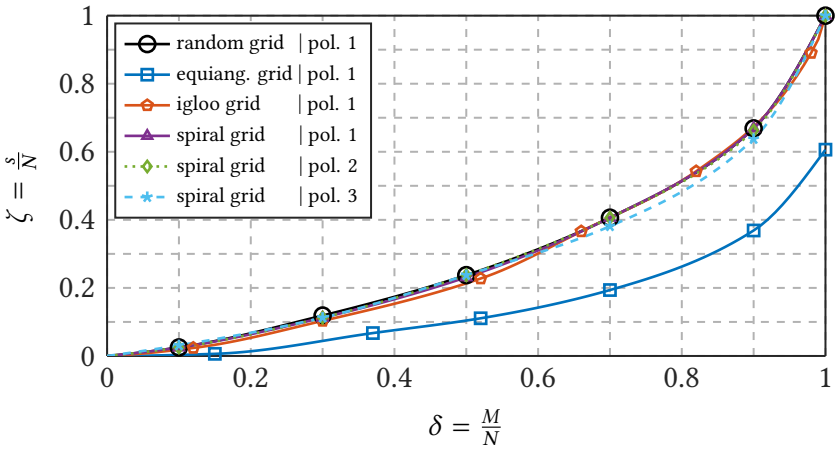

Fig. 8.5: Transition bounds corresponding to $\aleph \leq -60$ dB for different sampling grids using the BP as recovery strategy. The polarization (pol.) angles χ were chosen according to pol. 1: each selected uniformly at random from the interval $[0, \pi/2]$; pol. 2: each selected uniformly at random from $\{0, \pi/2\}$; pol. 3: for consecutive points the polarization is alternately 0 and $\pi/2$. © 2019 IEEE

Introducing the auxiliary parameters

$$h_m = -1 + \frac{2(m-1)}{M-1} \tag{8.12}$$

for $1 \leq m \leq M$, the measurement positions are computed as

$$\vartheta_m = \arccos(h_m) \tag{8.13}$$

and

$$\varphi_m = \left(\varphi_{m-1} + \frac{3.6}{\sqrt{M}} \frac{1}{\sqrt{1-h_m^2}} \right) \mod 2\pi \tag{8.14}$$

for $2 \leq m \leq M-1$, where $\varphi_1 = \varphi_M = 0$. Since the spiral grid is better suited for measurements than a random grid, it is used for all further investigations. While there are other grids which could work well with CS, each has to be checked individually with the proposed approach.

Concerning the selection process of the polarization angles two more options are considered. When the χ^{p} are randomly chosen to be either 0 or $\pi/2$ the transition bound is virtually the same as for polarization 1. Finally, if for consecutive points the polarization is alternately 0 and $\pi/2$ the transition bound shifts down slightly. However, the bound is still in a useful range despite no more randomness is involved in the measurement process. This is quite notable, since the predictions of strong transition bounds (to which it now has to be compared) are usually considerably more pessimistic.

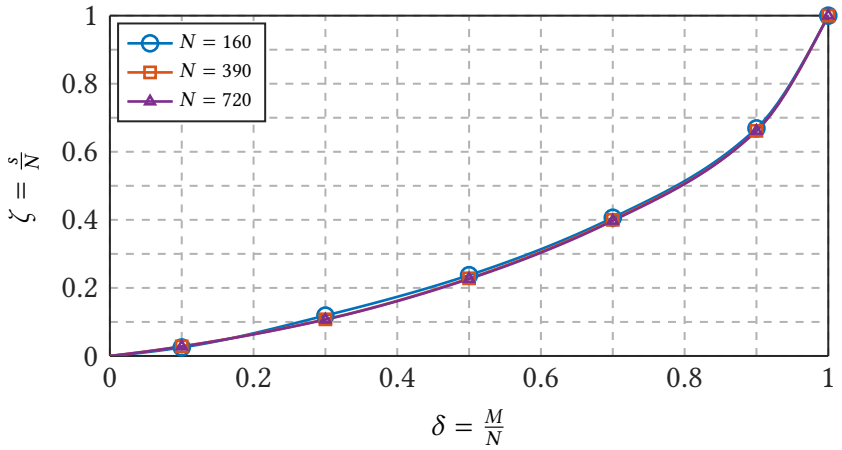

Fig. 8.6: Transition bounds corresponding to $\aleph \leq -60$ dB for different numbers of expansion coefficients N using the BP recovery strategy. © 2019 IEEE

8.3.5 Influence of the Problem Size

Using the spiral grid with pol. 1 it is verified in Fig. 8.6 that the number of expansion coefficients N can be increased without having influence on the transition bound. Consequently, the determined bounds are also valid for large antennas.

8.3.6 Influence of Sparsity Defects—Stability

In order to investigate the stability, that is, the influence of deviations from exact sparsity, sparsity defects are added to the coefficient vector $\boldsymbol{x}$. More precisely, scaled Gaussian noise such that the maximum value is equal to $\tau \max_{amn} |x_{amn}|$ is added to the vector $\boldsymbol{x}$ (see (8.7) for the definition of τ). However, it is added only to the $N-k$ coefficients which are initially zero. The resulting coefficients in $\boldsymbol{x}$ are the ones to be reconstructed and based on them the measurement samples are created ($\boldsymbol{y} \leftarrow \boldsymbol{A}\boldsymbol{x}$).

The resulting transition bounds for different τ-values and the reconstruction approach basis pursuit (BP) are shown in Fig. 8.7. In general with increasing τ the transition bound is shifted downwards. For $M = N$ all sparsity levels can always be reconstructed, which is evident from the fact that at most N coefficients can be different from zero and consequently, there is no difference for different τ-levels at $\delta = 1$. Important is that (as put in [Donoho et al. 2010b]) no "qualitative gap" occurs between the exact sparse case ($\tau = 0$) and compressible signals. The transition bounds shift downwards continuously. However, and in contrast to [Xu et al. 2011] the here presented approach can quantify the shift. Note, that the chosen values for τ appear to be in a practical range considering the expansion coefficients of different antennas (see also Section V).

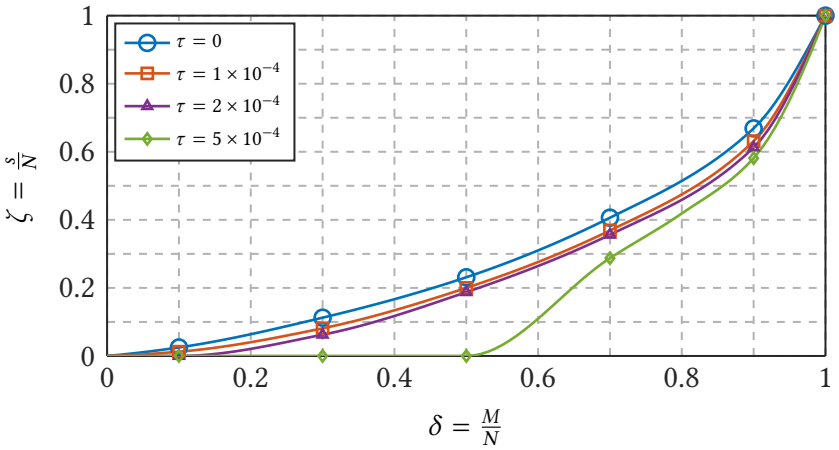

Fig. 8.7: Transition bounds corresponding to $\aleph \leq -60\,\text{dB}$ for different levels of sparsity defects τ using the BP recovery strategy. © 2019 IEEE

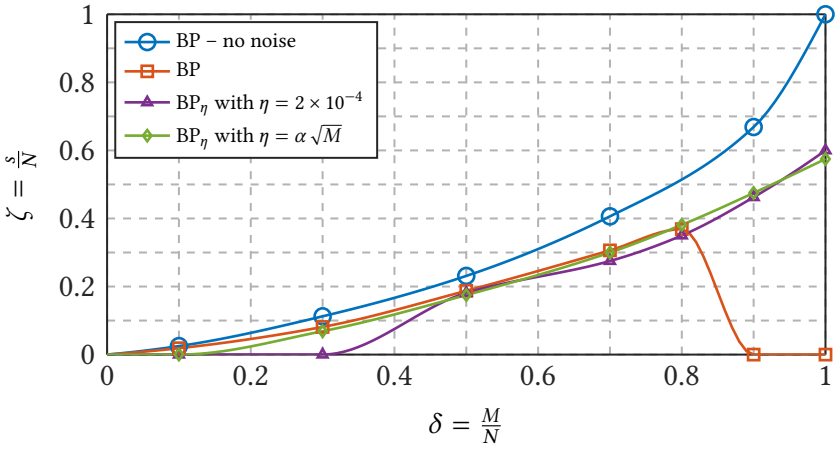

Fig. 8.8: Transition bounds corresponding to $\aleph \leq -45\,\text{dB}$ for an SNR of 60 dB and different recovery strategies, where $\alpha = 1.975 \times 10^{-5}$. The transition bound for the noiseless case is depicted as well. © 2019 IEEE

8.3.7 Influence of Noise—Robustness

Besides the stability against sparsity defects also the robustness against measurement noise is of interest. In order to examine such an influence, complex white Gaussian noise is added to the measurement vector in the form of $\boldsymbol{y} = \boldsymbol{A}\boldsymbol{x} + \boldsymbol{n}$. A certain signal to noise ratio (SNR) is achieved by measuring the maximum power of the signal $P_{\text{sig}} = \max |y_i|^2$ and scaling the noise level such that $\max |n_i| = \sqrt{P_{\text{sig}}/SNR}$.

As can be seen in Fig. 8.8 for an SNR of 60 dB, when the BP strategy is used, the bound in general shifts downwards compared to the noiseless case. While reconstruction errors of $\aleph \leq -55\,\text{dB}$ are still achievable the bounds for $\aleph \leq -45\,\text{dB}$ are depicted since otherwise the transition bounds shift downwards quite far. However, from a practical perspective an error of $\aleph \leq -45\,\text{dB}$ is still in a useful range. For $\delta \gtrsim 0.8$ the allowed sparsity level for a

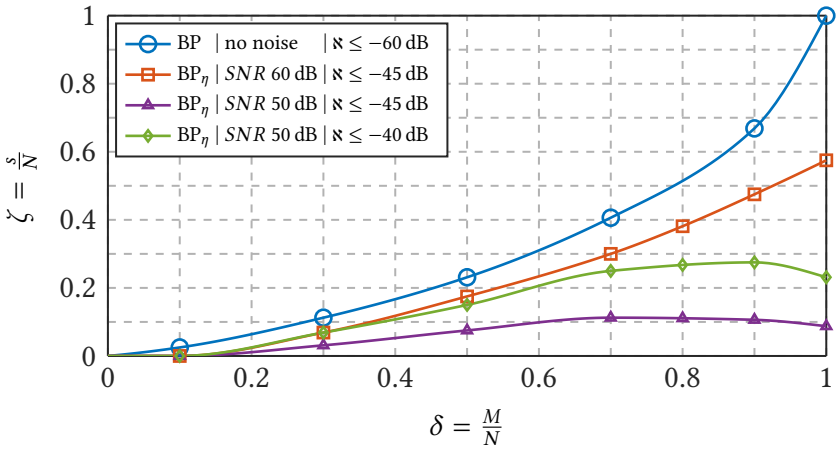

Fig. 8.9: Transition bounds for different noise levels and the recovery strategy BP$_\eta$, where η was chosen as $\eta = \alpha\sqrt{M}$ with $\alpha = 1.975 \times 10^{-5}$ for an SNR of 60 dB and $\alpha = 2.175 \times 10^{-5}$ for an SNR of 50 dB. © 2019 IEEE

successful reconstruction even decreases when the number of measurements is increased. A possible explanation for this decrease could be that the BP assumes all measurements to be exact due to the side condition in (8.8). Consequently, when more (noisy) measurements are added also more defective information is added.

As a remedy the quadratically constrained version of the BP, BP$_\eta$ (see (8.9)) is used. For a fixed (empirically determined) $\eta = 2 \times 10^{-4}$ the transition bound also increases for $\delta \gtrsim 0.8$, but is otherwise worse than the BP bound. The right choice of η is crucial, as is also shown theoretically in [Brugiapaglia et al. 2018]. However, since the measurement noise is not bounded by a fixed η (i.e., $\|\boldsymbol{n}\|_2 \leq \eta$) but rather Gaussian distributed there is no ultimate choice. One approach could be to leverage a tail bound which states that $\exists\, c > 0$ such that for any $\epsilon > 0$

$$\mathcal{P}\left(\|\boldsymbol{n}\|_2 \leq (1+\epsilon)\sigma\sqrt{M}\right) \geq 1 - \mathrm{e}^{-c\epsilon^2 M}, \tag{8.15}$$

where $\mathcal{P}(\mathcal{E})$ denotes the probability of the event $\mathcal{E}$ and σ is the variance [Eldar et al. 2012, p. 32]. Consequently, the parameter should be chosen depending on the number of measurements as $\eta = \alpha\sqrt{M}$, where α has to be increased with an increasing noise level. This is also verified numerically by the improved bound (compared to $\eta = 2 \times 10^{-4}$) shown in Fig. 8.8. Note, however, that the empirically chosen $\alpha = 1.975 \times 10^{-5}$ might not be optimal yet.

Using the approach with $\eta = \alpha\sqrt{M}$ transition bounds for different noise levels are determined. The results are depicted in Fig. 8.9. They show that the bound shifts downwards with decreasing SNR. While the bound for an SNR of 50 dB shifts down considerably, a relaxation of the requirement for the error to $\text{ϰ} \leq -40$ dB (also depicted in Fig. 8.9) suffices to shift the transition bound back to a useful area. Since such an error level is still reasonable for an SNR of 50 dB it can be concluded that the sparse recovery in the spherical NFFFT is sufficiently robust against measurement noise.

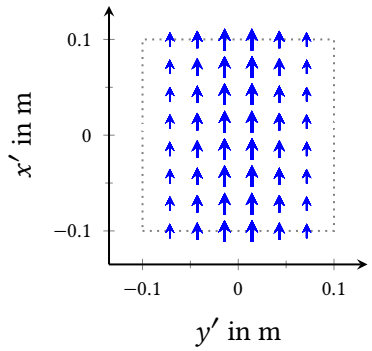

Fig. 8.10: HD array (6×8 in phase HDs with an amplitude taper) used as a synthetic higher-order probe antenna. © 2019 IEEE

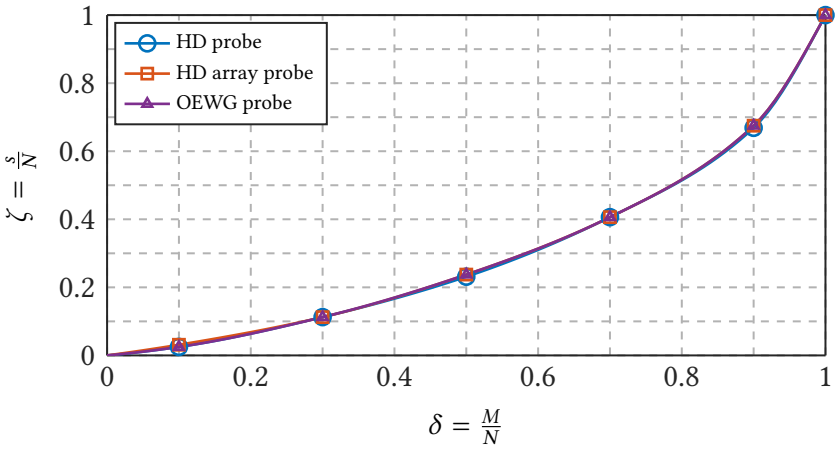

Fig. 8.11: Transition bounds corresponding to $\aleph \leq -70\,\mathrm{dB}$ for a HD array and an OEWG higher-order probe as well as a simple HD probe, all in the noiseless case and $\tau = 0$ using the BP recovery strategy. © 2019 IEEE

8.3.8 Influence of Probe Correction

To investigate a last possible influence on the transition bounds, the HD probe is replaced by a higher-order probe. Firstly, a 2-dimensional array of HDs as shown in Fig. 8.10 is used as a probe [Schmidt et al. 2011]. From the analytical FF expression the probe receiving coefficients $R^{\mathrm{p}}_{\sigma\mu\nu}$ (see (8.4)) are determined. Furthermore, the NSI-RF-WR284 open-ended waveguide (OEWG) [NSI-MI 2018] is used as a probe antenna[1]. Its probe receiving coefficients are determined from the FF computed by FEKO [FEKO 2017]. The resulting transition bounds are shown in Fig. 8.11 together with the bound for the HD probe. As all three bounds are almost identical, it can be concluded that the previous results are also valid for the considered higher-order probes, at least for the noiseless case. As shown in the following, when measurement noise is present and BP_η is used, it appears that α needs to be increased.

[1]Note, that OEWGs are sometimes considered as first-order probes. However, this is only an approximation.

8.3.9 Practically Relevant Case

After investigating the different influences on the recovery guarantees separately, the combination of sparsity defects and noise is of interest. To this end, a level of sparsity defects of $\tau = 2\times10^{-4}$ and noise levels of 60 dB, 50 dB, 40 dB, and 30 dB are simulated for a HD and the OEWG higher-order probe. The resulting PTDs (for the HD probe) and extracted bounds (for HD and OEWG probe) for different FF errors ℵ are shown in Fig. 8.12. In general, the higher the requirements are on the error level, the more samples are required. As can be seen especially for the SNRs of 40 dB and 30 dB in Fig. 8.12, only for extremely low sparsity levels an error below the SNR can be achieved. Furthermore, for all noise levels the transition bound slightly depends on the probe. Particularly, α has to be increased (using an empirical value) compared to the case using the HD probe. An explanation for this might be that a larger probe collects more noise. However, the determined bounds are still close to the ones using the HD probe, both lying in a useful range for NFFFTs based on simulation or measurement data of antennas.

In consequence, a practical approach could be to first of all determine the sparsity level of the spherical expansion coefficients of an AUT, for example, via simulation. Then the PTD with the fitting SNR, τ, probe, and sampling grid can be used (if not available it can be set up according to Subsection A) to deduce the minimum number of samples in order to achieve the desired error level.

8.4 NFFFT Results Using CS

In order to verify that the determined transition bounds hold for actual antennas, NFFFTs are performed with the number of sampling points predicted by the determined PTDs.

8.4.1 Simulation of a Horn Antenna

As a first example, a pyramidal horn antenna is considered. The NF data of the antenna is computed by FEKO, which determines a MoM solution based on the EFIE. Based on a rectangular WR90 waveguide as feeding structure, the antenna geometry is defined as shown in Fig. 8.13. Excited is only the fundamental (TE_{10}) mode at a frequency of 11 GHz. The diameter of the minimum sphere of the antenna is $D = 124\,\text{mm} \approx 4.6\lambda$. With an $\epsilon = 11$ the number of spherical modes is determined from (8.2) as $L = 26$, which leads to $N = 1456$ expansion coefficients. The sampling points are again placed on a spiral grid as defined in (8.12)-(8.14) with a fixed radius of 0.1 m. The magnitude of the spectrum of the expansion coefficients x_{amn} is shown in Fig. 8.14 (can be directly determined by FEKO). While there is no actual zero entry, only 29 % of the coefficients are larger in magnitude than 0.02 % of the largest coefficient, that is, for $\tau = 2\times10^{-4}$ the sparsity level is $\zeta \approx 0.29$. Consequently, for an error of $\text{ℵ} \leq 60$ dB it follows from Fig. 8.7 that $\delta \geq 0.6$ has to hold. This corresponds to a minimum amount of samples of $M = 874$.

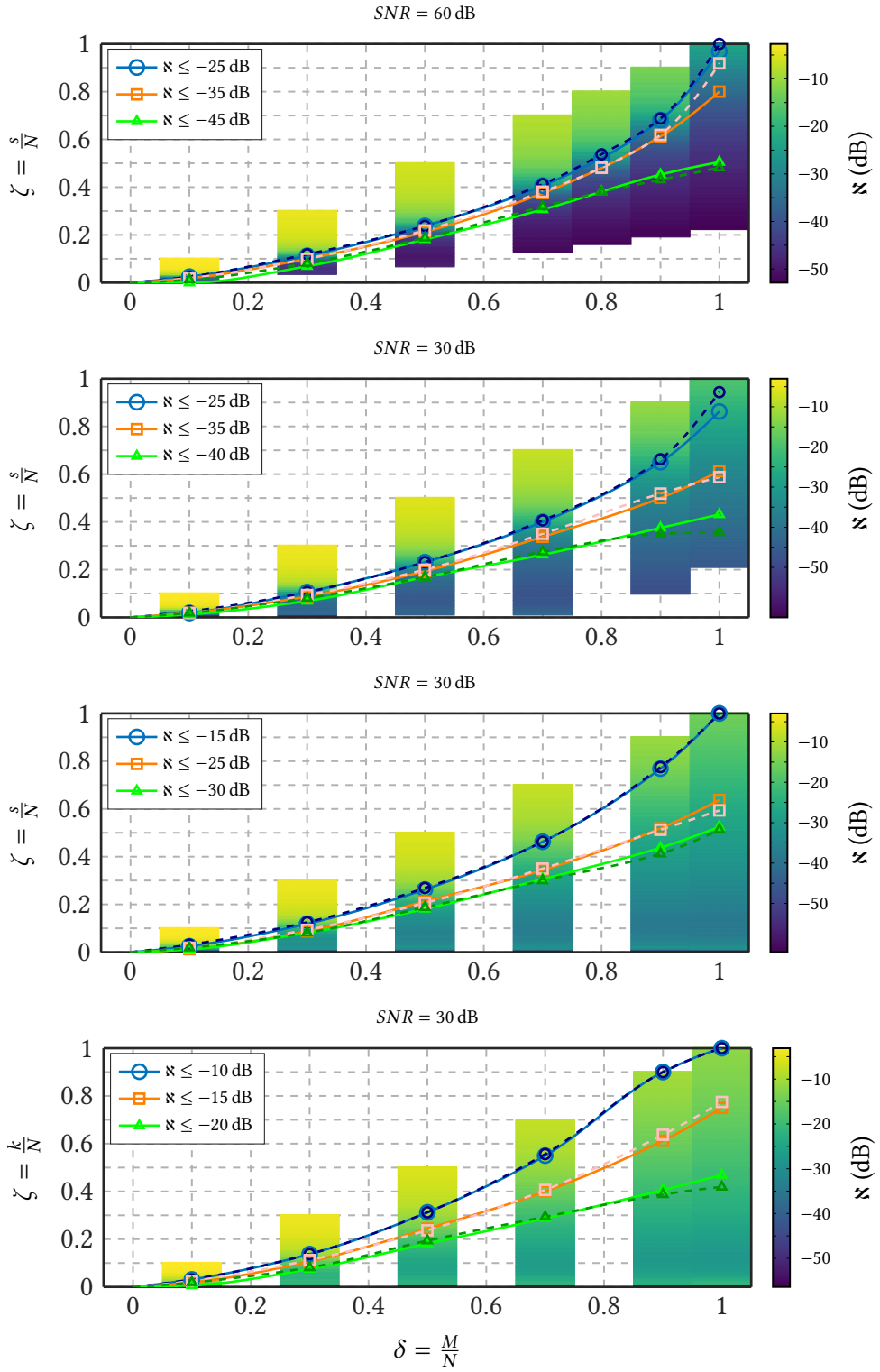

Fig. 8.12: PTDs for a HD probe as well as transition bounds for the HD probe and the OEWG higher-order probe (dashed). All for a level of sparsity defects of $\tau = 2 \times 10^{-4}$. As recovery strategy the BP_η is used with $\eta = \alpha\sqrt{M}$, where $\alpha = 1.975 \times 10^{-5}, 6.24 \times 10^{-5}, 1.975 \times 10^{-4}, 6.24 \times 10^{-4}$ for the HD probe and $\alpha = 5.139 \times 10^{-5}, 1.925 \times 10^{-4}, 5.639 \times 10^{-4}, 3.125 \times 10^{-3}$ for the OEWG probe for an $SNR = 60\,\mathrm{dB}, 50\,\mathrm{dB}, 40\,\mathrm{dB}, 30\,\mathrm{dB}$, respectively. © 2019 IEEE

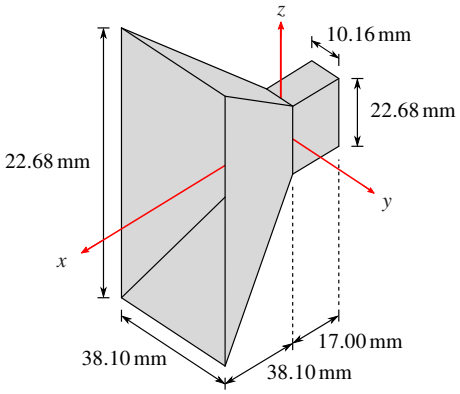

Fig. 8.13: Geometry of the simulated pyramidal horn antenna. The walls are PEC and infinitely thin. © 2019 IEEE

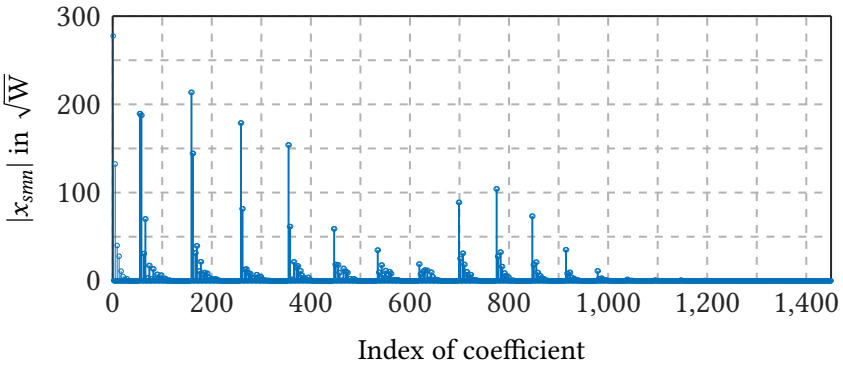

Fig. 8.14: Magnitude of the expansion coefficients of the simulated pyramidal horn antenna shown in Fig. 8.13. © 2019 IEEE

An H-plane and an E-plane cut of the reconstructed FF by the BP is shown in Fig. 8.15 together with a regularized least-squares (LS) solution using the same measurements. The regularization is achieved by solving the normal equation system $\boldsymbol{A}^{\mathrm{H}}\boldsymbol{y} = \boldsymbol{A}^{\mathrm{H}}\boldsymbol{A}\boldsymbol{x}$ associated with (8.5) with the iterative GMRES [Saad 2003], which stops at a relative residual of $1{\times}10^{-7}$. Both results are compared to the FF computed by FEKO. While the CS solution achieves the predicted FF error, the regularized LS solution shows only a coarse resemblance with the correct antenna pattern (be reminded that only one polarization per sample is used).

Also shown in Fig. 8.15 are the reconstructed patterns for the case when noise with an SNR of 60 dB and 40 dB is added to the measurements. With a reconstruction error of $\aleph \leq -45$ dB and $\aleph \leq -30$ dB the predictions of the (HD) transition bounds given in Fig. 8.12 are shown to hold. The bounds require at least $M = 0.7N \approx 1020$ sampling points in order to achieve the corresponding error levels.

The error level for different numbers of samples is depicted in Fig. 8.16. In the noiseless case for $\delta < 0.6$ the predicted $\aleph \leq -60$ dB from Fig. 8.7 can no longer be achieved by CS, however, above $\delta = 0.6$ even better error levels can be reached. In contrast, the regularized LS solution only leads to an acceptable accuracy for $\delta = 1.0$. For the noisy cases the predictions of the PTDs in Fig. 8.12 hold true, as well. Interestingly, for $\delta < 0.6$ the encountered errors are

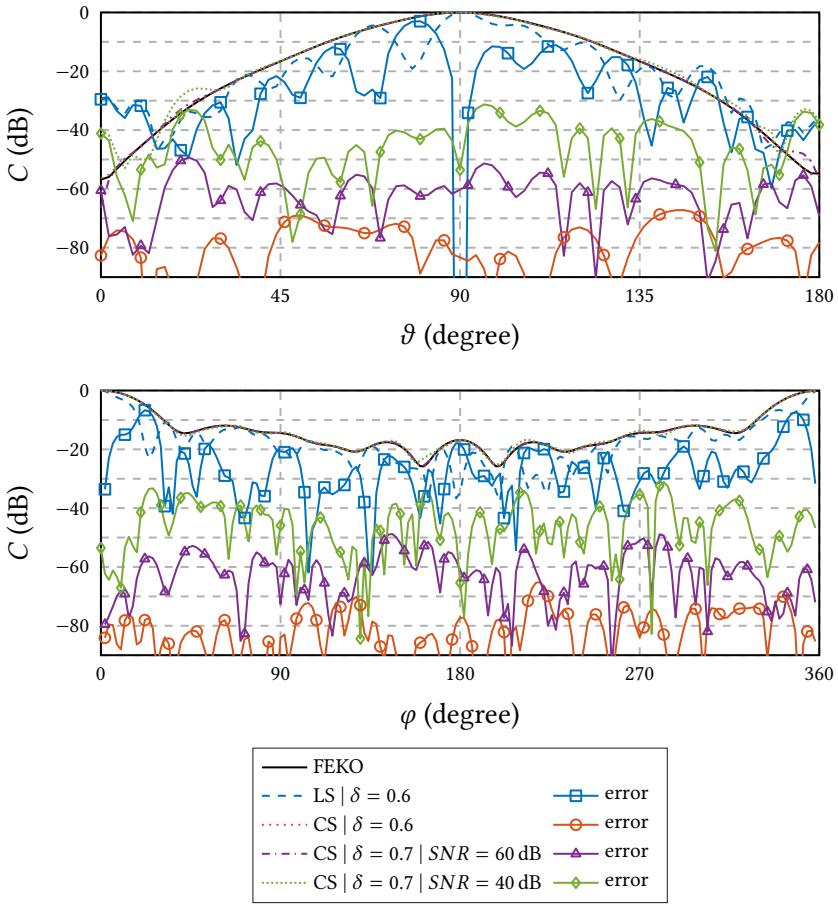

Fig. 8.15: Comparison of the reconstructed radiation characteristic C of the pyramidal horn antenna with the one from FEKO. The CS solutions use in the noiseless case the BP and in the noisy cases BP_η with $\eta = \alpha\sqrt{M}$. Top: H-plane ($\varphi = 0$); Bottom: E-plane ($\vartheta = \pi/2$). © 2019 IEEE

better than predicted by the PTDs in Fig. 8.12. Consequently, one could conclude that the determined bounds are too pessimistic. However, the bounds have to hold for all antennas and not only this specific one. Hence, in order to make to bound even closer to the absolute minimum of samples, presumably more information about the specific antenna would have to be included in some form.

8.4.2 Concerning the Absolute Minimum of Samples

As already indicated by the previous results, it should be noted that the presented approach does not necessarily determine the absolute minimum of samples for the spherical NFFFT. First of all, for certain configurations (antennas, sampling locations) CS might find a solution with the same error level from even less measurements. However, in contrast to the predictions by the PTDs there is no guarantee to achieve this error level. Also, the least squares solution could work sufficiently well, but again there is no guarantee. Finally, there

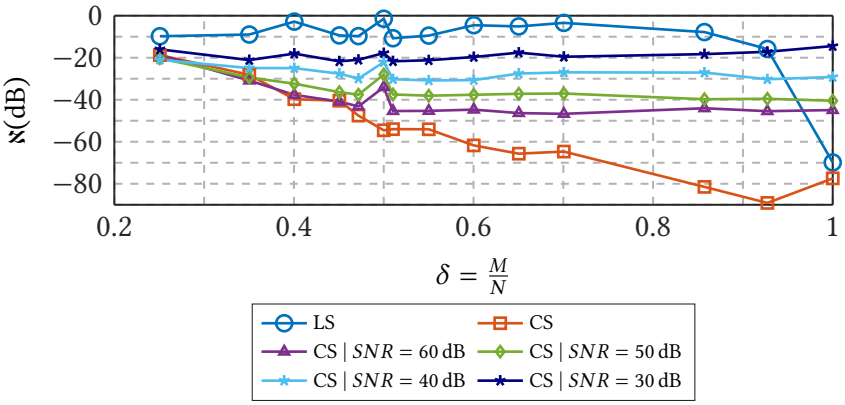

Fig. 8.16: Achieved error ℵ for the pyramidal horn antenna for different numbers of samples M using in the noiseless case CS with BP and the regularized LS solution, as well as CS with the BP_η in the noisy cases. © 2019 IEEE

is no definite way to choose ϵ in (8.2) and consequently the number of modes L. Selecting, for example, for the simulated horn antenna $\epsilon = 0$, a full rank LSE can be achieved with only $M = 510$ measurements. This would be less than the previously used $M = 874$ samples for CS. However, solving the corresponding LSE only an error of −30 dB can be achieved as shown in Fig. 8.17. Increasing the number of samples to $M = 1600$ and taking two orthogonal polarizations improves the error to only about −55 dB, showing that the solution accuracy is limited due to the degrees of freedom of the model. In contrast, when choosing $\epsilon = 3$ ($N = 720$) a sparsity level of about 50 % can be observed ($\tau = 2 \times 10^{-4}$). According to the PTD in Fig. 8.7 a CS reconstruction requires $N = 650$ samples. That the predicted error of about −60 dB is achieved can be seen from Fig. 8.17. The overdetermined solution for $\epsilon = 0$ using also $M = 650$ samples achieves only an error of −45 dB. Consequently, after choosing ϵ and L sufficiently large to represent the radiated fields of the AUT, the PTDs can predict the minimum amount of samples required for CS in order to achieve a certain error level.

8.4.3 Simulation of an Antenna Array

As a second example a 21 × 23 rectangular Dolph-Chebychev (in phase, amplitude tapered) array of z-directed Hertzian dipoles in the yz-plane is considered. At a frequency of 1 GHz the distances and amplitudes are determined according to [Dolph 1946; Safaai-Jazi 1994] such that a side lobe level of −30 dB is achieved. With a minimum sphere diameter of $D = 27.9\lambda$ and $\epsilon = 11$ the order of the spherical mode expansion is $L = 99$ resulting in $N = 19\,998$ expansion coefficients. The spectrum of the expansion coefficients is determined by taking two orthogonal polarizations at 22 000 sample locations and obtaining the LS solution. Using $\tau = 2 \times 10^{-4}$ a sparsity level of $\zeta \approx 18\,\%$ is found. According to the transition bound in Fig. 8.7 $M = 0.49N \approx 9800$ samples should suffice to achieve an error of $\aleph \leq -60$ dB. The results shown in Fig. 8.18 verify this. When measurement noise with an SNR of 50 dB is added, it follows from Fig. 8.12 that $M = 0.55N \approx 10\,999$ and $M = 0.45N \approx 9000$

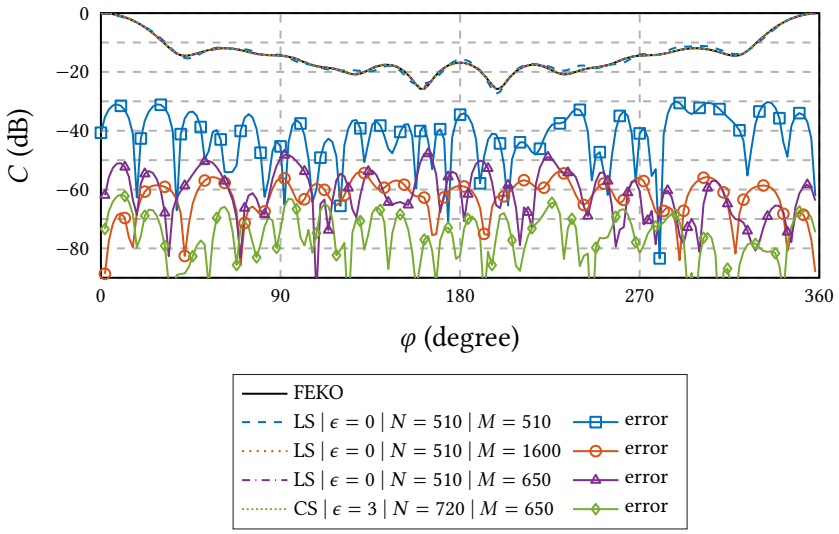

Fig. 8.17: Comparison of the E-plane of the reconstructed radiation characteristic C of the pyramidal horn antenna with the one from FEKO for different setups. The CS solution uses the BP. © 2019 IEEE

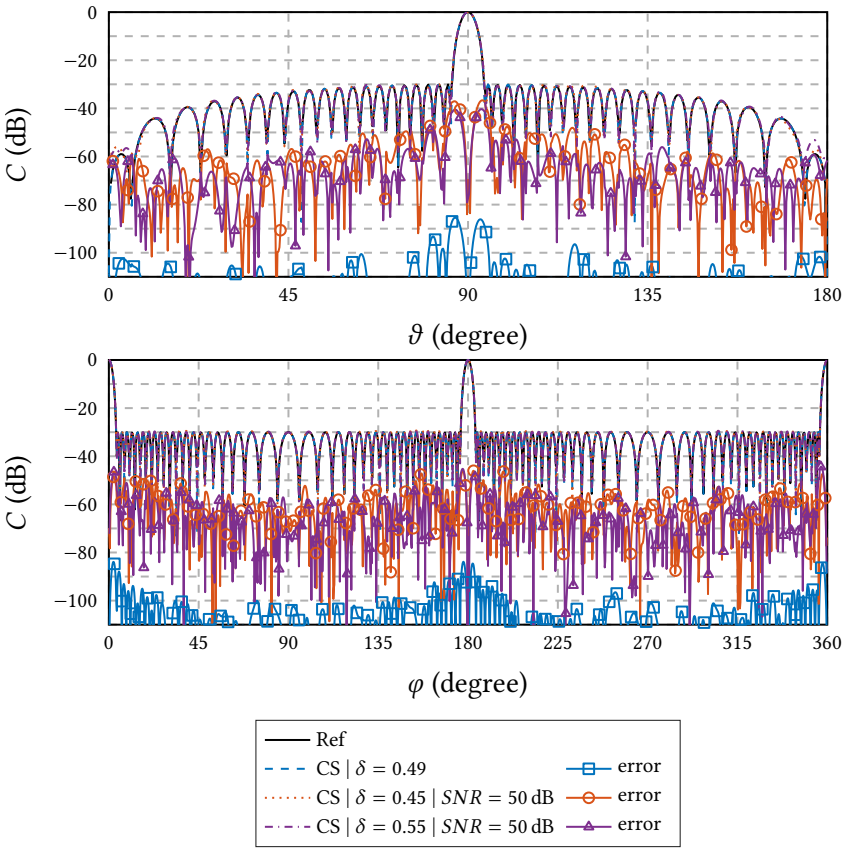

Fig. 8.18: Comparison of the reconstructed radiation characteristic C of the simulated Dolph-Chebychev array with the analytical reference solution. The reconstruction by CS uses in the noiseless case BP and in the noisy case BP_η. Top: E-plane ($\varphi = 0$); Bottom: H-plane ($\vartheta = \pi/2$). © 2019 IEEE

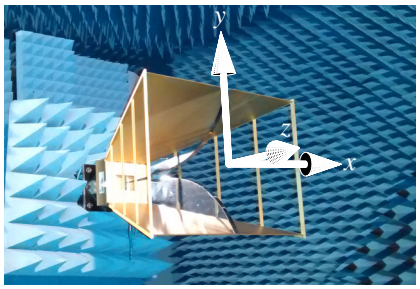

Fig. 8.19: Measured double-ridged DRH400 antenna from RFspin mounted in the anechoic chamber. © 2019 IEEE

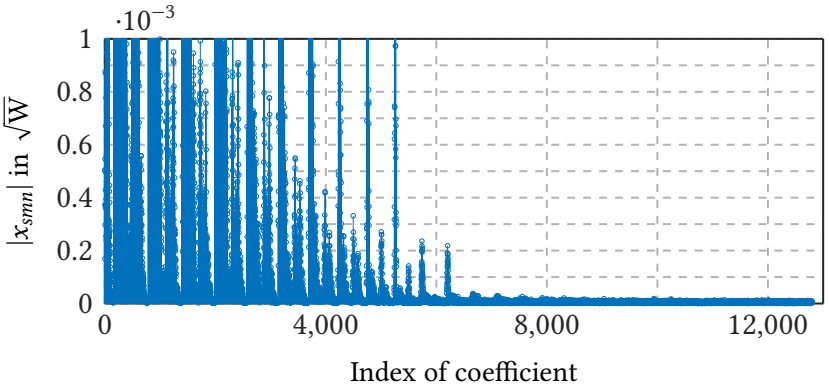

Fig. 8.20: Magnitude of the expansion coefficients of the measured double-ridged DRH400 antenna shown in Fig. 8.19. In order to visualize that none of the coefficients is zero, the large coefficients are cut off. The largest coefficient has a magnitude of 11×10^{-2} $\sqrt{\text{W}}$. © 2019 IEEE

samples are required for an error of $\varkappa \leq -40$ dB and $\varkappa \leq -25$ dB, respectively. That both predictions hold true, is verified in Fig. 8.12, as well.

The half power bandwidths $HPBW = 3.22^\circ$ in the E-plane and $HPBW = 2.91^\circ$ in the H-plane are reproduced in all cases at least up to the third decimal place. The directivity $D_{\text{dir}} = 26.92$ dB is reproduced with a relative error of -156 dB, -18.12 dB, and -16.76 dB for the setups with $\delta = 0.49$ (noiseless), $\delta = 0.55$, and $\delta = 0.45$, respectively.

8.4.4 Measurement of a Double-Ridged Horn Antenna

Finally, the double-ridged DRH400 horn antenna [RFspin 2017] as shown in Fig. 8.19 is measured in an anechoic chamber at a frequency of 3 GHz with the NSI-RF-WR284 open-ended waveguide [NSI-MI 2018] as probe antenna. Initially, two orthogonal polarizations are obtained for $M = 16\,380$ samples on an equiangular grid. With a diameter of the minimum sphere of $D \approx 1.6\,\text{m} \approx 16\lambda$ the number or spherical modes is determined as $L = 79$, leading to $N = 12\,798$ expansion coefficients. The magnitude of the spectrum of the expansion coefficients is depicted in Fig. 8.20. The spectrum is determined by using both polarizations

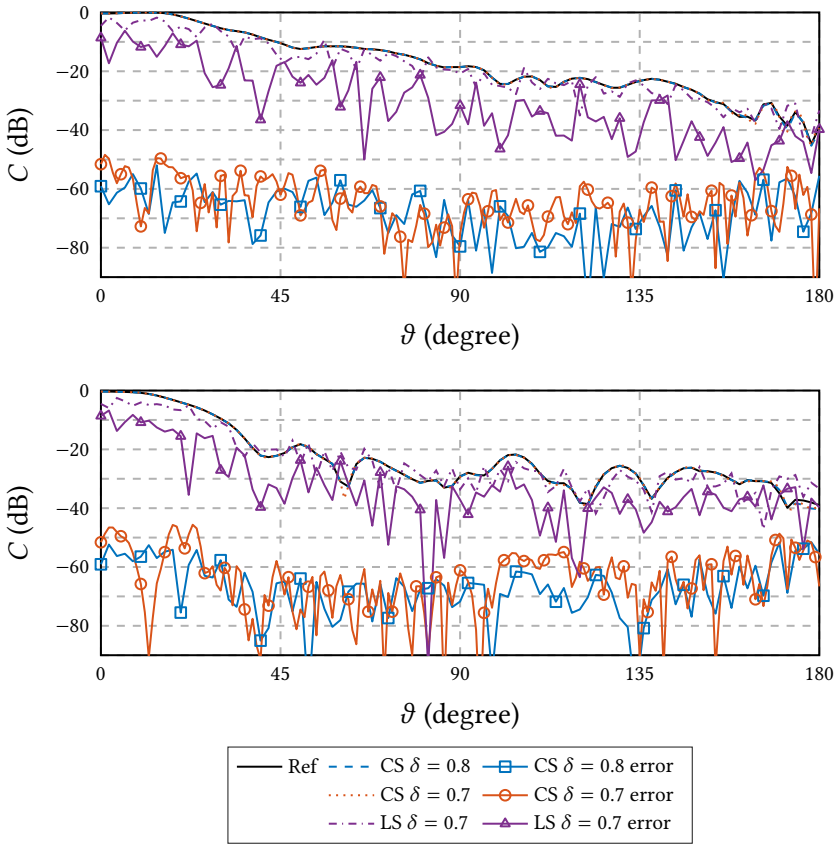

Fig. 8.21: Comparison of the reconstructed radiation characteristic C of the DRH400 antenna with a reference solution obtained by using two orthogonal polarizations for each of the $M = 16\,380$ sampling points. The reconstruction by CS uses for $\delta = 0.8$ corresponding to $M = 10\,239$ samples the BP_η ($\eta = 2.5 \times 10^{-3}$) and for $\delta = 0.7$ corresponding to $M = 8959$ samples the BP to reconstruct the $N = 12\,798$ expansion coefficients. The regularized LS solution uses also the $M = 8959$ samples.Top: H-plane ($\varphi = 0$); Bottom: E-plane ($\varphi = \pi/2$). © 2019 IEEE

at all $M = 16\,380$ sampling points and solving the normal equation system $\boldsymbol{A}^{\mathrm{H}}\boldsymbol{y} = \boldsymbol{A}^{\mathrm{H}}\boldsymbol{A}\boldsymbol{x}$ associated with (8.5) with the iterative GMRES [Saad 2003]. However, also a simulation of the antenna could be used. Using $\tau = 2 \times 10^{-4}$ a sparsity level of $\zeta \approx 0.33$ is determined. Since the SNR of the measurement is approximately 60 dB it follows from the transition bound in Fig. 8.12 that at least $M = 0.7N \approx 8959$ measurements are required in order to achieve an error level of $\aleph \leq -45$ dB.

In Fig. 8.21 the reconstructed FF in the H-plane and E-plane are depicted. For the reconstruction using CS, a spiral grid with the desired number of points is defined and the closest points of the equiangular grid are selected. For each selected point one of the two polarizations is chosen randomly. The deviation of the CS solution (using the BP) to the reference solution (using the $M = 16\,380$ sampling points) is for $M = 8959$ ($\delta = 0.7$) for all angles below the predicted -45 dB. Again, the regularized LS solution shows only a rough resemblance with the reference. If the number of measurements is increased to $M = 10\,239$ ($\delta = 0.8$) the

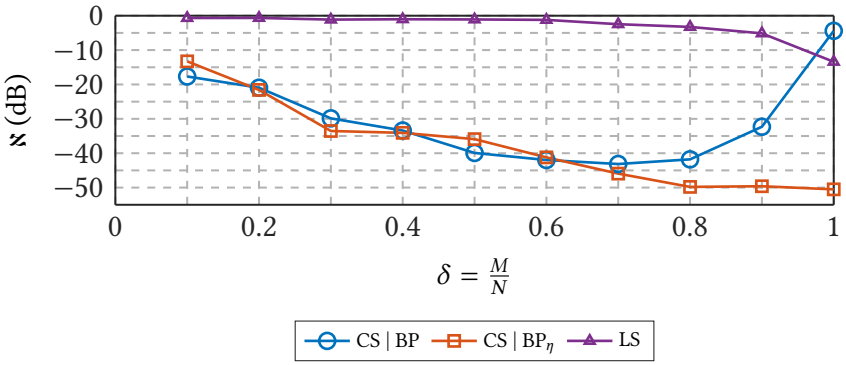

Fig. 8.22: Achieved error ϰ for the measured DRH400 antenna for different numbers of samples M using CS and the regularized LS solution. © 2019 IEEE

worst case deviation of CS decreases as expected to a level lower than −50 dB.

Investigating the error for different numbers of measurements M as shown in Fig. 8.22 verifies that BP$_\eta$ achieves $\varkappa \leq -45\,\text{dB}$ only for $\delta \geq 0.7$. Similar to the simulated horn antenna the encountered error is for $\delta < 0.7$ better than predicted by the PTD in Fig. 8.12. Furthermore, the insights from Fig. 8.8 concerning the performance of BP in the noisy case are confirmed. From about $\delta \geq 0.7$ on (note that a different probe is used) the error increases again.

8.5 Conclusion

It has been shown how to predict the minimum number of samples required for a CS reconstruction in the spherical NFFFT by using PTDs. The latter depend on the required error level in the FF. Consequently, CS can be applied to the spherical NFFFT in a reliable manner. This allows reducing the number of samples if prior knowledge about the sparsity of the spherical expansion coefficients can be obtained. The investigation of several influence factors showed that a deterministic spiral gird is well suited. Furthermore, measurement noise and sparsity defects increase the minimum number of measurements and decrease the achievable error level, but within a range which is still useful for antenna near-field measurements. For noisy measurements in combination with the quadratically constrained basis pursuit (BP$_\eta$) different probes require careful adjustment of the constraint.

For the considered antennas, the number of sampling points was reduced by up to 55 %. Relaxing the requirements on the FF error can lead to a further reduction. Considering that only one polarization has to be measured at each sampling point and that most other approaches so far usually acquire more samples than there are unknowns (e.g., in order to average out noise), the achieved reduction of sampling points is even higher.

The used approach with PTDs could also be adapted for other applications, where the possible influences can each be captured in one parameter.

Part IV

Addendum

9

Conclusion

> "There are no solved problems; there are only problems that are more or less solved."
>
> Herni Poincaré

Several paradigms have been presented in this thesis to low-frequency stabilize the EFIE and to advance the reconstruction of equivalent sources from field measurements: The proposed RHS stabilization for the quasi-Helmholtz decomposed EFIE in combination with the proposed self-adaptive frequency normalization enable the handling of arbitrary excitations without any ad-hoc adaptions or the need for any a-priori information about the excitation. Especially, in the context of equivalent current reconstruction, both of the proposed schemes are crucial, since a-priori information about the radiating source is difficult to obtain and preferably not incorporated: After all, the radiation behavior of the DUT shall be determined as much as possible by the measurements and not by assumptions. Moreover, ad-hoc adaptions such as the subtraction of static contributions appear not feasible for measurement data.

The derived quasi-Helmholtz decomposition for the B-spline based discretization of the EFIE constitutes a fundamental step to transfer the low-frequency stabilizing preconditioners known from the low-order mesh-based approaches to the curvilinear higher-order B-spline representations, while keeping the advantageous properties of the low-order preconditioners. This is of interest since geometrical approximation errors can be avoided and higher-order basis functions are known to be more efficient in terms of time and memory consumption than low-order basis functions [Donepudi et al. 2001; Valdés et al. 2011].

The determined capabilities of CS to reduce the number of samples for spherical NFFFTs have shown that CS can, in principle, be applied in a reliable manner. However, knowledge about the sparsity of the spherical expansion coefficients has to be obtained. This can, for example, be achieved by simulations, but deviations of the simulation models from the manufactured antenna can make the approach not fully reliable. Still, for the considered

AUTs (simulated and measured) considerable reductions in the number of the required samples could be achieved without sacrificing accuracy in the determined field patterns.

While the presented paradigms successfully address several problems in the area of CEM, they call for further research in intimately related areas. Concerning boundary integral scattering and radiation formulations, issues that call for further investigation are:

- The RHS stabilization scheme for the quasi-Helmholtz decomposed EFIE needs to be extended also to the MFIE such that a stabilized CFIE can be formed [Merlini et al. 2020]. In order for the MFIE to be discretized conformingly, Buffa-Christiansen (BC) testing functions are required [Buffa et al. 2007; Andriulli et al. 2008a; Cools et al. 2011], for which a RHS stabilization analogous to the proposed one for the RWG discretization needs to be derived.

- Analogously, the proposed self-adaptive normalization for the quasi-Helmholtz decomposed EFIE needs to be extended to address the MFIE. To this end, a scheme has been proposed in [Hofmann et al. 2023d], but further investigations are necessary to address the CFIE and formulations such as the PMCHWT or the MUIE for penetrable bodies.

- A conformingly B-spline based discretization of the MFIE needs to be established. To find one, a set of suitable dual basis functions in analogy to the BC functions is required. This also enables to define an optimal Calderón preconditioner [Buffa et al. 2007; Andriulli et al. 2008a] for the B-spline based discretization of the EFIE overcoming the dense-discretization breakdown and leading to a fast convergence of iterative solvers. A candidate set of dual basis functions is proposed in [Hofmann et al. 2024a; Hofmann et al. 2024b], but further investigations are necessary.

- Lately, adaptive mesh refinement strategies gained interest since they allow to maintain optimal convergence behavior for multiscale geometries [Kim et al. 2018; Tobon Vasquez et al. 2020]. To obtain a counterpart for a spline-based discretization, more flexibility needs to be introduced to the tensor-product structure of the B-spline basis functions for the EFIE, that is, a strategy for local refinement is of interest. To this end, so called analysis-suitable T-splines are interesting candidates [Bazilevs et al. 2010; Scott 2011; Veiga et al. 2013; Buffa et al. 2014a]. However, more investigations on possible capabilities and limitations for the EFIE are necessary.

Concerning equivalent sources reconstructions, further aspects to be addressed are:

- The influences of a realistic measurement setup need to be investigated carefully and taken into account when further designing the low-frequency stabilized field transformation algorithms: Limitations to the sensitivity of the probe antennas and the presence of noise are potentially crucial factors to whether enough information can be obtained for the field transformation to yield accurate results. Moreover, the influence of the coupling between the DUT and the probe antenna needs to be studied, since commonly the probe is placed in close proximity to the DUT. Similarly, the

shielding from reflections and surrounding signals needs to be taken into consideration.

- While the determined PTDs give a good quantification of the applicability of CS to spherical NFFFTs it would be desirable to have a precise undersampling theorem at hand (similarly to the ones known for certain random matrices [Donoho et al. 2009; Donoho et al. 2010b]), preferably taking parameters such as noise or the influence of the probe into account. This would allow to rapidly determine the required number of samples and make CS more practical, also for other equivalent source representations.

A

Asymptotic Scalings

In this appendix the asymptotic scalings in the sense of wavenumber $k \to 0$ of solenoidal and non-solenoidal components $\boldsymbol{e}_{\mathrm{sol,hsol}}$ and $\boldsymbol{e}_{\mathrm{nsol}}$, respectively, as defined in Table 3.1 are derived. The obtained scalings are central to the lines of argument in Chapter 4 and especially to the lines of argument in Chapter 5.

A.1 Right-Hand Side Scalings

In order to derive real and imaginary part of the solenoidal and non-solenoidal components of the RHS for the excitations in Table 5.2, the approach of [Bogaert et al. 2014] is generalized. More precisely, the corresponding excitation fields $\boldsymbol{e}^{\mathrm{ex}}$ are expressed via their electric currents $\boldsymbol{j}^{\mathrm{ex}}$ and magnetic currents $\boldsymbol{m}^{\mathrm{ex}}$ and the Green's function representation

$$\iint_\Gamma \boldsymbol{t}\cdot\boldsymbol{e}^{\mathrm{ex}}\,\mathrm{d}\boldsymbol{r} = -\mathrm{j}\omega\mu \iint_\Gamma \boldsymbol{t}\cdot\iiint_V g\,\boldsymbol{j}^{\mathrm{ex}}\,\mathrm{d}\boldsymbol{r}'\,\mathrm{d}\boldsymbol{r} - \mathrm{j}\frac{c\mu}{\omega}\iint_\Gamma \boldsymbol{t}\cdot\iiint_V \nabla'\cdot\boldsymbol{j}^{\mathrm{ex}}\,\nabla g\,\mathrm{d}\boldsymbol{r}'\,\mathrm{d}\boldsymbol{r} + \iint_\Gamma \boldsymbol{t}\cdot\iiint_V \nabla g\times\boldsymbol{m}^{\mathrm{ex}}\,\mathrm{d}\boldsymbol{r}'\,\mathrm{d}\boldsymbol{r} \quad \text{(A.1)}$$

where V is the volume enclosed by Γ. Using a Taylor series expansion of the Green's function

$$g(\boldsymbol{r},\boldsymbol{r}') = \frac{\mathrm{e}^{-\mathrm{j}kR}}{4\pi R} = \frac{1}{4\pi R}\sum_{q=0}^{\infty}\frac{(-\mathrm{j}kR)^q}{q!} \quad \text{(A.2)}$$

with the distance $R = |\boldsymbol{r}-\boldsymbol{r}'|$ between source point $\boldsymbol{r}'$ and observation point $\boldsymbol{r}$, as well as a Taylor series expansion of the gradient of the Green's function

$$\nabla g(\boldsymbol{r},\boldsymbol{r}') = \frac{\boldsymbol{R}}{4\pi R^3}\sum_{q=0}^{\infty}\frac{q-1}{q!}(-\mathrm{j}kR)^q \quad \text{(A.3)}$$

with $\boldsymbol{R} = \boldsymbol{r} - \boldsymbol{r}'$, we obtain the tabulated values by observing the dominant term (of the real and of the imaginary part) in the series expansion as $k \to 0$. In addition, we have to consider that certain contributions vanish: the scalar potential contribution vanishes when tested by a solenoidal function, that is,

$$\iint_\Gamma \boldsymbol{t} \cdot \iiint_V \nabla' \cdot \boldsymbol{j}^{\mathrm{ex}} \nabla g \, \boldsymbol{r}' \, \mathrm{d}\boldsymbol{r} = 0 \qquad \text{if } \nabla_\Gamma \cdot \boldsymbol{t} = 0\,, \tag{A.4}$$

a constant vector tested by a solenoidal function vanishes, that is,

$$\iint_\Gamma \boldsymbol{t} \cdot \boldsymbol{c} \, \mathrm{d}\boldsymbol{r}' = 0 \qquad \text{if } \nabla_\Gamma \cdot \boldsymbol{t} = 0 \quad \text{and} \quad \boldsymbol{c} = \mathrm{const}\,, \tag{A.5}$$

a solenoidal excitation current tested by a solenoidal function vanishes, that is,

$$\iint_\Gamma \boldsymbol{t} \cdot \iiint_V \boldsymbol{j}^{\mathrm{ex}} \, \mathrm{d}\boldsymbol{r}' \, \mathrm{d}\boldsymbol{r} = 0 \qquad \text{if } \nabla \cdot \boldsymbol{j}^{\mathrm{ex}} = 0\,, \tag{A.6}$$

we have [Chen et al. 2001]

$$\iint_\Gamma \boldsymbol{t} \cdot \iiint_V \frac{\boldsymbol{R}}{R^3} \times \boldsymbol{m}^{\mathrm{ex}} \, \mathrm{d}\boldsymbol{r}' \, \mathrm{d}\boldsymbol{r} = 0 \qquad \text{if } \nabla_\Gamma \cdot \boldsymbol{t} = 0 \text{ and } \nabla \cdot \boldsymbol{m}^{\mathrm{ex}} = 0\,, \tag{A.7}$$

and we have

$$\iint_\Gamma \boldsymbol{t} \cdot \iiint_V \boldsymbol{R} \times \boldsymbol{m}^{\mathrm{ex}} \, \mathrm{d}\boldsymbol{r}' \, \mathrm{d}\boldsymbol{r} = 0 \qquad \text{if } \nabla_\Gamma \cdot \boldsymbol{t} = 0 \text{ and } \nabla \cdot \boldsymbol{m}^{\mathrm{ex}} = 0\,. \tag{A.8}$$

A.2 Scaling of TE and TM Modes

Relevant to Section 5.2.1 we have that for a combination of TE_{mn} modes with largest appearing order $n = N_{\mathrm{TE}}$ and TM_{mn} modes with largest appearing order $n = N_{\mathrm{TM}}$, the ratio w of solenoidal and non-solenoidal tested field vectors as defined in (5.15) scales in accordance with Table 5.2 as

$$w = \frac{\|\boldsymbol{e}_{\mathrm{sol,hsol}}\|}{\|\boldsymbol{e}_{\mathrm{nsol}}\|} = \frac{\mathcal{O}\left(k^{-(N_{\mathrm{TM}}-1)} + k^{-N_{\mathrm{TE}}}\right)}{\mathcal{O}\left(k^{-(N_{\mathrm{TM}}+1)} + k^{-N_{\mathrm{TE}}}\right)} \quad \text{for } k \to 0\,. \tag{A.9}$$

For $N_{\mathrm{TE}} \geq N_{\mathrm{TM}} + 1$, we clearly have

$$w = \mathcal{O}(1)\,. \tag{A.10}$$

For $N_{\mathrm{TE}} < N_{\mathrm{TM}} + 1$ we have

$$w = \frac{\mathcal{O}\left(k^{-(N_{\mathrm{TM}}-1)} + k^{-N_{\mathrm{TE}}}\right)}{\mathcal{O}\left(k^{-(N_{\mathrm{TM}}+1)}\right)}\,. \tag{A.11}$$

In the case $N_{\mathrm{TE}} = N_{\mathrm{TM}}$, this leads to $w = \mathcal{O}(k)$ and for all $N_{\mathrm{TE}} = N_{\mathrm{TM}} - g$ with $g \geq 1$, it leads to $w = \mathcal{O}(k^2)$. In consequence, we have

$$\mathcal{O}(1) \leq w \leq \mathcal{O}(k^2) \tag{A.12}$$

for all possible combinations of N_{TE} and N_{TM}.

For the special case of scattering from a sphere placed in the origin, we have

$$w = \frac{\|\boldsymbol{e}_{\mathrm{sol,hsol}}\|}{\|\boldsymbol{e}_{\mathrm{nsol}}\|} = \frac{\left(k^{-N_{\mathrm{TE}}}\right)}{\mathcal{O}\left(k^{-(N_{\mathrm{TM}}+1)} + k^{-N_{\mathrm{TE}}}\right)}. \tag{A.13}$$

Again, for $N_{\mathrm{TE}} \geq N_{\mathrm{TM}} + 1$, this leads to $w = \mathcal{O}(1)$. On the other hand, for $N_{\mathrm{TE}} < N_{\mathrm{TM}} + 1$, we have the case $N_{\mathrm{TE}} = N_{\mathrm{TM}}$ leading to $w = \mathcal{O}(k)$ and the cases where $N_{\mathrm{TE}} = N_{\mathrm{TM}} - g$ with $g \geq 1$ resulting in

$$w = \mathcal{O}\left(k^{(g+1)}\right), \tag{A.14}$$

which is a case not satisfying (A.12).

B

Derivatives of NURBS Surfaces

This appendix briefly summarizes how to compute the derivatives of a NURBS surface

$$\boldsymbol{s}(u,v) = \begin{bmatrix} x(u,v) \\ y(u,v) \\ z(u,v) \end{bmatrix} = \frac{\sum_{i=1}^{N_u} \sum_{j=1}^{N_v} B_i^{q_u}(u)\, B_j^{q_v}(v)\, w_{ij}\, \boldsymbol{p}_{ij}}{\sum_{i=1}^{N_u} \sum_{j=1}^{N_v} B_i^{q_u}(u)\, B_j^{q_v}(v)\, w_{ij}} \tag{B.1}$$

with control points $\boldsymbol{p}_{ij} \in \mathbb{R}^3$, weights $w_{ij} \in \mathbb{R}_+$, and B-splines B_i defined in Section 6.1.1 with polynomial degrees $q_u, q_v \in \{0, 1, \dots\}$, to obtain the in Chapter 6 employed Jacobi matrix

$$\boldsymbol{J}(u,v) = \begin{bmatrix} \partial_u \boldsymbol{s} & \partial_v \boldsymbol{s} \end{bmatrix} = \begin{bmatrix} \partial_u x & \partial_v x \\ \partial_u y & \partial_v y \\ \partial_u z & \partial_v z \end{bmatrix} \tag{B.2}$$

of $\boldsymbol{s}(u,v)$ and the generalized determinant $D(u,v) = \sqrt{\det(\boldsymbol{J}^{\mathrm{T}}\boldsymbol{J})}$ which can be equivalently expressed as

$$D(u,v) = \|\partial_u \boldsymbol{s} \times \partial_v \boldsymbol{s}\|_2 = \sqrt{(\partial_u y\, \partial_v z - \partial_u z\, \partial_v y)^2 + (\partial_u z\, \partial_v x - \partial_u x\, \partial_z v)^2 + (\partial_u x\, \partial_v y - \partial_u y\, \partial_v x)^2}\,. \tag{B.3}$$

Following [Piegl 1995] and defining

$$\boldsymbol{\alpha}(u,v) = \sum_{i=1}^{N_u} \sum_{j=1}^{N_v} B_i^{q_u}(u)\, B_j^{q_v}(v)\, w_{ij}\, \boldsymbol{p}_{ij} \tag{B.4}$$

as well as

$$\omega(u,v) = \sum_{i=1}^{N_u} \sum_{j=1}^{N_v} B_i^{q_u}(u)\, B_j^{q_v}(v)\, w_{ij} \tag{B.5}$$

corresponding to the numerator and denominator in (B.1), the derivatives $\partial_d \boldsymbol{s}$ with $d \in \{u, v\}$ can be computed as [Piegl 1995, pp. 136ff]

$$\partial_d \boldsymbol{s}(u,v) = \frac{\partial_d \boldsymbol{\alpha}(u,v) - \boldsymbol{s}(u,v)\partial_d \omega(u,v)}{\omega(u,v)} \tag{B.6}$$

where the derivatives of $\boldsymbol{\alpha}$ and ω can be computed, for instance, with respect to u as

$$\partial_u \alpha(u,v) = \sum_{i=1}^{N_u} \sum_{j=1}^{N_v} \partial_u B_i^{q_u}(u)\, B_j^{q_v}(v)\, w_{ij}\, \boldsymbol{p}_{ij} \tag{B.7}$$

and

$$\partial_u \omega(u,v) = \sum_{i=1}^{N_u} \sum_{j=1}^{N_v} \partial_u B_i^{q_u}(u)\, B_j^{q_v}(v)\, w_{ij}\,. \tag{B.8}$$

The contained derivatives of the B-splines B can be computed as described in (6.6). While not employed in this work, higher order derivatives of $\boldsymbol{s}(u,v)$ can be expressed in closed form as well [Piegl 1995, pp. 136ff].

Nomenclature

List of Symbols

Symbol	Description
Accents and Operations	
$\hat{\boldsymbol{a}}$	Vector $\boldsymbol{a}$ is in the parametric domain
$\boldsymbol{A}^{\mathrm{T}}$	Transpose of the matrix $\boldsymbol{A}$
$\boldsymbol{A}^{\mathrm{H}}$	Conjugate complex transpose of the matrix $\boldsymbol{A}$
$\boldsymbol{A}^{-1}$	Inverse of the matrix $\boldsymbol{A}$
$\boldsymbol{A}^{+}$	Moore-Penrose pseudo-inverse of the matrix $\boldsymbol{A}$
Physical Quantities	
ε	Permittivity in $\mathrm{A\,s\,V^{-1}\,m^{-1}}$
ε_0	Permittivity of free space in $\mathrm{A\,s\,V^{-1}\,m^{-1}}$
ε_{r}	Relative permittivity
μ	Permeability in $\mathrm{V\,s\,A^{-1}\,m^{-1}}$
μ_0	Permeability of free space in $\mathrm{V\,s\,A^{-1}\,m^{-1}}$
μ_{r}	Relative permeability
η	Wave impedance in Ω
f	Frequency in Hz
k	Wavenumber in $\mathrm{m^{-1}}$, see (2.2)
ω	Angular frequency in Hz
$\boldsymbol{j}$	Normalized electric surface current density in $\mathrm{V\,m^{-1}}$, see Section 2.1
$\boldsymbol{j}_{\mathrm{V}}$	Normalized electric volume current density in $\mathrm{V\,m^{-2}}$, see Section 2.1
ρ	Electric surface charge density in $\mathrm{A\,s\,m^{-2}}$
ρ_{V}	Electric volume charge density in $\mathrm{A\,s\,m^{-3}}$
$\boldsymbol{e}$	Electric field in $\mathrm{V\,m^{-1}}$
$\boldsymbol{h}$	Normalized magnetic field in $\mathrm{V\,m^{-1}}$, see Section 2.1
$\boldsymbol{r}$	Position vector in $\mathbb{R}^3$
$\boldsymbol{r}'$	Source position vector in $\mathbb{R}^3$

Symbol	Description
Operators and Constants	
$\mathcal{T}$	Electric field integral operator, see (2.16)
$\mathcal{T}_\mathrm{A}$	Vector potential operator, see (2.11)
$\mathcal{T}_\Phi$	Scalar potential operator, see (2.13)
$\partial_u \psi(u)$	Partial derivative with respect to u of a scalar function $\psi(u)$
$\nabla\psi$	Gradient of a scalar function ψ
$\nabla_\Gamma\psi$	Surface gradient of a scalar function ψ defined on Γ
$\nabla \cdot \boldsymbol{f}$	Divergence of a vector function $\boldsymbol{f} \in \mathbb{R}^3$
$\nabla_\Gamma \cdot \boldsymbol{f}$	Surface gradient of a vector function $\boldsymbol{f} \in \mathbb{R}^2$ defined on Γ
$\nabla \times \boldsymbol{f}$	Curl of a vector function $\boldsymbol{f} \in \mathbb{R}^3$
Δ	Laplace operator
$\boldsymbol{\Delta}$	Vector Laplace operator
j	Imaginary unit with $\mathrm{j}^2 = -1$
e	Euler's number
Matrices	
$\mathbf{I}$	Identity matrix
$\boldsymbol{T}$	Discretized $\mathcal{T}$ operator, see (3.3)
$\boldsymbol{T}_\mathrm{A}$	Discretized $\mathcal{T}_\mathrm{A}$ operator, see (3.15)
$\boldsymbol{T}_\Phi$	Discretized $\mathcal{T}_\Phi$ operator, see (3.16)
$\boldsymbol{e}$	Discretized RHS, see (3.18)
$\boldsymbol{j}$	Vector of expansion coefficients for $\boldsymbol{j}$ (unknown vector)
$\boldsymbol{\Lambda}$	Loop mapping matrix, see (3.21)
$\boldsymbol{\Sigma}$	Star mapping matrix, see (3.20)
$\boldsymbol{H}$	Global loop mapping matrix, see Section 3.2.1
$\boldsymbol{Q}$	Loop star mapping matrix, see (3.24)
$\boldsymbol{P}_\Lambda$	Solenoidal projector, see (3.31)
$\boldsymbol{P}_H$	Quasi-harmonic projector, see (3.32)
$\boldsymbol{P}_\Sigma$	Non-solenoidal projector, see (3.30)
$\boldsymbol{P}_{\Lambda H}$	Solenoidal projector, see (3.36)
$\boldsymbol{J}$	Jacobi matrix, see (3.10)
Further Conventions	
$\boldsymbol{q}_{amn}$	Spherical vector wave functions, see (2.23) and (2.24)
f_m	mth Basis/testing function
$\boldsymbol{n}$	Normal vector
$\aleph$	Worst-case error, see (6.60)
$\boldsymbol{u}_r$	Unit vector in spherical coordinates in r-direction
$\boldsymbol{u}_\varphi$	Unit vector in spherical coordinates in φ-direction
$\boldsymbol{u}_\vartheta$	Unit vector in spherical coordinates in ϑ-direction
Λ_m	mth loop function function, see (3.22)

Symbol	Description
Σ_m	mth star function function, see (3.23)
$g(\boldsymbol{r}, \boldsymbol{r}')$	Scalar Green's function of free space, see (2.9)
B_i^p	ith B-spline of degree p, see (6.3)
D	Generalized Jacobi determinant, see (3.11)

Abbreviations

ACA	adaptive cross approximation
AMG	algebraic multigrid
AUT	antenna under test
BC	Buffa-Christiansen
BEM	boundary element method
BiCGstab	stabilized bi-conjugate gradient
BOS	bounded orthonormal systems
BP	basis pursuit
CEM	computational electromagnetics
CFIE	combined field integral equation
CG	conjugate gradient
CMB	cosmic microwave background radiation
CS	compressed sensing
CSIE	combined source integral equation
DUT	device under test
EFIE	electric field integral equation
EFIO	electric field integral operator
EMC	electromagnetic compatibility
FD	Fitzgerald dipole
FDTD	finite-difference time-domain
FEM	finite element method
FF	far field
FFT	fast Fourier transform
FIT	finite integration technique
GMRES	generalized minimum residual
GTD	geometrical theory of diffraction
HD	Hertzian dipole
IDR	induced dimension reduction
LSE	linear system of equations
MFIE	magnetic field integral equation
MLFMM	mulitlevel fast multipole method

MLMDA	multilevel matrix decomposition algorithm
MoM	method of moments
MUIE	Müller integral equation
NF	near field
NFFFT	near-field far-field transformation
NFNFT	near-field near-field transformation
NURBS	non-uniform rational B-splines
PDE	partial differential equation
PEC	perfectly electrically conducting
PEEC	partial element equivalent circuit
PMCHWT	Poggio-Miller-Chang-Harrington-Wu-Tsai integral equation
PO	physical optics
PTD	phase transition diagram
PWTD	plane-wave time-domain
QED	quantum electrodynamics
RCS	radar cross section
RHS	right-hand side
RIP	restricted isometry property
RWG	Rao-Wilton-Glisson
TLM	transmission-line matrix

Bibliography

Abrial et al. 2008
: Abrial, P., Y. Moudden, J.-L. Starck, J. Fadili, J. Delabrouille, and M. Nguyen (July 2008). "CMB data analysis and sparsity". *Statist. Methodology*, vol. 5, no. 4, pp. 289–298 (cit. on pp. 122, 126).

Adrian et al. 2014
: Adrian, S. B., F. P. Andriulli, and T. F. Eibert (Nov. 2014). "Hierarchical bases preconditioners for the electric field integral equation on multiply connected geometries". *IEEE Trans. Antennas Propag.*, vol. 62, no. 11, pp. 5856–5861 (cit. on p. 6).

Adrian et al. 2017
: — (Feb. 2017). "A hierarchical preconditioner for the electric field integral equation on unstructured meshes based on primal and dual haar bases". *J. Comp. Physics*, vol. 330, pp. 365–379 (cit. on p. 56).

Adrian et al. 2019
: — (Jan. 1, 2019). "On a refinement-free Calderón multiplicative preconditioner for the electric field integral equation". *J. Comput. Phys.*, vol. 376, pp. 1232–1252 (cit. on pp. 6, 41).

Adrian et al. 2021
: Adrian, S. B., A. Dély, D. Consoli, A. Merlini, and F. P. Andriulli (Oct. 2021). "Electromagnetic integral equations: insights in conditioning and preconditioning". *IEEE Open J. Antennas Propag.*, pp. 1143–1174 (cit. on pp. 5, 34, 35, 50, 57, 67, 68).

Ahmad et al. 2004
: Ahmad, F., G. Frazer, S. Kassam, and M. Amin (Jan. 2004). "Design and implementation of near-field, wideband synthetic aperture beamformers". *IEEE Trans. Aerosp. Electron. Syst.*, vol. 40, no. 1, pp. 206–220 (cit. on p. 7).

Alem et al. 2013
: Alem, Y. F., S. Akramus Salehin, D. H. Chae, and R. A. Kennedy (Dec. 2013). "Sparse recovery of spherical harmonic expansions from uniform distribution on sphere". In *7th Int. Conf. Signal Process. Commun. Syst. (ICSPCS)*. Carrara, VIC, Australia, pp. 1–5 (cit. on pp. 122, 126).

Alem et al. 2014
Alem, Y. F., D. H. Chae, and S. M. A. Salehin (June 2014). "Sparse recovery on sphere via probabilistic compressed sensing". In *IEEE Workshop Statist. Signal Process. (SSP)*. Gold Coast, VIC, Australia, pp. 380–383 (cit. on pp. 122, 126).

Alléon et al. 1997
Alléon, G., M. Benzi, and L. Giraud (Feb. 1, 1997). "Sparse approximate inverse preconditioning for dense linear systems arising in computational electromagnetics". *Numer. Algorithms*, vol. 16, no. 1, pp. 1–15 (cit. on p. 5).

Alonso Rodríguez et al. 2017
Alonso Rodríguez, A., J. Camaño, R. Ghiloni, and A. Valli (Oct. 2017). "Graphs, spanning trees and divergence-free finite elements in domains of general topology". *IMA J. Num. Anal.*, vol. 37, no. 4, pp. 1986–2003 (cit. on p. 36).

Alsnayyan et al. 2023
Alsnayyan, A. M. A., L. C. Kempel, and B. Shanker (Jan. 2023). "A complete Helmholtz decomposition on multiply connected subdivision surfaces and its application to integral equations". *IEEE Trans. Antennas Propag.*, vol. 71, no. 1, pp. 809–817 (cit. on pp. 6, 82).

Alvarez et al. 2007a
Alvarez, Y., F. Las-Heras, and M. R. Pino (Dec. 2007a). "Reconstruction of equivalent currents distribution over arbitrary three-dimensional surfaces based on integral equation algorithms". *IEEE Trans. Antennas Propag.*, vol. 55, no. 12, pp. 3460–3468 (cit. on p. 7).

Alvarez et al. 2007b
Alvarez, Y., T. K. Sarkar, and F. Las-Heras (June 2007b). "Improvement of the sources reconstruction techniques: analysis of the SVD algorithm and the RWG basis functions". In *Proc. IEEE Antennas Propag. Soc. Int. Symp.* Honolulu, HI, USA, pp. 5644–5647 (cit. on p. 7).

Andriulli et al. 2007
Andriulli, F. P., A. Tabacco, and G. Vecchi (Jan. 2007). "A multiresolution approach to the electric field integral equation in antenna problems". *SIAM J. Sci. Comput.*, vol. 29, no. 1, pp. 1–21 (cit. on p. 6).

Andriulli et al. 2008a
Andriulli, F. P., K. Cools, H. Bagci, F. Olyslager, A. Buffa, S. Christiansen, and E. Michielssen (Aug. 2008a). "A multiplicative Calderon preconditioner for the electric field integral equation". *IEEE Trans. Antennas Propag.*, vol. 56, no. 8, pp. 2398–2412 (cit. on pp. 6, 44, 57, 150).

Andriulli et al. 2008b
Andriulli, F. P., F. Vipiana, and G. Vecchi (Aug. 2008b). "Hierarchical bases for non-hierarchic 3-D triangular meshes". *IEEE Trans. Antennas Propag.*, vol. 56, no. 8, pp. 2288–2297 (cit. on p. 6).

Andriulli et al. 2010
Andriulli, F. P., A. Tabacco, and G. Vecchi (May 2010). "Solving the efie at low frequencies with a conditioning that grows only logarithmically with the number of unknowns". *IEEE Trans. Antennas Propag.*, vol. 58, no. 5, pp. 1614–1624 (cit. on pp. 5, 6, 25).

Andriulli et al. 2011
Andriulli, F. P. and E. Michielssen (July 2011). "Recovering the global loops by randomized projections". In *Proc. IEEE Antennas Propag. Soc. Int. Symp. URSI Nat. Radio Sci. Meeting*. Spokane, WA: IEEE, pp. 3197–3199 (cit. on p. 97).

Andriulli et al. 2013
Andriulli, F. P., K. Cools, I. Bogaert, and E. Michielssen (Apr. 2013). "On a well-conditioned electric field integral operator for multiply connected geometries". *IEEE Trans. Antennas Propag.*, vol. 61, no. 4, pp. 2077–2087 (cit. on pp. 6, 9, 13, 14, 25, 27, 28, 34, 35, 41, 44, 56–62, 71, 86, 98, 101, 109).

Andriulli 2012
Andriulli, F. P. (May 2012). "Loop-star and loop-tree decompositions : analysis and efficient algorithms". *IEEE Trans. Antennas Propag.*, vol. 60, no. 5, pp. 2347–2356 (cit. on pp. 5, 6, 26, 27, 42, 93, 98).

Arvas et al. 1983
Arvas, E., R. F. Harrington, and J. R. Mautȝ (Jan. 1983). *Radiation and Scattering from Electrically Small Conducting Bodies of Arbitrary Shape*. Tech. rep. Syracuse Univ. NY Dept. Elect. Comput. Eng. (cit. on p. 34).

Arvas et al. 1986
— (Jan. 1986). "Radiation and scattering from electrically small conducting bodies of arbitrary shape". *IEEE Trans. Antennas Propag.*, vol. 34, no. 1, pp. 66–77 (cit. on p. 34).

Atkinson 2009
Atkinson, K. E. (Mar. 1, 2009). *The Numerical Solution of Integral Equations of the Second Kind*. 1. Edition. Cambridge: Cambridge University Press. 572 pp. (cit. on p. 21).

Babuška 1971
Babuška, I. (Jan. 1, 1971). "Error-bounds for finite element method". *Numer. Math.*, vol. 16, no. 4, pp. 322–333 (cit. on p. 21).

Bangun et al. 2016
Bangun, A., A. Behboodi, and R. Mathar (Dec. 2016). "Sparse recovery in Wigner-D basis expansion". In *IEEE Global Conf. Signal Inf. Process. (GlobalSIP)*. Washington, DC, USA, pp. 287–291 (cit. on pp. 9, 122, 127, 130).

Bayliss et al. 1980
Bayliss, A. and E. Turkel (1980). "Radiation boundary conditions for wave-like equations". *Commun. Pure Appl. Math.*, vol. 33, no. 6, pp. 707–725 (cit. on p. 4).

Bazilevs et al. 2007
Bazilevs, Y., V. M. Calo, J. A. Cottrell, T. J. R. Hughes, A. Reali, and G. Scovazzi (Dec. 1, 2007). "Variational multiscale residual-based turbulence modeling for large eddy simulation of incompressible flows". *Comput. Methods Appl. Mech. Eng.*, vol. 197, no. 1, pp. 173–201 (cit. on p. 82).

Bazilevs et al. 2010
Bazilevs, Y., V. M. Calo, J. A. Cottrell, J. A. Evans, T. J. R. Hughes, S. Lipton, M. A. Scott, and T. W. Sederberg (Jan. 1, 2010). "Isogeometric analysis using T-splines". *Comp. Methods Appl. Mech. Eng.*, vol. 199, no. 5, pp. 229–263 (cit. on p. 150).

Bebendorf 2008
Bebendorf, M. (June 2008). *Hierarchical Matrices: A Means to Efficiently Solve Elliptic Boundary Value Problems*. Berlin: Springer (cit. on pp. 4, 50, 70).

Bendali 1984a
Bendali, A. (1984a). "Numerical analysis of the exterior boundary value problem for the time-harmonic maxwell equations by a boundary finite element method. i. the continuous problem". *Math. Comp.*, vol. 43, no. 167, pp. 29–46 (cit. on p. 6).

Bendali 1984b
— (1984b). "Numerical analysis of the exterior boundary value problem for the time-harmonic maxwell equations by a boundary finite element method. ii. the discrete problem". *Math. Comp.*, vol. 43, no. 167, pp. 47–68 (cit. on p. 6).

Berg et al. 2009
Berg, E. van den and M. P. Friedlander (Jan. 2009). "Probing the pareto frontier for basis pursuit solutions". *SIAM J. Sci. Comput.*, vol. 31, no. 2, pp. 890–912 (cit. on p. 129).

Berenger 1994
Berenger, J.-P. (Oct. 1, 1994). "A perfectly matched layer for the absorption of electromagnetic waves". *J. Comp. Phys.*, vol. 114, no. 2, pp. 185–200 (cit. on p. 4).

Blanchard et al. 2011
Blanchard, J. D., C. Cartis, and J. Tanner (Jan. 2011). "Compressed sensing: how sharp is the restricted isometry property?" *SIAM Rev.*, vol. 53, no. 1, pp. 105–125 (cit. on p. 127).

Bladel 2007
Bladel, J. G. van (May 2007). *Electromagnetic Fields*. Ed. by D. G. Dudley. IEEE Press Series on Electromagnetic Wave Theory. Hoboken, NJ, USA: John Wiley & Sons, Inc. (cit. on pp. 36, 89).

Bladel 1993
— (1993). "A discussion of Helmholtz theorem on a surface". *AEÜ-Archiv für Elektronik und Übertragungstechnik-Int. J. Electron. Commun.*, vol. 47, no. 3, pp. 131–136 (cit. on pp. 36, 89).

Bladel 1996
— (Jan. 1996). *Singular Electromagnetic Fields and Sources*. Oxford: IEEE (cit. on p. 14).

Bogaert et al. 2014
Bogaert, I., K. Cools, F. P. Andriulli, and H. Bağcı (Feb. 2014). "Low-frequency scaling of the standard and mixed magnetic field and Müller integral equations". *IEEE Trans. Antennas Propag.*, vol. 62, no. 2, pp. 822–831 (cit. on pp. 34, 46, 58, 59, 62, 153).

Boor 2001
Boor, C. de (Nov. 2001). *A Practical Guide to Splines*. 1st ed. Applied Mathematical Sciences 27. New York, NY: Springer (cit. on pp. 84, 87).

Boyd 2004
Boyd, S. (Mar. 2004). *Convex Optimization*. 1. Edition. Cambridge, UK ; New York: Cambridge University Press (cit. on p. 42).

Brown 1984
Brown, M. L. (Apr. 1984). "Scalar potentials in multiply connected regions". *Int. J. Num. Methods Eng.*, vol. 20, no. 4, pp. 665–680 (cit. on p. 41).

Brugiapaglia et al. 2018
Brugiapaglia, S. and B. Adcock (Jan. 2018). "Robustness to unknown error in sparse regularization". *IEEE Trans. Inf. Theory*, vol. 64, no. 10, pp. 6638–6661 (cit. on p. 136).

Bucci et al. 1987
Bucci, O. and G. Franceschetti (Dec. 1987). "On the spatial bandwidth of scattered fields". *IEEE Trans. Antennas Propag.*, vol. 35, no. 12, pp. 1445–1455 (cit. on p. 8).

Bucci et al. 1989
Bucci, O. and G. Franceschetti (July 1989). "On the degrees of freedom of scattered fields". *IEEE Trans. Antennas Propag.*, vol. 37, no. 7, pp. 918–926 (cit. on p. 8).

Bucci et al. 1994
Bucci, O., C. Gennarelli, G. Riccio, and C. Savarese (1994). "Fast and accurate far-field evaluation from a non redundant, finite number of plane polar measurements". In *Proc. IEEE Antennas Propag. Soc. Int. Symp.* Seattle, WA, USA, pp. 540–543 (cit. on p. 8).

Bucci et al. 1998
Bucci, O., C. Gennarelli, and C. Savarese (Mar. 1998). "Representation of electromagnetic fields over arbitrary surfaces by a finite and nonredundant number of samples". *IEEE Trans. Antennas Propag.*, vol. 46, no. 3, pp. 351–359 (cit. on p. 8).

Budak et al. 1973
Budak, B. M. and S. V. Fomin (1973). *Multiple Integrals, Field Theory And Series*. Moscow: Mir Publishers (cit. on p. 13).

Buffa et al. 2002
Buffa, A., M. Costabel, and C. Schwab (Oct. 1, 2002). "Boundary element methods for Maxwell's equations on non-smooth domains". *Numer. Math.*, vol. 92, no. 4, pp. 679–710 (cit. on p. 10).

Buffa et al. 2003a
Buffa, A. and S. Christiansen (Apr. 2003a). "The electric field integral equation on Lipschitz screens: definitions and numerical approximation". *Numer. Math.*, vol. 94, no. 2, pp. 229–267 (cit. on pp. 18, 21, 36).

Buffa et al. 2003b
Buffa, A. and R. Hiptmair (2003b). "Galerkin boundary element methods for electromagnetic scattering". In *Topics in Computational Wave Propagation*. Ed. by M. Ainsworth, P. Davies, D. Duncan, B. Rynne, and P. Martin. Red. by T. J. Barth, M. Griebel, D. E. Keyes, R. M. Nieminen, D. Roose, and T. Schlick. Vol. 31. Berlin, Heidelberg: Springer, pp. 83–124 (cit. on pp. 10, 18, 21, 24).

Buffa et al. 2007
Buffa, A. and S. Christiansen (Oct. 2007). "A dual finite element complex on the barycentric refinement". *Math. Comp.*, vol. 76, no. 260, pp. 1743–1769 (cit. on p. 150).

Buffa et al. 2010
Buffa, A., G. Sangalli, and R. Vázquez (Mar. 1, 2010). "Isogeometric analysis in electromagnetics: b-splines approximation". *Comput. Methods Appl. Mech. Eng.*, vol. 199, no. 17, pp. 1143–1152 (cit. on p. 82).

Buffa et al. 2014a
— (Jan. 15, 2014a). "Isogeometric methods for computational electromagnetics: B-spline and T-spline discretizations". *J. Comput. Phys.*, vol. 257, pp. 1291–1320 (cit. on pp. 82, 87, 150).

Buffa et al. 2014b
Buffa, A. and R. Vázquez (May 2014b). "Isogeometric analysis for electromagnetic scattering problems". In *Int. Conf. Num. Electrom. Modeling and Optimization for RF, Microw., and Terahertz Applications (NEMO)*, pp. 1–3 (cit. on p. 82).

Buffa et al. 2020
Buffa, A., J. Dölz, S. Kurz, S. Schöps, R. Vázquez, and F. Wolf (Jan. 1, 2020). "Multipatch approximation of the de Rham sequence and its traces in isogeometric analysis". *Numer. Math.*, vol. 144, no. 1, pp. 201–236 (cit. on pp. 82, 97).

Burq et al. 2012
Burq, N., S. Dyatlov, R. Ward, and M. Zworski (Jan. 2012). "Weighted eigenfunction estimates with applications to compressed sensing". *SIAM J. Math. Anal.*, vol. 44, no. 5, pp. 3481–3501 (cit. on pp. 122, 126).

Burton et al. 1995
Burton, M. and S. Kashyap (Nov. 1995). "A study of a recent, moment-method algorithm that is accurate to very low frequencies". *Appl. Comput. Electromagn. Soc. J.*, vol. 10, pp. 58–68 (cit. on pp. 5, 26).

Candes et al. 2005
Candes, E. and T. Tao (Dec. 2005). "Decoding by linear programming". *IEEE Trans. Inf. Theory*, vol. 51, no. 12, pp. 4203–4215 (cit. on p. 126).

Candes et al. 2006a
Candes, E., J. Romberg, and T. Tao (Feb. 2006a). "Robust uncertainty principles: exact signal reconstruction from highly incomplete frequency information". *IEEE Trans. Inf. Theory*, vol. 52, no. 2, pp. 489–509 (cit. on pp. 9, 121).

Candes et al. 2006b
Candes, E. J. and T. Tao (Dec. 2006b). "Near-optimal signal recovery from random projections: universal encoding strategies?" *IEEE Trans. Inf. Theory*, vol. 52, no. 12, pp. 5406–5425 (cit. on pp. 9, 121).

Carpentieri et al. 2004
Carpentieri, B., I. S. Duff, L. Giraud, and M. Magolu monga Made (2004). "Sparse symmetric preconditioners for dense linear systems in electromagnetism". *Numer. Linear Algebra Appl.*, vol. 11, no. 8-9, pp. 753–771 (cit. on p. 5).

Cessenat 1996
Cessenat, M. (July 15, 1996). *Mathematical Methods in Electromagetism: Linear Theory and Applications*. Singapore; River Edge, NJ: World Scientific Publishing Company. 394 pp. (cit. on p. 24).

Chang et al. 1977
Chang, Y. and R. Harrington (Nov. 1977). "A surface formulation for characteristic modes of material bodies". *IEEE Trans. Antennas Propag.*, vol. 25, no. 6, pp. 789–795 (cit. on p. 5).

Chao et al. 1995
Chao, J., Y. Liu, F. Rizzo, P. Martin, and L. Udpa (Dec. 1995). "Regularized integral equations and curvilinear boundary elements for electromagnetic wave scattering in three dimensions". *IEEE Trans. Antennas Propag.*, vol. 43, no. 12, pp. 1416–1422 (cit. on p. 5).

Chen et al. 2001
Chen, S. Y., W. C. Chew, J. M. Song, and J.-S. Zhao (Apr. 2001). "Analysis of low frequency scattering from penetrable scatterers". *IEEE Trans. Geosci. Remote Sens.*, vol. 39, no. 4, pp. 726–735 (cit. on p. 154).

Chew et al. 2001
Chew, W. C., J.-M. Jin, E. Michielssen, and J. Song (2001). *Fast and efficient algorithms in computational electromagnetics*. Artech House antennas and propagation library. Boston: Artech House. 931 pp. (cit. on p. 4).

Chhim et al. 2020
Chhim, T. L., A. Merlini, L. Rahmouni, J. E. O. Guzman, and F. P. Andriulli (Sept. 2020). "Eddy current modeling in multiply connected regions via a full-wave solver based on the quasi-Helmholtz projectors". *IEEE Open J. Antennas Propag.*, vol. 1, pp. 534–548 (cit. on pp. 34, 56).

Chiu et al. 2015
Chiu, P.-J., D.-C. Tsai, and Z.-M. Tsai (Sept. 2015). "Fast near-field antenna measurement technique". In *Proc. Eur. Microw. Conf. (EuMC)*. Paris, France, pp. 594–597 (cit. on p. 8).

Colton et al. 2013
Colton, D. L. and R. Kress (2013). *Inverse acoustic and electromagnetic scattering theory*. Third edition. Applied mathematical sciences volume 93. New York: Springer (cit. on pp. 10, 14).

Collin 1990
Collin, R. E. (Dec. 15, 1990). *Field Theory of Guided Waves*. New York: John Wiley & Sons. 864 pp. (cit. on p. 14).

Cools et al. 2009
Cools, K., F. P. Andriulli, F. Olyslager, and E. Michielssen (Oct. 2009). "Nullspaces of MFIE and Calderón preconditioned EFIE operators applied to toroidal surfaces". *IEEE Trans. Antennas Propag.*, vol. 57, no. 10, pp. 3205–3215 (cit. on pp. 13, 14).

Cools et al. 2011
Cools, K., F. P. Andriulli, D. De Zutter, and E. Michielssen (2011). "Accurate and conforming mixed discretization of the MFIE". *IEEE Antennas Wirel. Propag. Lett.*, vol. 10, pp. 528–531 (cit. on p. 150).

Cools 2021
Cools, K. (Nov. 2021). *BEAST*. Version v1.4.0 (cit. on p. 44).

Cornelius et al. 2016
Cornelius, R., D. Heberling, N. Koep, A. Behboodi, and R. Mathar (Apr. 2016). "Compressed sensing applied to spherical near-field to far-field transformation". In *Proc. 10th Eur. Conf. Antennas Propag. (EuCAP)*. Davos, Switzerland (cit. on pp. 9, 122, 126).

Courant 1943
Courant, R. (1943). "Variational methods for the solution of problems of equilibrium and vibrations". *Bull. Amer. Math. Soc.*, vol. 49, no. 1, pp. 1–23 (cit. on p. 4).

Cox 1972
Cox, M. G. (Oct. 1, 1972). "The numerical evaluation of b-splines". *J. Inst. Maths Applies*, vol. 10, no. 2, pp. 134–149 (cit. on p. 83).

CST Computer Simulation Technology 2022
CST Computer Simulation Technology (2022). *Microwave Studio*. Darmstadt, Germany (cit. on p. 77).

D'Agostino et al. 2017
D'Agostino, F., F. Ferrara, C. Gennarelli, R. Guerriero, and M. Migliozzi (2017). "Fast and accurate far-field prediction by using a reduced number of bipolar measurements". *IEEE Antennas Wireless Propag. Lett.*, vol. 16, pp. 2939–2942 (cit. on p. 8).

Darve 2000
Darve, E. (May 1, 2000). "The fast multipole method: numerical implementation". *J. Comp. Phys.*, vol. 160, no. 1, pp. 195–240 (cit. on p. 4).

de Boor 1972
De Boor, C. (July 1, 1972). "On calculating with B-splines". *J. Approx. Theory*, vol. 6, no. 1, pp. 50–62 (cit. on p. 83).

Dey et al. 2013
Dey, T. K., F. Fan, and Y. Wang (July 2013). "An efficient computation of handle and tunnel loops via Reeb graphs". *ACM Trans. Graph.*, vol. 32, no. 4, 32:1–32:10 (cit. on p. 36).

Dey 1994
Dey, T. K. (June 1994). "A new technique to compute polygonal schema for 2-manifolds with application to null-homotopy detection". In *Proc. Tenth Annu. Symp. Comput. Geom.* New York, NY, USA: Association for Computing Machinery, pp. 277–284 (cit. on p. 36).

Dlotko et al. 2013
Dlotko, P. and R. Specogna (Oct. 2013). "Physics inspired algorithms for (co)homology computations of three-dimensional combinatorial manifolds with boundary". *Computer Physics Communications*, vol. 184, no. 10, pp. 2257–2266 (cit. on p. 41).

Dlotko et al. 2014
— (Feb. 2014). "Lazy cohomology generators: a breakthrough in (co)homology computations for CEM". *IEEE Trans. Magn.*, vol. 50, no. 2, pp. 577–580 (cit. on p. 41).

Dölz et al. 2019
Dölz, J., S. Kurz, S. Schöps, and F. Wolf (Jan. 2019). "Isogeometric boundary elements in electromagnetism: rigorous analysis, fast methods, and examples". *SIAM J. Sci. Comput.*, vol. 41, no. 5, B983–B1010 (cit. on pp. 21, 82, 85, 97).

Dölz et al. 2020
— (Jan. 2020). "A numerical comparison of an isogeometric and a parametric higher order Raviart–Thomas approach to the electric field integral equation". *IEEE Trans. Antennas Propag.*, vol. 68, no. 1, pp. 593–597 (cit. on p. 82).

Dolph 1946
Dolph, C. L. (June 1946). "A current distribution for broadside arrays which optimizes the relationship between beam width and side-lobe level". *Proc. IRE*, vol. 34, no. 6, pp. 335–348 (cit. on p. 142).

Donepudi et al. 2001
Donepudi, K., J.-M. Jin, S. Velamparambil, J. Song, and W. C. Chew (July 2001). "A higher order parallelized multilevel fast multipole algorithm for 3-D scattering". *IEEE Trans. Antennas Propag.*, vol. 49, no. 7, pp. 1069–1078 (cit. on p. 149).

Donoho et al. 2001
Donoho, D. L. and X. Huo (Nov. 2001). "Uncertainty principles and ideal atomic decomposition". *IEEE Trans. Inf. Theory*, vol. 47, no. 7, pp. 2845–2862 (cit. on p. 126).

Donoho et al. 2005
Donoho, D. L. and J. Tanner (July 2005). "Neighborliness of randomly projected simplices in high dimensions". *Proc. Nat. Academy of Sci.*, vol. 102, no. 27, pp. 9452–9457 (cit. on p. 127).

Donoho et al. 2008
Donoho, D. L. and J. Tanner (July 2008). "Counting faces of randomly projected polytopes when the projection radically lowers dimension". *J. Amer. Math. Soc.*, vol. 22, no. 1, pp. 1–53 (cit. on p. 127).

Donoho et al. 2009
— (Nov. 2009). "Observed universality of phase transitions in high-dimensional geometry, with implications for modern data analysis and signal processing". *Philosoph. Trans. Roy. Soc. A, Math. Phys. Eng. Sci.*, vol. 367, no. 1906, pp. 4273–4293 (cit. on pp. 122, 127, 128, 151).

Donoho et al. 2010a
— (Apr. 2010a). "Exponential bounds implying construction of compressed sensing matrices, error-correcting codes, and neighborly polytopes by random sampling". *IEEE Trans. Inf. Theory*, vol. 56, no. 4, pp. 2002–2016 (cit. on pp. 127, 129, 130).

Donoho et al. 2010b
— (June 2010b). "Precise undersampling theorems". *Proc. IEEE*, vol. 98, no. 6, pp. 913–924 (cit. on pp. 122, 126, 127, 134, 151).

Donoho 2006a
Donoho, D. L. (Apr. 2006a). "Compressed sensing". *IEEE Trans. Inf. Theory*, vol. 52, no. 4, pp. 1289–1306 (cit. on pp. 9, 121).

Donoho 2006b
— (May 2006b). "High-dimensional centrally symmetric polytopes with neighborliness proportional to dimension". *Discrete & Comput. Geometry*, vol. 35, no. 4, pp. 617–652 (cit. on p. 127).

Duarte et al. 2011
Duarte, M. F. and Y. C. Eldar (Sept. 2011). "Structured compressed sensing: from theory to applications". *IEEE Trans. Signal Process.*, vol. 59, no. 9, pp. 4053–4085 (cit. on pp. 125, 126).

Dunavant 1985
Dunavant, D. A. (June 1985). "High degree efficient symmetrical gaussian quadrature rules for the triangle". *Int. J. Numer. Meth. Engng.*, vol. 21, no. 6, pp. 1129–1148 (cit. on p. 5).

Echeverri Bautista et al. 2014
Echeverri Bautista, M. A., M. A. Francavilla, F. Vipiana, and G. Vecchi (Mar. 2014). "A hierarchical fast solver for EFIE-MoM analysis of multiscale structures at very low frequencies". *IEEE Trans. Antennas Propag.*, vol. 62, no. 3, pp. 1523–1528 (cit. on p. 56).

Eibert et al. 2009
Eibert, T. F. and C. H. Schmidt (Apr. 2009). "Multilevel fast multipole accelerated inverse equivalent current method employing Rao-Wilton-Glisson discretization of electric and magnetic surface currents". *IEEE Trans. Antennas Propagat.*, vol. 57, no. 4, pp. 1178–1185 (cit. on p. 7).

Eibert et al. 2015
Eibert, T. F., E. Kilic, C. Lopez, R. A. M. Mauermayer, O. Neitz, and G. Schnattinger (2015). "Electromagnetic field transformations for measurements and simulations (invited paper)". *Prog. Electromagn. Res.*, vol. 151, pp. 127–150 (cit. on pp. 7, 110).

Eibert et al. 2016
Eibert, T. F., D. Vojvodic, and T. B. Hansen (Nov. 2016). "Fast inverse equivalent source solutions with directive sources". *IEEE Trans. Antennas Propag.*, vol. 64, no. 11, pp. 4713–4724 (cit. on p. 7).

Eibert et al. 1995
Eibert, T. F. and V. Hansen (Dec. 1995). "On the calculation of potential integrals for linear source distributions on triangular domains". *IEEE Trans. Antennas Propag.*, vol. 43, no. 12, pp. 1499–1502 (cit. on p. 5).

Eibert 2003
Eibert, T. F. (2003). "Iterative near-zone preconditioning of iterative method of moments electric field integral equation solutions". *IEEE Antennas Wirel. Propag. Lett.*, vol. 2, pp. 101–102 (cit. on p. 5).

Eibert 2004
— (June 2004). "Iterative-solver convergence for loop-star and loop-tree decompositions in method-of-moments solutions of the electric-field integral equation". *IEEE Antennas Propag. Mag.*, vol. 46, no. 3, pp. 80–85 (cit. on pp. 5, 27, 93).

Eibert 2005
— (Feb. 2005). "A diagonalized multilevel fast multipole method with spherical harmonics expansion of the k-space integrals". *IEEE Trans. Antennas Propag.*, vol. 53, no. 2, pp. 814–817 (cit. on p. 4).

Eldar et al. 2012
Eldar, Y. C. and G. Kutyniok, eds. (2012). *Compressed Sensing: Theory and Applications*. Cambridge: Cambridge University Press (cit. on pp. 126, 127, 136).

Elishakoff et al. 2004
Elishakoff, I. and M. Zingales (2004). "Convergence of Boobnov-Galerkin method exemplified". *AIAA J.*, vol. 42, no. 9, pp. 1931–1933 (cit. on p. 22).

Elishakoff et al. 2021
Elishakoff, I., J. Kaplunov, and E. Kaplunov (2021). "Galerkin's method was not developed by Ritz, contrary to the Timoshenko's statement". In *Nonlinear Dynamics of Discrete and Continuous Systems*. Ed. by A. K. Abramian, I. V. Andrianov, and V. A. Gaiko. Advanced Structured Materials. Cham: Springer International Publishing, pp. 63–82 (cit. on p. 22).

Ender 2013
Ender, J. (June 2013). "A brief review of compressive sensing applied to radar". In *Proc. 14th Int. Radar Symp. (IRS)*. Dresden, Germany, pp. 3–16 (cit. on p. 122).

Engquist et al. 1977
Engquist, B. and A. Majda (1977). "Radiation boundary conditions for the numerical simulation of waves". *Math. Comput*, vol. 31, no. 139, pp. 629–651 (cit. on p. 4).

Epstein et al. 2009
Epstein, C. L. and L. Greengard (Dec. 2009). "Debye sources and the numerical solution of the time harmonic Maxwell equations". *Commun. Pure Appl. Math.*, vol. 63, no. 4, pp. 413–463 (cit. on pp. 6, 56).

Epstein et al. 2012
Epstein, C. L., L. Greengard, and M. O'Neil (Aug. 2012). "Debye sources and the numerical solution of the time harmonic Maxwell equations II". *Commun. Pure Appl. Math.*, vol. 66, no. 5, pp. 753–789 (cit. on p. 6).

Erickson et al. 2004
Erickson, J. and S. Har-Peled (Jan. 2004). "Optimally cutting a surface into a disk". *Discrete Comput. Geom.*, vol. 31, no. 1, pp. 37–59 (cit. on p. 36).

Erickson et al. 2005
Erickson, J. and K. Whittlesey (Jan. 2005). "Greedy optimal homotopy and homology generators". In *Proc. Sixteenth Annu. ACM-SIAM Symp. Discrete Algorithms*. SODA '05. USA: Society for Industrial and Applied Mathematics, pp. 1038–1046 (cit. on p. 36).

Evans et al. 2020
Evans, J. A., M. A. Scott, K. M. Shepherd, D. C. Thomas, and R. Vázquez Hernández (Jan. 19, 2020). "Hierarchical B-spline complexes of discrete differential forms". *IMA J. Numer. Anal.*, vol. 40, no. 1, pp. 422–473 (cit. on p. 87).

FEKO 2017
FEKO (2017). *Version 14.0-273612 (x64)*. Troy, Michigan, United States: Altair Engineering, Inc. (cit. on p. 137).

Feynman 1961
Feynman, R. P. (1961). *Quantum Electrodynamics*. Frontiers in Physics. New York: W. A. Benjamin Inc. (cit. on p. 3).

Fornasier 2010
Fornasier, M., ed. (2010). *Theoretical foundations and numerical methods for sparse recovery*. Radon Series on Computational and Applied Mathematics. Berlin ; New York: De Gruyter (cit. on pp. 127, 130).

Foucart et al. 2013
Foucart, S. and H. Rauhut (2013). *A Mathematical Introduction to Compressive Sensing*. Applied and Numerical Harmonic Analysis. New York, NY: Springer New York (cit. on pp. 125, 126, 128, 130).

Freno et al. 2021
Freno, B. A., N. R. Matula, and W. A. Johnson (Oct. 2021). "Manufactured solutions for the method-of-moments implementation of the electric-field integral equation". *J. Comput. Physics*, vol. 443, p. 110538 (cit. on p. 50).

Fu et al. 2017
Fu, X., J. Li, L. J. Jiang, and B. Shanker (Oct. 2017). "Generalized debye sources-based efie solver on subdivision surfaces". *IEEE Trans. Antennas Propag.*, vol. 65, no. 10, pp. 5376–5386 (cit. on p. 6).

Fuchs et al. 2017
Fuchs, B., L. L. Coq, S. Rondineau, and M. D. Migliore (Oct. 2017). "Fast antenna far field characterization via sparse spherical harmonic expansion". *IEEE Trans. Antennas Propag.*, vol. 65, no. 10, pp. 5503–5510 (cit. on pp. 122, 126, 131, 132).

Gope et al. 2007
Gope, D., A. Ruehli, and V. Jandhyala (May 2007). "Solving low-frequency em-ckt problems using the peec method". *IEEE Trans. Adv. Packag.*, vol. 30, no. 2, pp. 313–320 (cit. on p. 6).

Grant et al. 2008
Grant, M. and S. Boyd (2008). "Graph implementations for nonsmooth convex programs". In *Recent Advances in Learning and Control*. Ed. by V. Blondel, S. Boyd, and H. Kimura. Lecture Notes in Control and Information Sci. Springer-Verlag Limited, pp. 95–110 (cit. on p. 129).

Grant et al. 2014
Grant, M. and S. Boyd (Mar. 2014). *CVX: Matlab Software for Disciplined Convex Programming, Version 2.1*. `http://cvxr.com/cvx` (cit. on p. 129).

Graglia et al. 1997
Graglia, R., D. Wilton, and A. Peterson (Mar. 1997). "Higher order interpolatory vector bases for computational electromagnetics". *IEEE Trans. Antennas Propag.*, vol. 45, no. 3, pp. 329–342 (cit. on p. 82).

Greengard et al. 1987
Greengard, L. and V. Rokhlin (Dec. 1, 1987). "A fast algorithm for particle simulations". *J. Comp. Phys.*, vol. 73, no. 2, pp. 325–348 (cit. on p. 4).

Hackbusch et al. 1989
Hackbusch, W. and Z. P. Nowak (July 1, 1989). "On the fast matrix multiplication in the boundary element method by panel clustering". *Numer. Math.*, vol. 54, no. 4, pp. 463–491 (cit. on p. 4).

Hackbusch 1995
Hackbusch, W. (1995). *Integral Equations: Theory and Numerical Treatment*. International Series of Numerical Mathematics 120. Basel: Birkhäuser Basel. 362 pp. (cit. on p. 21).

Hamming 1962
Hamming, R. W. (1962). *Numerical Methods for Scientists and Engineers*. New York: McGraw-Hill Book Company (cit. on p. 3).

Hamming 1994
— (Feb. 1994). *The Art of Probability: For Scientists and Engineers*. Redwood City, Calif: Westview Press (cit. on p. 109).

Hanson et al. 2013
Hanson, G. W. and A. B. Yakovlev (Mar. 2013). *Operator Theory for Electromagnetics: An Introduction*. New York: Springer Science & Business Media. 640 pp. (cit. on pp. 13, 14).

Hansen et al. 1999
Hansen, T. B. and A. D. Yaghjian (June 10, 1999). *Plane-Wave Theory of Time-Domain Fields: Near-Field Scanning Applications*. New York: IEEE Press. 402 pp. (cit. on pp. 12, 15).

Hansen 1935
Hansen, W. W. (Jan. 1935). "A new type of expansion in radiation problems". *Physical Review*, vol. 47, no. 2, pp. 139–143 (cit. on p. 15).

Hansen 1988
Hansen, J. E., ed. (Jan. 1988). *Spherical Near-Field Antenna Measurements*. repr. 2008. The Institution of Engineering and Technology, Michael Faraday House, Six Hills Way, Stevenage SG1 2AY, UK: IET (cit. on pp. 7, 8, 15–17, 29, 124).

Harrington 2001
Harrington, R. F. (2001). *Time-Harmonic Electromagnetic Fields*. New York: IEEE Press. 480 pp. (cit. on pp. 12, 17, 18).

Harrington 1993
— (May 5, 1993). *Field Computation by Moment Methods*. Reprint Edition. Piscataway, NJ: Wiley-IEEE Press. 240 pp. (cit. on p. 21).

Hazard et al. 1996
Hazard, C. and M. Lenoir (Nov. 1996). "On the solution of time-harmonic scattering problems for maxwell's equations". *SIAM J. Math. Anal.*, vol. 27, no. 6, pp. 1597–1630 (cit. on p. 21).

Hendijani et al. 2018
Hendijani, N., S. D. Gedney, R. McConnell, M. J. Roberts, J. C. Young, and R. J. Adams (Aug. 2018). "A broad-band Huygens surface source model for near-field to near-field transformations". *IEEE Trans. Electromagn. Compat.*, vol. 60, no. 4, pp. 926–936 (cit. on p. 8).

Hiptmair et al. 2002
Hiptmair, R. and J. Ostrowski (Jan. 2002). "Generators of $H_1(\Gamma_h, \mathbb{Z})$ for triangulated surfaces: construction and classification". *SIAM J. Comput.*, vol. 31, no. 5, pp. 1405–1423 (cit. on p. 36).

Hiptmair et al. 2005
— (Mar. 2005). "Coupled boundary-element scheme for Eddy-current computation". *J. Eng. Math.*, vol. 51, no. 3, pp. 231–250 (cit. on p. 41).

Hoefer 1985
Hoefer, W. (Oct. 1985). "The transmission-line matrix method - theory and applications". *IEEE Trans. Microw. Theory Tech.*, vol. 33, no. 10, pp. 882–893 (cit. on p. 4).

Hofmann et al. 2018a
Hofmann, B. and S. Kolb (Jan. 2018a). "A multistandard method of network analyzer self-calibration—generalization of multiline TRL". *IEEE Trans. Microwave Theory Techn.*, vol. 66, no. 1, pp. 245–254.

Hofmann et al. 2018b
Hofmann, B., O. Neitz, R. A. M. Mauermayer, and T. F. Eibert (Sept. 2018b). "Sparse recovery in spherical antenna near-field measurements". In *Kleinheubacher Tagung*. Miltenberg, Germany (cit. on p. 121).

Hofmann et al. 2019a
Hofmann, B. and T. F. Eibert (July 2019a). "Sparse recovery with predictable accuracy in noisy spherical antenna near-field measurements". In *Proc. IEEE Antennas Propag. Soc. Int. Symp.* Atlanta, GA, USA: IEEE, pp. 1857–1858 (cit. on pp. 121, 123).

Hofmann et al. 2019b
— (Aug. 2019b). "Sparse recovery with predictable accuracy in noisy spherical antenna near-field measurements". In *Forum Electromagn. Res. Methods Appl. Techn.* Vol. 34 (cit. on p. 121).

Hofmann et al. 2019c
Hofmann, B., O. Neitz, and T. F. Eibert (June 2019c). "Applying compressed sensing with predictable accuracy to spherical antenna near-field measurements". In *Proc. Photonics Electromagn. Res. Symp. (PIERS)*. Rome, Italy (cit. on p. 121).

Hofmann et al. 2019d
— (Aug. 2019d). "On the minimum number of samples for sparse recovery in spherical antenna near-field measurements". *IEEE Trans. Antennas Propagat.*, vol. 67, no. 12, pp. 7597–7610 (cit. on p. 121).

Hofmann et al. 2020
Hofmann, B., O. Kraus, and T. F. Eibert (July 2020). "Robustness of sparse reconstruction methods in spherical antenna near-field measurements". In *Proc. IEEE Antennas Propag. Soc. Int. Symp.* Montreal, Canada, pp. 1773–1774 (cit. on p. 121).

Hofmann et al. 2021a
Hofmann, B., T. F. Eibert, F. P. Andriulli, and S. B. Adrian (Dec. 2021a). "Low-frequency stable discretization of the electric field integral equation based on Poincaré's lemma". In *Proc. IEEE Antennas Propag. Soc. Int. Symp.* Singapore (cit. on p. 33).

Hofmann et al. 2021b
— (Aug. 2021b). "Towards accurate discretization of arbitrary right-hand side excitations on multiply-connected geometries". In *Int. Conf. Electromagn. Adv. Appl. (ICEAA)*. Honolulu, HI, USA, pp. 312–312 (cit. on p. 33).

Hofmann et al. 2022a
Hofmann, B., F. P. Andriulli, and S. B. Adrian (July 2022a). "Niederfrequente Stabilisierung der elektrischen Feldintegralgleichung für (fast) beliebige Anregungen". In *URSI Kommission B Workshop Felder und Wellen*. Raitenhaslach, Germany (cit. on pp. 33, 55).

Hofmann et al. 2022b
Hofmann, B., T. F. Eibert, F. P. Andriulli, and S. B. Adrian (Mar. 2022b). "Efficient combination of scalar-potential representations of solenoidal functions and quasi-Helmholtz projectors". In *Proc. 16th Eur. Conf. Antennas Propag. (EuCAP)*. Madrid, Spain (cit. on p. 33).

Hofmann et al. 2022c
Hofmann, B., T. F. Eibert, F. P. Andriulli, and S. B. Adrian (July 2022c). "Low-frequency-stabilized electric field integral equation on topologically non-trivial geometries for arbitrary excitations". In *Proc. IEEE Antennas Propag. Soc. Int. Symp.* Denver, CO, USA (cit. on p. 55).

Hofmann et al. 2022d
— (May 2022d). "Towards a low-frequency-stabilized electric field integral equation on simply-connected geometries for arbitrary excitations". In *URSI Atlantic / Asia-Pacific Radio Sci. Conf.* Gran Canaria, Spain (cit. on p. 33).

Hofmann et al. 2022e
— (Sept. 2022e). "Über die Stabilisierung von Feldtransformationen im niederfrequenten Bereich basierend auf dem elektrischen Feldintegralgleichungsoperator". In *Kleinheubacher Tagung*. Miltenberg, Germany (cit. on p. 109).

Hofmann et al. 2023a
— (Dec. 2023a). "A low-frequency stable, excitation agnostic discretization of the right-hand side for the electric field integral equation on multiply-connected geometries". *IEEE Trans. Antennas Propag.*, vol. 71, no. 12, pp. 9277–9288 (cit. on p. 33).

Hofmann et al. 2023b
— (May 2023b). "An excitation-aware and self-adaptive frequency normalization for low-frequency stabilized electric field integral equation formulations". *IEEE Trans. Antennas Propag.*, vol. 71, no. 5, pp. 4301–4314 (cit. on pp. 46, 55).

Hofmann et al. 2023c
— (Mar. 2023c). "Investigations on the low-frequency stability of inverse surface source field transformations based on the electric field integral operator". In *Proc. 17th Eur. Conf. Antennas Propag. (EuCAP)*. Florence, Italy (cit. on p. 109).

Hofmann et al. 2023d
— (July 2023d). "Towards a self-adaptive frequency normalization scheme for the low-frequency stabilized magnetic field integral equation". In *Proc. IEEE Antennas Propag. Soc. Int. Symp.* Portland, OR, USA, pp. 1213–1214 (cit. on pp. 55, 150).

Hofmann et al. 2023e
Hofmann, B., P. Respondek, and S. B. Adrian (Nov. 2023e). "SphericalScattering: a Julia package for electromagnetic scattering from spherical objects". *J. Open Source Softw.*, vol. 8, no. 91, pp. 1–4 (cit. on pp. 45, 49, 71, 100, 115).

Hofmann et al. 2024a
Hofmann, B., T. F. Eibert, F. P. Andriulli, and S. B. Adrian (Sept. 2024a). "A multiplicative Calderón preconditioner for the B-spline-based electric field integral equation". In *Int. Conf. Electromagn. Adv. Appl. (ICEAA)*. Lisbon, Portugal (cit. on p. 150).

Hofmann et al. 2024b
— (Sept. 2024b). "B-spline-based higher-order discretization of the magnetic field integral equation". In *Kleinheubacher Tagung*. Miltenberg, Germany (cit. on p. 150).

Hofmann et al. 2024c
Hofmann, B., M. Mirmohammadsadeghi, T. F. Eibert, F. P. Andriulli, and S. B. Adrian (Apr. 2024c). "Low-frequency stabilization for the B-spline-based isogeometric discretization of the electric field integral equation". *IEEE Trans. Antennas Propag.*, vol. 72, no. 4, pp. 3558–3571 (cit. on p. 81).

Hofmann et al. 2024d
— (July 2024d). "Quasi-Helmholtz projectors for the low-frequency stabilization of the isogeometrically discretized electric field integral equation". In *Proc. IEEE Antennas Propag. Soc. Int. Symp.* Florence, Italy (cit. on p. 81).

Hofmann 2022f
Hofmann, B. (Aug. 2022f). *SphericalScattering*. Version v0.5.0. Genève, Switzerland (cit. on pp. 45, 71, 100).

Hofmann 2023f
— (Aug. 2023f). *NURBS*. Version v0.5.1. Genève, Switzerland (cit. on p. 99).

Hsiao et al. 1997
Hsiao, G. and R. Kleinman (Mar. 1997). "Mathematical foundations for error estimation in numerical solutions of integral equations in electromagnetics". *IEEE Trans. Antennas Propag.*, vol. 45, no. 3, pp. 316–328 (cit. on pp. 24, 49).

Hughes et al. 2005
Hughes, T. J. R., J. A. Cottrell, and Y. Bazilevs (Oct. 1, 2005). "Isogeometric analysis: CAD, finite elements, NURBS, exact geometry and mesh refinement". *Comput. Methods Appl. Mech. Eng.*, vol. 194, no. 39, pp. 4135–4195 (cit. on pp. 82, 84).

Jackson 1999
Jackson, D. J. (1999). *Classical Electrodynamics*. Vol. 3. Hoboken, NJ: John Wiley & Sons, Inc (cit. on p. 3).

Jin 2014
Jin, J.-M. (Feb. 2014). *The Finite Element Method in Electromagnetics*. 3rd. Wiley-IEEE Press. 876 pp. (cit. on p. 4).

Jin 2015
— (2015). *Theory and Computation of Electromagnetic Fields*. Second edition. Hoboken, New Jersey: John Wiley & Sons, Inc (cit. on pp. 3, 4, 12, 14, 15, 17, 45, 71, 100, 115).

Johnson et al. 1990
Johnson, W. A., D. R. Wilton, and R. M. Sharpe (Jan. 1990). "Modeling scattering from and radiation by arbitrary shaped objects with the electric field integral equation triangular surface patch code". *Electromagnetics*, vol. 10, no. 1-2, pp. 41–63 (cit. on pp. 18, 36).

Jose Ma 2012
Jose Ma, G. (Aug. 2012). "An efficient framework for using higher-order curved div-conforming elements with cancellation of weak singularities in local space for surface integral equation". *IEEE Trans. Antennas Propag.*, vol. 60, no. 8, pp. 3736–3743 (cit. on p. 82).

Kellogg 1929
Kellogg, O. D. (1929). *Foundations of Potential Theory*. 1st ed. Die Grundlehren der Mathematischen Wissenschaften. Berlin, Heidelberg: Springer (cit. on p. 13).

Kiendl et al. 2010
Kiendl, J., Y. Bazilevs, M.-C. Hsu, R. Wüchner, and K.-U. Bletzinger (Aug. 1, 2010). "The bending strip method for isogeometric analysis of Kirchhoff–Love shell structures comprised of multiple patches". *Comput. Methods Appl. Mech. Eng.*, vol. 199, no. 37, pp. 2403–2416 (cit. on p. 82).

Kim et al. 2018
Kim, S. K. and A. F. Peterson (May 2018). "Adaptive h-refinement for the RWG-based EFIE". *IEEE J. Multiscale Multiphysics Comput. Tech.*, vol. 3, pp. 58–65 (cit. on p. 150).

Kordella et al. 2016
Kordella, S. C. and K. R. Grimm (Oct. 2016). "Determination of the far-field radiation pattern of an antenna from a set of sparse near-field measurements". In *AMTA Proc.* Austin, TX, pp. 1–6 (cit. on p. 8).

Kornprobst et al. 2021
Kornprobst, J., J. Knapp, R. A. M. Mauermayer, O. Neitz, A. Paulus, and T. F. Eibert (Aug. 2021). "Accuracy and conditioning of surface-source based near-field to far-field transformations". *IEEE Trans. Antennas Propag.*, vol. 69, no. 8, pp. 4894–4908 (cit. on p. 7).

Kotiuga 1987
Kotiuga, P. R. (Apr. 1987). "On making cuts for magnetic scalar potentials in multiply connected regions". *J. Appl. Phys.*, vol. 61, no. 8, pp. 3916–3918 (cit. on p. 41).

Kotiuga 1988
— (Apr. 1988). "Toward an algorithm to make cuts for magnetic scalar potentials in finite element meshes". *J. Appl. Phys.*, vol. 63, no. 8, pp. 3357–3359 (cit. on p. 41).

Kotiuga 1989
— (Sept. 1989). "An algorithm to make cuts for magnetic scalar potentials in tetrahedral meshes based on the finite element method". *IEEE Trans. Magn.*, vol. 25, no. 5, pp. 4129–4131 (cit. on p. 41).

Lax 2002
Lax, P. D. (2002). *Functional Analysis*. New York: John Wiley & Sons (cit. on p. 11).

Lebesgue 1924
Lebesgue, H. (1924). "Remarques sur les deux premiéres dèmonstrations du théoréme d'Euler relatif aux polyédres." *Bulletin de la Société Mathématique de France* (cit. on p. 33).

Lee et al. 2003
Lee, J.-F., R. Lee, and R. J. Burkholder (Aug. 2003). "Loop star basis functions and a robust preconditioner for efie scattering problems". *IEEE Trans. Antennas Propag.*, vol. 51, no. 8, pp. 1855–1863 (cit. on p. 6).

Li et al. 2016
Li, J., D. Dault, B. Liu, Y. Tong, and B. Shanker (Aug. 2016). "Subdivision based isogeometric analysis technique for electric field integral equations for simply connected structures". *J. Comp. Physics*, vol. 319, pp. 145–162 (cit. on pp. 6, 56, 82).

Lim et al. 1993
Lim, J. S., S. M. Rao, and D. R. Wilton (June 1993). "A novel technique to calculate the electromagnetic scattering by surfaces of arbitrary shape". In *URSI Radio Science Meeting Digest.* Ann Arbor, Michigan (cit. on p. 5).

Lim 1994
Lim, J. (1994). "The electromagnetic scattering from arbitrarily shaped bodies at very low frequency range using triangular patch modeling". Auburn: Auburn University (cit. on p. 5).

Liu et al. 2018a
Liu, Q. S., S. Sun, and W. C. Chew (Mar. 2018a). "A potential-based integral equation method for low-frequency electromagnetic problems". *IEEE Trans. Antennas Propag.*, vol. 66, no. 3, pp. 1413–1426 (cit. on p. 6).

Liu et al. 2018b
Liu, Y., X.-Y. Guo, and H.-J. Zhou (Mar. 2018b). "A memory saving augmented efie with modified basis functions for low-frequency problems". *IEEE Trans. Antennas Propagat.*, vol. 66, no. 3, pp. 1359–1365 (cit. on p. 6).

Livne et al. 2012
Livne, O. E. and A. Brandt (Jan. 2012). "Lean algebraic multigrid (LAMG): fast graph Laplacian linear solver". *SIAM J. Sci. Comput.*, vol. 34, no. 4, B499–B522 (cit. on pp. 42, 98).

Löschenbrand et al. 2016
Löschenbrand, D. and C. Mecklenbräuker (Sept. 2016). "Fast antenna characterization via a sparse spherical multipole expansion". In *4th Int. Workshop on Compressed Sensing Theory Appl. Radar, Sonar Remote Sensing (CoSeRa).* Aachen, Germany, pp. 212–216 (cit. on pp. 122, 126).

Massa et al. 2015
Massa, A., P. Rocca, and G. Oliveri (Feb. 2015). "Compressive sensing in electromagnetics - a review". *IEEE Antennas Propag. Mag.*, vol. 57, no. 1, pp. 224–238 (cit. on p. 122).

Mauermayer et al. 2015
Mauermayer, R. A. M. and T. F. Eibert (May 2015). "Combining the fast irregular antenna field transformation algorithm with asymptotic high frequency methods". In *AMTA Proc.* Piscataway, NJ, pp. 1–4 (cit. on p. 8).

Mauermayer et al. 2018
— (Mar. 2018). "Spherical field transformation above perfectly electrically conducting ground planes". *IEEE Trans. Antennas Propag.*, vol. 66, no. 3, pp. 1465–1478 (cit. on pp. 7, 129).

Mautz et al. 1978
Mautz, J. R. and R. F. Harrington (Apr. 1978). "H-field, E-field, and combined-field solutions for conducting bodies of revolution". *Int. J. Electron. Commun.*, vol. 32, pp. 157–164 (cit. on p. 18).

Mautz et al. 1979
— (July 1979). "A combined-source solution for radiation and scattering from a perfectly conducting body". *IEEE Trans. Antennas Propag.*, vol. 27, no. 4, pp. 445–454 (cit. on p. 18).

Mautz et al. 1980
— (June 1980). *An Improved E-Field Solution for a Conducting Body of Revolution.* Syracuse Univ. NY Dept. of Electrical and Comp. Engineering (cit. on p. 5).

Mautz et al. 1982
— (Sept. 1982). *A New E-Field Solution for a Conducting Surface Small or Comparable to the Wavelength.* Tech. rep. Syracuse Univ. NY Dept. Elect. Comput. Eng. (cit. on pp. 5, 9, 34, 37).

Mautz et al. 1984
— (Apr. 1984). "An E-field solution for a conducting surface small or comparable to the wavelength". *IEEE Trans. Antennas Propag.*, vol. 32, no. 4, pp. 330–339 (cit. on pp. 5, 9, 34, 38, 56, 59, 109).

Maue 1949
Maue, A.-W. (July 1949). "Zur Formulierung eines allgemeinen Beugungsproblems durch eine Integralgleichung". *Zeitschrift Phys.*, vol. 126, pp. 601–618 (cit. on pp. 4, 18).

Melin 1987
Melin, J. (Aug. 1987). "Measuring radar cross section at short distance". *IEEE Trans. Antennas Propag.*, vol. 35, no. 8, pp. 991–996 (cit. on p. 7).

Merlini et al. 2020
Merlini, A., Y. Beghein, K. Cools, E. Michielssen, and F. P. Andriulli (May 2020). "Magnetic and combined field integral equations based on the quasi-Helmholtz projectors". *IEEE Trans. Antennas Propag.*, vol. 68, no. 5, pp. 3834–3846 (cit. on p. 150).

Michielssen et al. 1996
Michielssen, E. and A. Boag (Aug. 1996). "A multilevel matrix decomposition algorithm for analyzing scattering from large structures". *IEEE Trans. Antennas Propag.*, vol. 44, no. 8, pp. 1086–1093 (cit. on p. 4).

Mie 1908
Mie, G. (Jan. 1908). "Beiträge zur Optik trüber Medien, speziell kolloidaler Metallösungen". *Ann. Phys.*, vol. 330, no. 3, pp. 377–445 (cit. on p. 3).

Migliore 2014
Migliore, M. D. (Apr. 2014). "A simple introduction to compressed sensing/sparse recovery with applications in antenna measurements". *IEEE Antennas Propag. Mag.*, vol. 56, no. 2, pp. 14–26 (cit. on p. 122).

Migliore 2015
— (Feb. 2015). "On the sampling of the electromagnetic field radiated by sparse sources". *IEEE Trans. Antennas Propag.*, vol. 63, no. 2, pp. 553–564 (cit. on p. 122).

Mirmohammadsadeghi et al. 2024
Mirmohammadsadeghi, M., B. Hofmann, T. F. Eibert, F. P. Andriulli, and S. B. Adrian (Mar. 2024). "A loop-star decomposition for the B-spline based discretization of the electric field integral equation". In *Proc. 18th Eur. Conf. Antennas Propag. (EuCAP)*. Glasgow, Scotland (cit. on p. 81).

Mitharwal et al. 2015
Mitharwal, R. and F. P. Andriulli (Nov. 2015). "A regularised boundary element formulation for contactless SAR evaluations within homogeneous and inhomogeneous head phantoms". *Comptes Rendus Physique*, vol. 16, no. 9, pp. 776–788 (cit. on p. 109).

MOSEK 2015
MOSEK (2015). *Version 7.1.0.12*. Copenhagen, Denmark: MOSEK ApS (cit. on p. 129).

Müller 1969
Müller, C. (1969). *Foundations of the Mathematical Theory of Electromagnetic Waves*. Berlin, Heidelberg: Springer Berlin Heidelberg (cit. on p. 5).

Nédélec 2001
Nédélec, J.-C. (2001). *Acoustic and Electromagnetic Equations*. Applied Mathematical Sciences. New York: Springer (cit. on pp. 10, 13, 14, 25).

Nédélec 1980
— (Sept. 1, 1980). "Mixed finite elements in $\mathbb{R}^3$". *Numer. Math.*, vol. 35, no. 3, pp. 315–341 (cit. on pp. 4, 101).

Neitz et al. 2019a
Neitz, O., B. Hofmann, and T. F. Eibert (June 2019a). "Plane-wave field synthesis for monostatic RCS prediction from multistatic near-field samples on irregular grids". In *Proc. Photonics Electromagn. Res. Symp. (PIERS)*. Rome, Italy (cit. on p. 7).

Neitz et al. 2019b
Neitz, O., R. A. M. Mauermayer, and T. F. Eibert (May 2019b). "3-D monostatic RCS determination from multistatic near-field measurements by plane-wave field synthesis". *IEEE Trans. Antennas Propag.*, vol. 67, no. 5, pp. 3387–3396 (cit. on p. 7).

Nolte et al. 2023a
Nolte, M., R. Torchio, S. Schöps, J. Dölz, F. Wolf, and A. Ruehli (Sept. 2023a). "A spline-based surface integral equation method". In *Kleinheubacher Tagung*. Miltenberg, Germany (cit. on p. 82).

Nolte et al. 2023b
Nolte, M., R. Torchio, S. Schöps, and A. Ruehli (Oct. 2023b). "Simulating multi-tapered coaxial baluns with an isogeometric surface integral equation method". In *Int. Conf. Electromagn. Adv. Appl. (ICEAA)*. Venice, Italy (cit. on p. 82).

NSI-MI 2018
NSI-MI (Nov. 2018). *Model NSI-RF-WR284 open ended waveguide* (cit. on pp. 137, 144).

Nyström 1930
: Nyström, E. J. (Jan. 1930). "Über die praktische Auflösung von Integralgleichungen mit Anwendungen auf Randwertaufgaben". *Acta Math.*, vol. 54 (none), pp. 185–204 (cit. on pp. 5, 21).

Ostrzyharczik et al. 2023
: Ostrzyharczik, D., J. Knapp, J. Kornprobst, and T. F. Eibert (Feb. 2023). "Inverse source solutions with Huygens' surface conforming distributed directive spherical harmonics expansions". *IEEE Trans. Antennas Propag.*, vol. 71, no. 2, pp. 1684–1696 (cit. on p. 7).

Peterson et al. 1995
: Peterson, A. F. and K. R. Aberegg (1995). "Parametric mapping of vector basis functions for surface integral equation formulations". *Appl. Comput. Electromagn. Soc. J. ACES*, pp. 107–115 (cit. on p. 82).

Peterson 2006
: Peterson, A. F. (Dec. 2006). *Mapped Vector Basis Functions for Electromagnetic Integral Equations*. Morgan & Claypool Publishers (cit. on pp. 24, 25, 82, 85, 88, 101).

Phillips et al. 1997
: Phillips, J. and J. White (Oct. 1997). "A precorrected-FFT method for electrostatic analysis of complicated 3-D structures". *IEEE Trans. Comput.-Aided Des. Integr. Circuits Syst.*, vol. 16, no. 10, pp. 1059–1072 (cit. on p. 4).

Piegl 1995
: Piegl, L. (1995). *The NURBS Book*. Berlin, Heidelberg: Springer Berlin Heidelberg (cit. on pp. 81, 83–85, 157, 158).

Poggio et al. 1973
: Poggio, A. J. and E. K. Miller (1973). "Integral equation solutions of three-dimensional scattering problems". *Comput. Tech. Electromagn.*, p. 159 (cit. on p. 5).

Qian et al. 2008a
: Qian, Z. and W. C. Chew (July 2008a). "An augmented electric field integral equation for low frequency electromagnetic analysis". In *Proc. IEEE Antennas Propag. Soc. Int. Symp. URSI Nat. Radio Sci. Meeting*. San Diego, CA, pp. 1–4 (cit. on p. 56).

Qian et al. 2008b
: Qian, Z. G. and W. C. Chew (2008b). "An augmented electric field integral equation for high-speed interconnect analysis". *Microw. Opt. Technol. Lett.*, vol. 50, no. 10, pp. 2658–2662 (cit. on p. 6).

Qian et al. 2010
: — (Oct. 2010). "Enhanced A-EFIE with perturbation method". *IEEE Trans. Antennas Propag.*, vol. 58, no. 10, pp. 3256–3264 (cit. on pp. 6, 56).

Rao et al. 1982
: Rao, S., D. Wilton, and A. Glisson (May 1982). "Electromagnetic scattering by surfaces of arbitrary shape". *IEEE Trans. Antennas Propag.*, vol. 30, no. 3, pp. 409–418 (cit. on pp. 5, 24, 25, 86, 110).

Rauhut et al. 2011
Rauhut, H. and R. Ward (Feb. 2011). "Sparse recovery for spherical harmonic expansions". *arXiv:1102.4097v1* (cit. on pp. 122, 126).

Ravelo et al. 2015
Ravelo, B., Y. Liu, and A. K. Jastrzebski (Dec. 2015). "PCB near-field transient emission time-domain model". *IEEE Trans. Electromagn. Compat.*, vol. 57, no. 6, pp. 1320–1328 (cit. on p. 8).

Regue et al. 2001
Regue, J.-R., M. Ribo, J.-M. Garrell, and A. Martin (Nov. 2001). "A genetic algorithm based method for source identification and far-field radiated emissions prediction from near-field measurements for pcb characterization". *IEEE Trans. Electromagn. Compat.*, vol. 43, no. 4, pp. 520–530 (cit. on p. 8).

Ren 2002
Ren, Z. (Mar. 2002). "T-Ω formulation for Eddy-current problems in multiply connected regions". Vol. 38, no. 2, pp. 557–560 (cit. on p. 41).

RFspin 2017
RFspin (Dec. 2017). *Model DRH400 double ridged waveguide horn* (cit. on p. 144).

Richeson 2012
Richeson, D. S. (Apr. 2012). *Euler's Gem: The Polyhedron Formula and the Birth of Topology*. Reprint edition. Princeton, NJ: Princeton University Press. 332 pp. (cit. on pp. 36, 37, 94).

Rinas et al. 2016
Rinas, D., P. Ahl, and S. Frei (Sept. 28, 2016). "PCB current identification based on near-field measurements using preconditioning and regularization". *Adv. Radio Sci.*, vol. 14, pp. 121–127 (cit. on p. 8).

Roache 2001
Roache, P. J. (Nov. 2001). "Code verification by the method of manufactured solutions". *J. Fluids Eng.*, vol. 124, no. 1, pp. 4–10 (cit. on p. 50).

Roth et al. 2019
Roth, T. E. and W. C. Chew (July 2019). "Role of classical time domain cem methods for quantum electromagnetics". In *Proc. IEEE Antennas Propag. Soc. Int. Symp. URSI Nat. Radio Sci. Meeting*, pp. 1063–1064 (cit. on p. 3).

Roth 2020
Roth, T. E. (Nov. 12, 2020). "Development of potential-based time domain integral equations for quantum electrodynamics modeling". Doctoral Thesis. University of Illinois at Urbana-Champaign (cit. on p. 3).

Ruge et al. 1987
Ruge, J. W. and K. Stüben (Jan. 1987). "4. algebraic multigrid". In *Multigrid Methods*. Frontiers in Applied Mathematics. Society for Industrial and Applied Mathematics, pp. 73–130 (cit. on pp. 98, 99).

Saad et al. 1986
Saad, Y. and M. H. Schultz (July 1986). "GMRES: a generalized minimal residual algorithm for solving nonsymmetric linear systems". *SIAM J. Sci. Stat. Comput.*, vol. 7, no. 3, pp. 856–869 (cit. on p. 69).

Saad 2003
Saad, Y. (Apr. 1, 2003). *Iterative Methods for Sparse Linear Systems*. 2. Edition. Philadelphia: Society for Industrial and Applied Mathematics (cit. on pp. 68, 140, 145).

Saff et al. 1997
Saff, E. B. and A. B. J. Kuijlaars (1997). "Distributing many points on a sphere". *Math. Intell.*, vol. 19, no. 1 (cit. on pp. 116, 132).

Safaai-Jazi 1994
Safaai-Jazi, A. (Mar. 1994). "A new formulation for the design of Chebyshev arrays". *IEEE Trans. Antennas Propag.*, vol. 42, no. 3, pp. 439–443 (cit. on p. 142).

Sarkar et al. 1999
Sarkar, T. and A. Taaghol (Mar. 1999). "Near-field to near/far-field transformation for arbitrary near-field geometry utilizing an equivalent electric current and MoM". *IEEE Trans. Antennas Propag.*, vol. 47, no. 3, pp. 566–573 (cit. on p. 7).

Sauter et al. 2011
Sauter, S. A. and C. Schwab (2011). *Boundary Element Methods*. Berlin, Heidelberg: Springer Berlin Heidelberg (cit. on pp. 13, 14, 21, 24, 99).

Saurer et al. 2022
Saurer, M. M., B. Hofmann, and T. F. Eibert (Sept. 2022). "A fully polarimetric multilevel fast spectral domain algorithm for 3-D imaging with irregular sample locations". *IEEE Trans. Microw. Theory Tech.*, vol. 70, no. 9, pp. 4231–4242 (cit. on p. 7).

Sauter et al. 1997
Sauter, S. A. and C. Schwab (Dec. 1997). "Quadrature for hp-Galerkin BEM in $\mathbb{R}^3$". *Numer. Math.*, vol. 78, no. 2, pp. 211–258 (cit. on pp. 5, 99).

Schmidt et al. 2008
Schmidt, C. H., M. M. Leibfritz, and T. F. Eibert (Mar. 2008). "Fully probe-corrected near-field far-field transformation employing plane wave expansion and diagonal translation operators". *IEEE Trans. Antennas Propag.*, vol. 56, no. 3, pp. 737–746 (cit. on p. 7).

Schmidt et al. 2011
Schmidt, C. H., D. T. Schobert, and T. F. Eibert (Apr. 2011). "Electric dipole based synthetic data generation for probe-corrected near-field antenna measurements". In *Proc. 5th Eur. Conf. Antennas Propag. (EUCAP)*. Rome, Italy, pp. 3269–3273 (cit. on p. 137).

Schobert et al. 2012
Schobert, D. T. and T. F. Eibert (Mar. 2012). "Low-frequency surface integral equation solution by multilevel Green's function interpolation with fast Fourier transform acceleration". *IEEE Trans. Antennas Propag.*, vol. 60, no. 3, pp. 1440–1449 (cit. on p. 4).

Schnattinger et al. 2014
Schnattinger, G., R. A. M. Mauermayer, and T. F. Eibert (Aug. 2014). "Monostatic radar cross section near-field far-field transformations by multilevel plane-wave decomposition". *IEEE Trans. Antennas Propag.*, vol. 62, no. 8, pp. 4259–4268 (cit. on p. 7).

Scott 2011
Scott, M. A. (Aug. 2011). "T-splines as a design-through-analysis technology". Doctoral Thesis. University of Texas at Austin (cit. on p. 150).

Shanker et al. 2003
Shanker, B., A. Ergin, M. Lu, and E. Michielssen (Mar. 2003). "Fast analysis of transient electromagnetic scattering phenomena using the multilevel plane wave time domain algorithm". *IEEE Trans. Antennas Propag.*, vol. 51, no. 3, pp. 628–641 (cit. on p. 4).

Shafieipour et al. 2014
Shafieipour, M., I. Jeffrey, J. Aronsson, and V. I. Okhmatovski (Feb. 2014). "On the equivalence of RWG method of moments and the locally corrected Nyström method for solving the electric field integral equation". *IEEE Trans. Antennas Propag.*, vol. 62, no. 2, pp. 772–782 (cit. on p. 5).

Silvester 1969
Silvester, P. (1969). "Finite element solution of homogeneous waveguide problems". *Alta Freq.*, vol. 38, no. 1, pp. 313–317 (cit. on p. 4).

Simpson et al. 2018
Simpson, R. N., Z. Liu, R. Vázquez, and J. A. Evans (June 1, 2018). "An isogeometric boundary element method for electromagnetic scattering with compatible B-spline discretizations". *J. Comp. Physics*, vol. 362, pp. 264–289 (cit. on pp. 82, 85–87).

Sleijpen et al. 1993
Sleijpen, G. L. and D. R. Fokkema (1993). "BiCGstab(L) for linear equations involving unsymmetric matrices with complex spectrum". *Electron. Trans. Num. Anal.*, vol. 1, pp. 11–32 (cit. on p. 69).

Sonneveld et al. 2008
Sonneveld, P. and M. B. van Gijzen (Nov. 2008). "IDR(s): a family of simple and fast algorithms for solving large nonsymmetric systems of linear equations". *SIAM J. Sci. Comput.* (cit. on p. 69).

Song et al. 2014
Song, E., H.-B. Park, and H. H. Park (Oct. 2014). "An evaluation method for radiated emissions of components and modules in mobile devices". *IEEE Trans. Electromagn. Compat.*, vol. 56, no. 5, pp. 1020–1026 (cit. on p. 8).

Song et al. 1997
Song, J., C.-C. Lu, and W. C. Chew (Oct. 1997). "Multilevel fast multipole algorithm for electromagnetic scattering by large complex objects". *IEEE Trans. Antennas Propag.*, vol. 45, no. 10, pp. 1488–1493 (cit. on p. 4).

Sreenivasiah et al. 1981
Sreenivasiah, I., D. Chang, and M. Ma (Aug. 1981). "Emission characteristics of electrically small radiating sources from tests inside a tem cell". *IEEE Trans. Electromagn. Compat.*, vol. EMC-23, no. 3, pp. 113–121 (cit. on p. 8).

Steinberg et al. 1985
Steinberg, S. and P. J. Roache (Jan. 1985). "Symbolic manipulation and computational fluid dynamics". *J. Comp. Physics*, vol. 57, no. 2, pp. 251–284 (cit. on p. 50).

Stewart 2002
Stewart, G. W. (Jan. 2002). "A Krylov–Schur algorithm for large eigenproblems". *SIAM J. Matrix Anal. Appl.*, vol. 23, no. 3, pp. 601–614 (cit. on p. 68).

Steinbach 2008
Steinbach, O. (2008). *Numerical Approximation Methods for Elliptic Boundary Value Problems*. New York, NY: Springer New York (cit. on p. 68).

Stojnic et al. 2008a
Stojnic, M., Weiyu Xu, and B. Hassibi (Mar. 2008a). "Compressed sensing – probabilistic analysis of a null-space characterization". In *Proc. IEEE Int. Conf. Acoust. Speech Signal Process.* Las Vegas, NV, pp. 3377–3380 (cit. on p. 128).

Stojnic et al. 2008b
— (July 2008b). "Compressed sensing of approximately sparse signals". In *Proc. IEEE Int. Symp. Inf. Theory*. Toronto, ON, Canada, pp. 2182–2186 (cit. on p. 128).

Stojnic 2010
Stojnic, M. (2010). "ℓ_1 optimization and its various thresholds in compressed sensing". In *Proc. IEEE Int. Conf. Acoust. Speech Signal Process.* Dallas, TX, pp. 3910–3913 (cit. on p. 128).

Strohmer 2012
Strohmer, T. (Dec. 2012). "Measure what should be measured: progress and challenges in compressive sensing". *IEEE Signal Process. Lett.*, vol. 19, no. 12, pp. 887–893 (cit. on pp. 121, 126).

Stratton 1941
Stratton, A. J. (1941). *Electromagnetic Theory*. Hoboken, New Jersey: Mcgraw Hill Book Company. 648 pp. (cit. on p. 15).

Sullivan 1996
Sullivan, M. C. (Mar. 1996). "Knots about Stokes' theorem". *Coll. Math. J.*, vol. 27, no. 2, pp. 119–122 (cit. on p. 52).

Tanner 2012
Tanner, J. (Apr. 2012). *Phase Transitions of the Regular Polytopes and Cone*. https://people.maths.ox.ac.uk/tanner/polytopes.shtml (cit. on p. 130).

Taskinen et al. 2006
Taskinen, M. and P. Yla-Oijala (Jan. 2006). "Current and charge integral equation formulation". *IEEE Trans. Antennas Propag.*, vol. 54, no. 1, pp. 58–67 (cit. on p. 6).

Tillmann et al. 2014
Tillmann, A. M. and M. E. Pfetsch (Feb. 2014). "The computational complexity of the restricted isometry property, the nullspace property, and related concepts in compressed sensing". *IEEE Trans. Inf. Theory*, vol. 60, no. 2, pp. 1248–1259 (cit. on p. 126).

Tobon Vasquez et al. 2020
Tobon Vasquez, J. A., Z. Peng, J.-F. Lee, G. Vecchi, and F. Vipiana (Feb. 2020). "Automatic localized nonconformal mesh refinement for surface integral equations". *IEEE Trans. Antennas Propag.*, vol. 68, no. 2, pp. 967–975 (cit. on p. 150).

Trefethen et al. 1997
Trefethen, L. N. and D. Bau (Jan. 1997). *Numerical Linear Algebra*. Philadelphia, PA 19104-2688: SIAM (cit. on p. 68).

Trefethen 1992
Trefethen, L. N. (Nov. 1992). "The definition of numerical analysis". *SIAM News* (cit. on pp. 3, 21, 55).

Tropp 2004
Tropp, J. (Oct. 2004). "Greed is good: algorithmic results for sparse approximation". *IEEE Trans. Inf. Theory*, vol. 50, no. 10, pp. 2231–2242 (cit. on p. 126).

Valdés et al. 2011
Valdés, F., F. P. Andriulli, K. Cools, and E. Michielssen (Apr. 2011). "High-order div- and quasi curl-conforming basis functions for Calderón multiplicative preconditioning of the EFIE". *IEEE Trans. Antennas Propag.*, vol. 59, no. 4, pp. 1321–1337 (cit. on p. 149).

Vázquez 2016
Vázquez, R. (Aug. 1, 2016). "A new design for the implementation of isogeometric analysis in Octave and Matlab: GeoPDEs 3.0". *Comput. Math. Appl.*, vol. 72, no. 3, pp. 523–554 (cit. on p. 99).

Vecchi et al. 2010
Vecchi, G. and J. L. Araque Quijano (Apr. 2010). "Field and source equivalence in source reconstruction on 3d surfaces". *Prog. Electromagn. Res.*, vol. 103, pp. 67–100 (cit. on p. 7).

Vecchi 1999
Vecchi, G. (Feb. 1999). "Loop-star decomposition of basis functions in the discretization of the EFIE". *IEEE Trans. Antennas Propag.*, vol. 47, no. 2, pp. 339–346 (cit. on pp. 5, 26, 36, 93, 94).

Veiga et al. 2013
Veiga, L. B. D., A. Buffa, G. Sangalli, and R. Vázquez (July 23, 2013). "Aanalysis-suitable T-splines of arbitrary degree: definition, linear independence and approximation properties". *Math. Models Methods Appl. Sci.* (cit. on p. 150).

Veiga et al. 2014
Veiga, L. B., A. Buffa, G. Sangalli, and R. Vázquez (May 2014). "Mathematical analysis of variational isogeometric methods". *Acta Numer.*, vol. 23, pp. 157–287 (cit. on pp. 82, 85, 97).

Verite 1987
Verite, J. (May 1987). "Calculation of multivalued potentials in exterior regions". *IEEE Trans. Magn.*, vol. 23, no. 3, pp. 1881–1887 (cit. on p. 36).

Vico et al. 2015
Vico, F., M. Ferrando-Bataller, T. B. Jiménez, and A. Berenguer (July 2015). "Decoupled potential integral equation applied to complex geometries". In *Proc. IEEE Antennas Propag. Soc. Int. Symp. URSI Nat. Radio Sci. Meeting*. Vancouver, BC, Canada, pp. 746–747 (cit. on p. 5).

Vico et al. 2016
Vico, F., M. Ferrando, L. Greengard, and Z. Gimbutas (Apr. 2016). "The decoupled potential integral equation for time-harmonic electromagnetic scattering". *Commun. Pure Appl. Math.*, vol. 69, no. 4, pp. 771–812 (cit. on pp. 6, 56).

Vives-Gilabert et al. 2007
Vives-Gilabert, Y., C. Arcambal, A. Louis, F. de Daran, P. Eudeline, and B. Mazari (May 2007). "Modeling magnetic radiations of electronic circuits using near-field scanning method". *IEEE Trans. Electromagn. Compat.*, vol. 49, no. 2, pp. 391–400 (cit. on p. 8).

Vives-Gilabert et al. 2009
Vives-Gilabert, Y., C. Arcambal, A. Louis, P. Eudeline, and B. Mazari (Nov. 2009). "Modeling magnetic emissions combining image processing and an optimization algorithm". *IEEE Trans. Electromagn. Compat.*, vol. 51, no. 4, pp. 909–918 (cit. on p. 8).

Weiland 2003
Weiland, T. (2003). "Finite integration method and discrete electromagnetism". In *Computational Electromagnetics*. Ed. by P. Monk, C. Carstensen, S. Funken, W. Hackbusch, and R. H. W. Hoppe. Lecture Notes in Computational Science and Engineering. Berlin, Heidelberg: Springer, pp. 183–198 (cit. on p. 4).

Weiland 1977
Weiland, T. (1977). "Eine Methode zur Lösung der Maxwellschen Gleichungen für sechskomponentige Felder auf diskreter Basis". *Arch. für Elektron. Übertrag.*, vol. 31, no. 3 (cit. on p. 4).

Wildman et al. 2004
Wildman, R. A. and D. Weile (Nov. 2004). "An accurate broad-band method of moments using higher order basis functions and tree-loop decomposition". *IEEE Trans. Antennas Propag.*, vol. 52, no. 11, pp. 3005–3011 (cit. on p. 82).

Wilton et al. 1981
Wilton, D. R. and A. W. Glisson (June 1981). "On improving the electric field integral equation at low frequencies". *Proc. URSI Radio Sci. Meet. Dig*, vol. 24, p. 33 (cit. on pp. 5, 109).

Wilton et al. 1984
Wilton, D., S. Rao, A. Glisson, D. Schaubert, O. Al-Bundak, and C. Butler (Mar. 1984). "Potential integrals for uniform and linear source distributions on polygonal and polyhedral domains". *IEEE Trans. Antennas Propag.*, vol. 32, no. 3, pp. 276–281 (cit. on p. 5).

Wu et al. 1977
Wu, T.-K. and L. L. Tsai (1977). "Scattering from arbitrarily-shaped lossy dielectric bodies of revolution". *Radio Sci.*, vol. 12, no. 5, pp. 709–718 (cit. on p. 5).

Wu et al. 1995
Wu, W.-L., A. W. Glisson, and D. Kajfez (Jan. 1995). "A study of two numerical solution procedures for the electric field integral equation at low frequency". *Appl. Comput. Electromagn. Soc. J.*, vol. 10, no. 3, pp. 69–80 (cit. on pp. 5, 9, 26, 34, 37).

Xu et al. 2003
Xu, J. and L. Zikatanov (Mar. 1, 2003). "Some observations on Babuška and Brezzi theories". *Numer. Math.*, vol. 94, no. 1, pp. 195–202 (cit. on p. 21).

Xu et al. 2011
Xu, W. and B. Hassibi (Oct. 2011). "Precise stability phase transitions for ℓ_1 minimization: a unified geometric framework". *IEEE Trans. Inf. Theory*, vol. 57, no. 10, pp. 6894–6919 (cit. on pp. 127, 134).

Yaghjian 1986
Yaghjian, A. (Jan. 1986). "An overview of near-field antenna measurements". *IEEE Trans. Antennas Propag.*, vol. 34, no. 1, pp. 30–45 (cit. on p. 7).

Yee 1966
Yee, K. (May 1966). "Numerical solution of initial boundary value problems involving maxwell's equations in isotropic media". *IEEE Trans. Antennas Propag.*, vol. 14, no. 3, pp. 302–307 (cit. on p. 4).

Yilmaz et al. 2004
Yilmaz, A., J.-M. Jin, and E. Michielssen (Oct. 2004). "Time domain adaptive integral method for surface integral equations". *IEEE Trans. Antennas Propag.*, vol. 52, no. 10, pp. 2692–2708 (cit. on p. 4).

Yin et al. 2007
Yin, X., M. Jin, and X. Gu (Dec. 2007). "Computing shortest cycles using universal covering space". *Visual Comput.*, vol. 23, no. 12, pp. 999–1004 (cit. on p. 36).

Yla-Oijala et al. 2003
Yla-Oijala, P. and M. Taskinen (Aug. 2003). "Calculation of CFIE impedance matrix elements with RWG and n×RWG functions". *IEEE Trans. Antennas Propag.*, vol. 51, no. 8, pp. 1837–1846 (cit. on p. 5).

Young et al. 2012
Young, J. C., Y. Xu, R. J. Adams, and S. D. Gedney (2012). "High-order Nyström implementation of an augmented electric field integral equation". *IEEE Antennas Wirel. Propag. Lett.*, vol. 11, pp. 846–849 (cit. on p. 5).

Zhao et al. 2000
Zhao, J. S. and W. C. Chew (Oct. 2000). "Integral equation solution of Maxwell's equations from zero frequency to microwave frequencies". *IEEE Trans. Antennas Propag.*, vol. 48, no. 10, pp. 1635–1645 (cit. on pp. 6, 38, 56, 59, 60).

Zhao et al. 2002
Zhao, J. S., W. C. Chew, T. J. Cui, and Y. Zhang (June 2002). "Cancellations of surface loop basis functions". In *Proc. IEEE Antennas Propag. Soc. Int. Symp. URSI Nat. Radio Sci. Meeting*. Vol. 1. San Antonio, TX, USA: IEEE, pp. 58–61 (cit. on p. 38).

Zhao et al. 2005a
Zhao, K., M. Vouvakis, and J.-F. Lee (Nov. 2005a). "The adaptive cross approximation algorithm for accelerated method of moments computations of EMC problems". *IEEE Trans. Electromagn. Compat.*, vol. 47, no. 4, pp. 763–773 (cit. on pp. 4, 50, 70).

Zhao et al. 2005b
— (Nov. 2005b). "The adaptive cross approximation algorithm for accelerated method of moments computations of emc problems". *IEEE Trans. Electromagn. Compat.*, vol. 47, no. 4, pp. 763–773 (cit. on p. 4).

Zhang 2013
Zhang, Y. (Mar. 2013). "Theory of compressive sensing via ℓ_1-minimization: a non-RIP analysis and extensions". *J. Oper. Res. Soc. China*, vol. 1, no. 1, pp. 79–105 (cit. on p. 128).

Zhu et al. 2014
Zhu, J., S. Omar, and D. Jiao (Aug. 2014). "Solution of the electric field integral equation when it breaks down". *IEEE Trans. Antennas Propag.*, vol. 62, no. 8, pp. 4122–4134 (cit. on p. 6).

Publications of the Author

Journal Articles

Hofmann et al. 2018a
: Hofmann, B. and S. Kolb (Jan. 2018a). "A multistandard method of network analyzer self-calibration—generalization of multiline TRL". *IEEE Trans. Microwave Theory Techn.*, vol. 66, no. 1, pp. 245–254.

Hofmann et al. 2019d
: Hofmann, B., O. Neitz, and T. F. Eibert (Aug. 2019d). "On the minimum number of samples for sparse recovery in spherical antenna near-field measurements". *IEEE Trans. Antennas Propagat.*, vol. 67, no. 12, pp. 7597–7610 (cit. on p. 121).

Hofmann et al. 2023a
: Hofmann, B., T. F. Eibert, F. P. Andriulli, and S. B. Adrian (Dec. 2023a). "A low-frequency stable, excitation agnostic discretization of the right-hand side for the electric field integral equation on multiply-connected geometries". *IEEE Trans. Antennas Propag.*, vol. 71, no. 12, pp. 9277–9288 (cit. on p. 33).

Hofmann et al. 2023b
: — (May 2023b). "An excitation-aware and self-adaptive frequency normalization for low-frequency stabilized electric field integral equation formulations". *IEEE Trans. Antennas Propag.*, vol. 71, no. 5, pp. 4301–4314 (cit. on pp. 46, 55).

Hofmann et al. 2023e
: Hofmann, B., P. Respondek, and S. B. Adrian (Nov. 2023e). "SphericalScattering: a Julia package for electromagnetic scattering from spherical objects". *J. Open Source Softw.*, vol. 8, no. 91, pp. 1–4 (cit. on pp. 45, 49, 71, 100, 115).

Hofmann et al. 2024c
: Hofmann, B., M. Mirmohammadsadeghi, T. F. Eibert, F. P. Andriulli, and S. B. Adrian (Apr. 2024c). "Low-frequency stabilization for the B-spline-based isogeometric discretization of the electric field integral equation". *IEEE Trans. Antennas Propag.*, vol. 72, no. 4, pp. 3558–3571 (cit. on p. 81).

Saurer et al. 2022
Saurer, M. M., B. Hofmann, and T. F. Eibert (Sept. 2022). “A fully polarimetric multilevel fast spectral domain algorithm for 3-D imaging with irregular sample locations”. *IEEE Trans. Microw. Theory Tech.*, vol. 70, no. 9, pp. 4231–4242 (cit. on p. 7).

Conference Proceedings

Hofmann et al. 2018b
Hofmann, B., O. Neitʒ, R. A. M. Mauermayer, and T. F. Eibert (Sept. 2018b). “Sparse recovery in spherical antenna near-field measurements”. In *Kleinheubacher Tagung*. Miltenberg, Germany (cit. on p. 121).

Hofmann et al. 2019a
Hofmann, B. and T. F. Eibert (July 2019a). “Sparse recovery with predictable accuracy in noisy spherical antenna near-field measurements”. In *Proc. IEEE Antennas Propag. Soc. Int. Symp.* Atlanta, GA, USA: IEEE, pp. 1857–1858 (cit. on pp. 121, 123).

Hofmann et al. 2019b
— (Aug. 2019b). “Sparse recovery with predictable accuracy in noisy spherical antenna near-field measurements”. In *Forum Electromagn. Res. Methods Appl. Techn.* Vol. 34 (cit. on p. 121).

Hofmann et al. 2019c
Hofmann, B., O. Neitʒ, and T. F. Eibert (June 2019c). “Applying compressed sensing with predictable accuracy to spherical antenna near-field measurements”. In *Proc. Photonics Electromagn. Res. Symp. (PIERS)*. Rome, Italy (cit. on p. 121).

Hofmann et al. 2020
Hofmann, B., O. Kraus, and T. F. Eibert (July 2020). “Robustness of sparse reconstruction methods in spherical antenna near-field measurements”. In *Proc. IEEE Antennas Propag. Soc. Int. Symp.* Montreal, Canada, pp. 1773–1774 (cit. on p. 121).

Hofmann et al. 2021a
Hofmann, B., T. F. Eibert, F. P. Andriulli, and S. B. Adrian (Dec. 2021a). “Low-frequency stable discretization of the electric field integral equation based on Poincaré’s lemma”. In *Proc. IEEE Antennas Propag. Soc. Int. Symp.* Singapore (cit. on p. 33).

Hofmann et al. 2021b
— (Aug. 2021b). “Towards accurate discretization of arbitrary right-hand side excitations on multiply-connected geometries”. In *Int. Conf. Electromagn. Adv. Appl. (ICEAA)*. Honolulu, HI, USA, pp. 312–312 (cit. on p. 33).

Hofmann et al. 2022a
Hofmann, B., F. P. Andriulli, and S. B. Adrian (July 2022a). “Niederfrequente Stabilisierung der elektrischen Feldintegralgleichung für (fast) beliebige Anregungen”. In *URSI Kommission B Workshop Felder und Wellen*. Raitenhaslach, Germany (cit. on pp. 33, 55).

Hofmann et al. 2022b
Hofmann, B., T. F. Eibert, F. P. Andriulli, and S. B. Adrian (Mar. 2022b). "Efficient combination of scalar-potential representations of solenoidal functions and quasi-Helmholtz projectors". In *Proc. 16th Eur. Conf. Antennas Propag. (EuCAP)*. Madrid, Spain (cit. on p. 33).

Hofmann et al. 2022c
— (July 2022c). "Low-frequency-stabilized electric field integral equation on topologically non-trivial geometries for arbitrary excitations". In *Proc. IEEE Antennas Propag. Soc. Int. Symp.* Denver, CO, USA (cit. on p. 55).

Hofmann et al. 2022d
— (May 2022d). "Towards a low-frequency-stabilized electric field integral equation on simply-connected geometries for arbitrary excitations". In *URSI Atlantic / Asia-Pacific Radio Sci. Conf.* Gran Canaria, Spain (cit. on p. 33).

Hofmann et al. 2022e
— (Sept. 2022e). "Über die Stabilisierung von Feldtransformationen im niederfrequenten Bereich basierend auf dem elektrischen Feldintegralgleichungsoperator". In *Kleinheubacher Tagung*. Miltenberg, Germany (cit. on p. 109).

Hofmann et al. 2023c
— (Mar. 2023c). "Investigations on the low-frequency stability of inverse surface source field transformations based on the electric field integral operator". In *Proc. 17th Eur. Conf. Antennas Propag. (EuCAP)*. Florence, Italy (cit. on p. 109).

Hofmann et al. 2023d
— (July 2023d). "Towards a self-adaptive frequency normalization scheme for the low-frequency stabilized magnetic field integral equation". In *Proc. IEEE Antennas Propag. Soc. Int. Symp.* Portland, OR, USA, pp. 1213–1214 (cit. on pp. 55, 150).

Hofmann et al. 2024a
— (Sept. 2024a). "A multiplicative Calderón preconditioner for the B-spline-based electric field integral equation". In *Int. Conf. Electromagn. Adv. Appl. (ICEAA)*. Lisbon, Portugal (cit. on p. 150).

Hofmann et al. 2024b
— (Sept. 2024b). "B-spline-based higher-order discretization of the magnetic field integral equation". In *Kleinheubacher Tagung*. Miltenberg, Germany (cit. on p. 150).

Hofmann et al. 2024d
Hofmann, B., M. Mirmohammadsadeghi, T. F. Eibert, F. P. Andriulli, and S. B. Adrian (July 2024d). "Quasi-Helmholtz projectors for the low-frequency stabilization of the isogeometrically discretized electric field integral equation". In *Proc. IEEE Antennas Propag. Soc. Int. Symp.* Florence, Italy (cit. on p. 81).

Mirmohammadsadeghi et al. 2024
Mirmohammadsadeghi, M., B. Hofmann, T. F. Eibert, F. P. Andriulli, and S. B. Adrian (Mar. 2024). “A loop-star decomposition for the B-spline based discretization of the electric field integral equation”. In *Proc. 18th Eur. Conf. Antennas Propag. (EuCAP)*. Glasgow, Scotland (cit. on p. 81).

Neitz et al. 2019a
Neitz, O., B. Hofmann, and T. F. Eibert (June 2019a). “Plane-wave field synthesis for monostatic RCS prediction from multistatic near-field samples on irregular grids”. In *Proc. Photonics Electromagn. Res. Symp. (PIERS)*. Rome, Italy (cit. on p. 7).

Software

Hofmann 2022f
Hofmann, B. (Aug. 2022f). *SphericalScattering*. Version v0.5.0. Genève, Switzerland (cit. on pp. 45, 71, 100).

Hofmann 2023f
— (Aug. 2023f). *NURBS*. Version v0.5.1. Genève, Switzerland (cit. on p. 99).

Supervised Student Projects

Research Internships

Ahmmad Zobaid 2023
: Ahmmad Zobaid, A. (Mar. 2023). *Comparison of Sparse Reconstruction Algorithms for Near-Field Antenna Measurements*. Research Internship. Munich, Germany: Technical University of Munich.

Fischer 2018
: Fischer, B. (Oct. 2018). *Analytic Field Expressions for Time-Harmonic Electric Current Loops*. Research Internship. Munich, Germany: Technical University of Munich.

Mirmohammadsadeghi 2021
: Mirmohammadsadeghi, M. (Sept. 2021). *Constructing Global Loops Employing a Topological Search Algorithm for a Low-Frequency Stabilization of the Electric Field Integral Equation*. Research Internship. Munich, Germany: Technical University of Munich.

Sturm 2020
: Sturm, S. (Feb. 2020). *Implementation and Performance Analysis of a Fast Basis Pursuit Solver in C/C++*. Research Internship. Munich, Germany: Technical University of Munich.

Bachelor's Theses

Hashas 2020
: Hashas, Ö. (Sept. 2020). *Comparison of Iterative Solvers in Inverse Surface Source Problems*. Bachelor's Thesis. Munich, Germany: Technical University of Munich.

Kraus 2019
: Kraus, O. (Dec. 2019). *Greedy and Thresholding Based Methods versus Basis Pursuit for Sparse Recovery in Spherical Antenna Near-Field Measurements*. Bachelor's Thesis. Munich, Germany: Technical University of Munich.

Yousfi 2022
: Yousfi, H. (July 2022). *Simulative Investigation of Small Loop Antennas for Near-Field Measurements*. Bachelor's Thesis. Munich, Germany: Technical University of Munich.

Master's Theses

Fruth 2023

Fruth, C. (Sept. 2023). *Subdivision Surfaces Based Discretization of the Electric Field Integral Equation*. Master's Thesis. Munich, Germany: Technical University of Munich.

Jukic 2023

Jukic, D. (Nov. 2023). *Implementation and Verification of the Multilevel Fast Multipole Method for Electromagnetic Scattering*. Master's Thesis. Munich, Germany: Technical University of Munich.

Luca 2022

Luca, L. I. (May 2022). *Global Loop Search via Reeb Graphs for Electromagnetic Scattering from Multiply Connected Geometries*. Master's Thesis. Munich, Germany: Technical University of Munich.

Mirmohammadsadeghi 2023

Mirmohammadsadeghi, M. (Feb. 2023). *Investigation of an Isogeometric Method-of-Moments Approach for the Electric Field Integral Equation*. Master's Thesis. Munich, Germany: Technical University of Munich.

Zimmermann 2022

Zimmermann, M. (Apr. 2022). *Investigation of Low-Frequency Stable Testing Schemes for the Magnetic Field Integral Equation*. Master's Thesis. Munich, Germany: Technical University of Munich.